Connective Tissue in the

Human Optic Nerve Head

A thesis submitted to Cardiff University for the degree of Doctor of

Philosophy

Hannah Jayne Jones

School of Optometry and Vision Sciences,

Cardiff University

April 2014

Abstract

Purpose: This thesis aimed to characterise and analyse the 3D micro- and nanoarchitecture of connective tissue within the lamina cribrosa (LC).

Methods: The microarchitecture of load-bearing connective tissue components, elastin and fibrillar collagen, of the young, elderly and glaucomatous optic nerve head (ONH) was analysed following two-photon excited fluorescence, second harmonic generation and small angle light scattering. Microfocus and conventional small angle X-ray scattering were used to analyse ONH nanoarchitecture and the potential of X-ray microtomography (XMT) as a 3D imaging technique was evaluated.

Results: Fibrillar collagen and elastic fibres stretched radially across the optic nerve (ON) canal in the LC, encircled the central retinal vessels and were absent in the prelamina. In the postlaminar ON septae, collagen was perpendicular to that in the LC. Differences in young and elderly ONH tissue included; wavy collagen bundles exclusively within the young ONH and distinct elastic fibres found in the elderly ONH. Analysis of ONH reconstructions of 3D SHG datasets revealed that elderly LCs contained higher fibrillar collagen content when compared to the young LCs. Interestingly, the connective tissue beams of the inferior-temporal LC quadrant were significantly more aligned in glaucoma when compared to age-matched controls. Distinct X-ray reflections, potentially elastin in the peripapillary sclera and representative of CNS myelin in the postlaminar ON were identified. XMT enabled quantification of the regional variation in LC thickness, connective tissue content, pore area and pore count, showing potential for 3D quantification without the need for tissue sectioning.

Conclusion: Differences in the young and elderly ONH microarchitecture and nanoarchitecture include fibrillar collagen content, alignment and packing and the presence of elastic fibres. These data will be important for the development of finite element models that can predict ONHs at risk of developing glaucomatous optic neuropathy.

Acknowledgments

I would like to thank the following people for their endless support and patience throughout my PhD.

Firstly, I would like to thank my supervisors, Dr. Julie Albon, Mr. Nick White, Dr. Craig Boote and Professor Keith Meek. Thank you to Craig and Keith for their expert knowledge of X-ray diffraction and putting up with my silly questions. Thank you to Nick for his patience while training me and for all of the interesting discussions we've had that have sparked my interest in microscopy and image analysis. Finally, I cannot thank my main supervisor Julie enough for the support and encouragement she has given me since my first day as her student. She has moulded me into a confident researcher and pushed me further than I could ever imagine.

I would also like to thank our numerous collaborators. Thank you to Professor Ross Ethier and Dr. Michael Girard for allowing us to use their small angle light scattering system and for their help during the analysis. Thank you to Dr. Nick Terrill and Dr. Jen Hiller of Diamond Light Source for their support during, and between, our visits. Thank you to Dr. Graham Davis and Dr. David Mills for performing the X-ray microtomagraphy imaging and useful correspondence afterwards. Thank you to Professor Tim Wess and Dr. Kate Patten for performing principal components analysis on our x-ray scattering datasets, which although did not make it into the PhD, will form an interesting future study.

Thank you to the BBSRC and Thermo Fisher Inspire Award for the funding of this PhD and to the staff of Bristol Corneal Transplant Service Eye Bank and Dr. Michael Fautsch of the Mayo Clinic for providing the human tissue, without all of which this PhD could not have been performed.

Thank you also to the research associates of the School of Optometry and Vision Sciences, past and present. I would like to thank Dr. Kate Powell and Dr. Debbie Tudor for knowledge, advice and a friendly ear when needed at the beginning of my PhD.

Table of Contents

List of Abreviations

ANOVA – Analysis of variance

CAT – Computed axial tomography

DOFA – Degree of fibre alignment

GAG – Glycosaminoglycan

IOP – Intraocular pressure

LAC – Linear attenuation coefficient

LC – Lamina cribrosa

ON – Optic nerve

ONH – Optic nerve head

PBS – Phosphate buffered saline

PFA – Paraformaldehyde

PFO – Preferred fibre alignment

POAG – Primary open angle glaucoma

PostL – Postlaminar region

PreL – Prelamina

PCA – Principal components analysis

PTA – Phosphotungstic acid

RGC – Retinal ganglion cell

SALS – Small angle light scattering

SAXS – Small angle X-ray scattering

SHG – Second harmonic generation

TPEF – Two photon excited fluorescence

WAXS – Wide angle X-ray scattering

XMT – X-ray microtomography

Table of Figures

Table of Tables

Chapter 1 - Introduction

1.1 The Optic Nerve and the Optic Nerve Head

When light enters the human eye through the pupil and causes photochemical reactions in the retinal photoreceptors, the information produced from the stimulus is transported from the retina to the brain by just over 1 million axons that constitute the optic nerve (ON). The majority of the axons are concerned with vision (Hogan et al., 1971) and arise from the neural retina's retinal ganglion cell (RGC) layer and synapse at the lateral geniculate body (Anderson, 1973). The axons track to the posterior of the eye where they converge at the optic disc. The ON axons are laterally separated from the retina and choroid by glial cells. After passing through the connective tissue plates of the lamina cribrosa (LC) the RGC axons become myelinated as they exit the eye globe (Figure 1.1).

The optic nerve head (ONH) can be thought of as the tissues that encompass the anterior termination of the ON; namely the optic disc surface, extending back to the LC and myelinated ON. The ONH is an important pathological site with regards to optic neuropathy as it can suffer from characteristic structural changes, such as those witnessed in glaucoma (Quigley and Addicks, 1981, Jonas et al., 1991, Fontana et al., 1998, Tezel et al., 2004), which may create an unfavourable environment for the traversing RGC axons that rely on the stability and support of the ONH connective tissue and glial framework.
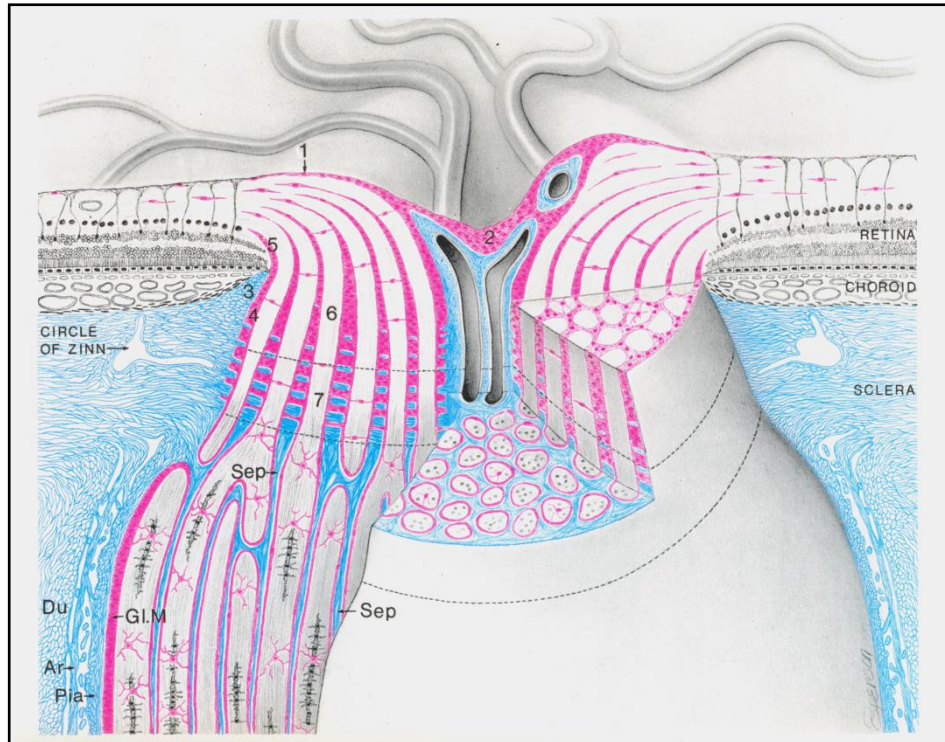
Figure 1.1. Diagram of the optic nerve head. (1) indicates the "inner limiting membrane of Elschnig" which thickens at the centre of the optic disc (2). (3) indicates the border tissue of Elschnig which lies between the stroma of the choroid and the astrocytes (coloured pink) at the periphery of the optic nerve canal (4). These astrocytes terminate at the retina at (5) and continue downwards along the nerve forming a surrounding mantle (GI.M). The nerve fibres of the retina are separated by astrocyte columns (6) and form fascicles (7) as they enter the lamina cribrosa (indicated by upper and lower dotted line). At the lamina cribrosa these fascicles are separated by an extracellular matrix of connective tissue that form cribriform plates (coloured blue). In the postlaminar region the nerve fibres become longitudinally separated by connective tissue (Sep) and become myelinated. The meninges, the dura mater (Du), arachnoid mater (Ar) and pia mater (Pia) are also indicated. Adapted from Anderson (1969) and reprinted with permission from the American Medical Association: Archives of Ophthalmology (Appendix 1).

1.2   Anatomy of the Optic Nerve Head

The ONH can be anatomically divided into prelamina, LC and postlaminar ON regions.

1.2.1   Prelamina

The prelamina of the ONH is composed of RGC axons that converge at the optic disc. Here they segregate into small axonal fascicles and rotate at a 90° angle as they traverse

the level of the sclera to form the ON. Populations of astrocytes in this region provide essential support to the fascicles. Glial fibrillary acidic protein (GFAP) positive astrocytes form the thin inner limiting membrane of Elschnig (Figure 1.1) that separate the optic disc from the vitreous surface (Oyama et al., 2006). Astrocytes that stain positive for both GFAP and the neural cell marker HNK-1/N-CAM form glial columns within the prelamina between the axon fascicles. Other GFAP positive astrocytes are found orientated perpendicularly to the axon fascicles that pass through (Ye and Hernandez, 1995). The latter astrocyte population extend delicate, thin processes into the axons forming supportive scaffolding (Elkington et al., 1990, Oyama et al., 2006).

1.2.2 Lamina Cribrosa

It is believed that the LC serves two purposes; namely that it forms a scaffold for the passage of nerve fibre fascicles and that it strengthens the posterior eye, therefore protecting it from injury at the site where the ON exits (Hogan et al., 1971). However, this region of the ONH is considered to be the site of axonal damage in glaucoma (Vrabec, 1976, Quigley and Addicks, 1981, Quigley et al., 1981, Howell et al., 2007).

The LC is composed of approximately 10 plates, known as cribriform plates, formed from connective tissue beams which extend across the ON canal at the level of the sclera (Hogan et al., 1971). It has been shown that the LC has an extracellular matrix that is distinct from the surrounding sclera tissue (Hernandez et al., 1986, Albon et al., 1995) and its insertion in the sclera is supported by tightly packed collagen and elastin containing fibres (Hernandez et al., 1987, Hernandez and Neufeld, 1989).

The cribriform plates contain numerous openings, or pores, that are approximately 100μm in diameter and allow for the exit of the fascicles of nerve fibres from the inner eye globe (Elkington et al., 1990, Oyama et al., 2006). These pores give the LC a "sieve-like" appearance (Figure 1.2).
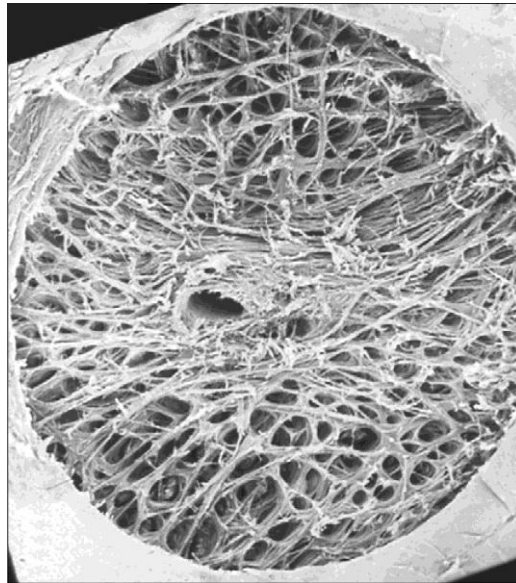
Figure 1.2. Sieve-like appearance of the human lamina cribrosa. Scanning electron micrograph, viewed from the vitreous side of the nerve. Copied from Quigley (2011) and reprinted with permission from Elsevier Limited (Appendix 2).

GFAP and HNK-1/N-CAM positive astrocyte columns surround the nerve fibre fascicles, separating them from the connective tissue beams (Ye and Hernandez, 1995, Oyama et al., 2006). Similar to the prelamina, GFAP positive astrocytes extend thin processes into the axon fascicles (Ye and Hernandez, 1995). The astrocyte/cribriform plate interface is also separated by a well-defined basement membrane (Morrison et al., 1989b). GFAP negative LC cells are found within the cribriform plates. These cells resemble myofibroblasts and, together with astrocytes, are thought to play a part in the maintenance and synthesis of the extracellular matrix components of the LC (Hernandez et al., 1988). The metabolic importance of the astrocytes of the LC has been highlighted

by a recent study using a hypertensive rat model which found that with elevated IOP, processes of "fortified" astrocytes disassociate from the circumferential ON connective tissue resulting in axonal loss (Dai et al., 2012).

The LC is not a homogenous structure. Research by Quigley and Addicks (1981), involving the use of scanning electron microscopic examination, demonstrated that the surface structure is saddle-like with the nasal-temporal axis placed closer to the vitreous surface than the superior and inferior zones. This is supported by optical coherence tomography *in vivo* imaging of the anterior surface of the human LC (Park et al., 2012c). The inferior and superior LC zones have also been observed to contain larger pores separated by thinner connective tissue beams when compared to the nasal and temporal zones (Quigley and Addicks, 1981, Radius, 1981, Oyama et al., 2006). This observation was quantitatively confirmed by Jonas et al. (1991) who found that the average single pore and summed pore areas were significantly larger in the superior and inferior zones when compared to the temporal and nasal zones. The pores also increased in size with greater distance from the central region towards the peripheral LC (Jonas et al., 1991).

1.2.3 Postlaminar Optic Nerve

The postlaminar ON is the site of transition from the connective tissue of the LC to connective tissue septa of the extra-ocular ON. In this region the axons become myelinated leading to thicker axon fascicles, reaching approximately 150μm in diameter (Oyama et al., 2006). This results in an overall widening of the ON canal.

The tissue septa are formed from collagenous extensions of the pia mater and partially enclose the nerve fascicles. The discontinuous septa appear thicker than the LC beams and fewer elastic fibres are found here when compared to the LC (Oyama et al., 2006).

The limiting membrane at the periphery of the nerve contains astrocytes that express only GFAP with occasional clusters of HNK-1/N-CAM and GFAP positive astrocytes (Ye and Hernandez, 1995). The myelinated nerve fascicles contain oligodendrocytes and astrocytes that express the neural cell marker A2B5 and GFAP (Ye and Hernandez, 1995).

1.3 Components of the Lamina Cribrosa Extracellular Matrix

The extracellular matrix of the ONH provides support and anchorage for the axon fascicles that pass through. The matrix is formed from an assembly of connective tissue components including collagen, elastin, glycoproteins and proteoglycans. The major load-bearing components of the ONH extracellular matrix are collagen and elastin and the distribution of these connective tissue elements within the LC is integral to its structure and supportive function.

1.3.1 Collagen

Collagen is the most prevalent component of the extracellular matrix and is important in giving structure, support and tensile strength to tissues (Vogel, 1974). There are twenty-nine genetically and chemically distinct types of collagen in vertebrates and a number of proteins contain collagenous domains (Veit et al., 2006, Shoulders and Raines, 2009). The different collagen types are often characterised by their biochemical make-up and classified according to their ability to form different supramolecular structures.

All collagen molecules are based on three, parallel left-handed polypeptide α chains that coil around each other to form a right-handed triple helix. The form of this triple helical structure is stabilised by hydrogen bonds between the polypeptide chains and relies on the high glycine content (33% of amino acid residues) within the chains. The primary structure of the α chain is a repetitive sequence of -Gly-X-Y-, where X and Y can be any amino acid. This repeat is found in all collagen types but may be interrupted in nonfibrillar collagens (Brazel et al., 1987). The amino acid at X is often proline and at Y is often the post-translational modification of proline, 4-hydroxyproline (Bella et al., 2006). There appears to be no constraint on the location of proline, as it can appear before and after the glycine residue, normally in hydroxylated form and non-hydroxylated form, respectively (Foster et al., 1973).

The collagen molecule is highly asymmetric and possesses three domains, the NH_2-terminal nonhelical domain, the central helical domain (which is interrupted by nonhelical domains in some collagen molecules), and the COOH- terminal nonhelical domain. Figure 1.3 shows an example of a type I collagen molecule.
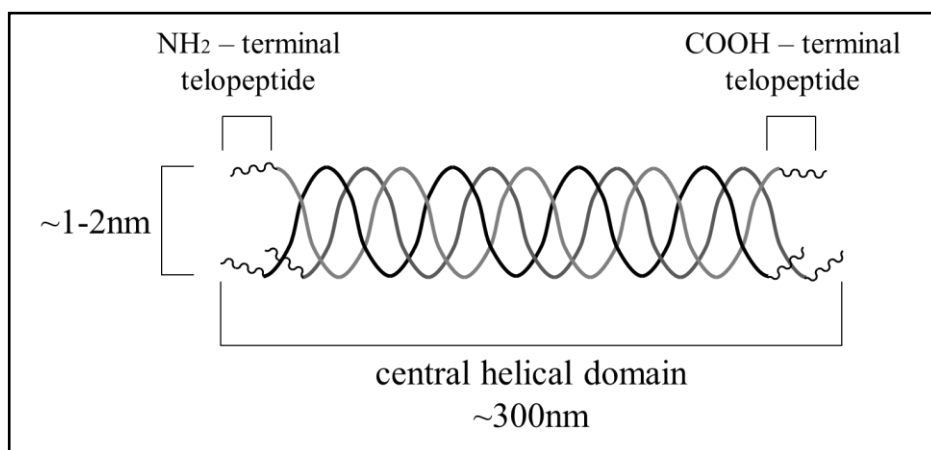
Figure 1.3. Schematic diagram of the helical and nonhelical domains and dimensions of a collagen type I molecule. Adapted from Gay and Miller (1978).

1.3.1.1 Collagen Types

Under appropriate conditions a collagen molecule can be denatured and its constituent chains recovered. Each α chain contains approximately 1050 amino acid residues (Gay and Miller, 1978). The α chains form the basis for the discrimination between the distinct types of collagen, which are denoted by roman numerals, e.g. type I, type II. Different α chains have different primary structures and are distinguished from each other with arabic numerals, e.g. α1, α2. The chains also differ between collagen types, i.e. α1(I) will have a different primary structure than α1(II). Some collagen are heterotrimeric so do not contain 3 identical α chains, for example, collagen type I contains two α1(I) chains and one α2(I) chain.

Collagens can be classified into fibrillar, network-forming, FACITs (fibril-associated collagens with interrupted triple helices), MACITs (membrane-associated collagens with interrupted triple helices) or MULTIPLEXINs (multiple triple-helix domains and interruptions) (Shoulders and Raines, 2009). The majority of collagen types that have been localised to the ONH can be classified as either fibrillar or network forming.

Typical fibrillar collagens are composed of molecules with a continuous helical domain (Exposito et al., 2010). The assembly of the fibrils formed from these collagens is regulated by charged and hydrophobic amino acid residues, and the fibrils themselves have an axial repeat pattern of 67nm and a homologous banding pattern (Kucharz, 1992) (Figure 1.4). Types I-III are sometimes referred to as the interstitial collagens as the fibres they form are commonly found in the spaces between cells.
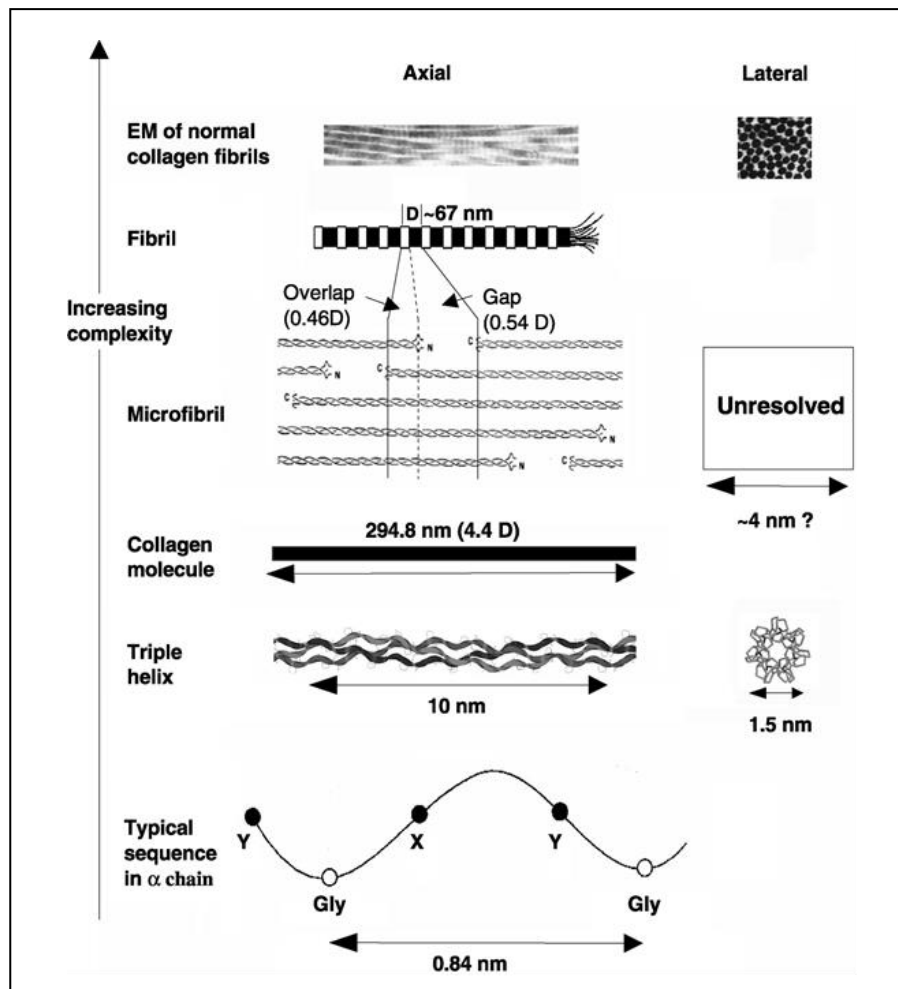
Figure 1.4. Collagen fibril formation. Collagen molecules, consisting of 3α chains arranged in a triple helical formation, aggregate in a 67nm staggered axial array to form fibrils. Copied from Orgel et al. (2001) and reprinted with permission from Elsevier Limited (Appendix 3).

Nonfibrillar, network forming collagens, such as type IV, are composed of molecules with helical domains that are interrupted by nonhelical regions. These collagens are not organised as fibrils but aggregate loosely to form lattice-like structures (Figure 1.5), such as those needed for the flexibility and mechanical stability of basement membranes (Timpl et al., 1981).
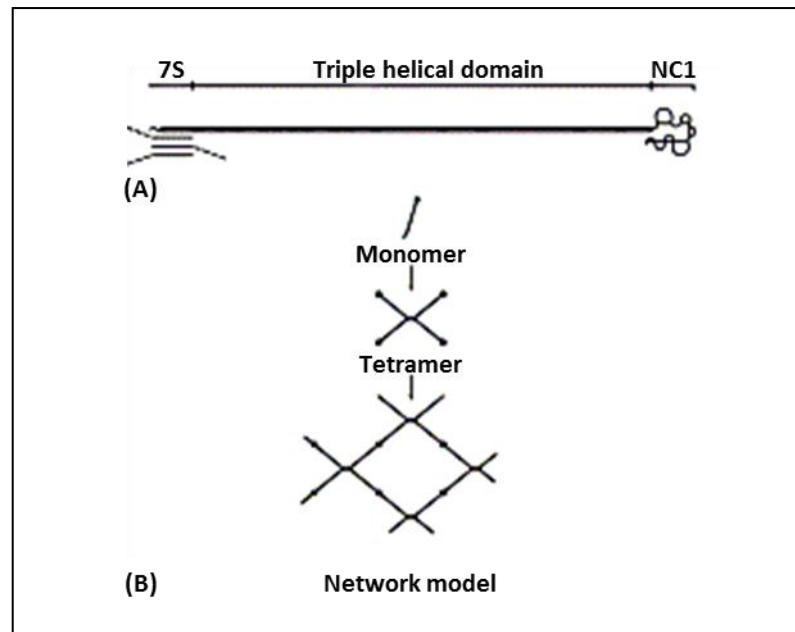
Figure 1.5. Proposed model for collagen network formation. (A) Type IV collagen molecules, consisting of 3α chains arranged in a triple helical formation with aminoterminal (7S) and carboxyterminal (NC1) domains, form (B) tetramers and larger networks through interactions between multiple NC1 domains. Copied from Krag and Andreassen (2003) and reprinted with permission from Elsevier Limited (Appendix 4).

Some collagen types form filamentous networks, e.g. type VI. These types form the microfibrillar components of tissue and may function in anchoring interstitial structures, such as nerves and blood vessels, to surrounding connective tissue (Keene et al., 1988, Bonaldo et al., 1990) and basement membranes (Kuo et al., 1997).

1.3.1.2 *Distribution of Collagen in the Lamina Cribrosa and Surrounding Tissue*

The specific characterisation of the extracellular components of the LC allows an understanding of the processes and biomechanics that are involved in its distortion, e.g. during elevated intraocular pressure (IOP). There are numerous immunolocalisation studies within the literature that examine the collagenous extracellular matrix of the LC in human (Hernandez et al., 1986, Hernandez et al., 1987, Rehnberg et al., 1987, Goldbaum et al., 1989, Morrison et al., 1989a, Albon et al., 1995, Albon et al., 2000a) and other animal (Morrison et al., 1988, Morrison et al., 1989b, Morrison et al., 1995,

Brooks et al., 2000, Albon et al., 2007) specimens. These studies have shown that collagen types I, III, IV, V and VI are distributed throughout the LC. Collagen type VIII has also been located in the cribriform plates using immunohistochemistry (Tamura et al., 1991), however evidence of the presence of this type is limited.

In human and primate specimens, network forming collagen type IV has been observed to co-distribute with laminin forming an interface between the LC beams and neural tissue and along the margins of the blood vessels within the beams (Hernandez et al., 1986, Hernandez et al., 1987, Morrison et al., 1988, Goldbaum et al., 1989, Morrison et al., 1989a, Morrison et al., 1989b). It forms a major constituent of the basement membrane of the astrocytes surrounding the axonal fascicles (Morrison et al., 1989b, Albon et al., 1995). It has also been shown to line the border of the LC insertion region and peripheral nerve fascicles in monkey specimens (Morrison et al., 1988, Morrison et al., 1989b) and to co-distribute with elastin at this site in humans (Hernandez et al., 1987).

Fibrillar collagen types I and III have been found to distribute within the cores of the cribriform plates and blood vessel walls (Hernandez et al., 1986, Hernandez et al., 1987, Morrison et al., 1988, Goldbaum et al., 1989, Morrison et al., 1989a, Quigley et al., 1991a, Albon et al., 1995). The fibrils formed by these collagens in the human LC have been shown to have a mean fibril diameter of 47.4nm, which is half of the mean diameter of the fibrils found in the peripapillary sclera (Quigley et al., 1991b).

Fibrillar collagen type V has been localised within the cribriform plates with types I and III and, like type IV, associated with vascular and astrocyte basement membranes

(Morrison et al., 1989b). It has also been found to co-distributed with type VI within the walls of the central retinal vessels (Goldbaum et al., 1989, Albon et al., 1995).

1.3.2 Elastin

Elastin is found within tissues in the form of elastic fibres. Elastin forms from the cross-linking and self-assembly of multiple tropoelastin monomers on a microfibril scaffold (Figure 1.6) thus, elastic fibres consist of two components; the first is an amorphous elastin component which is surrounded by a second elastin-associated microfibrillar component (Greenlee et al., 1966, Ross and Bornstein, 1969).
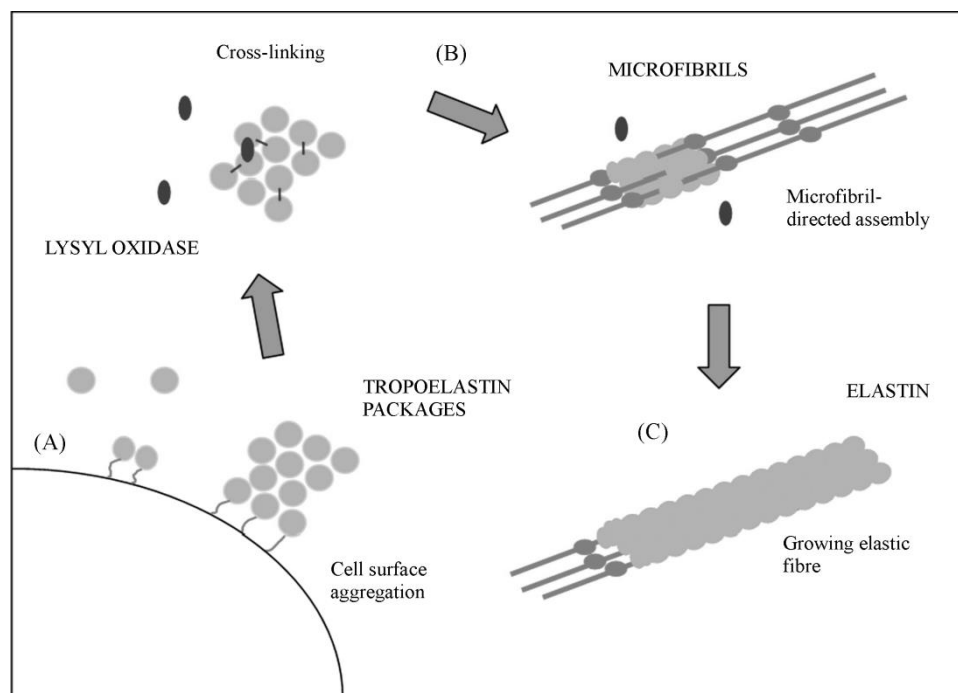
Figure 1.6. Assembly mechanism of elastic fibres. (A) Tropoelastin is secreted and forms aggregations on the cell surface. (B) Tropoelastin bundles are then released, cross-linked and (C) incorporated into microfibril scaffolds forming elastic fibres. Copied from Wise and Weiss (2009) and reprinted with permission from Elsevier Limited (Appendix 5).

The amorphous elastin core makes up 90% of the mature fibre and lacks any regular structure. Like collagen, elastin has a high glycine and proline content, occupying 33%

and approximately 11% of the amino acid residues, respectively (Rosenbloom et al., 1993). Unlike collagen, the proline residue is rarely hydroxylated and is usually found before a glycine residue and seldom proceeds it (Foster et al., 1973). The microfibrils are thought to contain more than one protein and exist as fine, tubular structures with a diameter of 10-12nm (Greenlee et al., 1966, Ross and Bornstein, 1969).

Elastic fibres behave like a biological rubber and provide connective tissue with elasticity. Although the mechanism of elastin elasticity is not fully understood, evidence suggests that it may be a combination of hydrophobic and librational entropic effects (Tarakanova and Buehler, 2013) where hydrophobic surface area increases on low elastic fibre extension (Wasserman and Salemme, 1990) and libration decreases on longer extensions (Chang and Urry, 1988).

1.3.2.1 *Distribution of Elastin in the Lamina Cribrosa and Surrounding Tissue*

The elastic fibres within the human LC and its surrounding areas has been investigated using techniques involving histological staining (Oyama et al., 2006), electron microscopy (Quigley et al., 1991a) and immunohistochemical analysis involving antibodies against α-elastin (Hernandez et al., 1987, Hernandez and Neufeld, 1989, Hernandez, 1992) and the microfibrillar component, fibrillin (Morrison et al., 1989a).

Within the LC beams, elastin has been shown to run parallel with the collagen bundles (Hernandez et al., 1987, Quigley et al., 1991a, Hernandez, 1992, Oyama et al., 2006). Studies using immunohistochemical analysis revealed that longitudinal elastin containing fibres formed part of the core of the cribriform plates with collagen type III (Hernandez et al., 1987, Hernandez and Neufeld, 1989, Hernandez, 1992).

Immunochemical studies have revealed that the peripapillary sclera contains more α-elastin and microfibrils than the sclera beyond this region (Morrison et al., 1989a, Quigley et al., 1991a). As previously mentioned, elastin has been found, with type IV collagen, at the LC insertion region forming major components of this area (Hernandez et al., 1987). The elastic tissue at this site forms a band that rings around the LC and enters the cribriform plates as fibres orientated perpendicularly from the circumference (Hernandez et al., 1987, Quigley et al., 1991a).

1.4 Age-related changes in the Lamina Cribrosa

1.4.1 Cross-linking

Both collagen and elastin have slow tissue turnover rates and so become predisposed to changes with age. During ageing of the LC, it has been proposed that the stiffness of collagen fibrils may be dramatically increased by the formation of intermolecular cross-links (Albon et al., 1995, Albon et al., 2000b). There are two major cross link processes: the stabilisation of collagen fibrils through lysyl oxidase and a process that is based on the reaction with glucose or its metabolites. These processes are also known as the enzyme-mediated cross-linking and non-enzymatic glycation, respectively.

Enzyme-mediated cross-linking involves the oxidative deamination of terminal lysines by lysyl oxidase forming lysyl aldehyde. This product is able to form covalent cross-links which bind molecules in fibril formation and aid inter-fibrillar cross-linking between adjacent fibrils.

Glycation involves an interaction between glucose and lysine forming hexo-lysines which in turn undergo the Amadori rearrangement and oxidative modification resulting in the formation of advanced glycation end-products (Bailey, 2001). These end-products are able to form inter-molecular cross-links after a series of complex reactions.

Levels of the cross-link pentosidine, an advanced glycation end product, i.e. a collagen cross-link derived from non-enzymatic glycation, increases in the LC as a result of increased tissue age (Albon et al., 1995). With regards to enzyme-mediated cross-links in the ageing LC, levels of the mature elastin cross-links, desmosine and isodesmosine, have been shown to increase with age (Albon et al., 2000a), whereas no variation in the levels of the mature collagen cross-link hydroxylysyl pyridinoline has been identified (Albon et al., 1995).

1.4.2 Changes of Lamina Cribrosa Extracellular Matrix with Age

1.4.2.1 Collagen

Total collagen present in the LC, as a percentage of dry tissue weight, has been shown to increase from 20% in the young LC to about 50% in the elderly LC (Albon et al., 1995). Collagen types I, III, IV (Hernandez et al., 1986, Hernandez and Neufeld, 1989, Morrison et al., 1989a) and VIII (Tamura et al., 1991) immunoreactivity have all been shown to increase with age.

Collagen type III has either been absent (Hernandez et al., 1986) or sparsely found along the LC beams (Morrison et al., 1989a) in young tissue. In contrast, heavy labelling for type III has been observed within the LC beams in adult donor material (Hernandez et al., 1986, Morrison et al., 1989a). Collagen type I has also been shown to

increase in density within the LC beams with age (Hernandez et al., 1989, Morrison et al., 1989a). This finding supports work by Quigley (1977) which suggest that collagen appears in the LC *in utero* and accumulates after birth.

With regards to the relationship between type I and III, Morrison et al. (1989a) found that young, neonatal LCs showed stronger labelling for type III than type I. Interestingly, Type III collagen has been seen to undergo a linear age related decrease relative to type I collagen (Albon et al., 1995). These results demonstrate that the relationship of high predominance of collagen type III and sparse levels of type I in young LCs is reversed as the tissue ages resulting in lower levels of type III relative to type I collagen in adult material. However, it is proposed that the levels of both types increase with age regardless of the change in their ratio (Hernandez et al., 1991, Albon et al., 1995).

Collagen type IV has also been observed to increase in density with age (Hernandez et al., 1986, Hernandez and Neufeld, 1989). However, changes with age of the thickness of basement membranes surrounding the cribriform plates has not been observed (Hernandez and Neufeld, 1989).

These results are further supported on a molecular basis by Hernandez et al. (1991) who demonstrated that collagen type I and IV mRNA expression is not abundant in foetal ONHs but highly expressed in adult ONHs suggesting that age-related accumulation of these proteins is due to their continuous synthesis throughout life.

1.4.2.2   Elastin

Like total collagen content, elastin content also increases as a function of age. It has been shown to increase from 7% of dry tissue weight in the 0-9 year old LC to 28% in the 80-89 year old LC (Albon et al., 2000a).

The arrangement of elastin has been shown to change from loosely packed, sparse fibres in young eyes to abundant, densely packed, distinct fibres within the LC beams in adult eyes (Hernandez and Neufeld, 1989). Labelled microfibril-associated elastic tissue has also been shown to follow this pattern of distribution with ageing (Morrison et al., 1989a). Furthermore, in the sclera, elastin and fibrillin labelling was restricted to the peripapillary sclera in the adult eye, while in the young eye it was observed in all regions of the posterior sclera (Hernandez and Neufeld, 1989, Morrison et al., 1989a).

Using immuno-electron microscopy, elastin was shown to distribute as fibres within the sclera adjacent to the ON in foetal eyes, aggregated as microfibrils within the LC beams in newborn eyes, and as long, distinct fibres running longitudinally through the cribriform plates in adult eyes (Hernandez, 1992). Fibre thickness was also found to increase with adult age (Hernandez, 1992).

1.5   Ageing of the Optic Nerve Head

Age-related changes within the ONH include an increase in optic cup diameter and area and subsequent increase in optic cup to disc ratio (Garway-Heath et al., 1997, Healey et al., 1997, Klein et al., 2006, Sung et al., 2009). The overall age-related total increase in connective tissue components of the LC indicates an increased thickness of the LC beams (Hernandez and Neufeld, 1989, Morrison et al., 1989a), subsequently leading to

changes in the ratio of pore to inter-pore tissue area within the cribriform plates (Ogden et al., 1988) and an increased thickness of the LC as measured from the most anterior LC plate to the point of axonal myelination (Kotecha et al., 2006).

Studies have also commented on the decrease of nerve fibre counts with increasing age (Dolman et al., 1980, Jonas et al., 1990). The extracellular matrix of the LC has been implicated as one of the factors that may contribute to this decrease due to the fact that the LC provides structural support to the nerve fibres. Therefore changes within its constituents, i.e. with age, will affect the function it provides.

It has been reported that the proportion of the LC occupied by pores decreased significantly with age as indicated by the increase of inter-pore tissue, without any change in cross-sectional area (Ogden et al., 1988). It was suggested that this results in a continuous loss of nerve fibres of about 5% per decade, amounting to a net loss of about 20% of the ON fibre mass by age 74. Therefore it is implied that age related loss of nerve fibre mass correlates with an increase in inter-pore connective tissue content within the LC.

The changes in specific connective tissue constituents with age, as described previously, and the overall increase in LC thickness (Kotecha et al., 2006) may influence the biomechanical compliance of the LC which has been shown to decrease with age (Albon et al., 2000b). The change in collagen type I: type III ratio with increasing age (Albon et al., 1995) is likely to contribute to the reduction in reversibility of the LC and its increased rigidity (Albon et al., 2000a) as collagen type I fibrils are larger and less flexible than type III (Silver et al., 2002). A stiffer and less resilient LC has the potential to influence the susceptibility of RGC axonal damage during increased IOP and may

contribute to the age-related increase in susceptibility of axons to chronic open-angle glaucoma. For instance, a change in LC response to IOP related stress could be especially detrimental to the 8-12% of axons that deviate from the direct route through the LC and run between the cribriform plates (Morgan et al., 1998).

1.6 The Optic Nerve Head in Glaucoma

The term glaucoma is used to encompass a range of ocular diseases that are associated with a loss of RGCs and their axons. This optic neuropathy is characterised by cupping of the optic disc (Figure 1.7B,D), changes within the ONH (Figure 1.7F) and a typical pattern of irreversible visual loss. It is the second most common cause of blindness is the UK (Bruce et al., 1991) attributing to approximately 10% of blindness registrations (NICE, 2009).

Glaucoma may be primary or secondary onset depending on whether the individual has a primary ocular defect, or whether the defect has been induced by a secondary condition such as inflammation, drug therapy or head trauma. Glaucoma may also be divided into open-angle or closed-angle subgroups depending on whether the angle between the iris and cornea is normal or narrow and mechanically blocking the trabecular meshwork in the anterior chamber of the eye.

The most common glaucoma type is primary open-angle glaucoma (POAG) affecting approximately 480, 000 individuals in the UK (NICE, 2009). POAG occurs when the trabecular meshwork becomes chronically obstructed, increasing resistance to aqueous humour outflow (Grant, 1955, Grant, 1958, Weinreb and Khaw, 2004). This obstruction, in most cases, leads to an increase in IOP, which is classed as a major risk

factor of POAG development, along with family history, ethnicity and age (Tielsch et al., 1991, Coleman and Miglior, 2008).
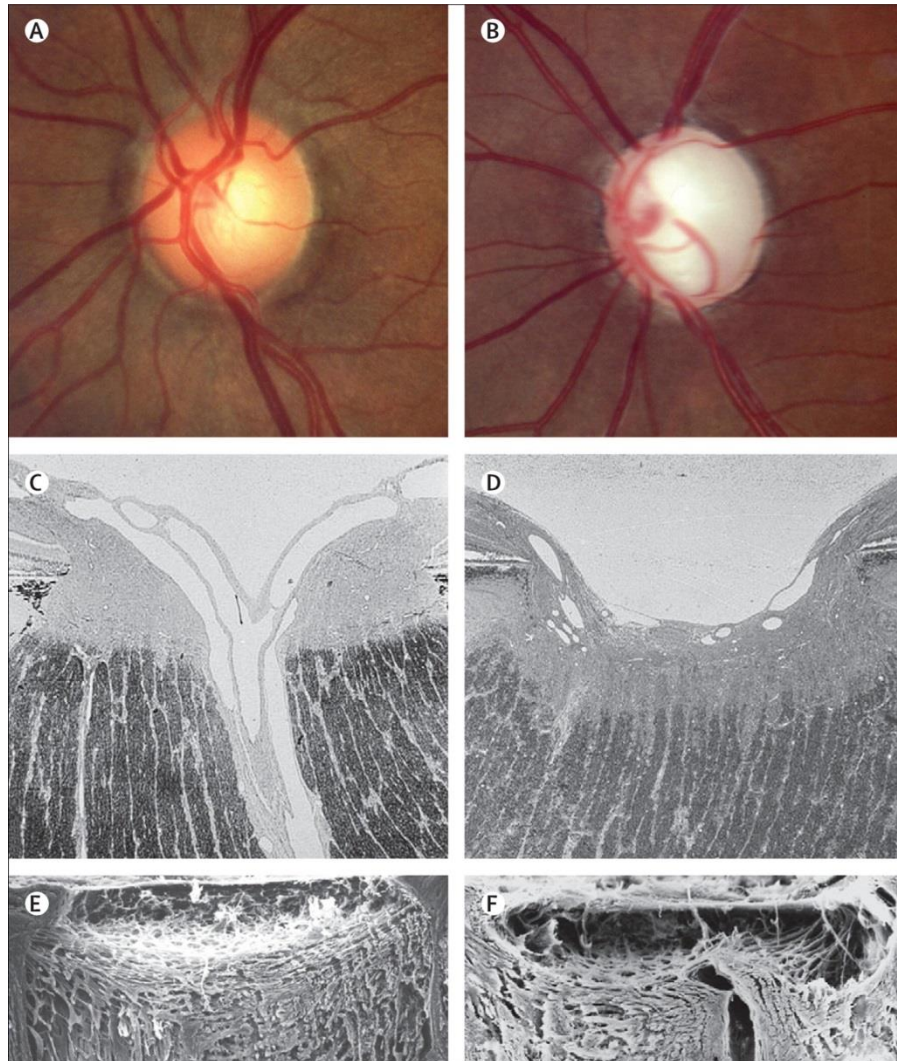
Figure 1.7. Features of a healthy and glaucomatous ONH. (A) The healthy optic disc has a small, central pale area (cup) surrounded by a rim of neuronal tissue while (B) the glaucomatous disc has no rim and a very pale cup occupying the majority of the disc. (D) Tissue loss causes the cup at the optic disc to become wider and deeper in glaucoma compared to (C) the normal histological structure of the ONH. (F) The connective tissue of the LC also becomes deformed and excavated in glaucoma compared to (E) the normal bowed LC. Taken from Quigley (2011) and reprinted with permission from Elsevier Limited (Appendix 2).

The LC has been shown to compress and deform backwards in human glaucoma (Quigley et al., 1981, Quigley et al., 1983), and monkey ocular-hypertensive models

(Bellezza et al., 2003, Yang et al., 2007, Roberts et al., 2009). Changes in the structural integrity of the LC combined with axonal damage in this area (Vrabec, 1976) have led to the hypothesis that this structure within the ONH is a major pathological site in POAG.

There are a number of theories proposed to describe the onset of glaucomatous damage (Figure 1.8).
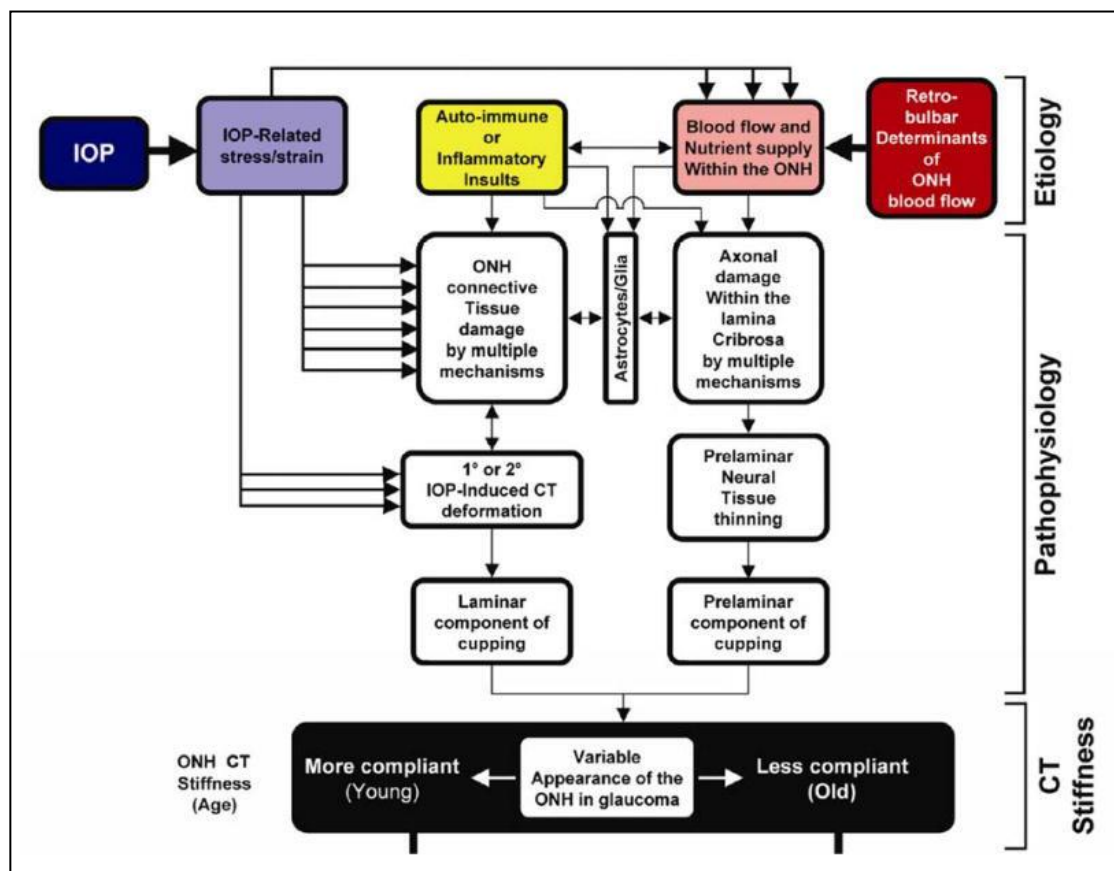
Figure 1.8. Theories of axonal and ONH connective tissue damage in glaucoma. IOP-related and non-IOP-related effects are thought to lead to connective tissue and axonal damage within the ONH which are thought to be mediated by astrocyte/glial responses. Differences in the appearance of the glaucomatous ONH are believed to be caused by differences in ONH mechanical properties. Copied from Burgoyne and Downs (2008) and reprinted with permission from Lippincott Williams and Wilkins/Wolters Kluwer Health: Journal of Glaucoma (Appendix 6).

IOP-related stress and strain in the ONH connective tissue are believed to cause connective tissue and axonal damage through mechanical and ischemic mechanisms (Burgoyne et al., 2005). Other theorised non-IOP-related mechanisms include autoimmune or inflammatory insults and retrobulbar determinants of ocular blood flow (Figure 1.8). Therefore, glaucoma is likely to be a multifactorial disease with a combination of factors leading to its pathology (Burgoyne and Downs, 2008).

1.7 Changes of the ONH Extracellular Matrix in Glaucoma

1.7.1 Collagen

Total collagen concentration, as measured by the quantification of collagen specific amino acids, was shown to be approximately 30% more in glaucomatous ONHs when compared to normal ONHs (Tengroth and Ammitzbøll, 1984). It was suggested that these results may either be due to an increase in the quantity of collagen or a change in collagen type ratios, therefore changing the connective tissue organisation of the ONH.

ONHs of glaucomatous human eyes (Hernandez et al., 1990) and ocular hypertensive monkey eyes (Morrison et al., 1990), showed an increase in basement membrane material. Intense immunohistochemical labelling for collagen type IV was observed posterior to the LC which corresponded to thickening of the astrocyte basement membrane (Morrison et al., 1990). Basement membrane material has also been shown to occupy larger areas between nerve fibres in the prelaminar region with progression of disease (Hernandez et al., 1990). These observations correspond to a two-fold increase in collagen type IV mRNA expression observed throughout the ONH in glaucoma specimens when compared to normal specimens (Hernandez et al., 1994b).

Within the LC, a large quantity of collagen types I, III and IV labelling was observed between the LC beams, occupying spaces formerly occupied by nerve fibres (Morrison et al., 1990). Basement membrane-like material formed a disorganised, longitudinal distribution within the pores, appearing perpendicular to the LC beams (Hernandez et al., 1990, Morrison et al., 1990). Within the core of LC beams in glaucomatous eyes, increased densities of collagen types IV and VI have been witnessed by immunofluorescent labelling (Hernandez et al., 1990). Collagen type I fibres appeared compact in severe disease cases, while type III showed no change in immunolabelling (Hernandez et al., 1990). In fact, numbers of collagen fibrils have been shown to decrease in glaucomatous monkey LC beams, when compared to normal monkey eyes, creating intervening spaces (Fukuchi et al., 1994).

It has been suggested that changes in collagen concentration precede nerve atrophy as the changes in specific collagen amino acid concentration is also observed in patient eyes with suspected glaucoma, i.e. increased IOP or disc cupping with no visual field defects (Tengroth and Ammitzbøll, 1984). Glaucomatous changes, with regards to extracellular matrix composition, have also been shown to be distinct from changes observed with experimental optic atrophy caused by transection of the ON. Both glaucomatous and transected ONHs experience thickening of astrocyte basement membranes, but only the glaucomatous ONHs encounter an abnormal organisation of basement membrane-like materials within the LC pores (Morrison et al., 1990).

Quantification of fibrils formed by collagen types I and III within the LC beam cores have also highlighted differences between normal and glaucomatous ONHs. High magnification photomicrographs revealed no significant difference in mean collagen fibril diameter between normal and diseased eyes, however there was a minor trend

towards a lower proportion of smaller collagen fibrils within the glaucomatous eyes (Quigley et al., 1991b). Interestingly, the monkey nerve heads showed an opposite tendency highlighting the scepticism needed when using primate material to model human disease. In contrast to fibril diameter, fibril density was approximately 17% lower in glaucomatous LCs and peripapillary sclerae compared to normal ONHs (Quigley et al., 1991b).

1.7.1.1 Elastin

Immunolabelling techniques have revealed a decrease in elastin label intensity and disorganisation of elastic fibres within the LC plates adjacent to the optic disc in glaucomatous ONHs when compared to normal ONHs (Hernandez et al., 1990, Fukuchi et al., 1992). In contrast, elastin containing fibres appeared normal in areas adjacent to the central vessel and in the periphery of the LC (Hernandez et al., 1990). Tissue compression was indicated in glaucomatous ONHs by a compact appearance of elastin fibres at the base of the glaucomatous optic cup (Hernandez et al., 1990).

However, quantitative analysis of the density of elastin containing fibres within the LC beams, as measured by the number of elastin containing fibres divided by the area of the LC beams, showed no differences between normal and diseased eyes throughout the LC and at the region of the peripapillary sclera (Quigley et al., 1991b).

With regards to progression of disease, electron microscopy has revealed a change in elastin containing fibre organisation with increased severity of glaucoma. In mild glaucoma elastin containing fibres became curvilinear in some LC beams, diverting from their normally straight appearance (Quigley et al., 1991a). One study found that

this elastin containing fibre curling appeared in approximately 61% of eyes with a history of glaucoma and at a variety of preparation conditions indicating that it is caused by the disease (Quigley et al., 1994). The normally long, tubular distribution of α-elastin containing fibres within the LC also changed as the core component became restricted to small fragments of elastic tissue throughout the beams (Hernandez, 1992).

This change in elastin containing fibre morphology was increased in moderate stages with the abnormal, curvilinear pattern witnessed in many beams (Quigley et al., 1991a) and in the insertion region (Hernandez, 1992). Dissociation between the collagen and elastin extracellular matrix components was also observed at this stage (Hernandez, 1992).

These changes accumulated to an extreme alteration in LC architecture in advanced glaucoma with elastin fibre curling correlating to regions of extensive neural loss (Quigley et al., 1991a). α-elastin labelled as ribbon-like fibres dispersed throughout the collagenous matrix that separated the remnant nerve fascicles (Hernandez, 1992). The internal structure of the cribriform plates became extremely disorganised at this stage, with an abundance of abnormal, non-fibrillar, honeycomb-like elastin aggregates occupying the prelaminar, LC and postlaminar regions (Hernandez, 1992).

New synthesis of these abnormal, non-fibrillar aggregates are thought to be represented by an increase in elastin mRNA expression within LC cells (Hernandez et al., 1994a). This notion, and its association with glaucoma, has further been supported by the observation that intracellular elastin and elastin synthesis increase significantly when LC cells are exposed to increasing pressures in culture (Hernandez et al., 2000).

1.8   Biomechanics of the Optic Nerve Head

The mechanical behaviour of the ONH is due to its material properties, geometry and mechanical loading (Burgoyne et al., 2005). The material properties of the LC and sclera have been identified as major influential factors in the response of the ONH to acute changes in IOP (Sigal et al., 2005). As previously mentioned, the major load-bearing materials within the ONH are fibrillar collagen and elastin. Therefore, changes in the organisation or content of these components, as a function of age (see section 1.4.2) and glaucoma (see section 1.7), will inevitably alter the biomechanical response of the ONH to IOP. Characterisation of the load-bearing connective tissue microarchitecture of the ONH is essential in understanding its biomechanical behaviour.

1.9   Hypothesis and Aims

The ONH extracellular matrix undergoes a number of changes with age, with an increase in total connective tissue content (Albon et al., 1995, Albon et al., 2000a) and decrease in mechanical compliance (Albon et al., 2000b). Age is a major risk factor in glaucoma (Coleman and Miglior, 2008), with an increase from 2% of over 40 year olds to 10% of over 75 year olds suffering from POAG (NICE, 2009).

The hypothesis of this PhD thesis is that age-related connective tissue changes in the LC compromise its biomechanical, supportive function *thus* increasing the susceptibility of the RGC axons to the development of glaucomatous optic neuropathy.

The aims of this thesis are directed at characterising how collagen and elastin is altered in the ONH as a function of age, in order to understand the implications of these

changes to a change in LC biomechanics and predisposition to glaucomatous optic neuropathy.

The studies within this PhD aim to:

- Investigate the distribution and micro- and nano-organisation of the load-bearing connective tissue components, collagen and elastin, of the human ONH

- Investigate differences in the distribution and organisation of load-bearing components in young and old ONHs

- Investigate differences in the distribution and organisation of ONH load-bearing components in healthy and glaucomatous tissue

- Characterise the microarchitecture of the ONH in 3D

Chapter 2 - Distribution of the Load-bearing Connective Tissue Components in the Human Optic Nerve Head

2.1 Introduction

Although regional connective tissue distribution within the LC has previously been investigated (Quigley and Addicks, 1981, Radius, 1981, Ogden et al., 1988, Jonas et al., 1991, Quigley et al., 1991b, Roberts et al., 2009, Winkler et al., 2010), little is known about the effect that ageing has on the distribution of the load-bearing LC connective tissue components. Therefore, nonlinear microscopy was utilised in the current study to investigate the age-related changes in the connective tissue microarchitecture of the human ONH.

Nonlinear microscopy techniques have a number of advantages in biological imaging and use near infrared, pulsed lasers that enable the penetration of thick tissue sections. The multiphoton reaction occurs at a single optical plane and avoids the generation of "out of focus" signal enabling imaging with a 3D resolution (Zipfel et al., 2003a). The nonlinear techniques utilised in the current study were two photon excited fluorescence (TPEF) and second harmonic generation (SHG) imaging.

During TPEF imaging, the pulsed laser is used to excite endogenous fluorophores within the tissue that would normally be excited by a higher energy, single photon UV laser. TPEF has previously been used to image elastic fibres in the mouse pineal gland and mouse arteriole tissue (Zipfel et al., 2003b) as well as human skin tissue (Chen et al., 2009).

In the case of SHG, the pulsed laser illumination interacts with non-centrosymmetric structures within the tissue specimen, without absorption, and scatters in a non-random phase (Zipfel et al., 2003a). The second harmonic signal that is produced from the sample is half the wavelength and twice the frequency of the incident laser beam (Mohler et al., 2003) and, if the size of the scattering structure is greater than the illumination wavelength, most of the signal is propagated in the same direction as the incident light (Zipfel et al., 2003b).

With its tertiary triple helical conformation, fibrillar collagen is highly non-centrosymmetric and has been shown to produce strong SHG signal (Williams et al., 2005, Theodossiou et al., 2006). This principle has previously been used to image and reconstruct the collagenous matrix within the human ONH (Brown et al., 2007, Winkler et al., 2010). Brown et al. (2007) used backward scattered SHG signal while Winkler et al. (2010) used forward scattered SHG signal from thin (2µm), embedded serial sections to produce an elegant, 3D reconstruction of the ONH.

The current study aimed to improve on these methods by using thick (100µm) cryosections to simultaneously produce 3D TPEF and forward scattered SHG datasets, therefore reducing the amount of sections needed for 3D reconstruction of the load-bearing ONH connective tissue components.

OBJECTIVES

- To visualise collagen and elastin fibre organisation and content in the young and old human ONH

- To reconstruct 3D nonlinear microscopy datasets of young and old ONHs

- To compare connective tissue structural parameters in the LCs of young and old ONHs

2.2 Materials and Methods

2.2.1 Source of Human Tissue and Tissue Preparation

Human eyes, after corneo-scleral disc removal, with no history of ocular disease were received from the Bristol Corneal Transplant Service Eye Bank, UK, with consent for research purposes. All tissue was stored at 4°C and used for research in accordance with Human Tissue Act regulations. All eyes were orientated by observing the position of the macular and a block of sclera which encompassed the ONH was dissected. All tissue (eye globes or dissected tissue), if not used fresh, was fixed in 4% paraformaldehyde (PFA; lab stock, see Appendix 7) within 48 hours of donor death until experimentation.

2.2.2 Validation of Nonlinear Microscopy Signals

Two ONHs (aged 62 years) were snap frozen in liquid nitrogen-cooled isopentane (Fisher, UK), without fixation, and embedded in Cryo-M-Bed medium (TAAB, UK). The embedded tissue blocks were then sectioned (8μm thickness), one transverse to the ON and one longitudinal to the ON, using a cryostat (Leica CM3050 S; Leica Microsystems, UK). Sections were mounted onto Superfrost® Plus slides (Thermo Scientific, UK) and used for nonlinear microscopy validation studies.

Adjacent ONH cryosections (transverse and longitudinal) were subjected to nonlinear microscopy, namely TPEF and SHG, Masson's trichrome green or elastin immunolocalisation. Other sections were subjected to SHG and immunolocalisation of collagen type specific antibodies in the same section.

2.2.2.1 Nonlinear Microscopy Techniques: Second Harmonic Generation and Two Photon Excited Fluorescence

Sections, mounted in 1:1 phosphate buffered saline (PBS, pH 7.4; lab stock, see Appendix 7):glycerol, were subjected to nonlinear optical microscopy TPEF and SHG imaging. Sections were imaged using a mode-locked, Ti:Sapphire laser (Chameleon®; Coherent UK Ltd, UK) with a 140 fs pulsewidth and a LSM510 META laser scanning microscope with a 20x Plan-APOCHROMAT objective lens (Carl Zeiss Ltd, UK). All images were obtained using LSM 510 Version 4.2 SP1 software (Carl Zeiss, UK) following excitation at 800nm.

TPEF signal derived from endogenous fluorophores within the tissue was collected in an epi-detection channel (Figure 2.1). TPEF emission between 500-550nm was collected as this wavelength range falls within the broad emission spectrum that has previously been attributed to elastin (~410–600 nm) (Zoumi et al., 2004). Forward scattered SHG signal, which was half the wavelength (400nm) of the excitation wavelength, was collected following transmission through the sample (Figure 2.1).

Single TPEF and SHG images (1024x1024x1 pixel) of the LC, insertion region, peripapillary sclera and postlaminar ON septae were acquired from the ONH sections.
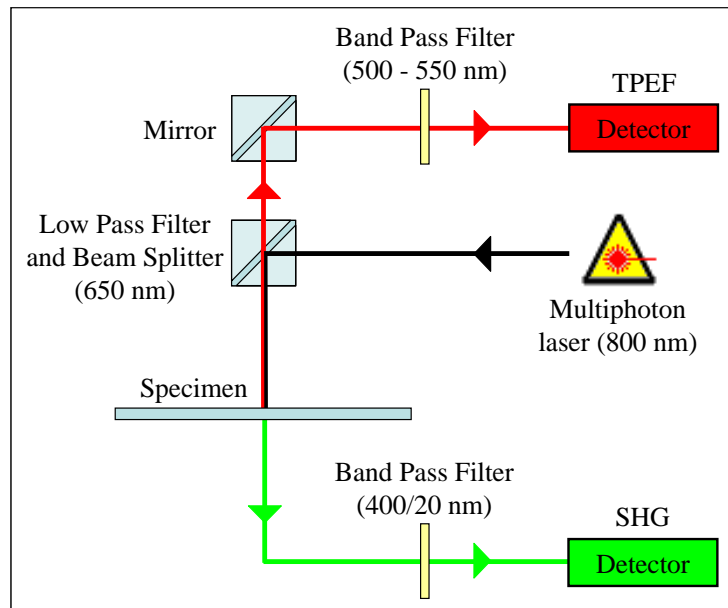
Figure 2.1. Optical setup of the LSM510 META laser scanning microscope and multiphoton laser used for nonlinear microscopy imaging. TPEF signal ($\lambda_{ex/em}$=800nm/500-550nm) was collected in an epi-detector and SHG signal ($\lambda_{ex/em}$=800nm/400nm) was collected in the transmission light path. The low pass filter and beam splitter ensured that wavelengths above 650nm were reflected down to the sample and wavelengths below 650nm were transmitted to the TPEF detector. Band pass filters ensured that specific wavelengths entered the TPEF and SHG detectors.

2.2.2.2 *Masson's Trichrome Green*

Following a 10-minute immersion in PBS, ONH tissue sections were fixed in Bouin's solution (3:1:0.2, picric acid: 37% formaldehyde (37-40%):glacial acetic acid) for 1 hour at 56ºC, rinsed in tap water and stained with Harris's haematoxylin (Thermo Fisher, UK) for 8 minutes. After washing in tap water, sections were stained in 1% w/v Beibrich scarlet solution (Sigma-Aldrich, UK) for 10 minutes, followed by a 5-minute wash in distilled water and differentiation in 1:1 5% w/v phosphotungstic acid (Sigma-Aldrich, UK) and 5% w/v phosphomolybdic acid (Sigma-Aldrich, UK). Then sections were stained in 2% fast green (Sigma-Aldrich, UK) in 2% glacial acetic acid (Fisher Scientific, UK) for 5 minutes. Excess stain was removed by washing in distilled water, and sections were then dehydrated through a series of graded alcohols (50%, 70%, 90%,

and 100%) before clearing in xylene (Fisher, UK) and mounting in DPX (RA Lamb Ltd, UK). Sections were viewed, under bright field illumination, using a light microscope (Leica DM RA2; Leica Microsystems, UK) and images were captured using Leica QWin image analysis software (Leica Microsystems, UK) and digital camera (Leica DC 500; Leica Microsystems, UK).

2.2.2.3 *Indirect Immunofluorescence*

ONH tissue sections were immersed in PBS for 10 minutes then incubated for two hours at room temperature in primary antibodies diluted in PBS. Primary antibodies included monoclonal mouse anti-human collagen types I (COL-1, 1 in 100 dilution), IV (COL-94, 1 in 100 dilution; BioScience AUTOGEN Bioclear, UK), III (FH-7A, 1 in 500 dilution) and elastin (BA-4, 1 in 500 dilution; Sigma, UK). Negative control ONH tissue sections were incubated for 2 hours with no primary antibody or a monoclonal mouse anti-GFP (green fluorescent protein, GFP-20, Sigma, UK) antibody at a 1 in 100 or 1 in 500 dilution, as appropriate, in place of collagen and elastin primary antibodies.

After thrice washing in PBS, the sections were incubated for 2 hours at room temperature in donkey anti-mouse Alexa Fluor® 488 (Ex/Em ~495/519nm, Invitrogen Ltd, UK), diluted 1:1000 in PBS, washed thrice in PBS, and mounted in non-fluorescing mounting media (Hydromount; National Diagnostics, UK). Immunofluorescence was observed and captured using confocal microscopy (LSM510 META laser scanning microscope) using an Argon/2 laser with LSM 510 Version 4.2 SP1 software.

2.2.2.4 Comparison with Human Retinal Pigment Epithelial Lipofuscin

Purified human lipofuscin (a gift from Professor ME Boulton) was prepared as described by Boulton and Marshall (1985).

An aliquot of the lipofuscin was dropped onto a microscopy slide and coverslipped. The slide was subjected to TPEF imaging and compared to TPEF images of ONH sections from the level of the postlaminar ON.

2.2.3 Three Dimensional Nonlinear Microscopy of Thick Human Optic Nerve Head Sections

Fixed ONHs (n = 14, age range 2 to 88years) were immersed in PBS (pH 7.4) overnight then were sectioned transverse to the ON (100μm, from prelamina to postlaminar ONH, n = 8) or longitudinal to the ON (160μm, through central ONH, n = 9) using a sledge microtome (MICROM HM 440E; Thermo Fisher, UK). Sections were mounted onto Superfrost® Plus slides in 1:1 PBS:glycerol. The coverslips were sealed with nail varnish and the slides were stored at -20°C until time of imaging.

TPEF and SHG signals were generated as described in 2.2.2.1. 3D image stacks of each ONH were acquired as sequences of optical sections (256x256x1 pixel), at calibrated 1μm increments of focus using a fully automated motorised stage (Scanning stage DC 4"x4"; Carl Zeiss Ltd, UK). To decrease noise, each pixel line within each image frame was scanned twice and averaged. 3D, tiled image acquisition time ranged from approximately 3h to 4h 30mins. Serial 3D image stacks were then tiled together to create a 3D dataset for each ONH tissue section, using LSM 510 Version 4.2 SP1.

Higher resolution (1024x1024x1 pixel) single images were also captured from regions of interest within the ONHs.

2.2.3.1   Nonlinear Microscopy Method Development

Although the near-infrared wavelength of the laser used during nonlinear microscopy allows for deeper penetration through optically thick specimens, the nonlinear signals still became attenuated at the deeper section levels (Figure 2.2A). To attempt to overcome this, the percentage of laser power at the sample was increased while imaging through the section depth using the Auto Z Brightness Correction option of the LSM 510 Version 4.2 SP1 software. This option allows the user to set different laser intensities near the top and bottom of the sample and linearly adjusts the laser power between the set positions during image acquisition. Optimisation of this method was carried out on 100µm thick tree shrew ONH sections (Figure 2.2) which were prepared on the sledge microtome as described in section 2.2.1.
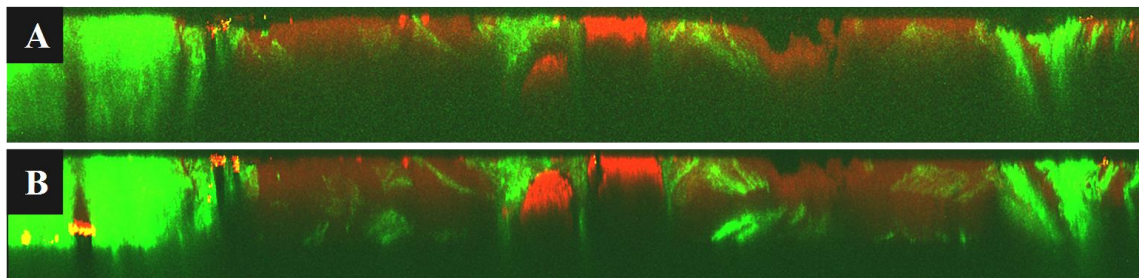
Figure 2.2. Correcting for laser attenuation using the Auto Z Brightness Correction option of the LSM 510 Version 4.2 SP1 software. (A) Attenuation of the nonlinear signals, SHG (green) and TPEF (red), in a 100µm tree shrew ONH section was substantially improved (B) when the laser power was increased by 4% from top to bottom of the sample. This allowed visualisation of deeper tissue structures. Improvement of the SHG signal intensity was more apparent than for the TPEF signal intensity.

It was found that a 4% laser increase from the first to last optical slice of the tissue section was sufficient to correct for the majority of laser attenuation though the SHG

signal intensity showed greater improvement than the TPEF signal intensity (Figure 2.2B). Five out of 6 human ONH samples were imaged using the Auto Z Brightness Correction option.

2.2.4 3D Reconstruction of Second Harmonic Generation Datasets

Due to the autofluorescence from ONH components other than elastic fibres that contributed to TPEF signals, 3D reconstruction of each ONH was restricted to SHG datasets.

The 3D, tiled, SHG image stacks of each tissue section (a prelamina section, all LC sections and 2 adjacent postlaminar ON sections) of 6 ONH datasets (aged 2yrs to 88yrs) were imported into Amira® visualisation software (version 5.4.1, Visualization Sciences Group, Germany) and any tilt in the section dataset, caused by tilt in the microscopy stage, was corrected for as necessary using "Transform Editor" and "ApplyTransform". The corrected SHG datasets were then concatenated in Fiji (a distribution of ImageJ image processing package (Schindelin et al., 2012)), producing a single ONH image stack per donor.

The SHG datasets within the image stack were then aligned to each other using the maximum intensity function of the AlignSlices module in Amira®. As there were multiple image slices above and below the ONH data that did not contain any structural data associated with the tissue section, each aligned stack was separated back into its individual SHG section stacks and stitched together with an overlap using the Grid/Collection Stitching plugin in Fiji (Preibisch et al., 2009). The Max. Intensity fusion method was utilised when using the plugin and the percentage of overlap was

initially judged by the amount of signal-free optical slices above and below the tissue

section data and was adjusted depending on the quality of the output stack. The signal to

noise ratio of each complete, merged image stack was then improved using the noise

reduction median filter in Amira® and the background was subtracted using the rolling

ball function, with a ball radius of 40 pixels, in Fiji (Figure 2.3B).
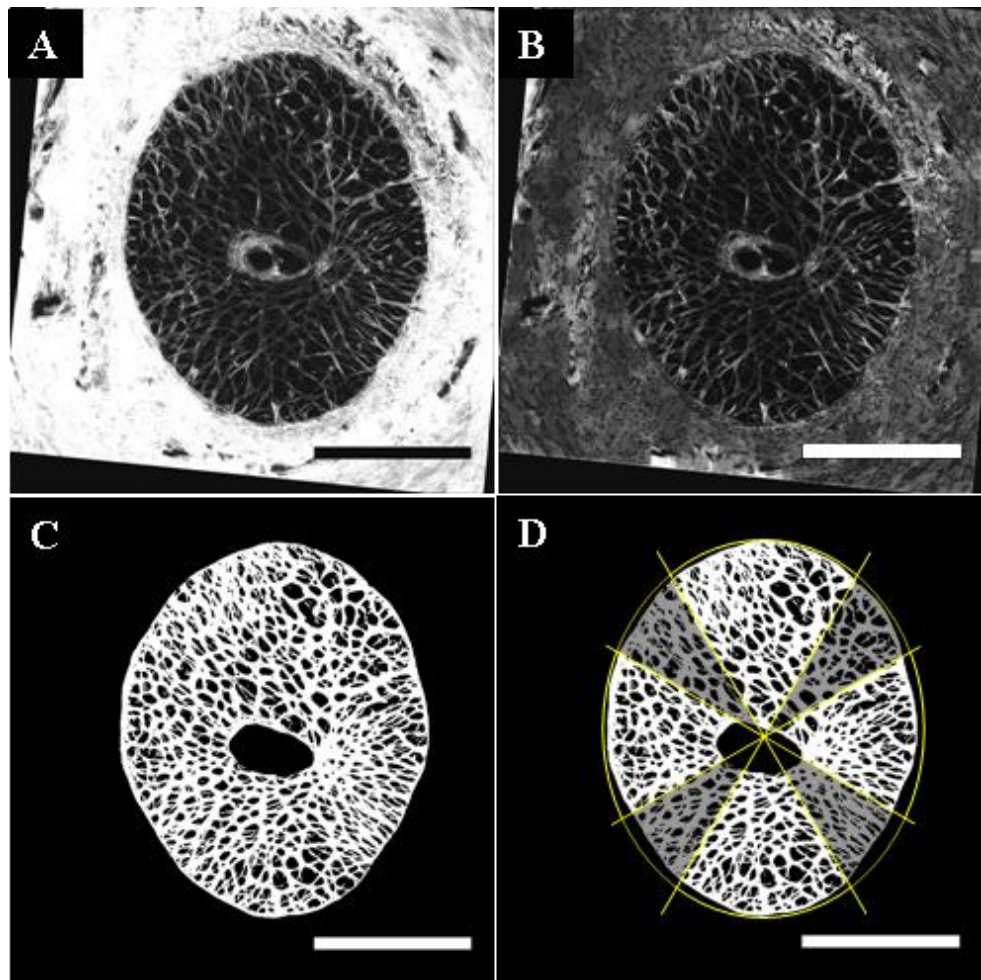
Figure 2.3. ONH SHG data processing and segmentation. (A) Each SHG image slice was (B) subjected to a noise reduction median filter and the background removed. (C) Binary image following segmentation of SHG related pixels in the LC. (D) The LC was split, *en face*, into superior, temporal, inferior and nasal polar quadrants for regional analysis. Scale bars: 1000μm

2.2.5 Segmentation of Fibrillar Collagen in the 3D Human Optic Nerve Head

The voxels containing SHG signal, and thus attributed to ONH fibrillar collagen, were segmented out and separated from the non-SHG voxels in the dataset using the threshold segmentation option in the Amira® segmentation editor (Figure 2.3C). The whole ON canal and LC were manually segmented in each image slice using the brush tool in the Amira® segmentation editor. The resultant segmented materials were saved as 8-bit binary image stacks. The central retinal vessels were included in datasets of the whole ON canal and LC, but excluded from the ONH datasets that were segmented for fibrillar collagen quantification.

2.2.6 Lamina Cribrosa Surface Reconstruction

The anterior and posterior LC surfaces were constructed using the landmark tool and PointWrap module in Amira®. Using the binary segmented LC volume, multiple landmarks were placed along the anterior and posterior LC surfaces at 12º intervals around the centre of the ON canal. The anterior and posterior LC surface landmarks were then reconstructed into two surfaces, allowing for the analysis of the anterior and posterior LC surface area, before being combined to form a continuous surface that enclosed the LC volume.

2.2.7   3D Optic Nerve Head Analysis

2.2.7.1   *Fibrillar Collagen Distribution*

Segmented fibrillar collagen-related voxels were quantified within each ONH dataset using the Analyse Particles function in ImageJ (version 1.45s (http://rsb.info.nih.gov/ij)). A ratio of SHG pixels:ON canal area was calculated for each optical slice enabling the distribution of fibrillar collagen to be plotted as a function of ONH depth. Plotting the fibrillar collagen content as a ratio allowed for the relative fibrillar collagen content to be compared between ages, without bias introduced as a consequence of differences in ON canal size. Unfortunately, SHG signal attenuation was apparent at section borders (solid line in Figure 2.4) within each sample. Therefore, the average relative collagen content (i.e. number of SHG pixels divided by ON canal area) of every100 optical slices was plotted to summarise the change in fibrillar collagen content through the ONH (dashed black line in Figure 2.4).
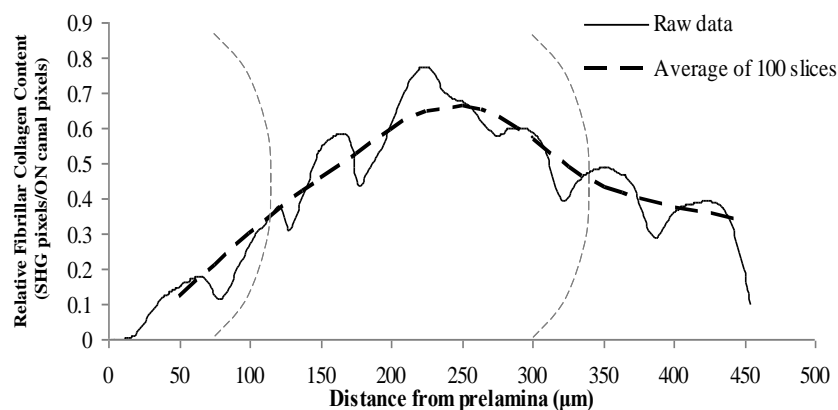
Figure 2.4. Relative fibrillar collagen content plotted as SHG pixels:ON canal area through the ONH depth in an 87 year old ONH. Data are plotted from the 3D ONH dataset (assembled from the prelamina section immediately preceding the LC through to the postlaminar ON). A decrease in relative fibrillar collagen content occurred between each histological section due to signal attenuation (black solid line) therefore, fibrillar collagen density was averaged from every 100 optical slices to summarise changes through the ONH depth (black dashed line). Grey dashed curves denote the approximate positions of the anterior and posterior LC surfaces.

To determine if any regional variation in relative fibrillar collagen content existed within the LC, the ON canal was divided into superior, temporal, inferior and nasal quadrants as shown in Figure 2.3D. The *en face* LC was first split into 12 radial sectors and the 2 most polar sectors were combined to form the 4 regional quadrants. To ensure no data overlap between the 4 quadrants, data in the sectors between the quadrants were excluded from the analysis. The fibrillar collagen density within each LC region was calculated as the ratio of fibrillar collagen to LC area and compared between ages.

2.2.7.2   Lamina Cribrosa Geometry

Anterior and posterior LC surface areas and LC volume were quantified in each 3D ONH dataset using the SurfaceArea option in Amira®. LC thickness maps were generated for each ONH from the surface enclosing the LC volume using the Amira® SurfaceThickness module. This function computes the perpendicular distances between opposite surface faces and was used to visualise the regional variability in LC thickness which is displayed as a colour map. Anomalous thickness data (measuring approximately 1000µm and above), resulting from erroneous perpendicular distances measured laterally across the LC from surface triangles on the edges of the LC volume, were emitted from the thickness map visualisation and analysis.

LC thicknesses from the 3D datasets were compared to 2D measurements from five optical slices, 10µm apart, through nonlinear image stacks from 160µm thick longitudinal ONH sections (n = 8 donors aged between 11 and 90). These measurements were performed equidistance from the central vessel wall and peripapillary sclera, starting at the first LC sheet adjacent to the prelamina, to the last

sheet before the connective tissue septa of the postlaminar ON, using the line tool in ImageJ.

2.2.8 Statistical Analysis

All statistical analysis was performed using SPSS version PASW 18 (SPSS Inc., USA). Normality of data was determined using the Shapiro-Wilk test with a significance level of 0.05. Fibrillar collagen density and LC surface areas in young and elderly age groups were compared using the independent samples t-test and LC volume was compared using the Mann-Whitney U test.

Since LC thickness measurements from 3D datasets were not normally distributed, Kruskal-Wallis tests were used to determine if there were any significant differences in between LCs of different ages. Where appropriate, multiple Mann-Whitney U tests were used with a Bonferroni corrected significance level ($p<0.003$), that accounted for type I errors, to identify where the differences fell.

When comparing 2D LC thickness measurements between LCs from different aged donors, significant differences were determined using an ANOVA with a Tukey post hoc test ($p<0.05$).

All statistical comparisons of the data are presented as bar charts with error bars depicting the precision of each measurement. These error bars are either the standard error of the mean following parametric comparisons or 95% confidence intervals of the median (calculated using the Ratio Statistics option in PASW) following non-parametric comparisons.

2.3 Results

2.3.1 Validation of Nonlinear Microscopy Signals

2.3.1.1 Masson's Trichrome Green

Masson's Trichrome Green, a general connective tissue stain (collagen and elastin), was evident, but differentially distributed throughout the prelamina, LC and postlaminar ONH in both transverse (Figure 2.5A-C) and longitudinal (Figure 2.5G) orientated sections. The stain was localised to the sheaths surrounding the central retinal vessels (Figure 2.5A-C and G), beams encircling the LC pores and sclera (Figure 2.5B,G) and meningeal sheaths and connective tissue septae of the postlaminar region (Figure 2.5C,G). Minimal stain was observed within the ON canal at the prelamina ONH level (Figure 2.5A,G).

Nonlinear signals, SHG and TPEF, were generated from corresponding regions (Figure 2.5D-F and H), in sections adjacent to those subjected to the trichrome green stain. Signals were lacking in the prelamina ON canal, except for the surrounding sclera and sheaths of the central retinal vessels (Figure 2.5D,H). The TPEF signal was distinct in the elastic lamina of the central retinal artery (Figure 2.5D,E and H). Intense nonlinear signals were emitted from the LC beams (Figure 2.5E,H) and postlaminar septae (Figure 2.5F,H). The SHG signal was intense in the sclera (Figure 2.5E,H) and meningeal sheaths (Figure 2.5F,H).
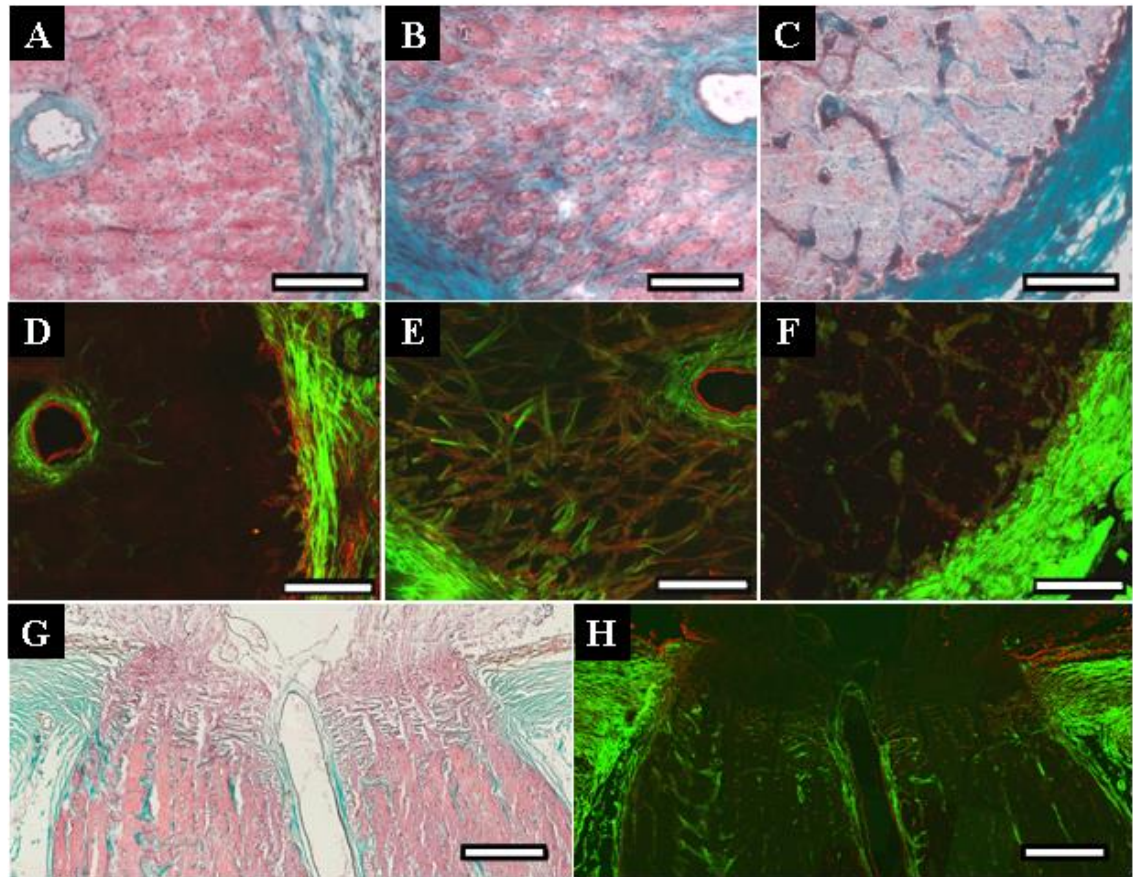
Figure 2.5. Nonlinear signal validation using Masson's trichrome green. (A-C and G) Masson's trichrome green connective tissue stain and (D-F and H) nonlinear signals, SHG (green) and TPEF (red), in adjacent sections of the (A,D) prelamina, (B,E) LC, (C,F) postlaminar and (G,H) longitudinal human ONH. Masson's trichrome green stains connective tissue within the section green, the nuclei blue/black and the cytoplasmic/neuronal areas pink. Good correlation between nonlinear signals and stain localisation was observed. Scale bars: (A-F) 200µm, (G-H) 500µm

2.3.1.2 Indirect Immunofluorescence

SHG has been recognised to be generated from noncentrosymmetric molecular configurations including those that make up collagen (Freund and Deutsch, 1986, Campagnola et al., 2002, Zipfel et al., 2003b). To confirm the origin of SHG signal generation in the human ONH, immunolocalisation of fibrillar collagen types I (Figure 2.6A,B) and III (Figure 2.6C,D) and non-fibrillar collagen type IV (Figure 2.6E,F), known to be present within the LC (Hernandez et al., 1986, Hernandez et al., 1987,

Morrison et al., 1989a, Albon et al., 1995), and SHG (Figure 2.6G-L) were performed in the same LC sections and images superimposed (Figure 2.6M-R).

Collagen type I (Figure 2.6A,B) and III (Figure 2.6C,D) immunolabelling co-distributed in the LC beams, sclera and within the walls of the central retinal vessels. The SHG signal appeared to be generated from these same regions (Figure 2.6G-J), illustrated by combining SHG and immunofluorescence of the same LC section (Figure 2.6M-P).

Collagen type IV immunolabelling was minimal in the sclera (Figure 2.6E), absent from the walls of the central retinal artery but distinct on the borders of the lumina of the artery and vein (Figure 2.5F). Collagen type IV was also sparsely dispersed within the LC beams but more distinct along the borders of the beams (Figure 2.6E). In comparison, SHG signal was intensely evident in the sclera and walls of both central retinal artery and vein, as well as the LC beams (Figure 2.6K,L). Visualising SHG and type IV collagen immunofluorescence in the same LC section emphasised their distinct localisation (Figure 2.6Q,R).
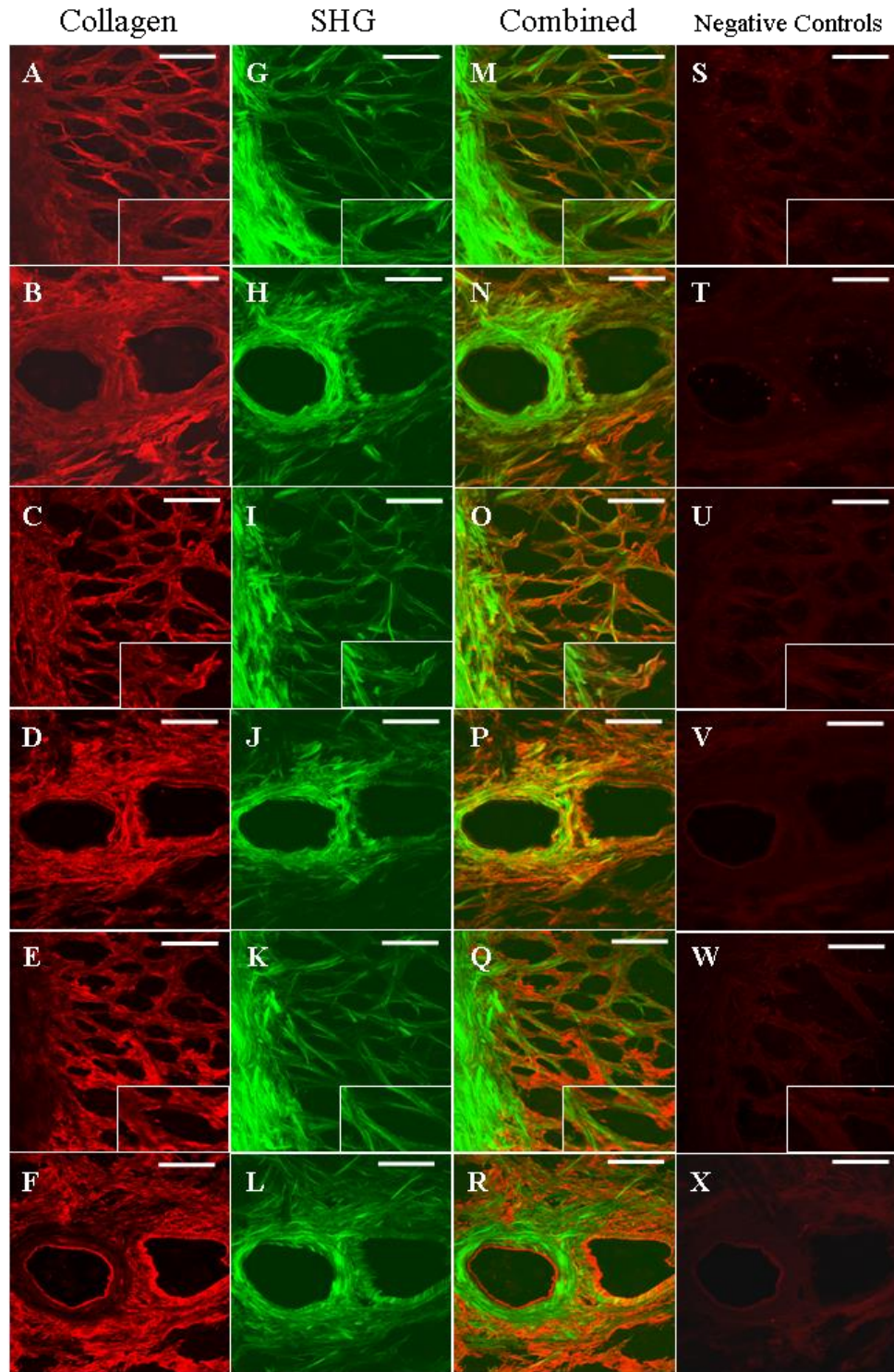
Figure 2.6. Immunolocalisation of collagen types (A,B) I, (C,D) III and (E,F) IV and (G-L) corresponding SHG in transverse sections of human LC. (M-R) Combining the immunolabelling and SHG signals indicates that SHG signals emit from regions equivalent to immunolocalisation of (A-D) fibrillar collagen types rather than (E-F) non-fibrillar type IV within the human LC and its central retinal vessels. Note the lack of collagen type IV immunolocalisation in sclera, where SHG is intense. Sections incubated with an anti- GFP primary antibody (1:100 (S,T) and 1:500 (U,V)) or no primary antibody (W,X) show no immunoreactivity. Insets show 2-fold magnification of LC beams. Scale bars: 100μm

Negative control sections (using an anti-GFP antibody; 1 in 100 (Figure 2.6S,T) and 1 in 500 Figure 2.6U,V)) or no primary antibody (Figure 2.6W,X) displayed no immunoreactivity (Figure 2.6S-X).

TPEF has been shown to be derived from a number of endogenous fluorophores in biological tissues (Xu et al., 1996, Zipfel et al., 2003b). Amongst these is elastin, thus immunofluorescent localisation of elastin in the LC was compared to TPEF of adjacent unlabelled sections (Figure 2.7).
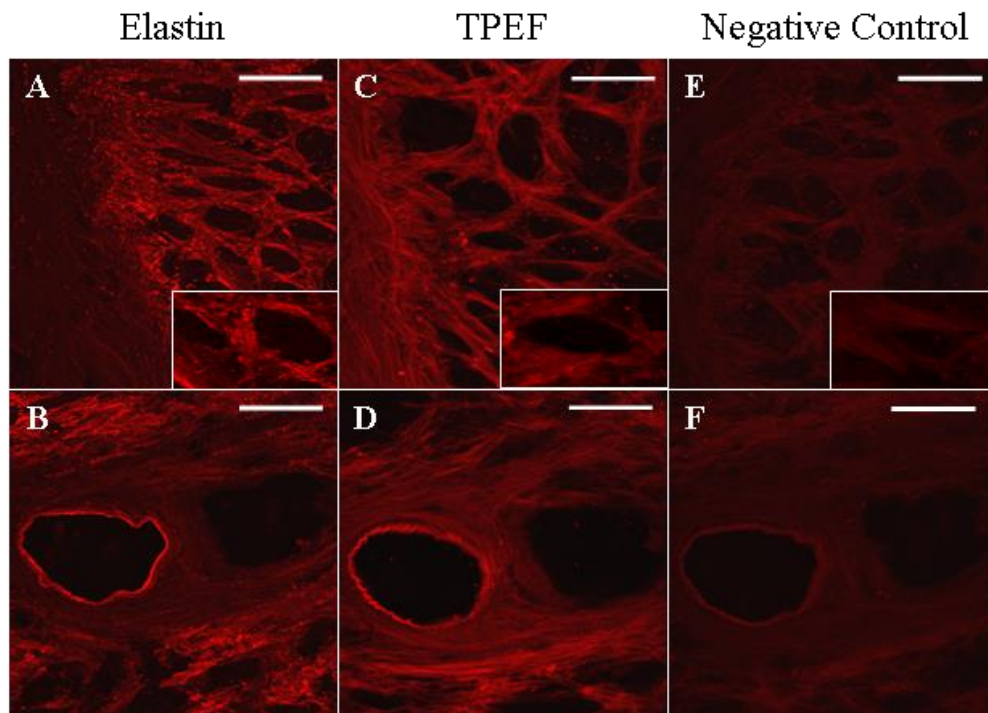
Figure 2.7. Immunolocalisation of (A,B) elastin and (C,D) TPEF in adjacent human LC transverse sections. Elastin immunoreactivity was observed in the (A) LC beams, (B) the elastic lamina of the central retinal artery and (E,F) absent in the negative controls (anti-GFP antibody; 1 in 500). Similar to elastin immunoreactivity, TPEF was evident in (C) the LC beams and (D) the elastic lamina of the central retinal artery lumen. (C) However, TPEF emitted from sclera, where minimal elastin immunoreactivity (A) was identified. Insets show 100% magnification of LC beams. Scale bars: 100μm

Elastin immunofluorescence was mainly localised to the LC beams (Figure 2.7A) and the elastic lamina of the central retinal artery (Figure 2.7B), with minimal labelling observed in the sclera and walls of the central retinal vessels (Figure 2.7A,B). TPEF demonstrated a corresponding distribution to elastin immunoreactivity in the LC beams and central retinal vessels (Figure 2.7C,D). TPEF was also found to strongly and distinctively emit from fibres within the sclera (Figure 2.7C).

2.3.2 Collagen and Elastin Distribution in the Human ONH

High resolution, single images of the central retinal vessels (Figure 2.8A-F), LC connective tissue beams (Figure 2.8G-L) and insertion of the LC beams into the peripapillary sclera (Figure 2.8M-R) were captured in an unfixed ONH to further characterise connective tissue fibres in the human ONH.

Fibrillar collagen and elastin form a thick connective tissue sheath around the central retinal vessels (Figure 2.8A-C). Collagen and elastic fibres were observed circumferentially around the central retinal artery (Figure 2.8D,E). A distinct ring of elastin (elastic lamina) easily distinguished the central retinal artery from the vein (Figure 2.8B,C).

Both fibrillar collagen and elastin co-localised within the LC beams forming interconnected, fibre bundles that subdivided to create interconnected, fenestrated sheets through which the nerve fascicles passed (Figure 2.8G-L).
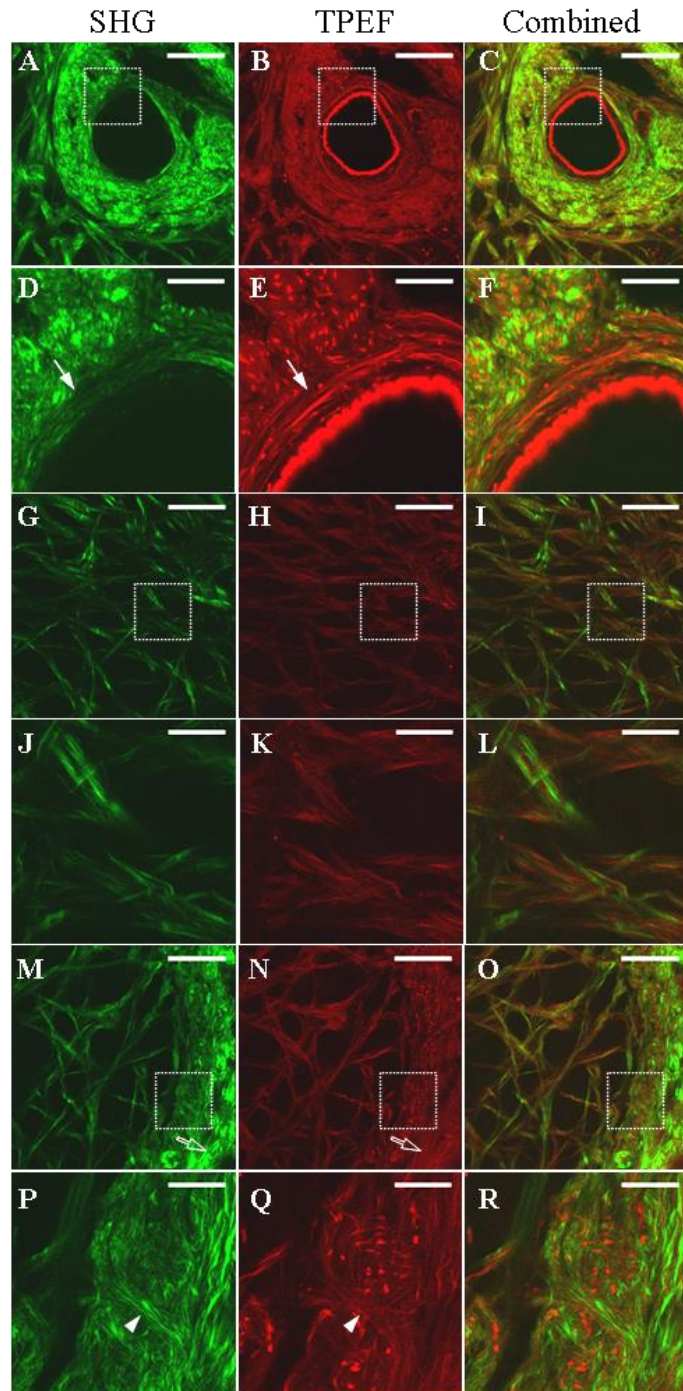
Figure 2.8. High resolution images depicting nonlinear signals (SHG = green, TPEF = red) from (A-F) the central retinal vessels, (G-L) LC beams and (M-R) insertion of the LC beams into the peripheral sclera. (D-F), (J-L) and (P-R) show a 4-fold magnification of the areas denoted by the squares in (A-C), (G-I) and (M-O), respectively. Both fibrillar collagen and elastin were found to co-localise in (C) the sheaths surrounding the central retinal vessels, (I) the LC beams and (O) the insertion region. Fibrillar collagen and elastin were also found circumferentially around (D,E, block arrows) the central retinal artery and (M-N, outlines arrows) the ON canal. Some fibres (P,Q, block arrow heads) were also observed entering the LC at the insertion region. Scale bars: (A-C, G-I, M-O) 100μm, (D-F, J-L, P-R) 25μm

Co-distribution of fibrillar collagen and elastin also existed in fibre bundles circumferentially orientated around the canal within the peripapillary sclera (Figure 2.8M-R). In some areas along the insertion region both fibrillar collagen and elastic fibres were also observed in an orientation perpendicular to that of the circumferential fibres, pointing towards the ON canal opening (Figure 2.8P,Q).

Interestingly, small "dots" of TPEF were evident in the connective tissue sheath surrounding the central retinal vessels (Figure 2.8E) and in the insertion region (Figure 2.8Q). Volume rendering of the TPEF signal within the insertion region showed that these specks were actually transects of interwoven, twisting elastic fibres encircling the ON canal (Figure 2.9).
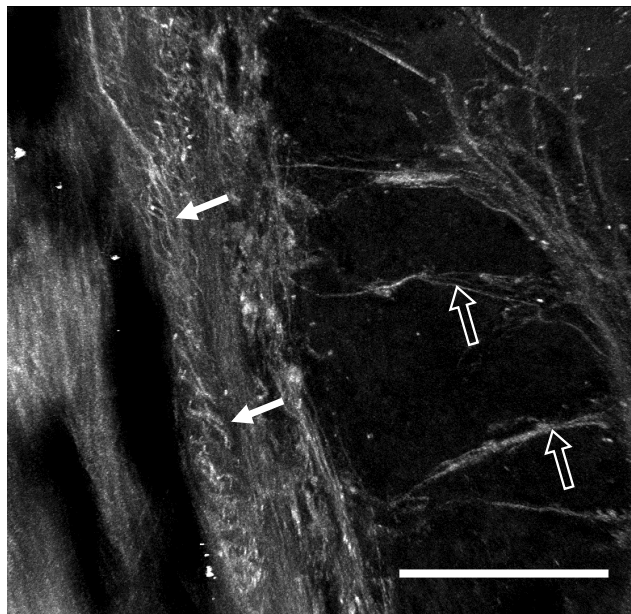
Figure 2.9. High resolution, 3D rendering of the TPEF-related to elastic fibres in the insertion region at the level of the LC. Elastic fibres appeared to intricately interweave within the insertion region (solid, white arrows) and form straight fibres within the LC beams (open arrows). Scale bar: 100µm

The anatomical differences between the prelamina, LC and postlaminar region of the ONH were evident in the tiled nonlinear microscopy images of fixed ONH sections cut transverse (Figure 2.10) and longitudinal (Figure 2.11) to the ON.
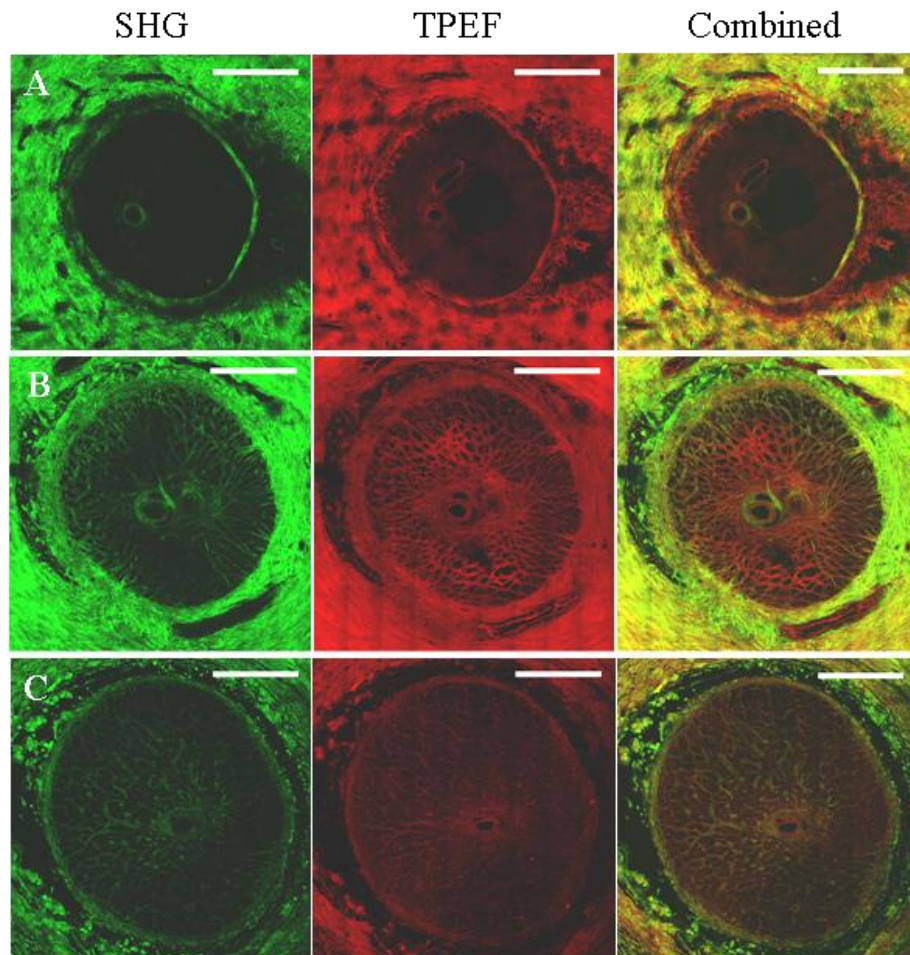
Figure 2.10. Tiled images of the human ONH from an 88 year old donor depicting nonlinear signals (SHG = green, TPEF = red) from the (A) prelamina, (B) LC and (C) postlaminar ON. Fibrillar collagen and elastin encircled the optic nerve canal within the sclera of the (A) prelamina, (B) LC and in the pia mater surrounding the (C) postlaminar ON region. (B) The predominantly radial connective tissue beams of the LC give way to the connective tissue septae in the (C) postlaminar region. Scale bars: 1000μm

At the level of the prelamina, SHG signal was at its most intense from the collagen within the sclera surrounding the ON canal (Figure 2.10A, Figure 2.11). A strong TPEF signal emitted from the pigment in the choroidal tissue (Figure 2.10A, Figure 2.11). Within the prelamina ON canal connective tissue content appeared to be minimal with

exception to that confined to sheaths surrounding the central retinal vessels (Figure 2.10A, Figure 2.11).
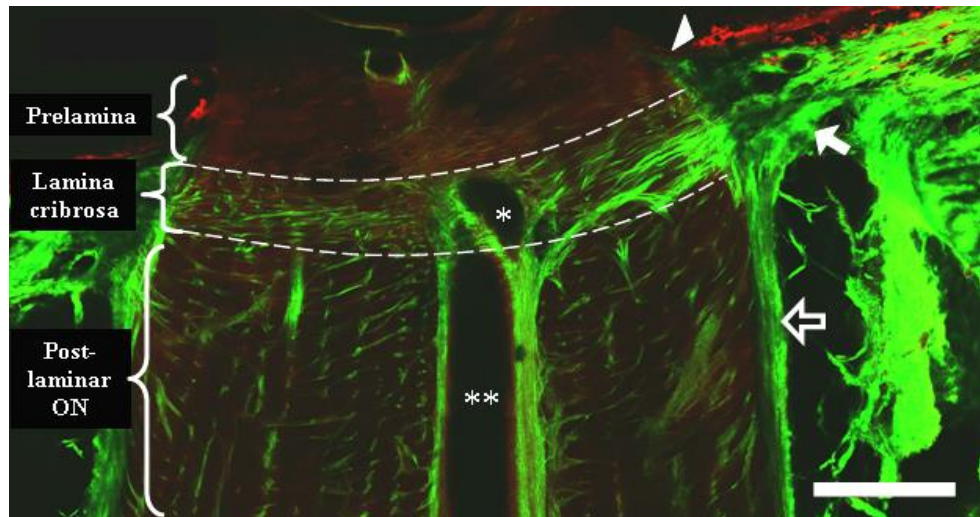
Figure 2.11. Nonlinear signals (SHG = green, TPEF = red) from a longitudinal section of the human ONH. The prelamina, LC and postlaminar ON are indicated. The dense connective tissue cribriform plates of the LC traversed the ON canal and inserted into the central retinal vessels (*vein, **artery) and peripapillary sclera (white arrow). The postlamina ON septae ran parallel to the nerve bundles and inserted into the pia mater (open arrow). Minimal nonlinear signal was observed in the prelamina region with exception of the intense TPEF signal in the choroid (white arrow head). The dashed lines denote the upper and lower boundaries of the LC. Scale bar: 500μm

At the level of the LC, both connective tissue components formed beams that stretched almost radially across the ON canal, forming discrete pores, and connecting the sheaths that encircled the central retinal vessels (Figure 2.10B). From the longitudinal view, these beams were found to form the distinct cribriform plates that inserted into the peripapillary sclera (Figure 2.11).

In the postlaminar ON, the connective tissue formed discontinuous septae (Figure 2.10C) that ran longitudinal to the nerve fascicles (Figure 2.11) and inserted into the pia mater. Both the pia mater and dura mater emitted an intense SHG signal (Figure 2.10C,

Figure 2.11). Widening of the ON canal diameter was evident as it progressed from prelamina to LC to postlaminar ON (Figure 2.10, Figure 2.11).

Figure 2.12 shows tiled nonlinear images of serial tissue sections from a young (6 years old) and elderly (87 years old) ONH. The anatomical differences between the prelamina, LC and postlaminar ON were evident in both ages.
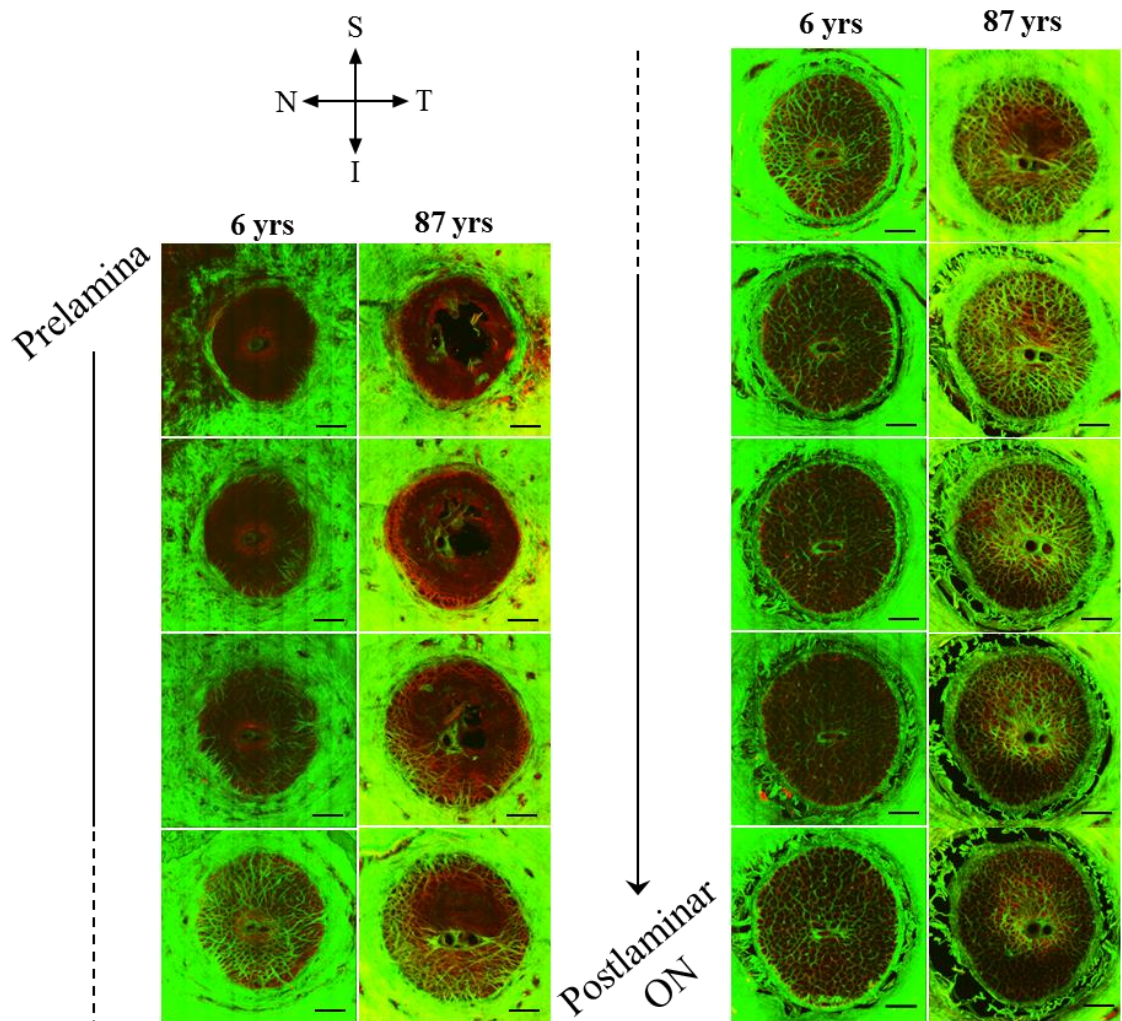
Figure 2.12. Maximum intensity projections of 3D tiled images of the human ONH depicting nonlinear signals (SHG = green, TPEF = red) from a 6 year old donor and an 87 year old donor. S = superior, T = temporal, I = inferior, N = nasal. Scale bars: 500μm

Tiled images of young (Figure 2.13) and elderly (Figure 2.14) ONH sections revealed that the overall anatomical makeup of the ONH is similar between extreme age groups.
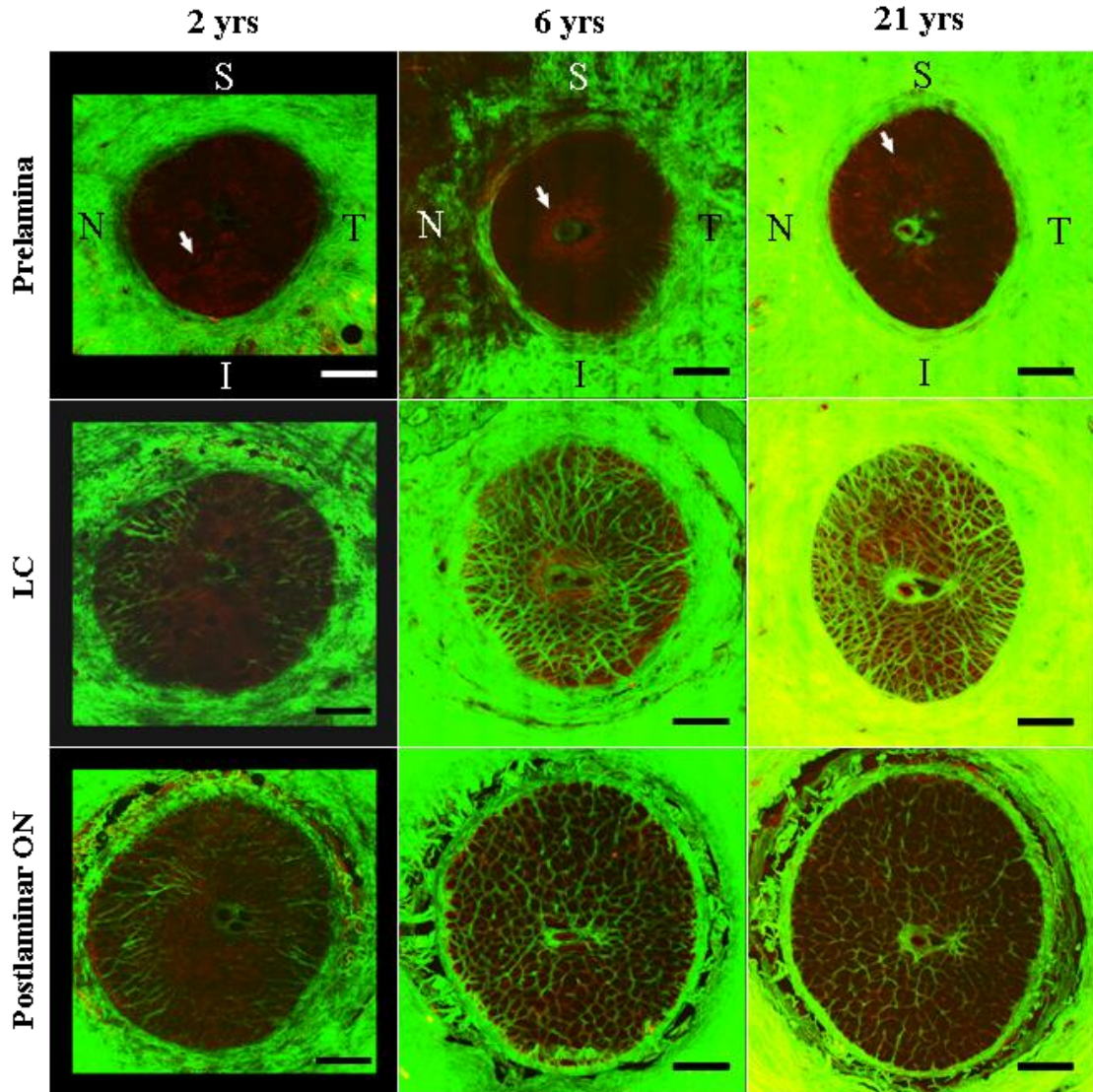
Figure 2.13. Maximum intensity projections of 3D tiled images of young ONHs depicting nonlinear signals (SHG = green, TPEF = red) from the prelamina, LC and postlaminar ON from a 2 year old, 6 year old and 21 year old donor. (A,B) Neuronal tissue related autofluorescence was apparent in the prelamina region (arrows). S = superior, T = temporal, I = inferior, N = nasal. Scale bars: 500μm
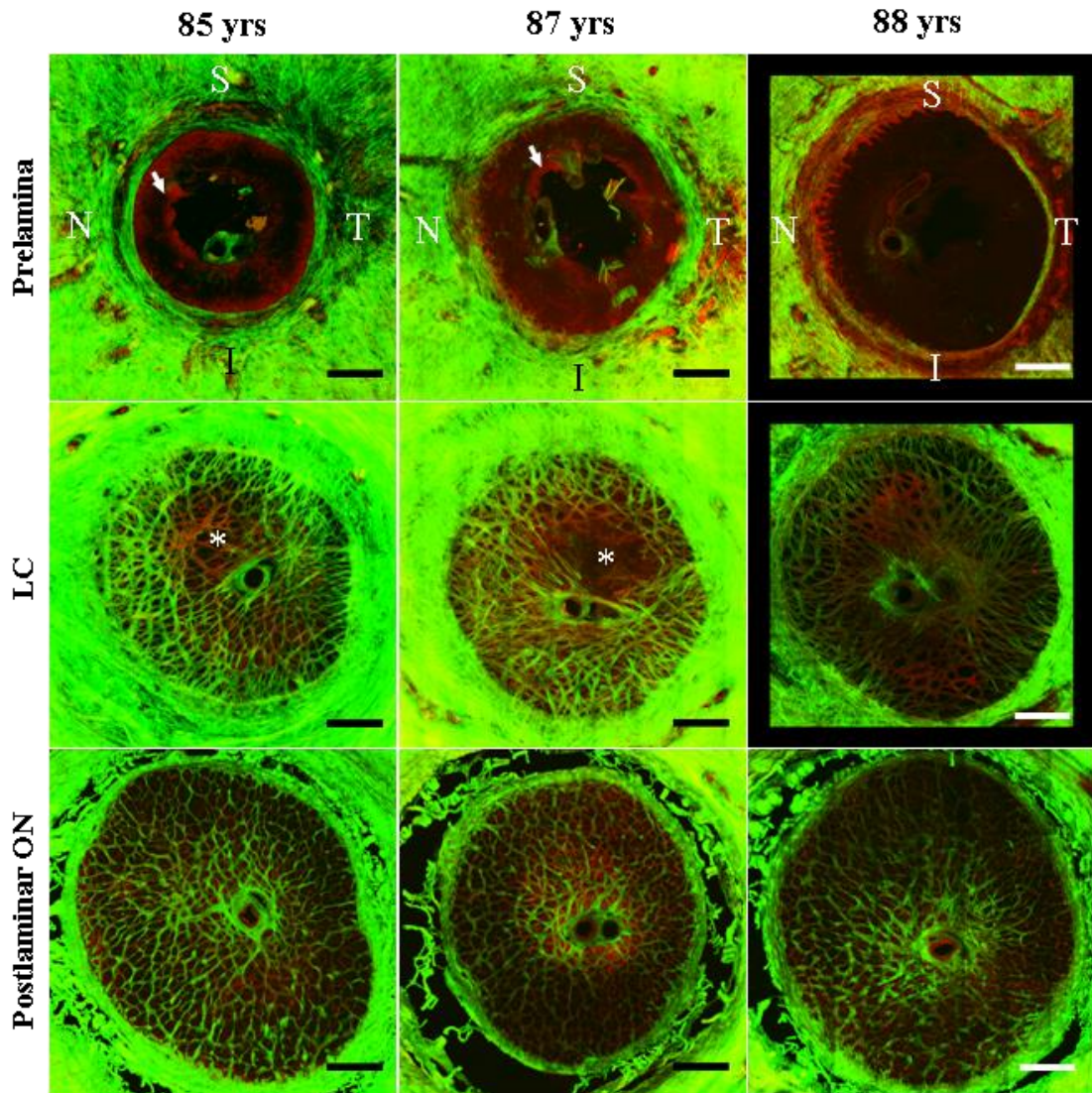
Figure 2.14. Maximum intensity projections of 3D tiled images of elderly ONHs depicting nonlinear signals (SHG = green, TPEF = red) from the prelamina, LC and postlaminar ON from a 85 year old, 87 year old and 88 year old donor. Similar to the young ONH, neuronal tissue related autofluorescence was apparent in the 85 year old and 87 year old prelamina region (arrows). The 85 year old and 87 year old LC also contained a region of minimal connective tissue in the superior region (asterisks). S = superior, T = temporal, I = inferior, N = nasal. Scale bars: 500μm

Both age groups showed minimal connective tissue in the prelamina region, radial connective tissue beams in the LC and connective tissue septae in the postlaminar ON (Figure 2.13, Figure 2.14). The 2 year old ONH appeared to contain less connective tissue than the other ages (Figure 2.13) and both the 85 year old and 87 year old ONHs contained a region of low connective tissue content in the superior LC (Figure 2.14).

Longitudinal sections of young (21 years old) and elderly (78 years old) ONH sections (Figure 2.15) cut in a superior-inferior (Figure 2.15A,C) and nasal-temporal (Figure 2.15B,D) orientation confirmed higher TPEF signal within the elderly LC (Figure 2.15C,D). A higher connective tissue content was apparent in the young nasal-temporal LC (Figure 2.15B) when compared to the superior-inferior (Figure 2.15A), although was less evident in the elderly donor.
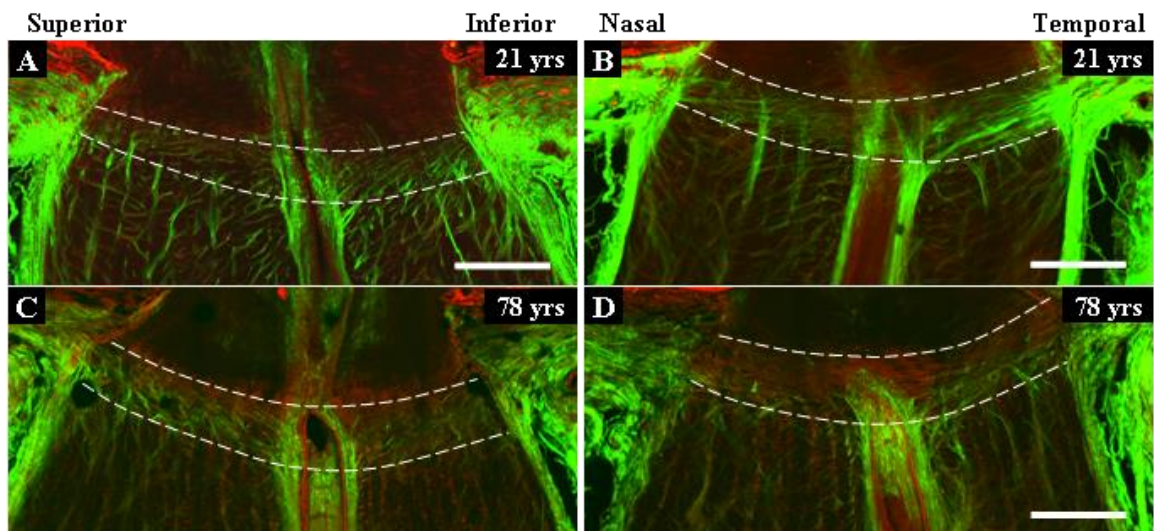
Figure 2.15. Maximum intensity projections depicting nonlinear signals (SHG = green, TPEF = red) of 3D tiled, longitudinal images of the central human ONH sectioned parallel to the (A,C) superior and inferior poles and (B,D) nasal and temporal poles from a (A,B) 21 year old donor and (C,D) an 78 year old donor. Dotted lines denote the anterior and posterior boundaries of the LC. (B) Connective tissue appeared denser in the nasal to temporal orientation in the young LC than in the (A) superior and inferior LC. TPEF signal emitted from (C,D) the elderly LC beams but was minimal in the (A,B) young LC. Scale bars: 500μm

There was no apparent age-related trend in LC thickness when comparing LCs from a range of donor ONHs (aged 11-88 years) (Figure 2.16A). The only significant difference in LC thickness occurred between the 21 and 57 year old LCs (Figure 2.16A). No significant difference in LC thickness was found when averaging LC

thickness in young (11-21 years, n = 2), middle aged (57-63 years, n = 3) and elderly (78-88 years, n = 3) age groups (Figure 2.16B).

Regional LC thickness data indicated that the temporal LC was significantly thicker than the superior and inferior LC (Figure 2.16C).
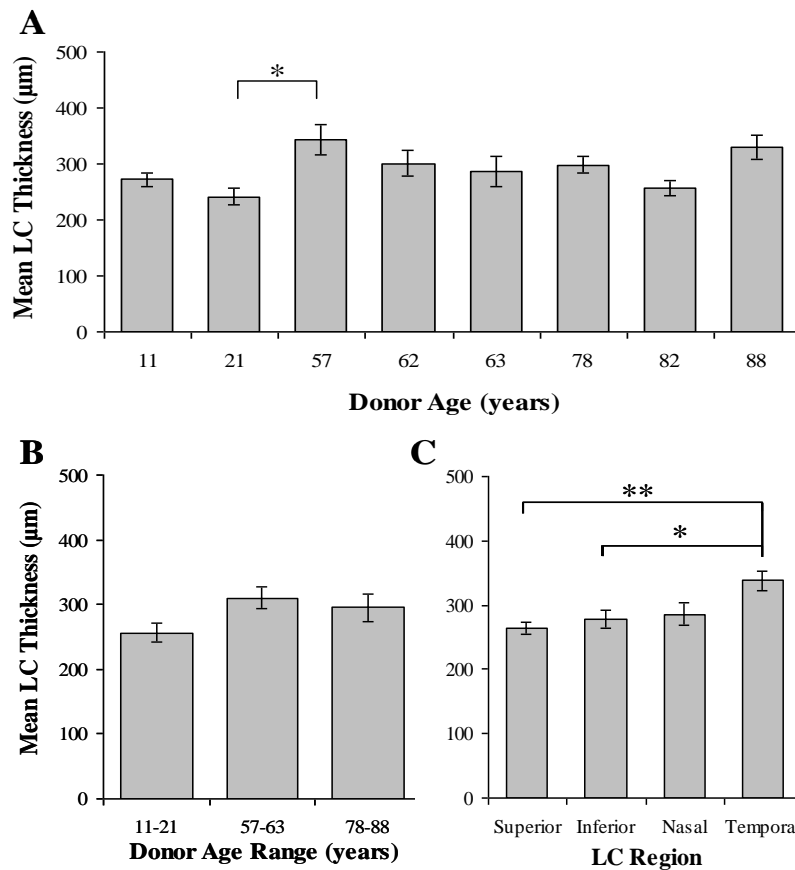
Figure 2.16. LC thicknesses (mean +/- standard error) from 2D ONH measurements of different age donors. (A) A significant difference between the 21 and 57 year old LC was found however, (B) there were no age-related significant differences in LC thickness between the three age groups. (C) The temporal region was significantly thicker than the superior and inferior regions. Significant differences were determined using ANOVA (*p<0.05, **p<0.01).

2.3.3 High Resolution Nonlinear Microscopy: Differences in Collagen and Elastin Distribution in the Young and Old Human Optic Nerve Head

High resolution, single images from the LC connective tissue beams (Figure 2.17A-C, G-I), LC insertion region (Figure 2.17D-F, J-L), peripapillary sclera (Figure 2.18), and postlaminar connective tissue septae (Figure 2.19) were obtained from the ONH sections of a young (6 yrs) and elderly (87 yrs) donors.

Fibrillar collagen appeared to be denser in the elderly LC beams (Figure 2.17G), the insertion region (Figure 2.17J) and peripapillary sclera (Figure 2.18D) than in corresponding regions in the young ONH. LC beams appeared to be thicker (Figure 2.17G) and fibre bundles within the peripapillary sclera were more tightly packed (Figure 2.18D) in the elderly LC.

The fibrillar collagen within the young LC beams (Figure 2.17A), insertion region (Figure 2.17D) and peripapillary sclera (Figure 2.18A) displayed a wavy like appearence which was not evident in the elderly sections. There was no observable difference between fibrillar collagen of the young and elderly postlaminar connective tissue septae (Figure 2.19A,D).
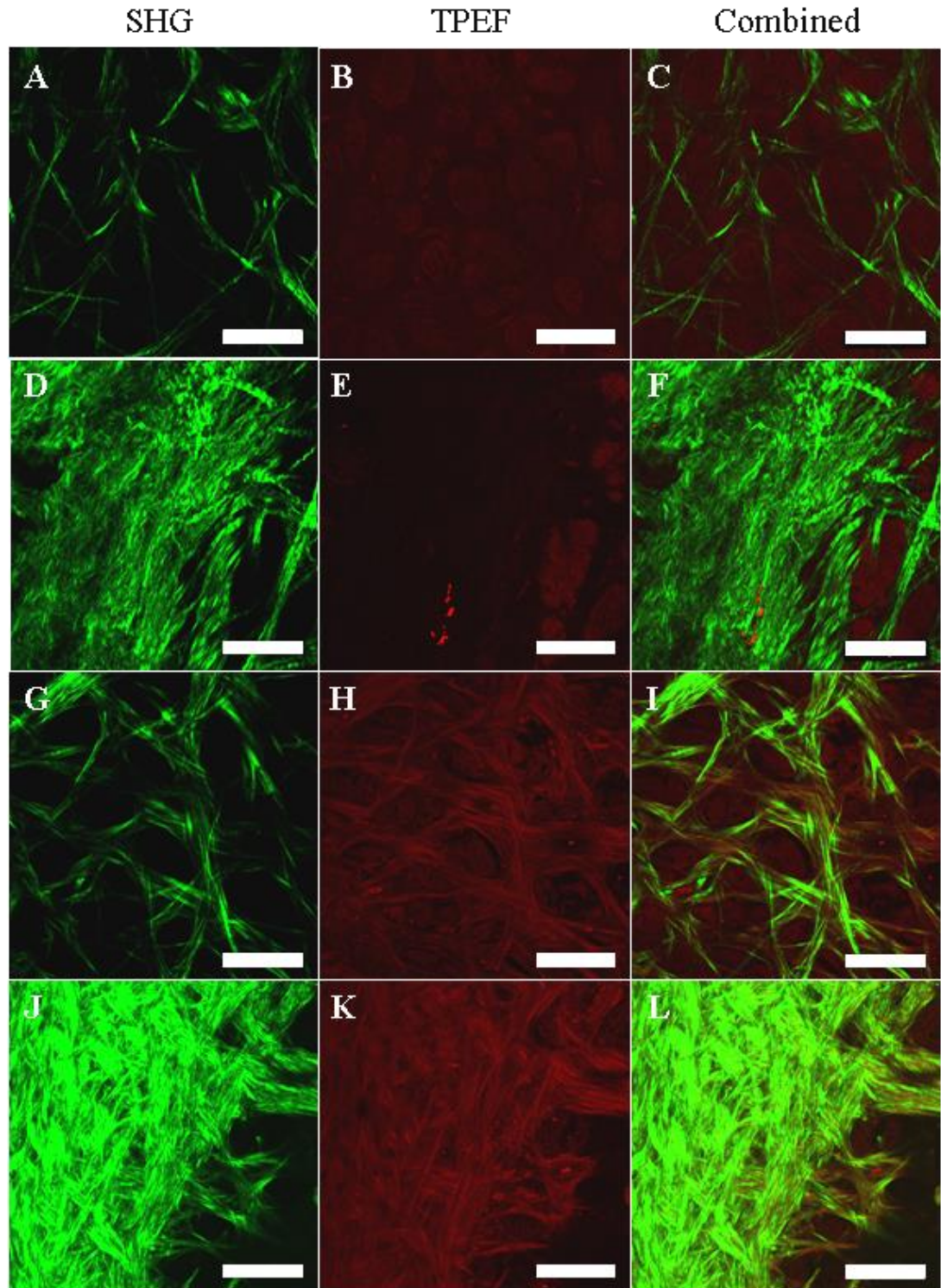
Figure 2.17. High resolution images depicting nonlinear signals (SHG = green, TPEF = red) from the (A-C, G-I) nasal LC connective tissue beams and (D-F, J-L) nasal LC insertion region from a (A-F) 6 year old donor and (G-L) 87 year old donor. (G,J) Fibrillar collagen appeared dense, and (H,K) TPEF was emitted from elastic fibres in the 87 year old LC beams and insertion region. (A,D) Fibrillar collagen appeared sparser and was wavy like and (B,E) TPEF was minimal in the 6 year old LC beams and insertion region. Scale bars: 100μm

TPEF signal was minimal and not associated with visible elastic fibres in the connective tissue of the young LC beams (Figure 2.17B), insertion region (Figure 2.17E), peripapillary sclera (Figure 2.18B) and postlaminar septae (Figure 2.19B). TPEF was only apparent in the diffuse autofluorescence of the axonal bundles between the LC beams.

In contrast, TPEF signal enabled the visualisation of elastic fibres within the LC beams (Figure 2.17H), insertion region (Figure 2.17K) and peripapillary sclera (Figure 2.18E) within the elderly tissue samples. These elastic fibres were straight in morphology and aligned with the collagen fibre bundles.
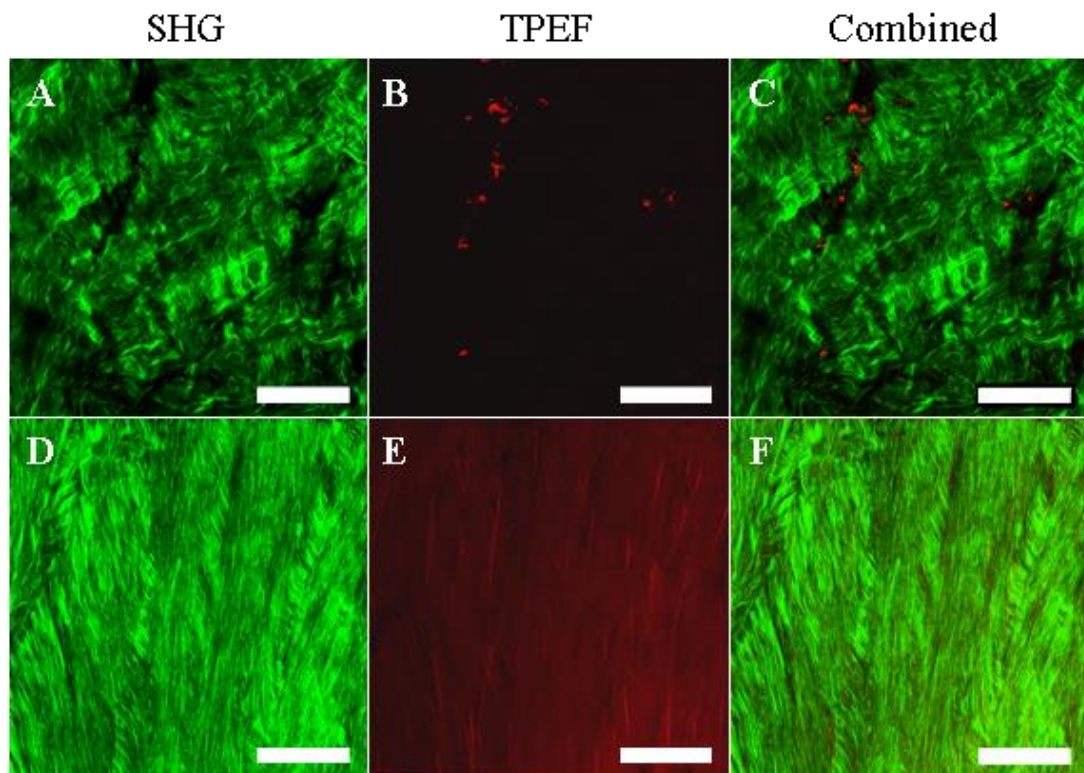
Figure 2.18. High resolution images depicting nonlinear signals (SHG = green, TPEF = red) from the peripapillary sclera situated l000µm nasally from the ON canal from (A-C) a 6 year old donor and (D-F) an 87 year old donor. (D) Fibrillar collagen fibres appeared to be more tightly packed in the elderly peripapillary sclera than the young in which (A) the fibres were more dispersed but displayed an obvious wave-like appearance. Scale bars: 100µm

TPEF signal also emitted from the elderly postlaminar septae and from irregular particles within the postlaminar ON (Figure 2.19E). These particles were absent in the young ON section (Figure 2.19B).
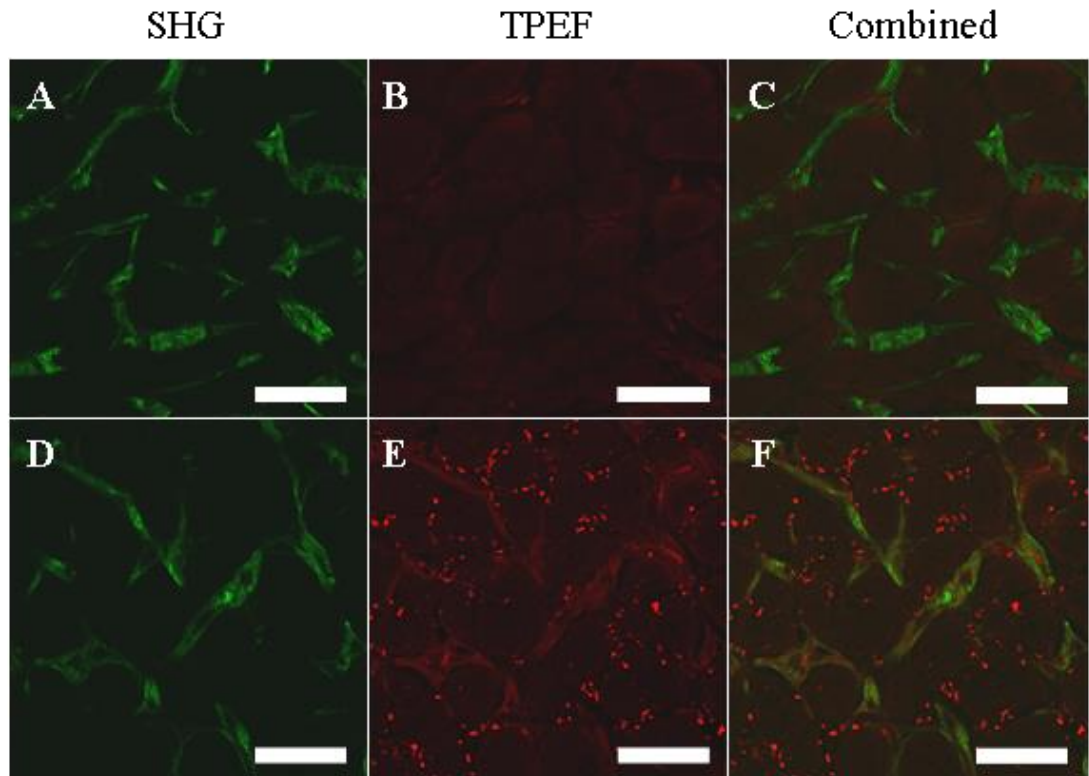
Figure 2.19. High resolution images depicting nonlinear signals (SHG = green, TPEF = red) from the postlaminar ON of a (A-C) 6 year old donor and (D-F) 87 year old donor. (A,D) There was no apparent difference in the fibrillar collagen distribution in the young and elderly postlaminar connective tissue septae. However, (E) the septae in the elderly emitted a stronger TPEF signal and was surrounded by irregular shaped particles which were absent in (B) the young postlaminar ON. Scale bars: 100μm

Interestingly, purified lipofuscin emitted TPEF signals that were similar in shape and size to these particles (Figure 2.20).
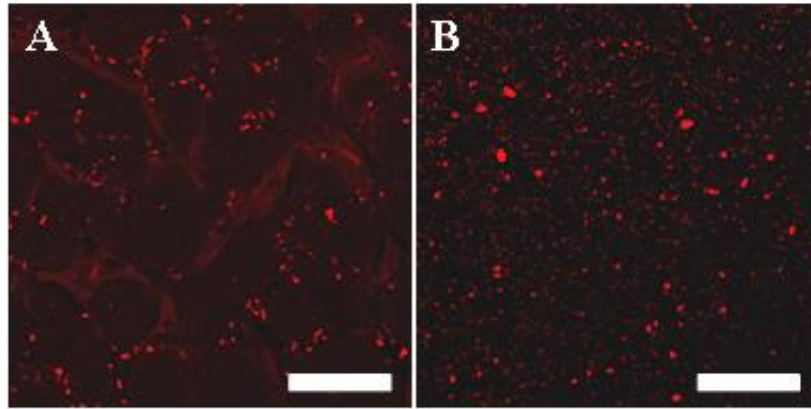
Figure 2.20. High resolution TPEF images of irregular, fluorescent particles in (A) an elderly (87 years old) postlaminar ON and (B) purified lipofuscin. Scale bars: 100μm

2.3.4 3D Reconstruction of Second Harmonic Generation Datasets in Young and Elderly Human Optic Nerve Heads

3D reconstruction of the SHG datasets allowed the visualisation of the arrangement of fibrillar collagen throughout ONH and peripapillary sclera (Figure 2.21) which enabled the whole LC volume to be segmented (Figure 2.21B). Volume rendering of the SHG dataset highlighted the complex collagenous architecture within the ONH (Figure 2.21A,C) and bowed cribriform plates of the LC (Figure 2.21E). The peripapillary sclera contained a dense arrangement of fibrillar collagen bundles which formed a circumferential ring around the ON canal (Figure 2.21C,D).

Prior to fibrillar collagen quantification, visual differences in the collagen density in the ON canals of young (Figure 2.22A-C) and elderly (Figure 2.22D-F) ONHs were apparent in 3D volume renders of each SHG dataset.
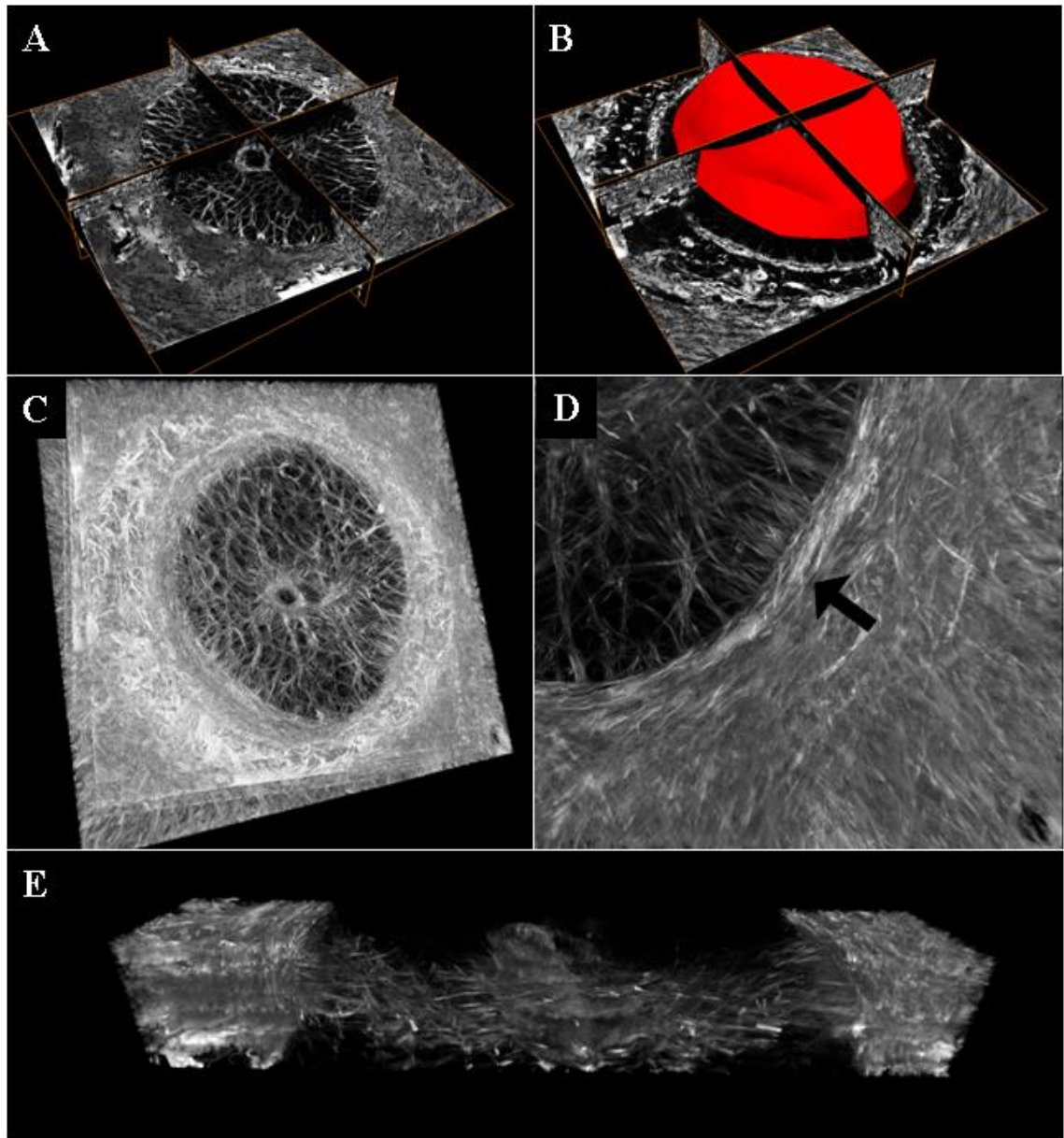
Figure 2.21. 3D reconstruction of the fibrillar collagen within the ONH. (A) Three orthoslice views in the XY, XZ and YZ axis showing a complete reconstructed ONH dataset and (B) segmented LC volume from a 21 year old donor eye. (C) Volume rendering of the dataset highlighted the complex fibrillar collagen meshwork within the ON canal which was surrounded by (D) circumferential fibre bundles (black arrow). (E) The bowed nature of the LC cribriform plates was emphasised by rotating the dataset and isolating a block through the LC.

The LC appeared to increase in complexity with increasing age (Figure 2.22). The 2 year old ON canal contained regions of sparse fibrillar collagen density, especially in

the inferior region (Figure 2.22A) while the 6 and 21 year old ON canals contained well

defined LC beams and clearly visible LC pores (Figure 2.22B,C).
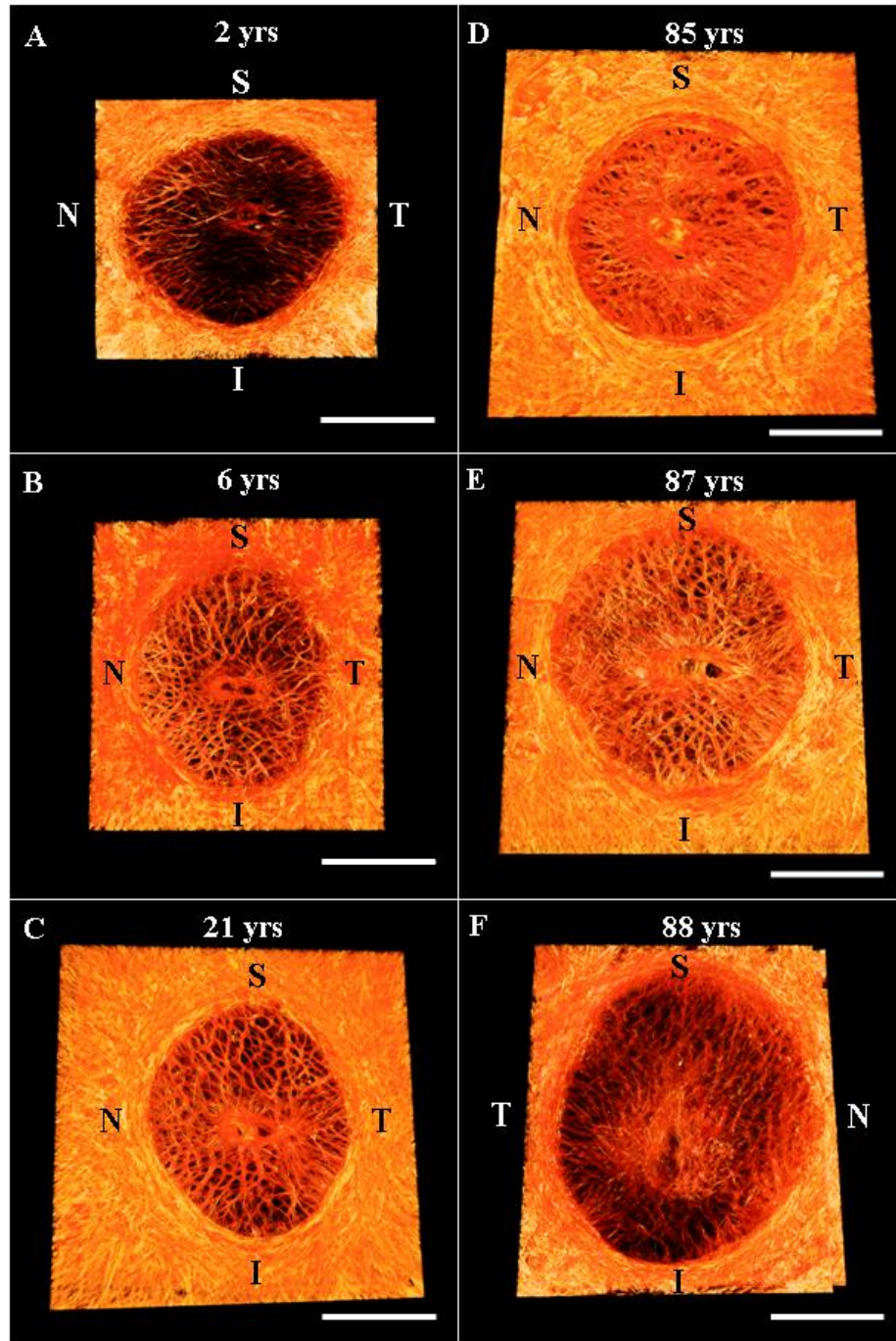
Figure 2.22. Volume rendering of reconstructed 3D SHG datasets from ONHs of different ages. (A-C) The young ON canals appeared to contain less fibrillar collagen and more defined LC pores than the (D-F) elderly ON canals. (F) Interestingly, the 88 year old ON canal appeared to have less fibrillar collagen than the (D) 85 and (E) 87 year old ON canals. S = superior, T = temporal, I = inferior, N = nasal. Scale bars: 1000μm

LC pores within the 85 and 87 year old ON canals were harder to delineate as the fibrillar collagen appeared to become more dense within these ages (Figure 2.22D,E). Interestingly, similar to the 2 year old, the 88 year old ON canal also contained regions of less dense fibrillar collagen within the inferior region (Figure 2.22F). However, in contrast to the 2 year old, the 88 year old ON canal was larger in size and contained a thick collagen network surrounding the central retinal vessels.

2.3.4.1 *Fibrillar Collagen Content in Young and Elderly Human Optic Nerve Heads*

Relative fibrillar collagen content increased from the anterior LC to postlaminar ON, appearing to peak at within the LC in all ages, with exception of the 2 year old ONH in which fibrillar collagen density continued to increase in the postlaminar ON (Figure 2.23).

The LC peak in fibrillar collagen density occurred at a greater distance from the prelamina in the 85 and 88 year old ONHs than in the young and 87 year old ONHs (Figure 2.23) which implies that the 85 and 88 year old LCs may be more posterior positioned. The highest peaks in fibrillar collagen density occurred in the 85 and 87 year old ONHs and lowest peak occurred in the 2 year old ONH (Figure 2.23).

Within the LC volume, fibrillar collagen appeared to increase with age in all regions with the exception of the 88 year old ONH where it was lower than the 87 year old ONH (Figure 2.24A).
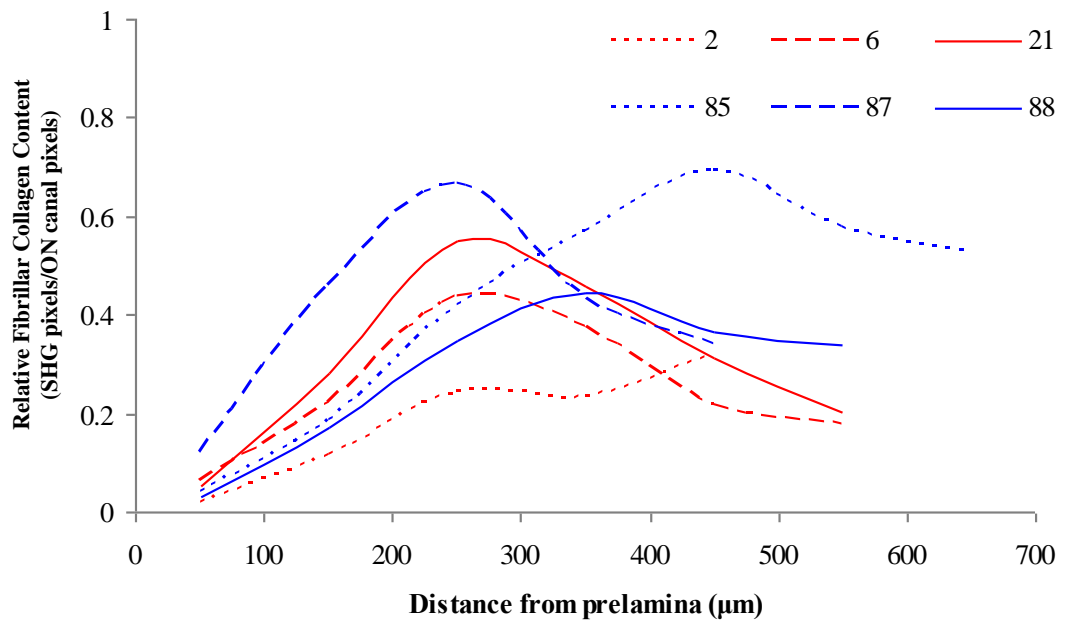
Figure 2.23. Change in fibrillar collagen distribution from prelamina to postlaminar ON in ONHs of different ages (2 to 88 years old). SHG pixels:ON canal pixels were averaged from every 100 optical slices through 3D ONH datasets (assembled from the prelamina section immediately preceding the LC through to the postlaminar ON). In all ages, with exception of the 2 year old ONH, fibrillar collagen density increased from the prelamina and peaked at the region of the LC before decreasing in the postlaminar ON.

When quantifying relative fibrillar collagen content in 4 LC regions of the young (ages 2, 6 and 21 years) and elderly (85, 87, 88 years) ONHs, it was found that relative fibrillar collagen content was highest in the nasal region and lowest in the inferior region (Figure 2.24B).

65
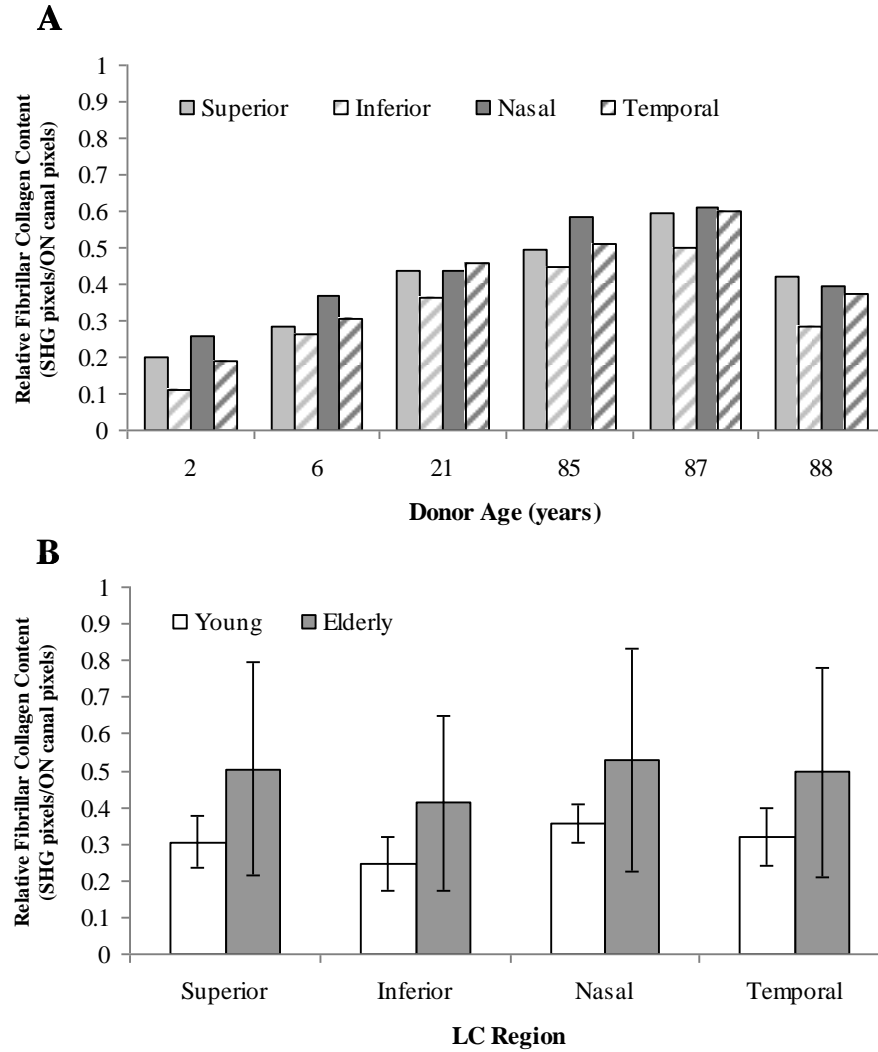
Figure 2.24. Regional LC relative fibrillar collagen content in ONHs of different ages. (A) Fibrillar collagen:ON canal area ratios increased from the 2 year old to 87 years old ONH and decreased in the 88 year old ONH. (B) In all LC regions, mean relative fibrillar collagen content (+/- standard error) was greater in the elderly than in the young, though no statistically significant differences were found.

Furthermore, mean LC relative fibrillar collagen content was higher in the elderly age group compared to the young age group in all regions, though, due to the high variability in the elderly age group, no statistical significant differences were found ($p > 0.05$).

2.3.4.2 *Lamina Cribrosa Surface Area and Volume in Young and Elderly Optic Nerve Heads*

In all ages the anterior LC surface area was smaller than the posterior LC surface area (Table 1), although this did not reach statistical significance ($p > 0.05$). Both anterior and posterior LC surfaces areas increased with age (Table 1).

Age (years)	Anterior LC Surface Area (mm^2)	Posterior LC Surface Area (mm^2)	LC Volume (mm^3)
2	2.59	3.05	0.71
6	2.32	3.14	0.99
21	2.49	3.42	0.99
85	2.8	3.77	1.05
87	3.45	3.96	0.82
88	3.86	4.81	1.13

Table 1. Anterior and posterior LC surface areas and LC volume from ONHs of different ages.

When comparing the surface area results from the young and elderly age groups it was found that the elderly mean anterior and posterior LC surface areas were significantly greater than the young mean anterior and posterior surface areas (Figure 2.25).

Interestingly, young and elderly LC volumes were not significantly different ($p > 0.05$; Figure 2.26).
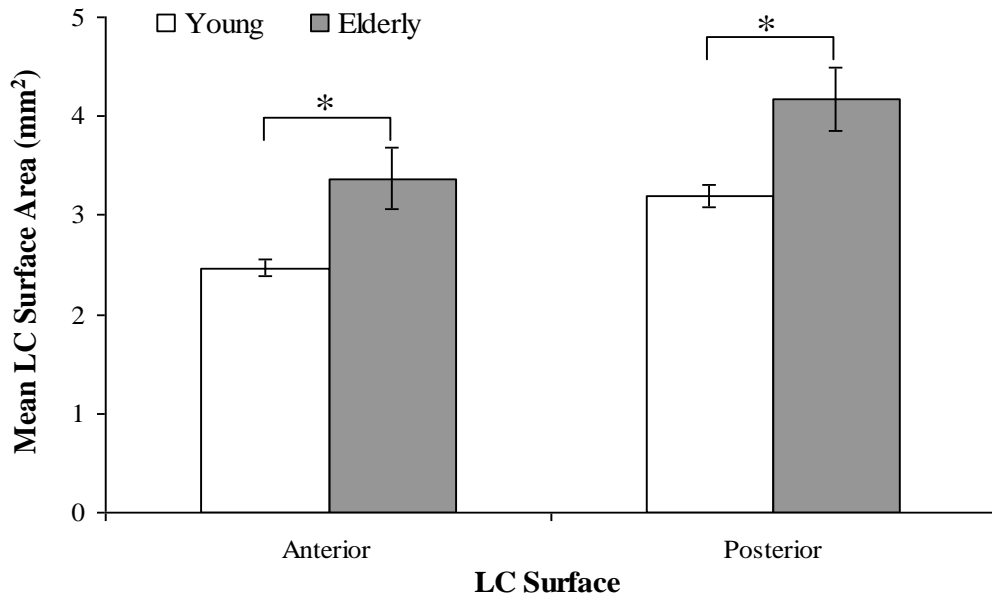
Figure 2.25. Comparisons of mean anterior and posterior LC surface area (+/- standard error) from young and elderly LCs. Elderly anterior and posterior LC surface areas were significantly greater than young anterior and posterior LC surface areas. Significant differences were determined using the independent samples t-test (*p<0.05).
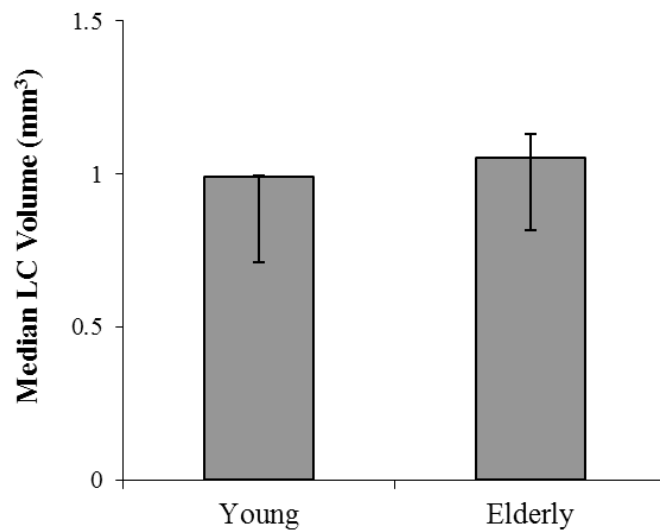
Figure 2.26. Comparisons of median LC volume (+/- 95% confidence intervals) from young and elderly LCs. Using the Mann-Whitney U test, no significant difference was observed between the young and elderly LC volumes (p>0.05).

2.3.4.3 Lamina Cribrosa Thickness in Young and Elderly Optic Nerve Heads

LC thickness maps were produced from the reconstructed SHG signal from each sample and therefore represented the anatomy of the LC as constructed from the fibrillar collagen only. Regional variation was observed in the thickness of the LC in all ages (Figure 2.27). Thickness maps indicated that the superior region was thinnest compared to the other LC regions in the 6, 21, 85, 87 and 88 year old LCs (Figure 2.27B-F). However, the thinnest region of the 2 year old LC was the inferior region (Figure 2.27A).
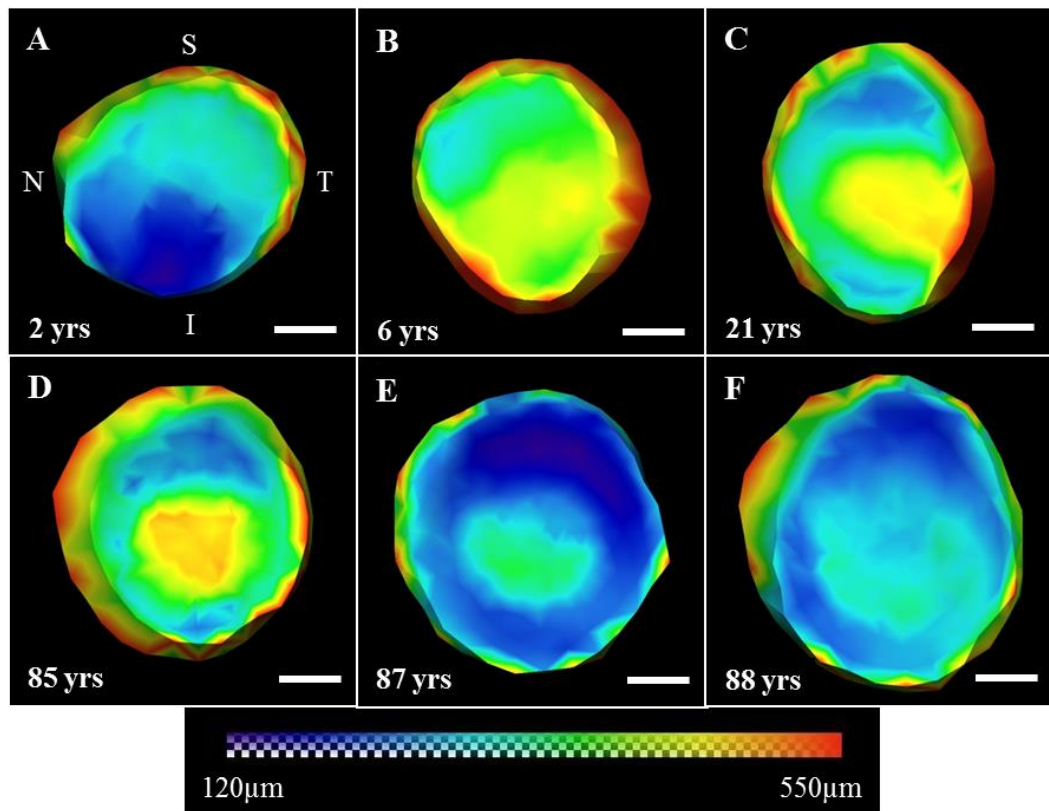
Figure 2.27. Regional LC thicknesses represented as 3D thickness maps from (A-C) young and (D-F) elderly ONHs. Regional variation in LC thickness was observed in all samples. The superior region in all ages, with exception of (A) the 2 year old LC, appeared to be the thinnest LC region. In contrast, (A) the 2 year old LC contained a thinner inferior region. All maps are in the same orientation as (A), S = superior, T = temporal, I = inferior, N = nasal. Scale bars: 500μm

The central LC, and most probable site of LC insertion into the central retinal vessels, was thicker than the surrounding areas in all samples with exception of the 2 year old LC (Figure 2.27B-F). This thicker central area was very distinct in the 21, 85 and 87 year old LCs (Figure 2.27C-E) and extended inferior-nasally in the 6 year old LC (Figure 2.27B) and temporally in the 21 year old LC (Figure 2.27C).

Averaging the LC thickness measurements per sample indicated that the 87 year old LC was the thinnest and 6 year old LC was the thickest (Figure 2.28A).
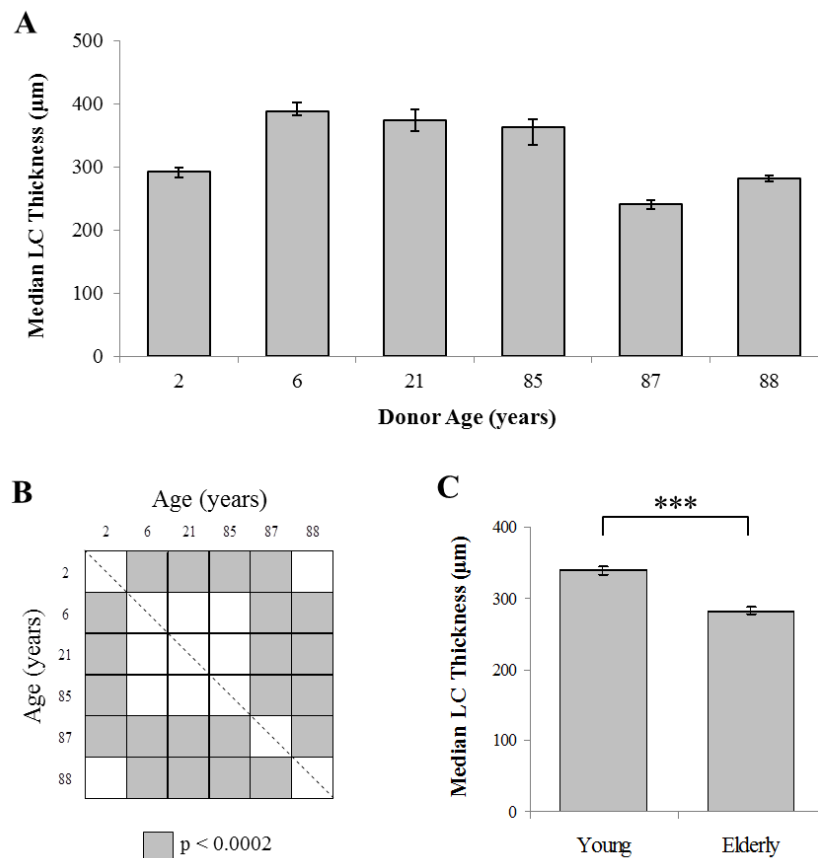
Figure 2.28. LC thicknesses (median +/- 95% confidence intervals) from 3D ONH measurements of different aged donors. (A) The thickest LC belonged to the 6 year old ONH and thinnest to the 87 year old. (B) The 87 year old LC was significantly thinner than all other LCs while the 2 and 88 year old LCs and 6, 21 and 85 year old LCs showed no significant difference in thickness. (C) Overall, the elderly LC was significantly thinner than the young LC. Significant differences were determined using the Mann-Whitney U test (B, Bonferroni adjusted: *p<0.0033, **p<0.0017 and ***p<0.0002; C, ***p<0.001)

The 2 year old and 88 year old LCs were similar in thickness but significantly thinner than the 6, 21 and 85 year old LCs and significantly thicker than the 87 year old LC (Figure 2.28B). The 87 year old LC was significantly thinner than all other LCs (Figure 2.28B).

3D thickness measurements were comparable to those measured from 2D nonlinear images (Figure 2.16). Similar to the 2D measurements, no age-related trend in LC thickness was found. However, in contrast to the 2D measurements, the young age group LC thickness was significantly greater than the elderly age group LC thickness (Figure 2.28C).

2.4 **Discussion**

Nonlinear microscopy techniques enabled the non-invasive identification of the distribution of fibrillar collagen and elastic fibres within the LC and surrounding tissues. Validation of these signals against a general connective tissue trichrome green stain and immunolabelling for specific collagen types and elastin supports the use of SHG and TPEF as surrogate indicators of fibrillar collagen and elastin respectively.

Fibrillar collagen was found as fibrillar bundles within the LC beams and central vessel walls and encircled the ON canal within the peripapillary sclera. In the middle aged and elderly ONH, elastin was found in the form of distinct elastic fibres which co-distributed with fibrillar collagen within the LC beams and peripapillary sclera and formed interwoven elastic fibres around the circumference of the ON canal.

The TPEF related elastic fibres were not apparent in the young ONH tissue sections but were found within the LC beams, insertion regions and peripapillary sclera of the elderly ONH. In young eyes, the microfibrillar components of elastic fibres have been shown to aggregate within the LC cribriform plates (Hernandez, 1992) forming sparse, thin fibres (Morrison et al., 1989a). Within adult eyes, elastic fibres are long and distinct and run longitudinally through the cribriform plates (Morrison et al., 1989a, Hernandez, 1992). They have also been shown to increase in thickness (Hernandez, 1992) and are thought to accumulation with age (Hernandez et al., 1989).

The α-elastin core of elastic fibres has also been localised to the peripapillary sclera in young eyes (Hernandez et al., 1989, Hernandez, 1992), however, no TPEF related elastic fibres were observed in the young sclera in the current study. Elastin is thought to contain several fluorophores, one of which is attributed to the enzyme-mediated cross-link pyridinoline (Deyl et al., 1980). Although hydroxylysyl pyridinoline has not shown an age-related increase in the LC (Albon et al., 1995), the elastin cross-links desmosine and isodesmosine have been shown to increase (Albon et al., 2000a). Therefore, the intensity of TPEF of elastic fibres imaged in the current study may depend on the amount of elastin cross-linking present. Consistent with findings by Albon et al. (2000a), this indicates that elastin cross-linking increases with age in the LC and peripapillary sclera.

Unfortunately, due to the number of endogenous fluorescent contributing factors other than elastin, elastin could not be easily segmented and quantified from the nonlinear ONH datasets. One of these contributing factors was found in the elderly postlaminar ON in the form of small, irregular particles. The particles were of similar size and shape to purified lipofuscin and shared the same excitation and emission maxima (800/500-

550nm) as lipofuscin in the human RPE (Bindewald-Wittich et al., 2006). The presence of lipofuscin in the ON has been reported in the past by Dolman et al. (1980) and, more recently, was quantified in the ageing ON (Fernandez de Castro et al., 2013). Consistent with the current findings, Fernandez de Castro et al. (2013) found an accumulation of lipofuscin granules in the ON with age. Lipofuscin was found within the nerve fibre bundles, associated with the neuroglial cells (Fernandez de Castro et al., 2013). Lipofuscin is considered the best marker for cellular ageing (Porta, 2002) and neuronal lipofuscin is thought to result from incomplete digestion of mitochondrial products (Sulzer et al., 2008). Interestingly, Fernandez de Castro et al. (2013) also found that ON lipofuscin granules were greater in size and density in glaucomatous samples and theorised that the presence of larger amounts of lipofuscin may contribute to ON damage in glaucoma.

As well as differences in elastic fibre composition, age-related differences in SHG related fibrillar collagen were also observed in the current study. High resolution SHG images of the LC, insertion region and peripapillary sclera revealed fibrillar collagen to be wave-like in the young ONH. This wave pattern was not apparent in the elderly ONH. The wave-like patterns of fibrillar collagen are termed collagen crimping and are believed to be related to tissue biomechanical behaviour. Collagen crimp is considered to represent the "relaxed" conformation of collagen fibrils when they are free from external load (Weiss and Gardiner, 2001). "Uncoiling" of the crimp may represent the initial nonlinear stress response when a collagenous tissue is stretched (Freed and Doehring, 2005). The "relaxed" state of the fibrillar collagen in the young ONH tissue and lack of crimping in the elderly ONH is consistent with the age-related decrease in LC reversibility and increase in stiffness (Albon et al., 2000b). ONHs were dissected

from excised eyes that would not have been under physiological IOP. In the young eyes, this release in pressure could have led to the relaxed, crimped nature of the collagen fibril bundles. If the elderly eyes were stiffer, due to increases in non-enzymatic glycation and an alteration in the ratio of collagen types I:III (Albon et al., 1995), the collagen fibrils would be less able to reverse back to a relaxed state after a release in pressure and would therefore remain stretched.

Collectively, relative fibrillar collagen content within the elderly LCs was greater than in the young LCs, although no statistical significant difference was found due to the high variation in the elderly. The LC is believed to fully mature in the 7th month of gestation (Varma and Spaeth, 1992) but its connective tissue content increases with age (Albon et al., 1995, Albon et al., 2000a). Interestingly, LC connective tissue volume fraction is predicted to be inversely proportional to tissue tensile strain, therefore an LC with high connective tissue content will not deform as much as an LC with low connective tissue content (Roberts et al., 2010a). As fibrillar collagen is the major load-bearing component of the LC, it is presumed that the elderly LC is less compliant than the young (Albon et al., 2000b). The low relative fibrillar collagen content within the 88 year old LC was an interesting finding and a higher number of samples are needed to fully investigate the age-related changes and inter-individual variability in fibrillar collagen content. This is important to determine if total collagen content may contribute to ONH susceptibility to glaucoma.

The current study also found that elderly LC anterior and posterior surface areas were significantly greater than those of the young. This finding contradicts previous studies which did not find a relationship between LC area and age (Ogden et al., 1988, Jonas et al., 1991). However, the current study investigated the 3D surface area of the LC which

takes the curvature of the structure into consideration whereas past studies measured the 2D LC area (Ogden et al., 1988, Jonas et al., 1991).

The LC thicknesses measured in the current study (241.10-383.75μm) were similar to those published by Jonas and Holbach (2005) (378.1μm (±117.8)). Interestingly, the general increase in relative LC fibrillar collagen content with age, as witnessed here and indicated by Albon et al. (1995), did not lead to an increase in overall LC thickness. No age related differences in LC thickness were found from 2D thickness measurements. However, the average elderly LC thickness was significantly thinner than the young LC thickness, when comparing thickness measurements calculated in 3D volumes. Since collagen content increases with age, this implies that the LC collagen fibre bundles possibly become more compact with age which may consequently affect the flexibility of the structure. A more compact, and potentially more rigid (Albon et al., 2000b) elderly LC may lead to a heightened susceptibility of the RGC axons to damage under changes in IOP.

Previous LC thickness studies interested in anatomical relationships between LC, cornea and peripapillary sclera also found LC thickness to be independent of age (Jonas and Holbach, 2005, Ren et al., 2009, Ren et al., 2010b). However a study by Kotecha et al. (2006), which specifically looked at age-related changes in human LC thickness, found that the LC became significantly thicker with age. Discrepancies between Kotecha et al. (2006) and the current study may be due to a number of factors. Firstly, 2D measurements are subject to inaccuracies due to tissue folding or an oblique histological sectioning angle and therefore, measurements in 3D are considered more accurate. Secondly, the 2D and 3D thickness measurements were collected from SHG and TPEF, or SHG only datasets, respectively. The latter represented the fibrillar

collagen architecture of the LC. Age-related increase in the non-fibrillar components of the LC, such as collagen type IV (Hernandez et al., 1986, Hernandez and Neufeld, 1989) may contribute to LC thickness but could not be visualised using nonlinear microscopy in this study. However, changes with age of the thickness of basement membranes surrounding the cribriform plates has not been observed (Hernandez and Neufeld, 1989). Lastly, the current study is limited by its small samples size. Future investigations will aim to 3D reconstruct a larger number of samples from a larger age-range to fully investigate age-related changes in connective tissue of the LC.

2.5 **Conclusion**

Nonlinear microscopy is a valuable tool for the visualisation of the intricate fibrillar collagen and elastic fibre organisation within the human ONH. High resolution imaging of young and elderly ONH tissue sections revealed that young ONHs contain compliant fibrillar collagen but no TPEF related elastic fibres whereas elderly ONHs contain unrelaxed fibre bundles and distinct elastic fibres. Lipofuscin like particles were also found within the elderly ON which were absent from the young ON. 3D analysis revealed that the average elderly LC also had higher relative fibrillar collagen content and was significantly thinner than the young. Further analysis is needed to determine if connective tissue content and LC thickness are factors that predispose the elderly eye to glaucomatous optic neuropathy.

Chapter 3 - Nano-architecture of the Connective Tissue in the Human Optic Nerve Head

3.1 Introduction

The mechanical properties of the LC are considered one of the five most influential features with respect to ONH biomechanics (Sigal et al., 2005). One of the major load-bearing components of the LC is fibrillar collagen. Collagen fibril diameter and distribution within a tissue determines how effectively collagen fibrils provide reinforcement against an applied force (Hukins and Aspden, 1985, Parry, 1988). The diameter of a collagen fibril is also believed to relate to the critical length at which the fibril can provide effective tissue support (Hukins and Aspden, 1985). Therefore, knowledge of collagen fibril sizes (and the distribution of these sizes) and spacings within the ONH is critical in understanding the biomechanical response of the ONH to fluctuations in IOP.

In the current study, microfocus and conventional small angle X-ray scattering (SAXS) was utilised with the aim of quantifying collagen fibril parameters within the human ONH. SAXS can resolve structures on a nanometre scale by recording tissue X-ray scatter at low angles (typically 0.1-10º) and has previously been effectively used to study ocular tissues including cornea collagen (Sayers et al., 1982, Meek et al., 1987, Boote et al., 2003), lens crystallins (Regini et al., 2004) and ON myelin (Chandross et al., 1978).

OBJECTIVES

- To investigate the nano-scale organisation of connective tissue (collagen and elastin) and associated nervous tissue in the human ONH

- To quantify collagen interfibrillar spacing, fibril diameter and axial periodicity in different regions of the LC, insertion region and peripapillary sclera

- To determine if collagen interfibrillar spacing, fibril diameter and fibril axial periodicity differ between young and old ONHs

3.2 Methods

3.2.1 Sample Preparation

Donor eyes, with no history of ocular disease, were received from the Bristol Corneal Transplant Service Eye Bank, UK. ONHs were immersed in 4% PFA and orientated as previously described in section 2.2.1. The ONH surrounded by a block of sclera was dissected. The tissue blocks were washed overnight in PBS (pH 7.4) and snap frozen in liquid nitrogen-cooled isopentane (Fisher, UK). The frozen tissue blocks were mounted onto a sledge microtome (MICROM HM 440E, Thermo Fisher, UK) and sectioned transverse or longitudinal to the ON. Tissue sections were wrapped in polyvinyl chloride film (Cling film; Lidl UK GmbH, UK) which was labelled with the section's orientation and number, and stored at -80°C until scanned.

3.2.2 Small Angle X-ray Scattering

All SAXS experiments were carried out on station I22 at the Diamond Light Source synchrotron, Oxfordshire, UK. Each section was placed into a custom made sample holder which clamped the specimen between two Mylar film (DuPont Teijin Films, UK) windows (Figure 3.1). The sample holder was then fixed onto a motorised stage so that the ONH sections faced the incident X-ray beam. During SAXS scanning, a lead beam-stop was positioned between the detector and sample to block the high intensity, direct beam from hitting the detector.
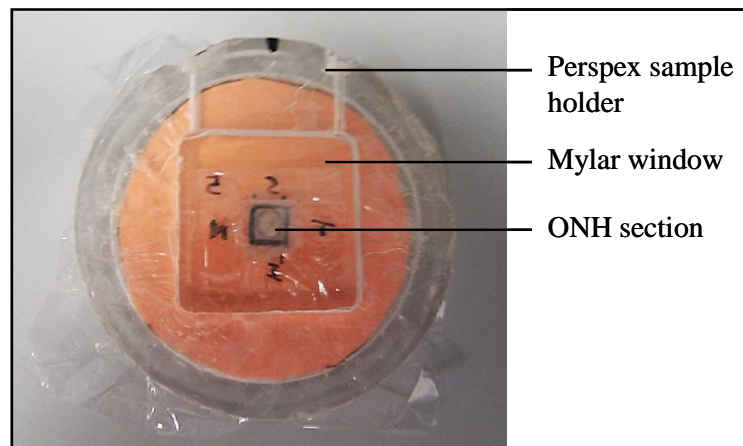
Figure 3.1. Custom made sample holder showing mylar window containing a human ONH tissue section.

3.2.2.1 Microfocus Small Angle X-ray Scattering

Microfocus SAXS data were collected from ONH sections (250µm thickness), from 3 donors aged 61, 87 and 90 years of age, using a microfocus X-ray beam ($\lambda = 0.09$nm) with a 12µm x 19µm beam size at the sample. The sample to detector distance was 0.9m (Figure 3.2). Images were collected, at 100µm intervals, over a 10s exposure time by a RAPID detector. An in-line microscope, which was calibrated to the approximate X-ray

beam position, was used to position the section to the appropriate starting point via the motorised stage.
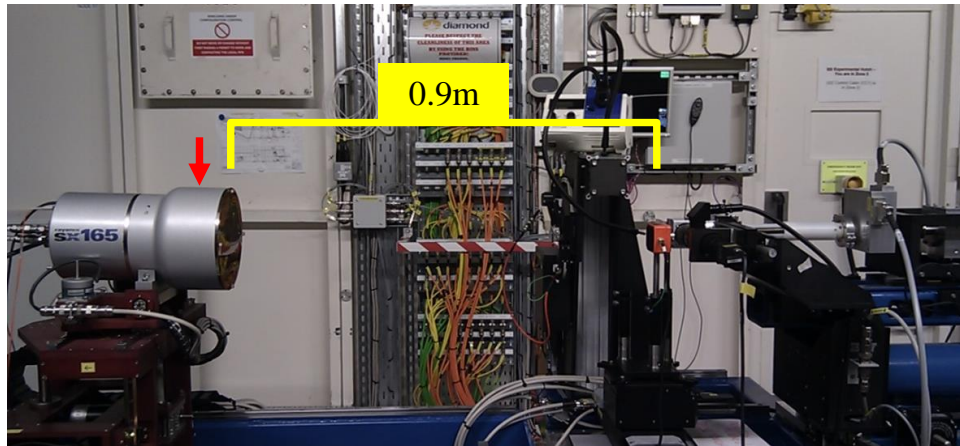
Figure 3.2. Experimental set up for microfocus SAXS. The RAPID detector (red arrow) was situated 0.9m away from the sample position.

Single rows of images were collected across the superior/inferior and nasal/temporal axis within the transverse ONH sections and from prelamina to postlaminar ON within the longitudinal ONH sections covering a distance of 3000-4000μm and 1000μm, respectively.

3.2.2.2 *Conventional Small Angle X-ray Scattering*

Conventional SAXS data were collected from transverse ONH sections (500μm thickness), from 5 donors aged 33 to 91 years of age, using an X-ray beam (λ = 0.1nm). Sections were imaged with a 200μm x 200μm beam, 6m sample to detector distance (Figure 3.3) and images were collected at 250μm intervals using a 20s exposure time by a PILATUS 2M detector. Images were collected as raster scans across the ONH sections covering an area of 3000μm x 3000μm
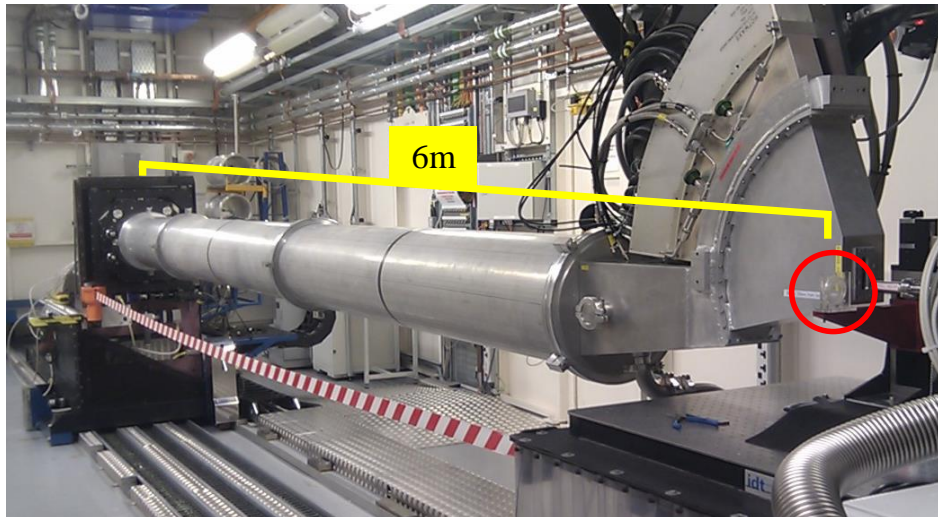
Figure 3.3. Experimental set up for conventional SAXS. The PILATUS 2M detector was situated 6m away from the sample position (red circle).

3.2.3 Data Analysis

When X-rays interact with a sample they may be absorbed or scattered. The differing resultant angles and levels of interference of the scattered photons depend on the arrangement and order of the structures within the sample. The resultant pattern of the scattered photons is detected and converted into a 2D image frame of corresponding pixel intensities (Figure 3.4) allowing for determination of the arrangement and size of the structures within the sample.

3.2.3.1 Calibration

To calibrate the scatter pattern positions produced from ONH tissue sections, hydrated rat tail tendon was subjected to microfocus (Figure 3.4A) and conventional (Figure 3.4B) SAXS.
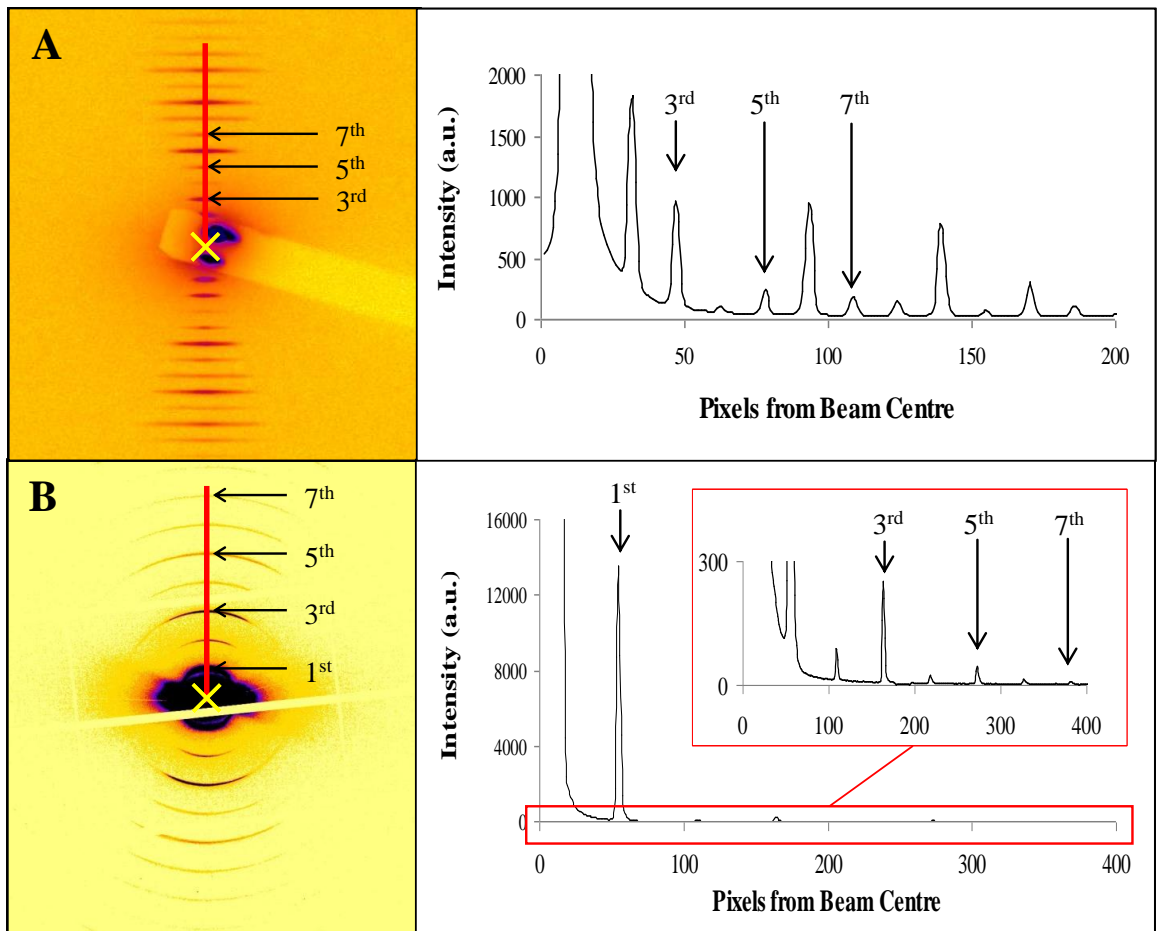
Figure 3.4. Meridional SAXS reflections from rat tail tendon used for ONH image calibration. Intensity peaks, plotted against distance from the beam centre (yellow cross), from (A) microfocus and (B) conventional SAXS images correspond to the quarter stagger axial molecular spacing found in type I collagen. The odd numbered orders (1-7) are highlighted (arrows). Note that the first order Bragg reflection in (A) is obscured by the beam-stop and the strong 2nd and 6th order reflection may indicate that the sample was dehydrated.

Rat tail tendon is mainly composed of type I collagen and produces meridional Bragg reflections representative of the orders of 67nm quarter stagger axial molecular spacing (Figure 3.4). The distance in pixels of the first order reflection from the beam centre occurs at 67nm, the second order occurs at 67/2nm, third order at 67/3nm and so on. These well characterised distances of the orders of reflections from the centre of the beam allowed calibration of each microfocus and conventional SAXS image.

The relative intensities of the meridional orders of hydrated rat tail tendon have been shown to be higher for the 3rd and 5th orders than the 2nd, 4th, 6th and 7th (Tomlin and Worthington, 1956). This can be seen in Figure 3.4B. However, this is not the case in the microfocus rat tail tendon image which shows higher intensity reflections for the 2nd and 6th orders compared to the 3rd and 5th (Figure 3.4A).

A change in the relative intensity of meridional orders indicates that the rat tail tendon used for microfocus SAXS calibration may have become dehydrated (Tomlin and Worthington, 1956). Therefore, microfocus reflections within the current study were determined using a rat tail tendon collagen D periodicity of 65nm which has been previously reported for dry tendon (Wess and Orgel, 2000).

3.2.3.2 Determining Positions of Bragg Reflections

The SAXS image frames were output as .BSL files which were viewed and analysed in the Unix-based graphics program Fit2D (ESRF, Grenoble, France). The centre of each SAXS pattern was calculated using the Beam Centre function which calculates the beam centre from a series of user defined points (Figure 3.5A) positioned on an arc or circular pattern around the centre (Figure 3.5B).
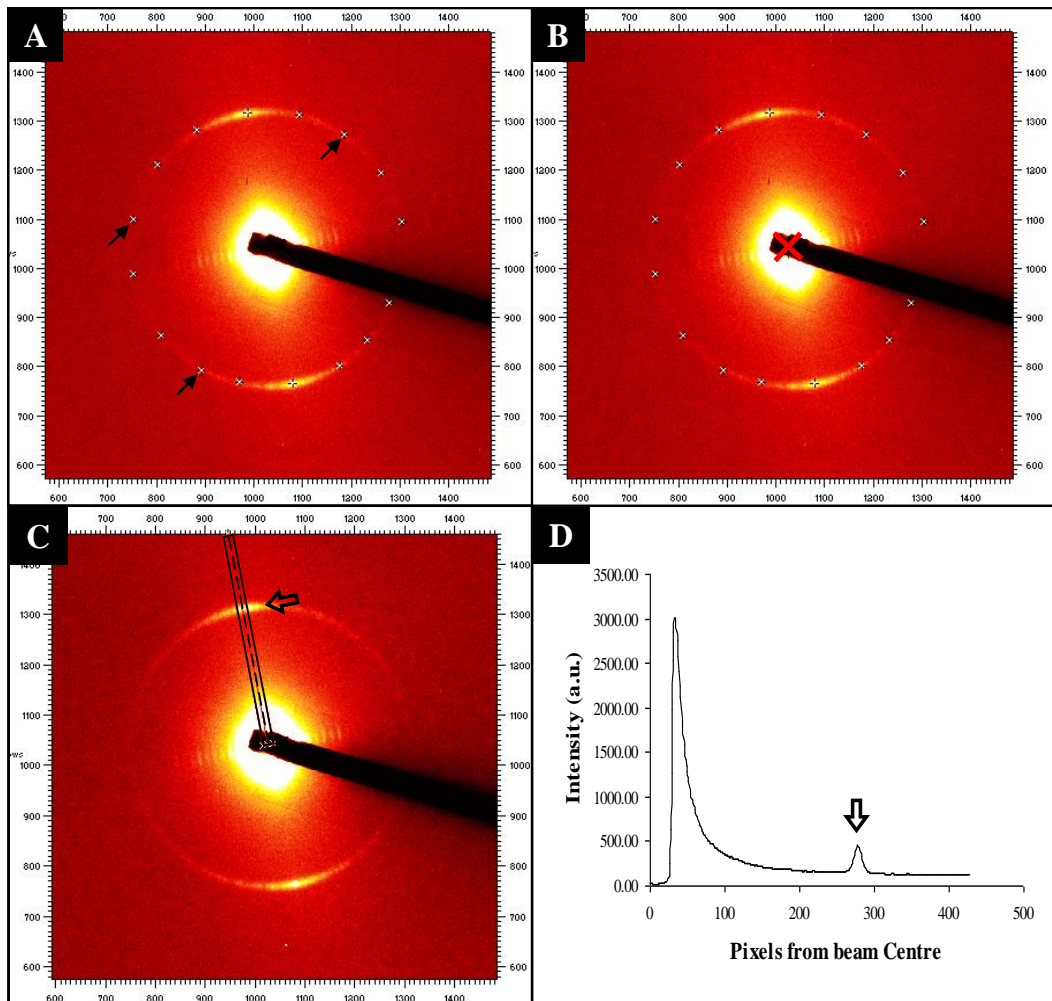
Figure 3.5. Determining the positions of Bragg reflections in SAXS images of ONH tissue. (A) The beam centre was determined by entering user defined points around the SAXS pattern (black arrows) which allowed (B) the centre of gravity to be calculated (red cross). (C) A projection line was then drawn, from the beam centre, over the reflection of interest (open arrow in (C)) and (D) the pixel intensities along the projection line were plotted as a scatter graph allowing for the measurement of the distance of the reflection peak (open arrow in (D)) from the beam centre.

Integrated projections of the scatter intensities of each SAXS image frame were then created from user defined projection lines with 20 pixel widths. These projection lines started from the coordinates of the beam centre and extended over the SAXS reflection of interest (Figure 3.5C). The integrated pixel intensities along the projection and corresponding pixel number from beam centre were saved as .chi files.

The .chi files were then opened in Excel$^{®}$ (Microsoft, Redmond, WA, USA) and the pixel intensities were plotted against pixel number as 2D line graphs (Figure 3.5D). The positions of intensity peaks of interest were transformed from pixel number to distance in nm using:

$$\frac{1st\ order\ meridional\ postion\ of\ calibrant\ (pixels) \times D\ spacing\ of\ calibrant\ (nm)}{Position\ of\ data\ peak\ (pixels)}$$

The calibrant used was hydrated rat tail tendon (Grynpas, 1977) (see 3.2.3.1).

From the above equation it can be seen that the higher the pixel number, the smaller the distance in nm, i.e. the distance in nm becomes smaller with progressing distance from the beam centre. Because of this, intensity profiles presented in the results section of this chapter are plotted against the scattering vector (Q), which represents the structure in reciprocal space, using:

$$Q = \frac{2\pi}{d}$$

Where:

d　　= the position or periodicity of the data peak (nm)

Q　　= the length of the scattering vector (nm^{-1})

3.2.3.3　Determining Collagen Interfibrillar Bragg Spacing and Fibril Diameter

SAXS frames from regions of the ONH sections containing collagen fibrils were distinguishable by the presence of distinct meridional Bragg reflections (Figure 3.6A) which, as previously mentioned, arise from the axial staggering of collagen molecules. The equatorial scatter of collagen fibres (Figure 3.6B), perpendicular to the meridional

reflections, contains information relating to the packing and diameter of the collagen fibrils (Eikenberry et al., 1982).
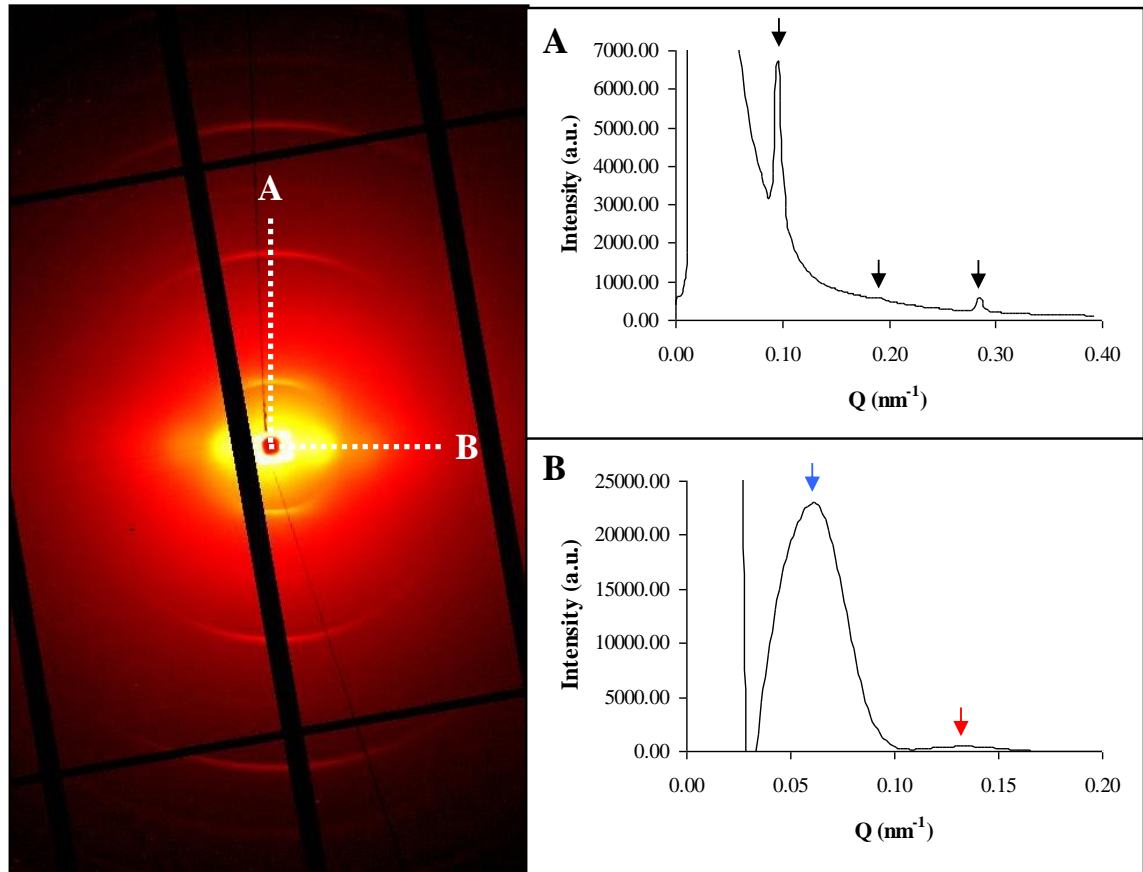
Figure 3.6. SAXS scatter from collagen fibrils in ONH tissue sections. (A) The meridional reflections correspond to the axial staggering of collagen molecules along a fibril and (B) the equatorial scatter contains information relating to the packing and diameter of the collagen fibrils. Black arrows in (A) highlight the first to third meridional peak. The blue arrow in (B) points to the position of the interference function and the red arrow in (B) points to the first subsidiary maximum of the fibril transform which are used to determine collagen interfibrillar Bragg spacing and fibril diameter, respectively.

Prior to analysis of the equatorial scatter, a power law background curve was fitted to the data and removed. This allowed for background scattering and scattering from components of the ONH, other than fibrillar collagen, to be filtered out. Firstly, equatorial projections (such as Figure 3.6B) were produced as described in 3.2.3.2. Excel® files containing the data projections were imported into the analytical software

Statistica (StatSoft, UK) and a macro (courtesy of Dr. Craig Boote) was used to convert the Excel® files into .sta worksheets and plot projection data on a logarithmic scale (Figure 3.7A). The macro then allowed for a user defined square-power law function, which was determined by drawing a linear transect within the logarithmic space (Figure 3.7B), to be subtracted from the data (Figure 3.7C).

Once the background scatter had been removed, the equatorial scatter peaks were more easily identified (Figure 3.7C). The equatorial scatter of collagen fibrils is a product of the fibril (cylinder) transform (scattering from a system of uniform diameter fibrils) and the interference function (order of packing of cylinders) (Oster and Riley, 1952).

The interference function consists of a first order reflection (blue arrow in Figure 3.6B) with a peak position corresponding to the mean centre-to-centre collagen interfibrillar Bragg spacing, which can be calculated in nm using:

$$\frac{1st\ order\ meridional\ postion\ of\ calibrant\ (pixels) \times D\ spacing\ of\ calibrant\ (nm)}{Position\ of\ Interference\ Function\ peak\ (pixels)}$$
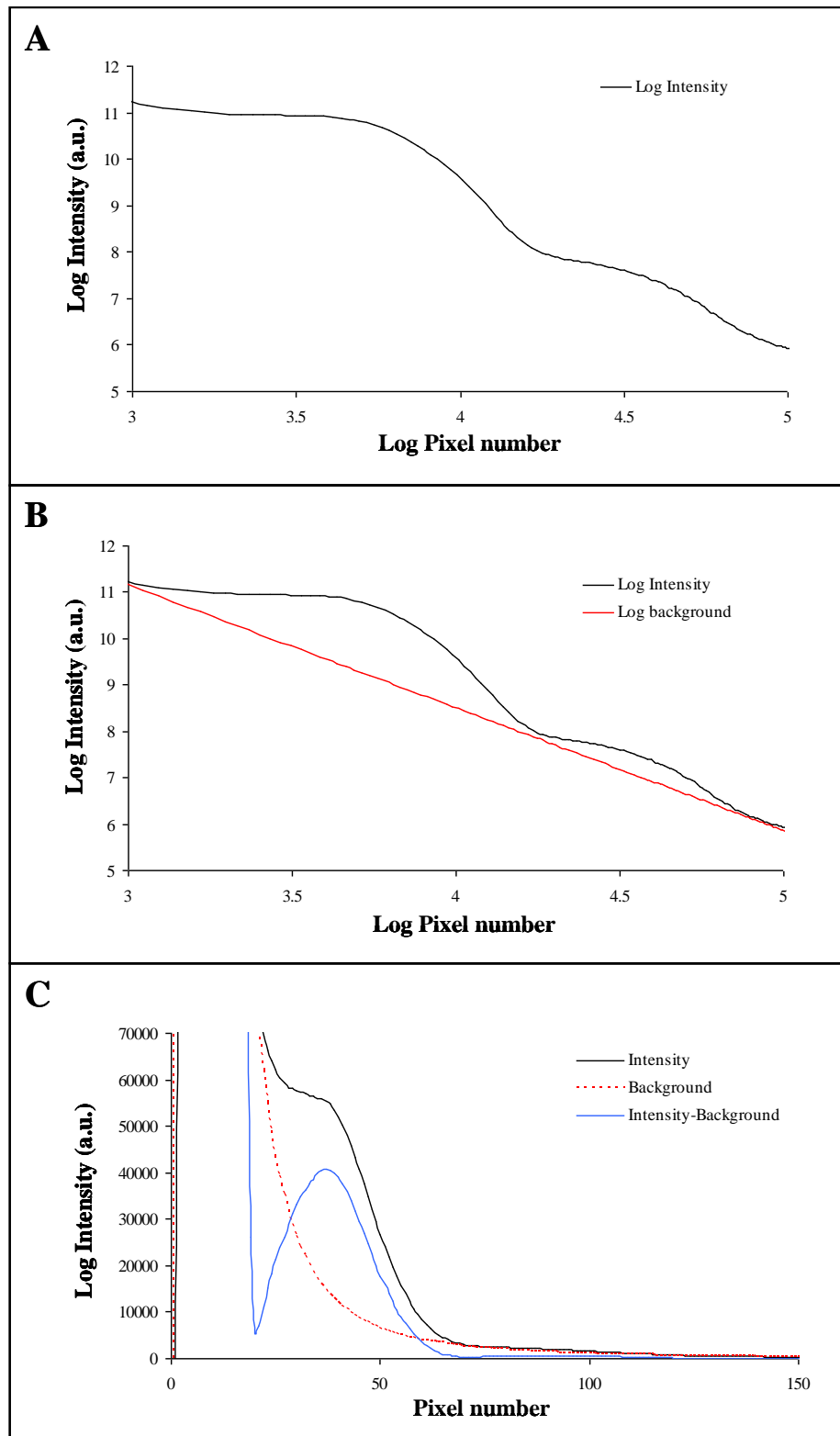
Figure 3.7. Removal of background relating to scattering from components of the ONH other than fibrillar collagen. (A) The intensity and pixel distance from the beam centre were logged and (B) a user-defined linear transect was drawn beneath the data. (C) The area under the transect was subtracted from the data allowing for the intensity peaks to be more easily identified.

The fibril transform consists of subsidiary maxima peaks with the first subsidiary maximum (red arrow in Figure 3.6B) expecting to occur at:

$$2r = \frac{5.14}{\pi Q}$$

Where:

2r   = the fibril diameter (nm)

5.14   = numerical factor defined by the position of the first maximum of the Bessel function of solid cylinders (Oster and Riley, 1952)

Q   = the reciprocal space coordinate of the first subsidiary maximum peak (nm^{-1})

3.2.4 Comparisons of Collagen Interfibrillar Bragg Spacing, Fibril Diameter and D Periodicity in Young and Elderly Optic Nerve Heads

Collagen interfibrillar Bragg spacing, fibril diameter and D periodicities were calculated, as described in 3.2.3.2 and 3.2.3.3, from conventional SAXS intensity profiles located in the superior, inferior, nasal and temporal regions of the peripapillary sclera. Six patterns, within 0 - 500µm from the ON canal border, were analysed from each region. Beyond 500µm the collagen fibres become more variable in size (Quigley et al., 1991b, Huang and Meek, 1999) and the SAXS projections for these parameters are harder to accurately analyse.

SAXS profiles were analysed from the superior, inferior, nasal and temporal regions of peripapillary sclera in a 33 year old donor ONH and compared to the superior, inferior and temporal regions of a 90 year old donor ONH and nasal region of a 91 year old

donor ONH. Two elderly samples were used as the scanned area of the 90 year old donor ONH did not include the nasal peripapillary sclera.

The first subsidiary maxima could not be located in 10 of the 48 SAXS profiles (6 from the young and 4 from the elderly), however, each region contained at least 3 fibril diameter measurements.

3.2.4.1   Statistical Analysis

All statistical analysis was performed using SPSS version PASW 18 (SPSS Inc., USA). Normality of data was determined using the Shapiro-Wilk test with a significance level of $p<0.05$. Collagen interfibrillar Bragg spacing, fibril diameter and D periodicities were compared between young and old using the independent samples t-test or the Mann-Whitney U test depending on the normality of the data.

As regional data were not normally distributed, Kruskal-Wallis tests were used to determine if there were any significant differences in regional collagen interfibrillar Bragg spacing, fibril diameter and D periodicities. Where appropriate, multiple Mann-Whitney U tests were used with a Bonferroni corrected significance level ($p<0.008$) that accounted for type I errors, to identify where the differences fell.

All statistical comparisons of the data are presented as bar charts with error bars depicting the precision of each measurement. These error bars are either the standard error of the mean following parametric comparisons or 95% confidence intervals of the median (calculated using the Ratio Statistics option in PASW) following non-parametric comparisons.

3.3 **Results**

3.3.1 **Microfocus Small Angle X-ray Scattering**

A microfocus SAXS setup was employed with the aim of gaining precise ONH structural information from 12µm x 19µm tissue regions.

No measurable SAXS reflections were observed within the ON canal when scanning the transverse (Figure 3.8A,B) or longitudinal (Figure 3.8C,D) ONH sections at the level of the LC. Signal within the LC was limited to a diffuse scatter around the beam centre (Figure 3.8).
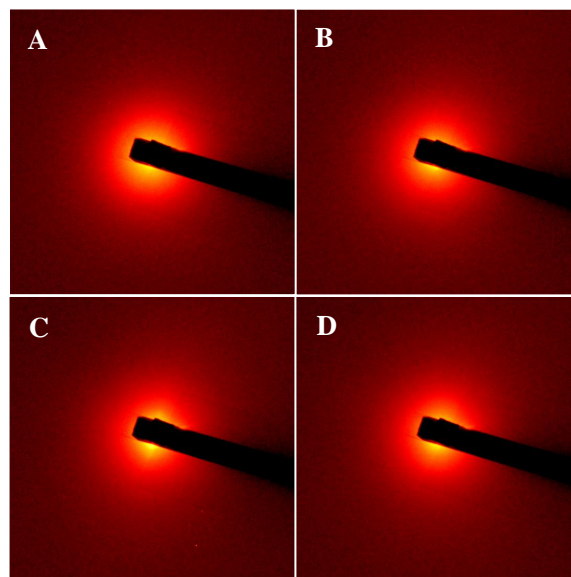
Figure 3.8. Diffuse microfocus SAXS scatter from the region of the LC. (A) and (B) are representative images from a transverse LC section from a 61 year old and (C) and (D) are representative LC images from a longitudinal section from 87 year old.

However, meridional fibrillar collagen reflections were found within the peripapillary sclera of transverse sections (Figure 3.9A-D) and showed a periodicity of approximately 62nm (Figure 3.9E). The area of scatter which contained equatorial information relating

to collagen fibril diameter and spacing, found near the position of the first order of fibrillar collagen, was concealed by the beam-stop in the majority of scans. Therefore these parameters could not be calculated.
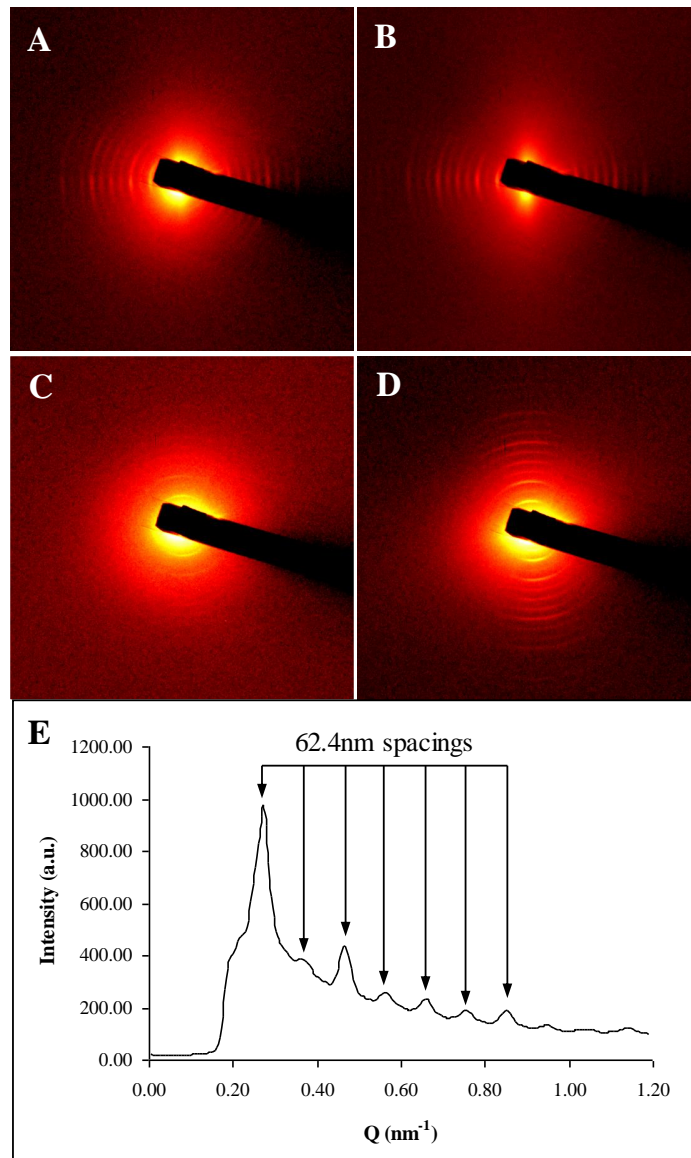
Figure 3.9. Meridional microfocus SAXS reflections from the peripapillary sclera. Representative images from the (A) superior, (B) inferior, (C) nasal and (D) temporal peripapillary sclera showing reflections with (E) 62.4nm spacings.

Arced reflections were observed in the postlaminar ON in both transverse (Figure 3.10A,B) and longitudinal sections (Figure 3.10D). The reflections were more intense in

the 61 year old postlaminar ON than the 90 and 87 year old postlaminar ON sections. The first reflection (and most probably the second order) was at 7.8nm and the later orders showed a periodicity of approximately 15nm (Figure 3.10E).
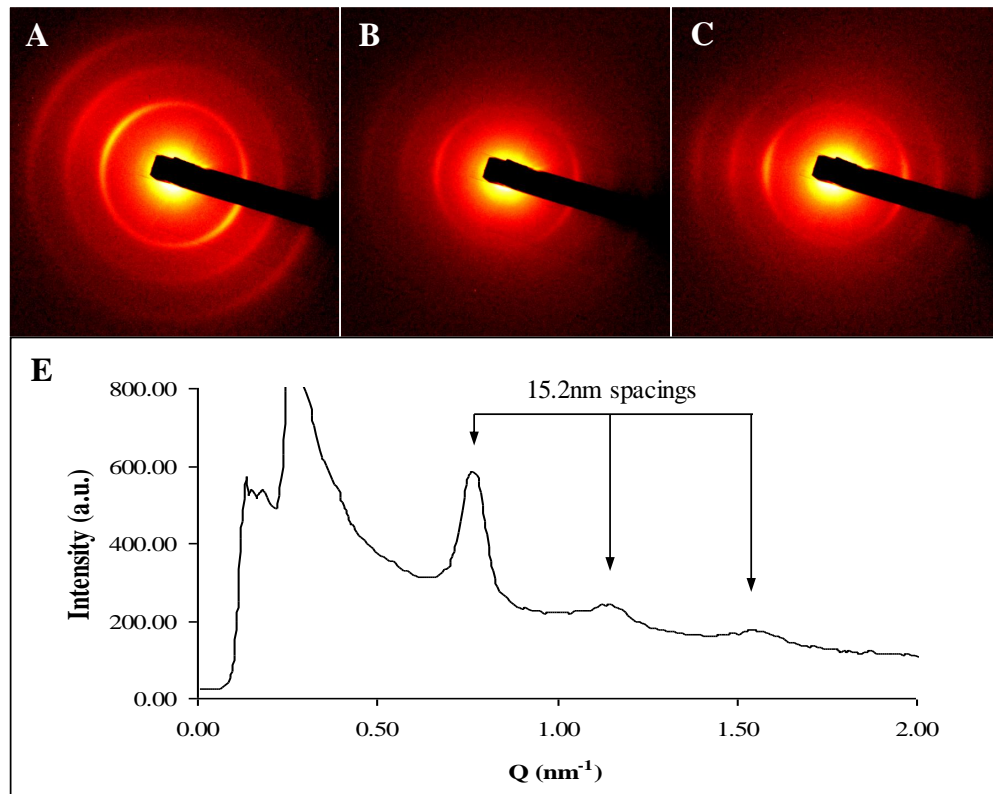
Figure 3.10. Circular microfocus SAXS reflections from the postlaminar ON. Representative images from the postlaminar ON of a (A) 61 year old, (B) 90 year old and (C) 87 year old ONH. (E) The circular reflections had a spacing of 15.2nm. (A) and (B) are from transverse ONH sections and (C) is from a longitudinal ONH section.

Interestingly, single exposures performed to sample the boundary of the ON canal, within the peripapillary sclera, of longitudinal ONH sections showed a distinct arced reflection (Figure 3.11A-D) at approximately 4nm (Figure 3.11E). This distinct ring was not found in the transverse ONH sections.
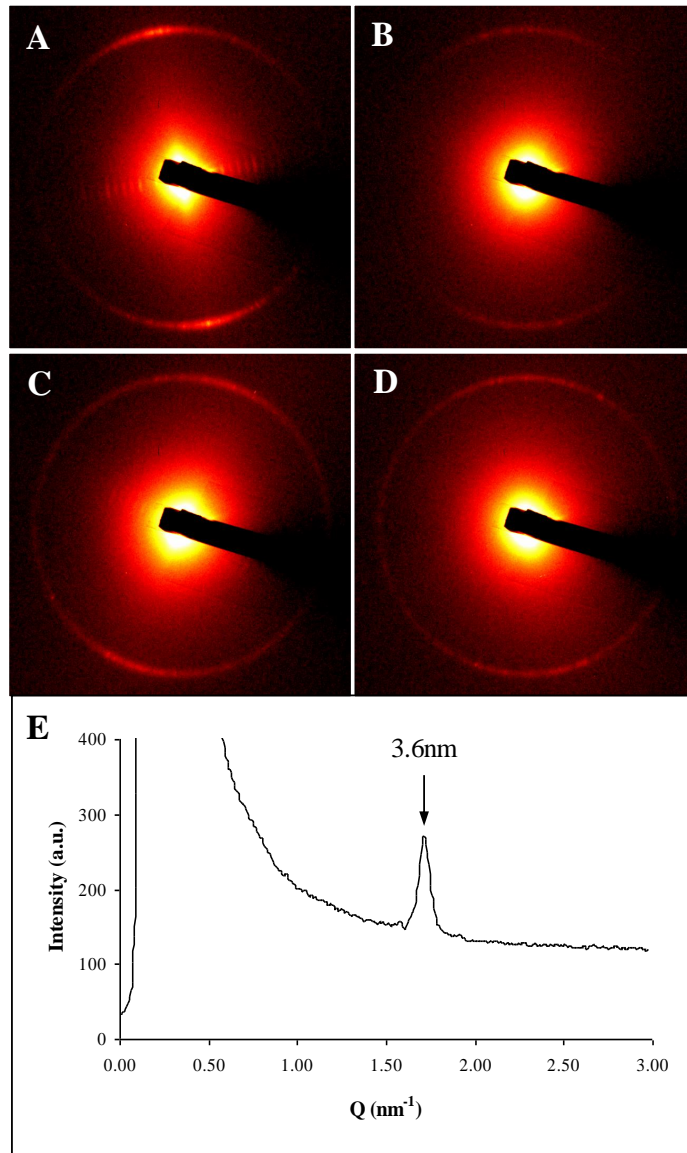
Figure 3.11. The circular microfocus SAXS reflection from the ON canal boundary. (A-D) Representative images from the ON canal boundary from an 87 year old longitudinal ONH section. (E) The circular reflections appeared at 3.6nm.

3.3.2 Conventional Small Angle X-ray Scattering

Due to the obscured information by the beam-stop and lack of reflections within the LC when using microfocus SAXS, conventional SAXS was used to investigate larger areas (200µm x 200µm) of the ONH in thicker (500µm) transverse tissue sections.

A grid scan of the first ONH section from a 33 year old donor which is composed of images cropped to 200x200 pixels around the beam centre is shown in Figure 3.12B. The peripapillary sclera/ON canal boundary was distinguishable due to strong patterns obtained from the highly ordered collagen fibres in the peripapillary sclera (Figure 3.12A-C).
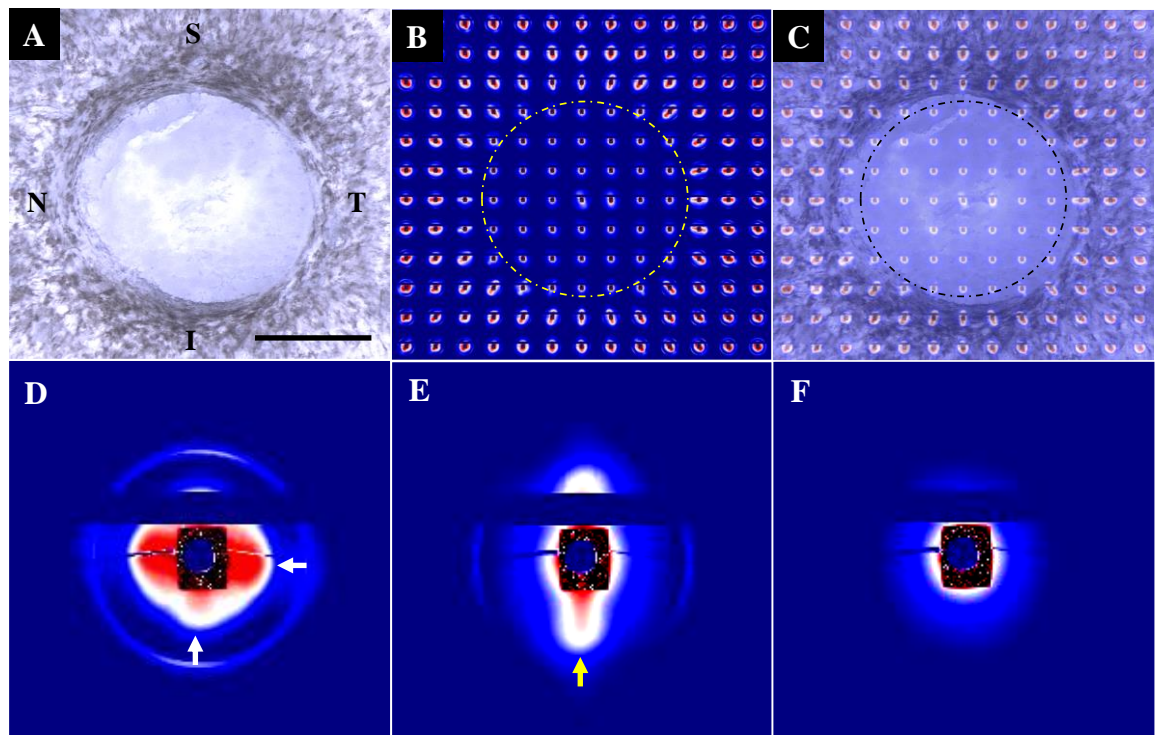
Figure 3.12. Conventional SAXS patterns (200 x 200 pixels round the beam centre) from the human ONH. (A) A light microscopy image of an ONH section from a 33 year old donor and (B) corresponding SAXS reflections showing the fibrillar collagen related SAXS scatter in the peripapillary sclera which enabled differentiation of the ON canal boundary (hashed circle in (B) and (C)). (D) Peripapillary sclera SAXS patterns, beyond 500µm from the ON canal border, showed broad, arced meridionals and multiple regions of equatorial scatter (white arrows). (E) Peripapillary sclera SAXS patterns within 500µm from the ON canal border showed orientated meridionals and equatorial scatter (yellow arrow). (F) No SAXS reflections were found in the ON canal. Scale bar in (A): 1000µm

SAXS frames from the sclera beyond 500µm from the ON canal border showed multiple orientations of meridional and equatoral scatter (Figure 3.12D). In contrast, patterns from the collagen fibres directly adjacent to the ON canal contained more

orientated equatorial scatter and meridional reflections (Figure 3.12E) implying that fibrils in this region have a preferred alignment. No obvious diffraction patterns were found in the 200x200 pixel area in frames located in the ON canal (Figure 3.12F).

Further away from the beam centre (1100x1100 pixels around the beam centre), beyond the fibrillar collagen equatorial scatter, a diffuse ring was found within the frames that were situated in the ON canal of the 33 year old donor in both the first (Figure 3.13A) and second 500μm section.
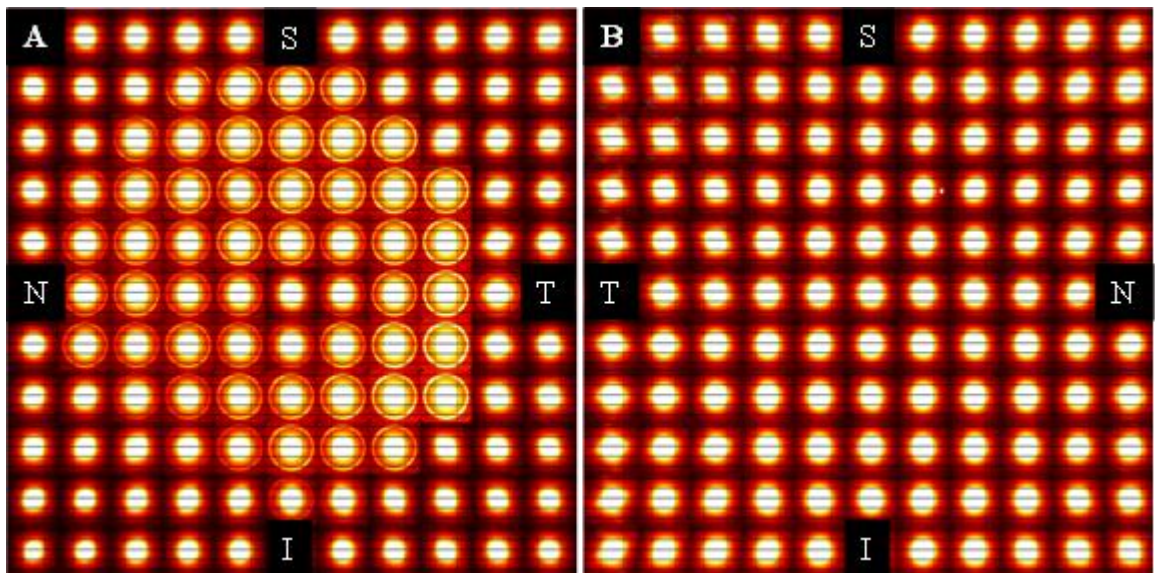
Figure 3.13. Conventional SAXS patterns (1100 x 1100 pixels round the beam centre) from the human ONH. (A) A diffuse ring was found within the ON canal of the 33 year old ONH which was absent in (B) the 65 year old ONH. S = superior, T = temporal, I = inferior, N = nasal.

These rings were found at approximately 8nm (Figure 3.14D) and were absent in sections from the 65 (Figure 3.13B, Figure 3.14B) and 91 year old ONHs (Figure 3.14C).
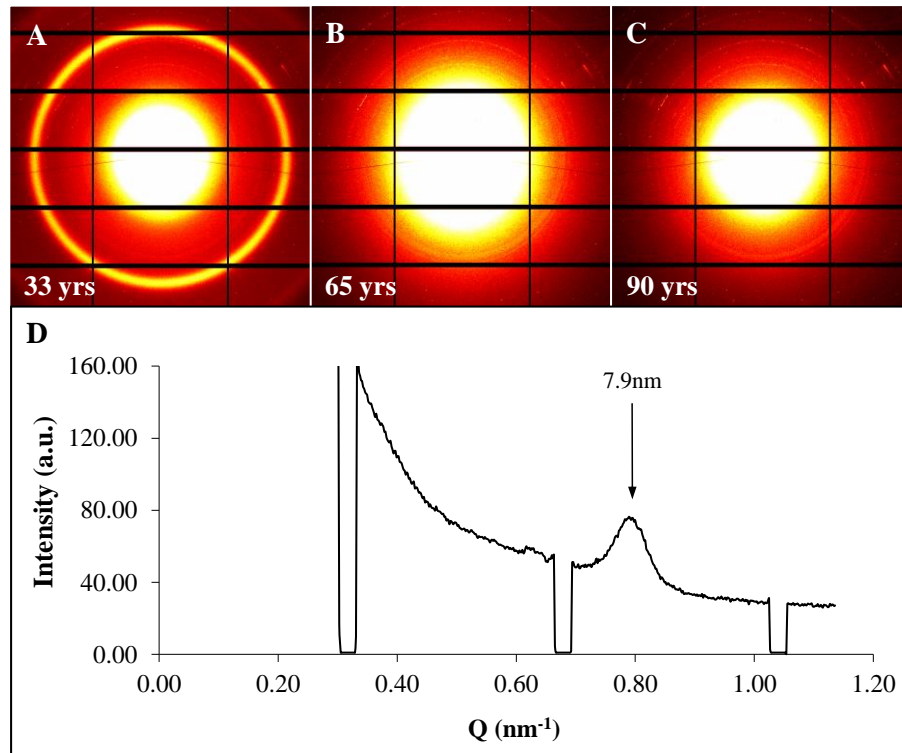
Figure 3.14. SAXS frames from the 33, 65 and 90 year old ON canals. (A) The diffuse rings which were apparent in the 33 year old ON canal were not found in (B) the 65 year old or (C) 90 year old ON canals. (D) The rings within the 33 year old ON canal appeared at 7.9nm.

3.3.3 Collagen Interfibrillar Bragg Spacing, Fibril Diameter and D periodicity in Young and Elderly Peripapillary Sclera

Collagen interfibrillar Bragg spacing, fibril diameter and D periodicity were calculated from 6 conventional SAXS images within each of the superior, inferior, nasal and temporal regions of the peripapillary sclera of young and elderly ONHs (Figure 3.15).
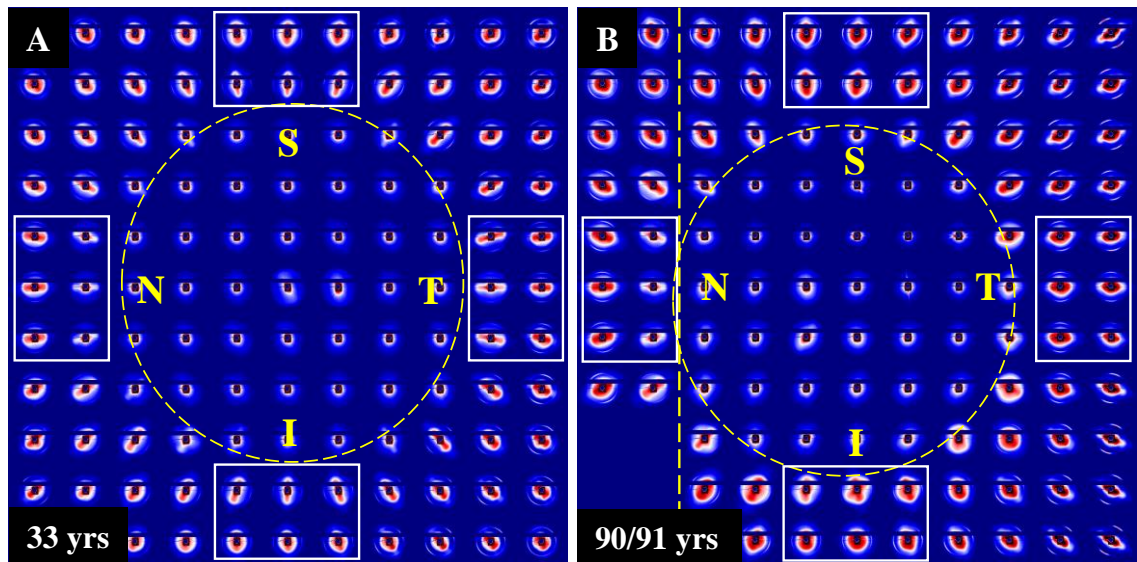
Figure 3.15. Conventional SAXS patterns (200 x 200 pixels round the beam centre) from the young and elderly human ONH. Comparisons of collagen parameters were made from 6 SAXS frames (boxes) from 4 regions of the (A) young and (B) elderly peripapillary sclera. The nasal region of the elderly ONH was taken from a 91 year old donor (denoted by dashed line in (B)) as this information was not included in the 90 year old SAXS dataset. S = superior, T = temporal, I = inferior, N = nasal.

The average interfibrillar Bragg spacing was significantly higher in the elderly (120.5nm ($\pm$ 21.9)) compared to the young (100.7nm ($\pm$ 13.0)) (Figure 3.16A). Interfibrillar Bragg spacing was in the order of temporal region > superior > inferior > nasal (Figure 3.16B). However, no significant differences were found between the regions (p>0.008).

Young and elderly peripapillary sclera collagen fibril diameters were not significantly different (Figure 3.17A, p>0.05), with an average to of 68.9nm ($\pm$ 7.8) and 67.3nm ($\pm$ 2.8), respectively. Collagen fibril diameters showed no significant differences in temporal, nasal, inferior or superior regions (p>0.008).
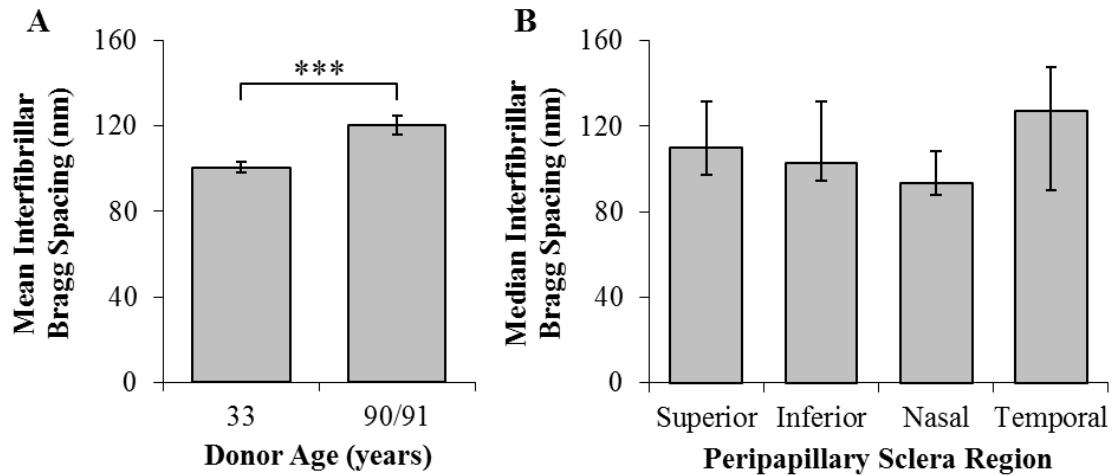
Figure 3.16. Young and elderly (mean +/- standard error) and regional (median +/- 95% confidence intervals) differences in peripapillary sclera interfibrillar Bragg spacing. (A) The elderly peripapillary sclera interfibrillar Bragg spacing was significantly larger than the young. (B) No significant differences were found between regional peripapillary sclera interfibrillar Bragg spacing.
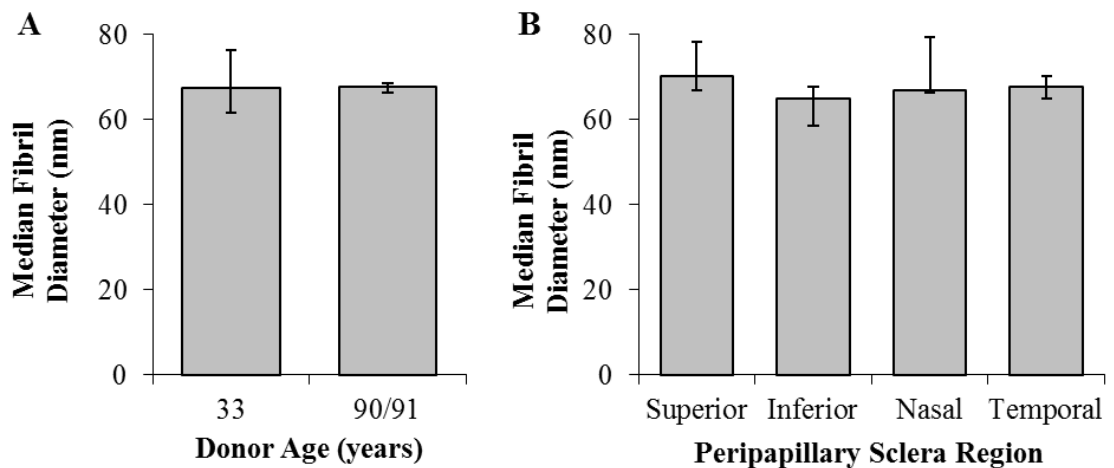
Figure 3.17. Young and elderly and regional peripapillary sclera collagen fibril diameter (median +/- 95% confidence intervals). No significant differences in collagen fibril diameters were observed between (A) the young and elderly peripapillary sclera or (B) regional peripapillary sclera.

D periodicity was 65.0nm ($\pm$ 0.8) in the young peripapillary sclera and 65.1nm ($\pm$ 1.3) in the elderly peripapillary sclera. No significant differences in D periodicity were found between the young and elderly (Figure 3.18A, $p > 0.05$) or regionally (Figure 3.18B, $p > 0.05$).
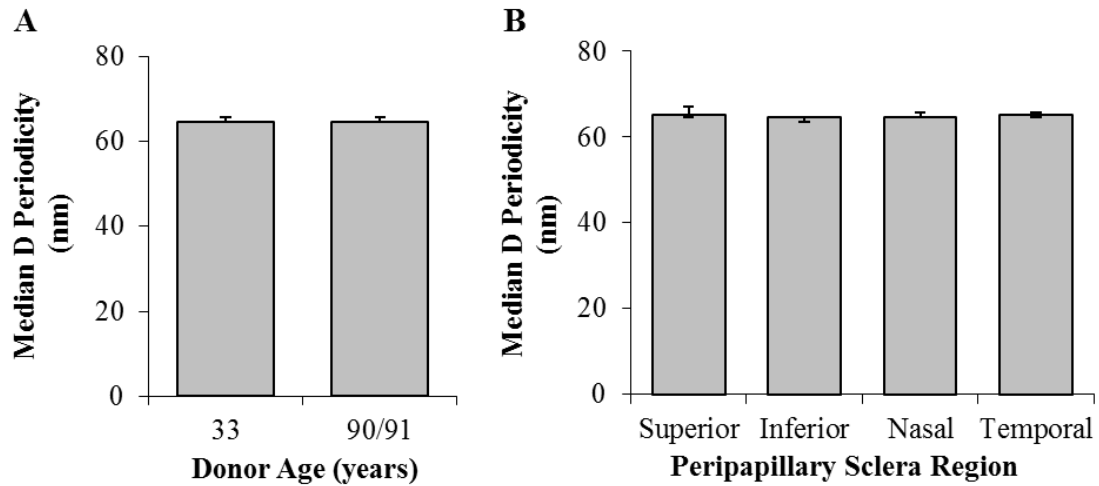
Figure 3.18. Young and elderly and regional peripapillary sclera fibrillar collagen D periodicity (median +/- 95% confidence intervals). No significant differences in D periodicity were observed between (A) the young and elderly peripapillary sclera or (B) regional peripapillary sclera.

3.4 Discussion

This chapter aimed to characterise the fibrillar nano-architecture of the human ONH. However, no measurable SAXS reflections were identified in the LC. This was surprising as the major components of the LC extracellular matrix are collagen and elastin (Hernandez et al., 1986, Hernandez et al., 1987, Rehnberg et al., 1987, Albon et al., 1995, Albon et al., 2000a). The lack of reflections within the LC may reflect its low connective tissue density and the porosity of the structure in comparison to the dense surrounding sclera. Nevertheless, some interesting SAXS reflections were found in the peripapillary sclera and postlaminar ON.

When using microfocus SAXS, a distinct ring at approximately 4nm was found within the peripapillary sclera adjacent to the ON canal of a longitudinal ONH section. This ring was not found in transverse tissue sections and would not have been visible in the conventional SAXS images as, due to the increased camera length, its position would

have fallen outside of the image window. The peripapillary sclera surrounding the ON canal has been shown to consist of fibrillar collagen (Hernandez et al., 1986, Hernandez et al., 1987, Morrison et al., 1989b, Albon et al., 1995), elastin (Morrison et al., 1989a, Quigley et al., 1991a, Hernandez, 1992) and glycosaminoglycans (GAGs) including chondroitin-4 sulphate, chondroitin-6 sulphate (Morrison et al., 1994) and keratan sulphate (Caparas et al., 1991).

It is unlikely that the distinct ring was produced by fibrillar collagen as it did not correspond to collagenous meridional or equatorial reflections. Furthermore, it cannot be confirmed whether the ring was produced from GAGs as previous SAXS studies of ocular GAGs have been limited to the use of specific GAG-null animal models (Quantock et al., 2001, Meek et al., 2003) and cupromeronic blue staining (Meek et al., 1986, Quantock and Meek, 1988) and GAG specific reflections have not been reported.

Evidence of elastin diffraction is minimal and has in the past been dismissed due to the amorphous nature of the protein. Serfani-Fracassini et al. (1977) isolated and dried elastin from bovine nuchal ligament and subjected the preparation to SAXS. This investigation reported a reflection at 4.5-5nm when the elastin strips were extended by 65%. Furthermore, a short report by Ali et al. (2004) reported a sharp intense ring at 4.5nm in equine nuchal ligament and porcine aorta using wide-angle X-ray scattering (WAXS). Therefore, it is a possibility that the ring reflection at 4nm in the current study may correspond to elastin and discrepancies between the positions may be due to differences in sample preparation or extension. Further investigation is needed to determine if the ring is in fact derived from elastin or associated microfibrils. If confirmed, this finding implies a regular organisation of elastin nano-architecture visible in the longitudinal ONH tissue plane.

In 250μm thick transverse and longitudinal ONH sections, diffuse circular reflections with a 15.2nm periodicity were observed in the postlaminar ON. These reflections were most likely produced by myelin which is known to surround the axons in the postlaminar ON, but not in the prelamina or LC regions. This is further supported by previous SAXS studies which show that the repeating unit of protein-lipid-protein in central nervous system myelin membranes is approximately 15.5-16nm (Chandross et al., 1978, Karthigasan and Kirschner, 1988, Oliveira et al., 2010). Myelin is also the most probable source of the diffuse ring observed in the ON canal of the 33 year old ONH which, akin to the first myelin reflection in the microfocus SAXS images, occurred at approximately 8nm. The 500μm thickness of the ONH section of the 33 year old donor may have contained part of the postlaminar ON which could explain why myelin was present within the first ONH section.

Interestingly, the myelin related SAXS patterns appeared less intense in the 90 year old and 87 year old microfocus SAXS images and were completely absent in the 65 year old and 90 year old conventional SAXS images in both the first 500μm and second 500μm ONH tissue sections. A WAXS study of the myelin from the human brain indicated that a reflection corresponding to myelin lipid became less intense in samples from donors aged over 50 years which implies that the myelin lipid becomes less ordered with age (Chia et al., 1983). Furthermore, a study of the ageing monkey ON has shown ballooning and the accumulation of vesicles in myelin of aged monkeys (Sandell and Peters, 2001). It would be interesting to further investigate the affect of ageing on the structure of myelin using SAXS and determine the age at which the myelin reflections diminish. This technique could be further utilised to determine alterations in myelin structure in optic neuropathies such as glaucoma.

Although no collagen related SAXS reflections were observed within the ON canal, strong, orientated, collagen-related reflections were observed 0-500µm from the ON canal border. These reflections indicate high alignment of fibrillar collagen adjacent to the canal. SAXS frames from the preipapillary sclera beyond 500µm from the ON canal border showed circular meridional reflections and multiple orientations of equatoral scatter which indicates a higher variation in the preferred collagen fibril orientations within this tissue plane (Quantock and Meek, 1988).

Reflections from the peripapillary sclera indicated that sclera fibrillar collagen has an axial D periodicity of approximately 62-65nm, which is shorter than the D periodicity of type I collagen in rat tail tendon. This shorter collagen D periodicity is closer to that observed in skin (65nm) (Brodsky et al., 1980) and may be caused by collagen molecular tilt along the fibril axis (Hulmes et al., 1981) or presence of collagen types other than type I. The D periodicity of the peripapillary sclera did not differ between the young and elderly ONHs indicating that the axial stagger of collagen molecules is not affected by age.

Peripapillary sclera collagen fibril diameters fell within published ranges (Quigley et al., 1991b) and did not differ with age. In contrast, centre-to-centre collagen interfibrillar Bragg spacing was significantly larger in the elderly peripapillary sclera when compared to the young peripapillary sclera. The similar fibril diameters but increase in collagen interfibrillar spacing implies that the elderly collagen fibrils, within collagen fibre bundles, are less compact than young which may lead to larger collagen fibre bundle sizes.

An increase in interfibrillar spacing within the peripapillary sclera may in part be caused by age-related changes in proteoglycan content (Rada et al., 2000, Dunlevy and Rada, 2004). For instance, aggrecan core protein has been shown to increase with age in the posterior sclera (Rada et al., 2000) where it is located between collagen fibrils and thought to maintain fibril spatial orientation (Rada et al., 2006).

An increase in interfibrillar spacing may also have an impact on the biomechanics of the elderly peripapillary sclera. A higher collagen fibril packing density, and subsequent higher collagen volume fraction, has been proposed to strengthen the central cornea (Boote et al., 2003). Therefore, the collagenous network of the elderly peripapillary sclera may be structurally weaker than the young. However, the elderly peripapillary sclera may gain structural reinforcement through mechanisms such as nonenzymatic collagen cross-linking (Schultz et al., 2008) or the retention of proteoglycan complexes (Dunlevy and Rada, 2004).

Further investigations with an increase in sample size are needed to fully explore age-related changes in collagen fibril size and organisation in the peripapillary sclera. Additionally, previous work has highlighted the affect that tissue hydration has on collagen fibril spacing (Fratzl and Daxer, 1993), therefore, future studies should incorporate a measurement of the hydration state of the ONH tissue sections prior to and following SAXS imaging.

3.5 Conclusion

Although no SAXS reflections were produced from the LC, reflections attributed to the presence of elastin in the peripapillary sclera or insertion region were a surprising and

interesting finding. Furthermore, age-related changes in the structure of ON myelin were indicated from the change in appearance of SAXS reflections from the postlaminar ON. Preliminary analysis of SAXS images from the aligned fibrillar collagen adjacent to the ON canal indicated that while collagen fibril diameter does not appear to change with age, there is a potential age-related increase in interfibrillar spacing which may impact on the biomechanics of the ageing peripapillary sclera and therefore the LC.

Chapter 4 - Connective Tissue Fibre Orientation and Alignment in the Human Optic Nerve Head

4.1 Introduction

Quantifying LC connective tissue microstructural parameters is critical for the future production of accurate human LC finite element models. Although connective tissue volume fraction within the LC has previously been investigated (Quigley and Addicks, 1981, Radius, 1981, Ogden et al., 1988, Jonas et al., 1991, Quigley et al., 1991b, Roberts et al., 2009, Winkler et al., 2010), the LC fibre alignment and orientation have not been quantified before in humans. Along with connective tissue content and knowledge of material properties, these structural parameters are important in determining how the ONH responds to changes in IOP.

Small angle light scattering (SALS) was undertaken in the current study to further investigate the microarchitecture of the connective tissue within the LC. SALS has previously been used to investigate the fibre architecture and ultrastructure of a range of tissues including heart valves (Sacks et al., 1998, Joyce et al., 2009), cranial dura mater (Hamann et al., 1998), cornea (Bettelheim and Kumbar, 1977, Bettelheim and Magrill, 1977), and sclera (Girard et al., 2011a, Yan et al., 2011). In this chapter, SALS has been used, for the first time, to quantify connective tissue fibre alignment and orientation in the LC and its adjacent tissues.

High variation in ON size and structure has been shown to occur within the normal population (Jonas et al., 1988, Jonas et al., 1990, Jonas et al., 1991). Therefore, this

study aimed to determine if variation in interocular connective tissue fibre organisation occurred in 2 ONHs of the same donor.

Age related changes in the connective tissue components of the LC have also been documented (Hernandez et al., 1989, Morrison et al., 1989a, Albon et al., 1995, Albon et al., 2000a). Therefore, SALS was also used to determine if such changes affect the connective tissue fibre make-up within the young and old ONH.

OBJECTIVES

- To quantify the connective tissue degree of fibre alignment (DOFA) and its preferred fibre orientation (PFO) in the human LC and adjacent tissues

- To determine if interocular differences in DOFA and PFO occur within the ONH

- To determine if interocular differences in DOFA and PFO occur between young and old ONHs

4.2 Materials and Methods

4.2.1 Sample Preparation

4.2.1.1 Human Tissue

Donor eyes (n = 21 eyes total; 5 left eyes and 8 pairs) with no history of ocular disease were received from the Bristol Corneal Transplant Service Eye Bank, UK. ONHs were immersed in 4% paraformaldehyde (PFA) within 48 hours of donor death. The eyes were orientated using the position of the macular and a block of sclera which encompassed the ONH was dissected. The tissue blocks were washed overnight in phosphate buffered saline (PBS, pH 7.4) and snap frozen in liquid nitrogen-cooled isopentane (Fisher, UK). The frozen tissue blocks were mounted onto a sledge microtome (MICROM HM 440E, Thermo Fisher, UK) and sectioned transverse (100μm thickness, n = 7 ONHs) and longitudinal (160μm thickness, n = 14 ONHs) to the ON. Sections were mounted onto Superfrost® Plus microscopy slides (Thermo Scientific, UK) in 1:1 PBS:glycerol and coverslipped. The coverslips were sealed with nail varnish and the slides were stored at -20°C until imaged.

4.2.1.2 Rat Tail Tendon

Rat tail tendon was used as a control sample to validate the SALS technique as it is known to have highly aligned, unidirectional collagen fibres. Rat tail tendons were removed from normal, male Brown Norway rats, fixed in 4% PFA and washed in PBS (pH 7.4) prior to sectioning. The tendons were snap frozen as described above, embedded in Cryo-M-Bed medium (TAAB, UK) and sectioned (100μm thickness) along the fibre axis using a cryostat (Leica CM3050 S, Leica Microsystems, UK).

Sections were mounted onto Superfrost® Plus microscope slides in 1:1 PBS:glycerol and stored at -20°C until imaged.

4.2.2 Second Harmonic Imaging

Second harmonic generation (SHG) microscopy was used to image the ONH tissue sections prior to SALS to determine the position of ONH structures so as to correctly allocate SALS scatter patterns to the LC, ON, sclera and dural sheaths. Tissue sections were imaged on a META laser scanning microscope (Carl Zeiss Ltd, UK) with a multiphoton Ti:Sapphire laser (Chameleon®, Coherent UK Ltd, UK) as described in section 2.2.2.1. Following excitation at 800nm, 3D forward scattered SHG ONH datasets (256x256x1 pixel) were collected and converted into maximum intensity projections using ImageJ (version 1.45s (http://rsb.info.nih.gov/ij)) image analysis software.

4.2.3 Small Angle Light Scattering

4.2.3.1 Image Acquisition

SALS was performed at the Department of Bioengineering, Imperial College, London as previously described by Girard et al. (2011a) (Figure 4.1). Briefly, tissue sections were mounted into a custom holder and scanned using a 5-mW nonpolarised, 632.8nm HeNe laser (model 1125, JDS Uniphase, Milpitas, CA). A customised spatial-filter beam-shrinker assembly (modified from KT310/M; Thorlabs, Newton, NJ) was used to generate a laser beam with a 300μm diameter. Sections were raster scanned at 100μm intervals, covering an area that encompassed the ON canal and peripapillary sclera (approximately 5.5 x 5.5mm in the transverse sections and 6 x 3mm in the longitudinal

sections) resulting in transverse and longitudinal section datasets containing approximately 3000 and 1800 images, respectfully.

Light scattered from the fibrous proteins within the tissue was projected onto a diffuser screen behind the specimen. Intense, non-scattered light was blocked by a blackout beam-block placed in the centre of the diffuser screen. Tiff images of each scatter pattern (Figure 4.2A) were collected using a CCD camera (model B953; Pixelink, Ottawa, ON, Canada) equipped with a red band-pass filter (model FL632.8-3; Thorlabs), which eliminated background light, positioned behind the diffuser screen.
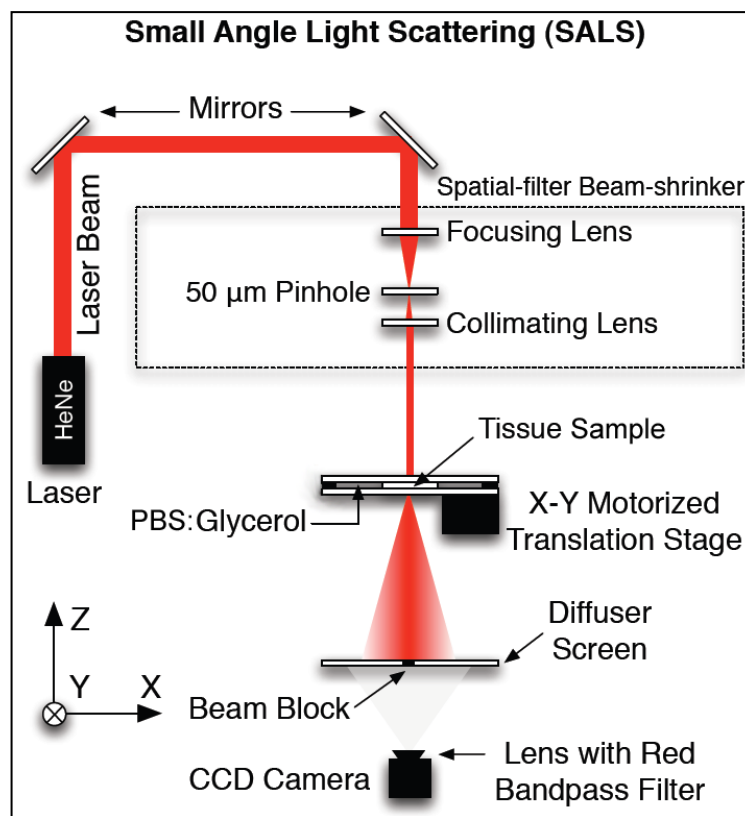
Figure 4.1. Schematic diagram of SALS apparatus. The 632.8nm HeNe laser was reflected into a spatial-filter beam-shrinker which reduced the beam diameter from 800μm to 300μm. The beam was then focused onto the tissue sample and subsequent scattered light was projected into the diffuser screen and imaged using a CCD camera. Adapted from Girard et al. (2011a) and reprinted with permission from Investigative Ophthalmology and Visual Science/ARVO (Appendix 8).

4.2.3.2   *Analysis of SALS Scatter*

ONH connective tissue fibre microstructural parameters were extracted from each scatter pattern as previously described by Girard et al. (2011a). Custom written MATLAB (Mathworks, Natick, MA) script was used to determine the centre of each SALS pattern (Figure 4.2B) and the fibre distribution responsible for each light scatter pattern about this centre was ascertained using a simplified Fraunhofer diffraction equation (McGee and McCullough, 1984, Girard et al., 2011a). Following a 90° shift of each fibre distribution, which accounted for the perpendicular scatter from the fibre axis, the peak of each distribution was used to determine the preferred fibre orientation (PFO) and the width of the peak that included 50% of the total area under the fibre distribution was used to quantify the fibre spread (termed orientation index, OI), as determined by Sacks et al. (1997) (Figure 4.2C). A transformation of 1-(OI/90°) was used to convert the fibre spread (measured as an angle) into a value between 0 and 1. This new value, termed the degree of fibre alignment (DOFA) from here on, increased with the degree of fibre anisotropy (Joyce et al., 2009, Girard et al., 2011a). The PFO and DOFA values at each exposure across the tissue were then summarised in MATLAB as fibre distribution maps with orientation lines and a colour gradient, respectively (Figure 4.3A).
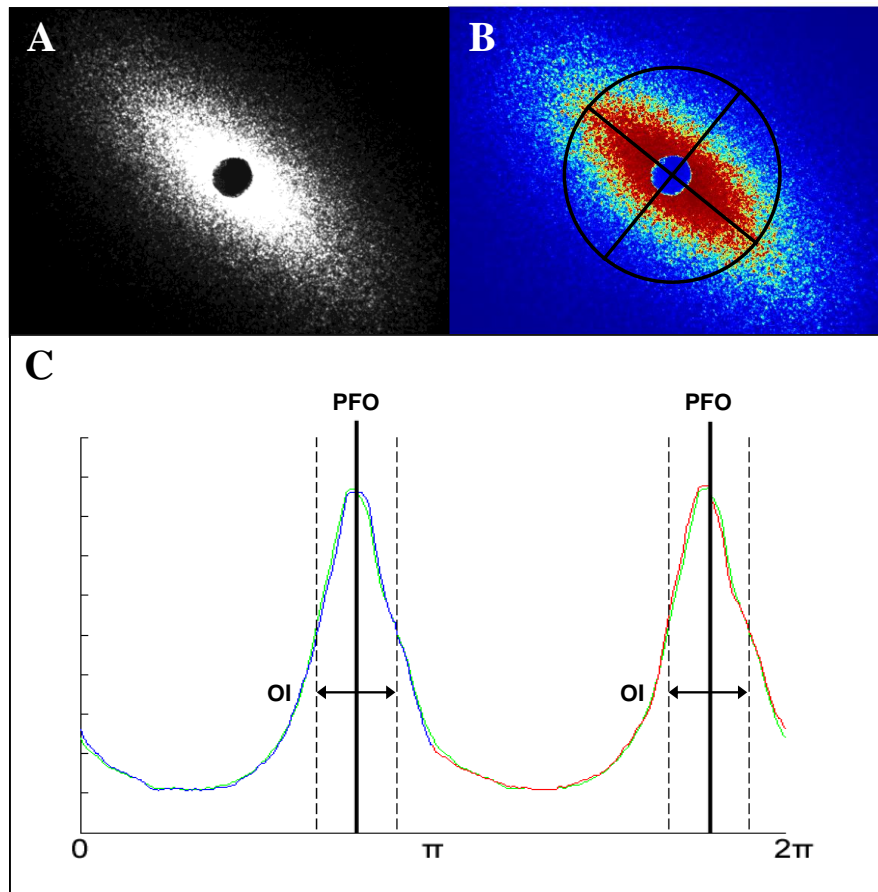
Figure 4.2. Analysis of SALS. (A) A single SALS scatter pattern from the human LC, (B) computed centre of the scatter and (C) azimuthal plot of the normalised scattered light intensity that represents the fibre distribution with a 90° shift. The preferred fibre orientation (PFO) was deduced from the distribution peak and the orientation index (OI, from which the degree of fibre alignment was computed) was calculated from the width encompassing 50% of the scatter.

4.2.4 Defining Regions of Interest

To establish which regions of the fibre distribution map corresponded to regions of interest within the ON canal and sclera, SALS fibre maps were rescaled to match the scale of the SHG images and both images were imported as separate layers into Adobe PhotoShop (version 6.0.1; Adobe, San Jose, CA). The SHG layer was made semi-transparent using the layer blending option and was translated to the correct position in relation to the fibre map (Figure 4.3B). A number grid relating to the SALS scatter image frames was created in Excel®, saved as a .png image and imported into

PhotoShop as a third layer. The number grid was then positioned so that each number sat on top of the correct orientation line (Figure 4.3C). Finally, a "region of interest" grid was imported as a fourth layer and centred on the ON canal. This grid defined 12 radial sections of the inner and outer ON canal (Figure 4.3E), the insertion region (circumferential ring situated 150μm outside of the canal) and peripapillary sclera (circumferential ring situated 150-1000μm outside of the canal) (Figure 4.3D). The frame numbers that fell into each region of interest, excluding those located over the central retinal vessels, were then entered into custom written MATLAB code that listed the DOFAs and PFOs of the entered frames and calculated their mean and standard deviation DOFA and their circular PFO mean and angular deviation as defined by Batschelet (1981). This allowed comparisons and statistical tests to be performed using the raw DOFA and PFO data between different ONH regions and samples.

4.2.5 Statistical Analysis

Statistical comparisons of DOFAs were performed using PASW 18 package (SPSS version PASW 18; SPSS Inc., USA). The Shapiro-Wilk test was used to test for normally distributed data. When comparing DOFAs between inner and outer ON canal and between the right and left eye the normally distributed data sets were compared using the independent samples t-test and not normally distributed data sets were compared using the Mann-Whitney U test with a significance level of $p < 0.05$.

When comparing DOFAs within and between ONHs from different aged donors significant differences were determined using an ANOVA with a Tukey post hoc test when data was normally distributed and a Kruskal-Wallis test when data was not normally distributed ($p < 0.05$). As there is no post hoc test for Kruskal-Wallis, multiple
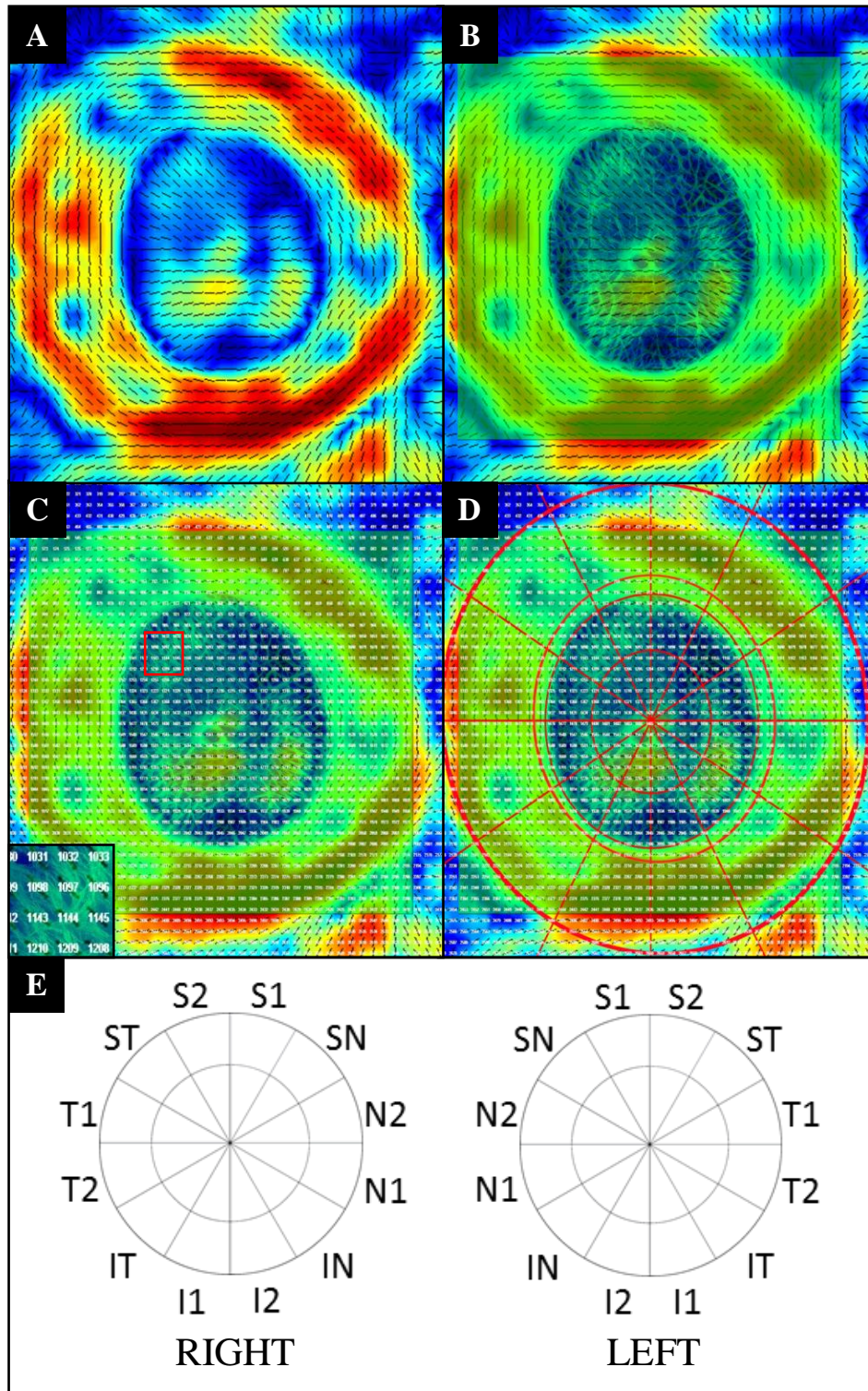
Figure 4.3. SALS data analysis of LC sections. (A) The fibre orientation (black lines represent the preferred fibre orientation) and degree of fibre alignment maps (colour plots) were (B) overlaid with the corresponding SHG image, (C) scan exposure numbers and (D) a region of interest grid (red). The latter defined the LC, insertion region, peripapillary sclera and 12 radial regions of the ONH canal, as indicated in (E).

Mann-Whitney U tests were used to determine where the differences arose with a Bonferroni adjusted significance level to account for type I errors.

All statistical comparisons of the data are presented as bar charts with error bars depicting the precision of each measurement. These error bars are either the standard error of the mean following parametric comparisons or 95% confidence intervals of the median (calculated using the Ratio Statistics option in PASW) following non-parametric comparisons.

Where data were not statistically compared, standard deviation error bars were used to show the variation within each dataset.

4.3 Results

4.3.1 Validation of SALS Scatter using Rat Tail Tendon

The narrow scatter pattern from the collagen fibres within the rat tail tendon (Figure 4.4A-C) produced SALS maps with high DOFA (Figure 4.4D-F). The maps and PFO correlated well with the fibrillar collagen orientation and alignment visualised in the SHG images of the same tissue (Figure 4.4G-I). These results confirmed that SALS scatter fibre maps are consistent with the fibre makeup of soft tissues and are therefore suitable for determining collagen fibre bundle distributions in the human ONH.
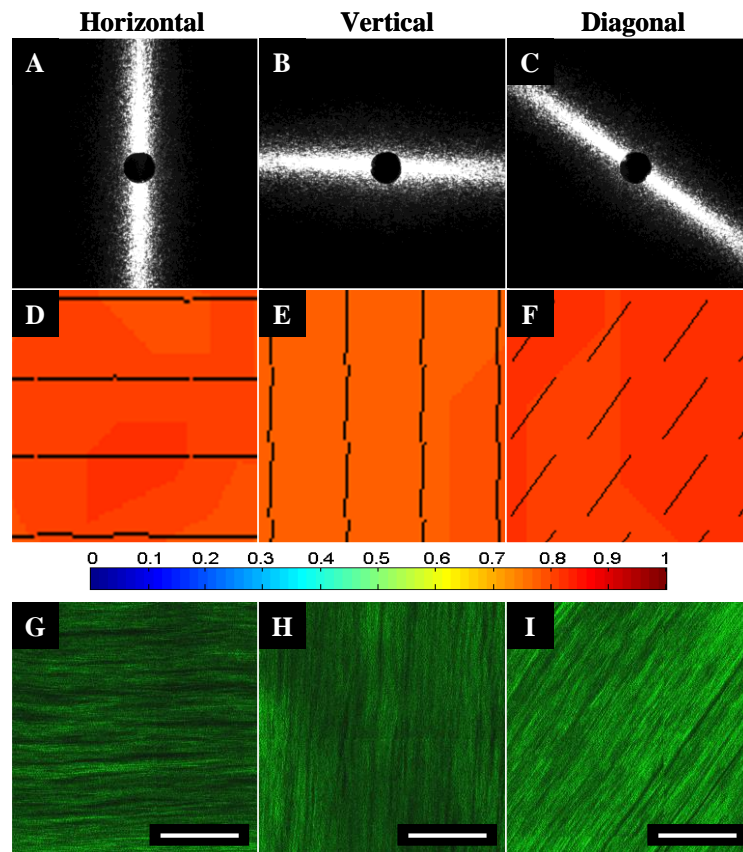
Figure 4.4. SALS in rat tail tendon. (A-C) Single SALS scatter patterns from rat tail tendon and resultant (D-F) SALS fibre maps made from multiple SALS patterns at 100μm intervals (colours represent DOFA: blue = low alignment, red = high alignment; black lines denote the PFO). The SALS fibre maps indicate a high DOFA of collagen fibres within the tendon approaching 1 which is representative of almost perfect alignment. The PFO lines correlate with the fibre orientation illustrated in (G-I) corresponding SHG images. Scale bars: 100μm

4.3.2 Connective Tissue Fibre Organisation within the Human ONH

Figure 4.5 demonstrates connective tissue fibre organisation within transverse ONH sections at the level of the prelamina, LC and postlaminar region of the left eye of an 88 year old female donor. The corresponding SHG images (Figure 4.5G-I) enable the visualisation of fibrillar collagen within each section and the SALS fibre maps (Figure 4.5D-F) illustrate differences within the ON canal and adjacent tissues.

116

The highest DOFA was evident in the circumferentially oriented fibres adjacent to the ON canal (Figure 4.5D-F). These fibres were situated within the peripapillary sclera (Figure 4.5G,H) of the prelamina or LC and the dura mater of the postlaminar ON (Figure 4.5F).

Within the prelamina section the peripapillary sclera surrounding the ON canal contained regions of low DOFA dispersed amongst regions of higher DOFA directly adjacent to the canal (Figure 4.5D). Within the ON canal DOFA was low with small patches of higher alignment. By comparing to the SHG image it was evident that the regions of low alignment were consistent with areas with little or no fibrillar collagen and patches of higher DOFA were associated with the central retinal vessels or peripherally emerging LC beams (Figure 4.5G).

At the level of the LC, the peripapillary sclera contained larger regions of high DOFA as compared to the prelaminar level (Figure 4.5E). These areas of higher alignment correlated to the highly aligned, dense, collagenous network within the sclera that surrounds the ON canal (Figure 4.5E,H).

SALS scatter within the ON canal at this level was indicative of the fibrillar collagen bundles forming the LC beams that were evident in the SHG images (Figure 4.5E). There appeared to be high variability in DOFA within the LC with regions of low alignment neighbouring regions of higher alignment. The boundary between the canal and peripapillary sclera showed a change in PFO from radial to circumferential orientation (Figure 4.5E).
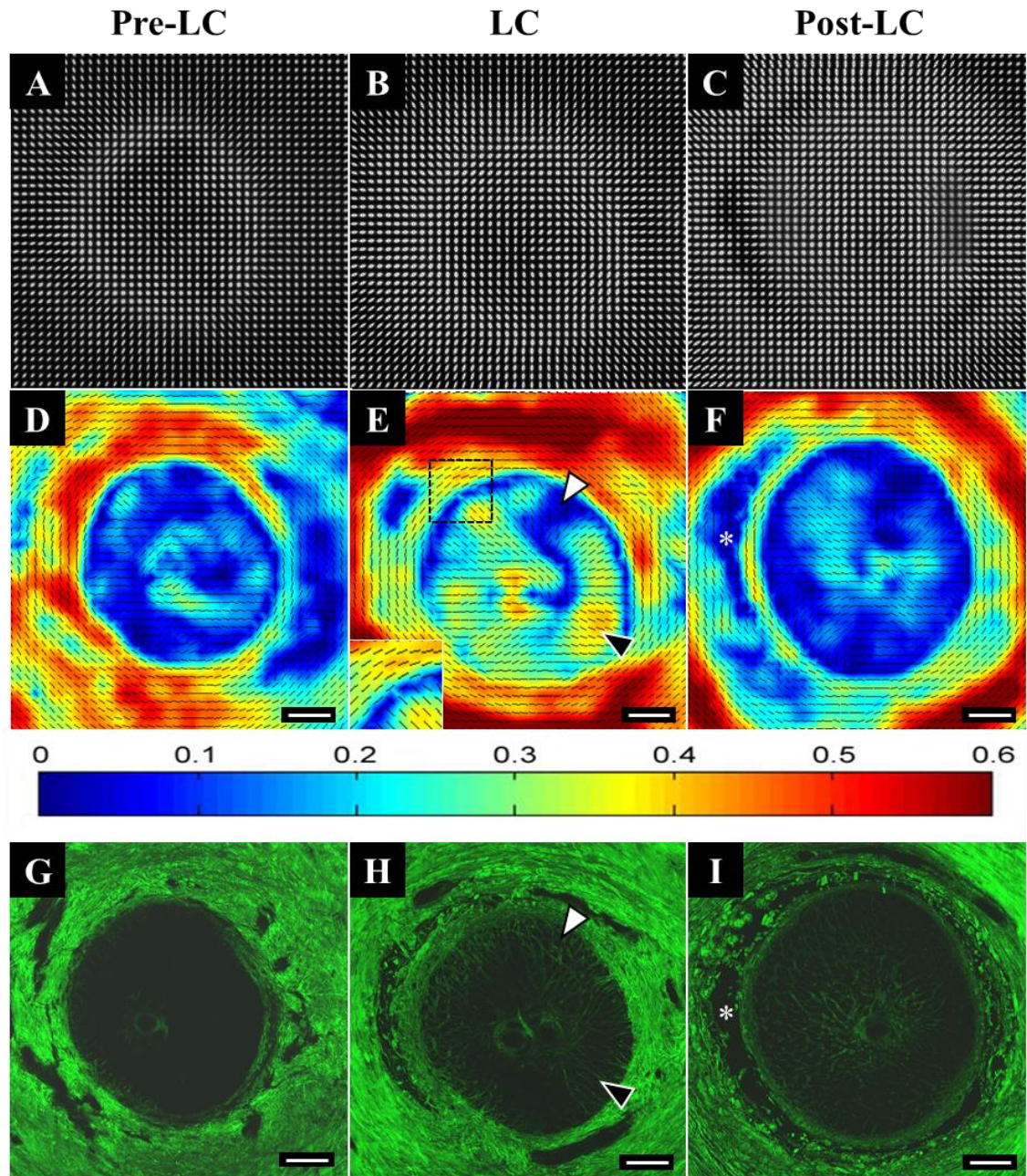
Figure 4.5. SALS in the human ONH. (A-C) Montage of SALS scatter patterns and (D-F) corresponding SALS fibre maps and (G-I) SHG images representative of those derived from transverse sections through the (A,D,G) prelamina, (B,E,H) LC and (C,F,I) postlaminar ON. In fibre plots: colours are indicative of DOFA (blue: low alignment, red: high alignment); black lines at 100μm intervals denote the PFO. In all regions DOFA was highest in the sclera and dural sheaths surrounding the IN canal. In the LC, regions of higher DOFA (black arrow heads in E and H) were neighboured by regions of lower DOFA (white arrow heads in E and H) and PFO changed from circumferential to radial orientation at the ON canal boundary (inset in E; 150% magnification of the area denoted by the square). DOFA was low in the ON canal in the postlaminar region and in the adjacent subarachnoidal space (asterisk in F and I). Scale bars: 500μm

In the postlaminar ON section the regions of high alignment surrounding the canal were localised to the dura mater (Figure 4.5F,I). Regions of lower alignment corresponded to the subarachnoid space and arachnoid mater. The pockets of higher alignment that were observed within the LC were absent in the postlaminar ON (Figure 4.5F) with the majority of the ON canal showing low DOFA in this tissue plane.

Regional differences in DOFA and PFO were also apparent in sections cut longitudinally to the ON (Figure 4.6). Excluding the high DOFA in the central retinal vessel walls, the highest regions of alignment were once again observed in the peripapillary sclera adjacent to the ON canal (Figure 4.6B).

At the level of the LC, distinct regions of aligned fibres, corresponding to the LC cribriform plates (Figure 4.6B,C) were surrounded by areas of low alignment. These low DOFAs corresponded to the region of LC insertion into the sclera, LC insertion into the central retinal vessels and transition from LC to postlaminar ON (Figure 4.6B). In the latter, the change in fibre orientation was apparent as the horizontal connective tissue of the LC, oriented across the canal, changed into highly aligned fibres of the postlaminar ON septa running parallel to the ON canal (Figure 4.6B,C).
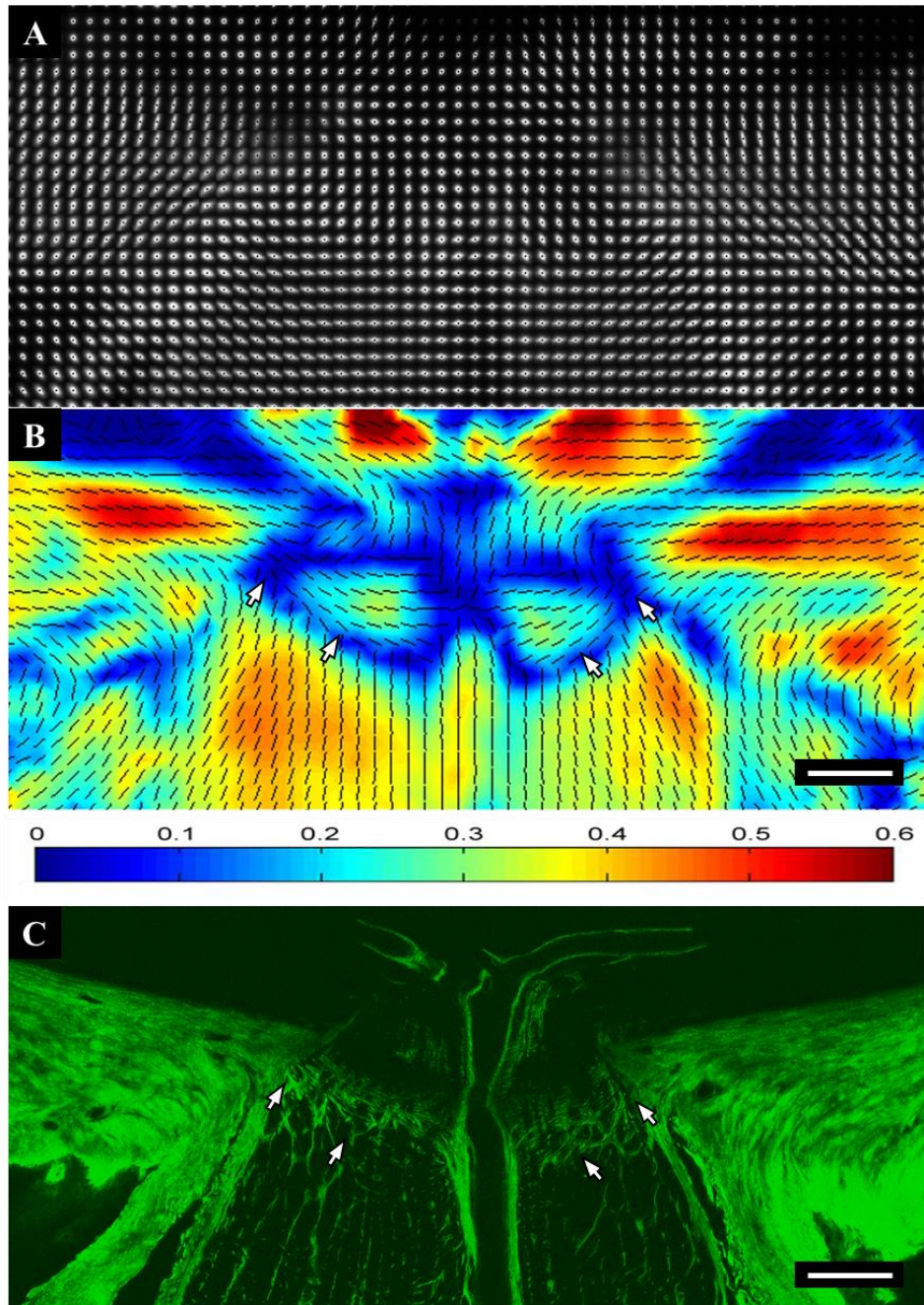
Figure 4.6. SALS of longitudinal human ONH sections. (A) Montage of a SALS scatter patterns and (B) corresponding SALS fibre map and (C) SHG image from a central longitudinal section of the human ONH. In fibre plots: colours are indicative of DOFA (blue: low alignment, red: high alignment); black lines at 100μm intervals denote the PFO. Within the ON canal, regions of lowest DOFA were found at the LC insertion into the peripapillary sclera and central retinal vessels and LC/postlaminar ON boundary (white arrows in B and C). Scale bars: 500μm

4.3.3 Quantification of Degree of Fibre Alignment in the Human ONH

4.3.3.1 Intra-donor Variability in the Human Optic Nerve Canal

Intra-donor ON canal variation in DOFA was apparent in SALS maps from serial ONH sections (Figure 4.7). To investigate the extent of intra-donor regional variation, change in DOFA in the inner and outer ON canal within a pair of donor eyes was plotted as a function of ONH depth (Figure 4.8).

Significant differences in DOFA were identified between inner and outer regions ($p<0.05$) of all sections through the ONH with the exception of the third LC section (LC3) in both eyes, and prelamina and fourth LC section (LC4) of the left eye (Figure 4.8A,B).

In both right and left ONHs, the inner and outer region DOFA index followed similar patterns from prelaminar to LC to postlaminar ON, with the peak DOFA apparent in the second or third LC section (LC2 or LC3) of the right and left ONH respectively. In both eyes, the DOFA increased from prelamina to LC and, in the left eye, decreased in postlaminar ON sections (Figure 4.8B).
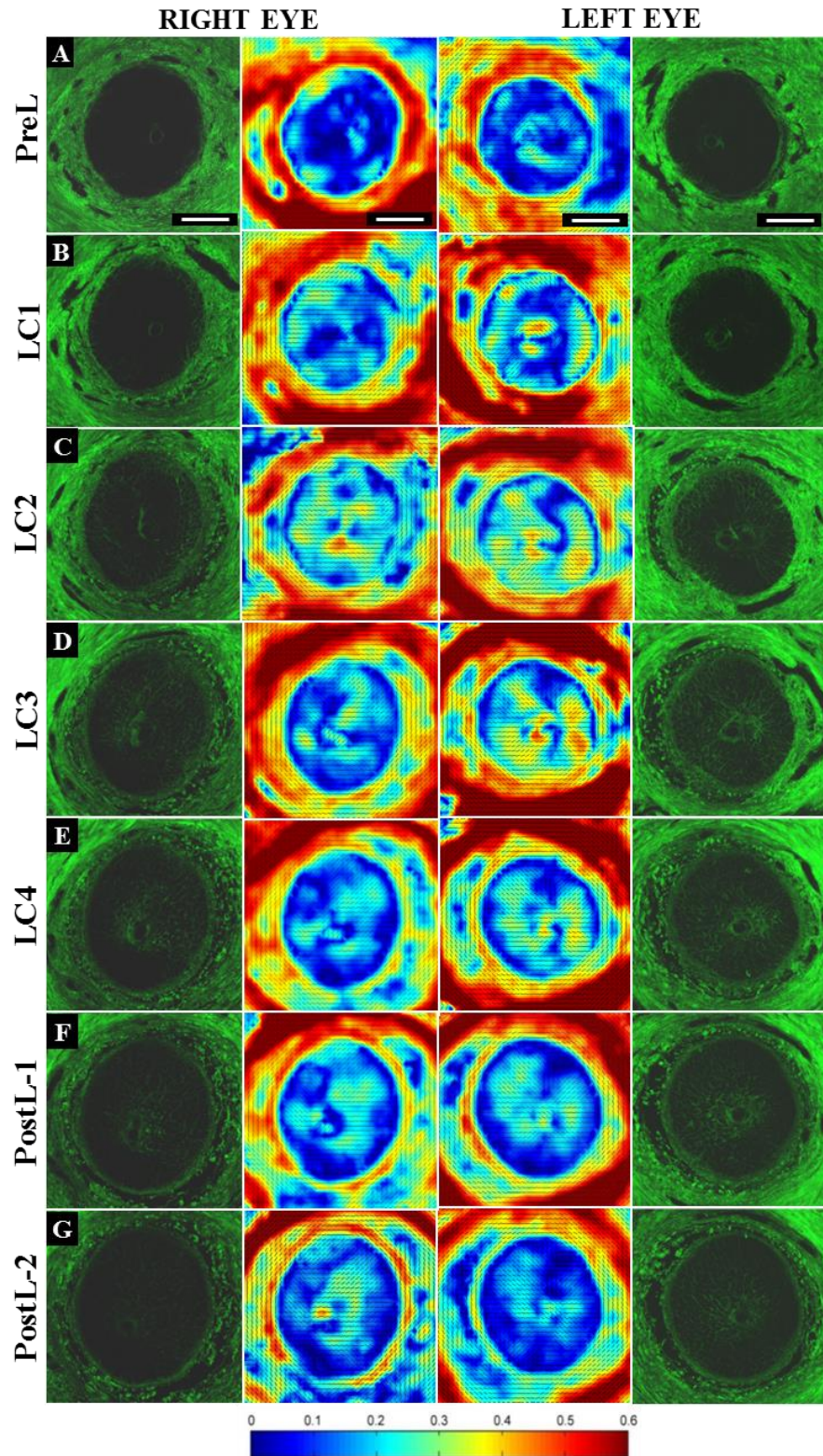
Figure 4.7. Intra-donor DOFA variation. SALS fibre maps with corresponding SHG images of serial 100μm transverse sections from a pair of human ONHs from (A) prelamina (PreL), (B,C,D,E) LC (LC1-4) and (F,G) postlaminar ON (PostL-1,2). In fibre plots: colours are indicative of DOFA (blue: low alignment, red: high alignment); black lines at 100μm intervals denote the PFO. Regional differences in DOFA are apparent between ONH regions and between eyes from the same donor. Scale bars: 1000μm
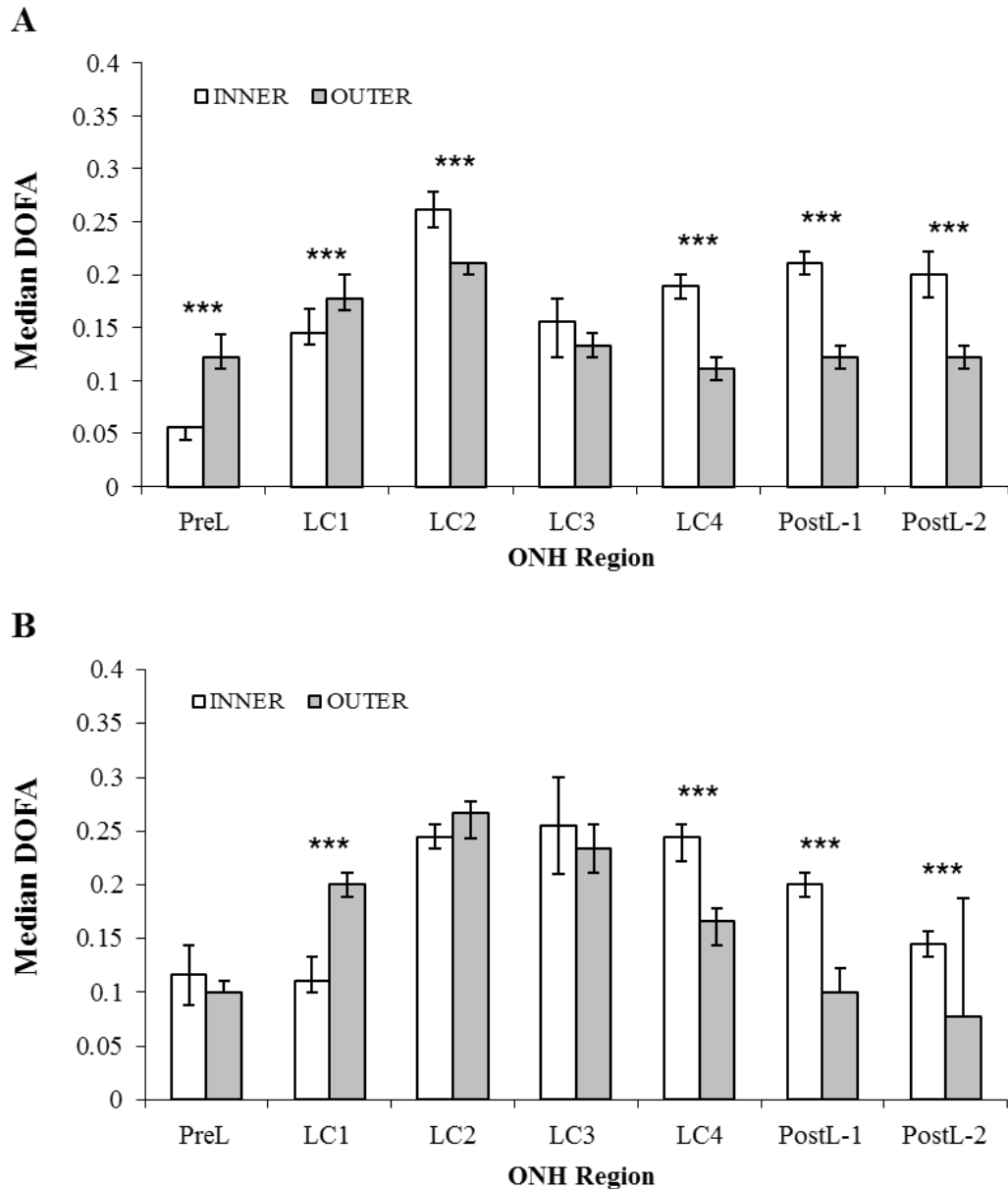
Figure 4.8. Degree of fibre alignment (DOFA, median +/- 95% confidence intervals) in the ON canal from serial 100μm thick tissue sections through the ONH; from prelaminar (PreL) to postlaminar ON (PostL-1,2) in (A) right and (B) left ONHs from the same donor. Significant differences between inner and outer ON canal were determined using the Mann-Whitney U test (*** = p<0.001). However, the DOFA showed a similar pattern in inner (white) and outer (grey) regions of the ON canal; with fibre alignment highest in the mid-LC (LC2, LC3).

By separating the ON canal into 12 radial regions of interest (Figure 4.3E), inner and outer DOFAs in the right and left ONH were further compared within each region of each LC section (Figure 4.9). The majority of regions within the first LC sections of the

right and left ONHs contained significantly higher aligned fibres in the outer canal when compared to the inner canal (depicted in red in Figure 4.9; p<0.05). At this level no difference was observed between outer and inner fibre alignment in the inferior region in both the right and left ONHs.
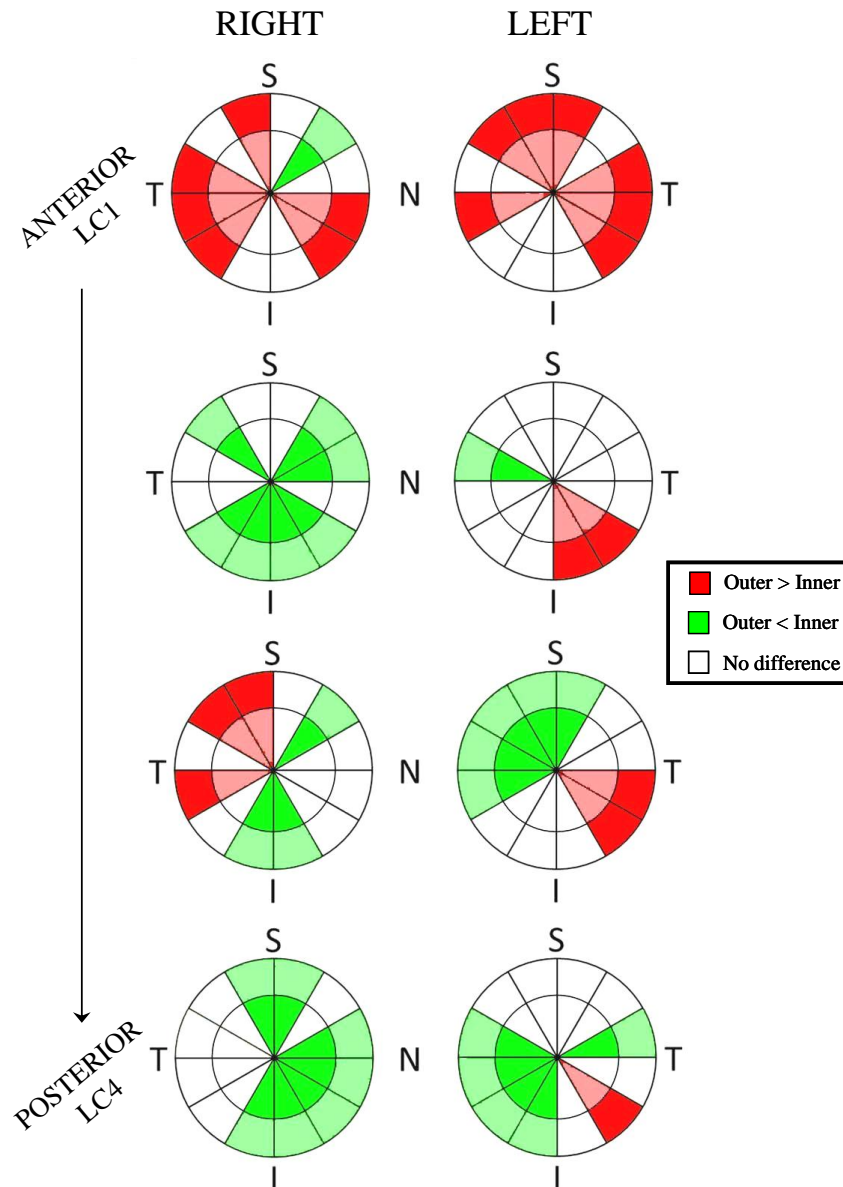
Figure 4.9. Schematic plots of intra-LC differences in DOFA in paired ONHs. Coloured regions indicate significant intra-LC differences (determined using the Mann-Whitney U test; p<0.05) in DOFA between outer and inner canal regions. Red: outer DOFA > inner DOFA. Green: outer DOFA < inner DOFA. The deeper colour represents highest DOFA in each. S = superior, T= temporal, I = inferior, N = nasal. Variation in DOFA differences was apparent between LC sections within a single ONH and between paired ONHs.

The only similarity between the second LC sections of the right and left ONH was in the nasal region (N2) where the inner canal was significantly more aligned than the outer canal (depicted in green in Figure 4.9; $p < 0.05$).

There was also little similarity between third LC sections of the right and left eye. The only regions with the same directional differences were the superior-nasal (SN), where the inner canal alignment was significantly higher than the outer canal alignment, and the temporal region (T2), where the outer canal alignment was significantly higher than the inner canal alignment ($p < 0.05$).

In the last LC sections all of the regions containing significant differences in the right eye and all but one of the regions containing significant differences in the left eye showed the inner canal as significantly more aligned than the outer canal ($p < 0.05$). These differences were mirrored between right and left eye in the nasal and inferior-nasal regions (I2-N2; Figure 4.9).

When directly comparing the right and left LCs from the same donor, few similarities in DOFA were found (Figure 4.10, $p > 0.05$). The regions showing the least differences between right and left were the inner regions of the LC1. In this region, differences in DOFA existed between the superior (S1 and S2), superior-temporal (ST) and nasal (N1 and N2) poles ($p < 0.05$). Inter-ocular variation in DOFA within the inner canal region of the LC increased with depth into the LC (i.e. LC1 to LC4), with no consistent pattern identified.
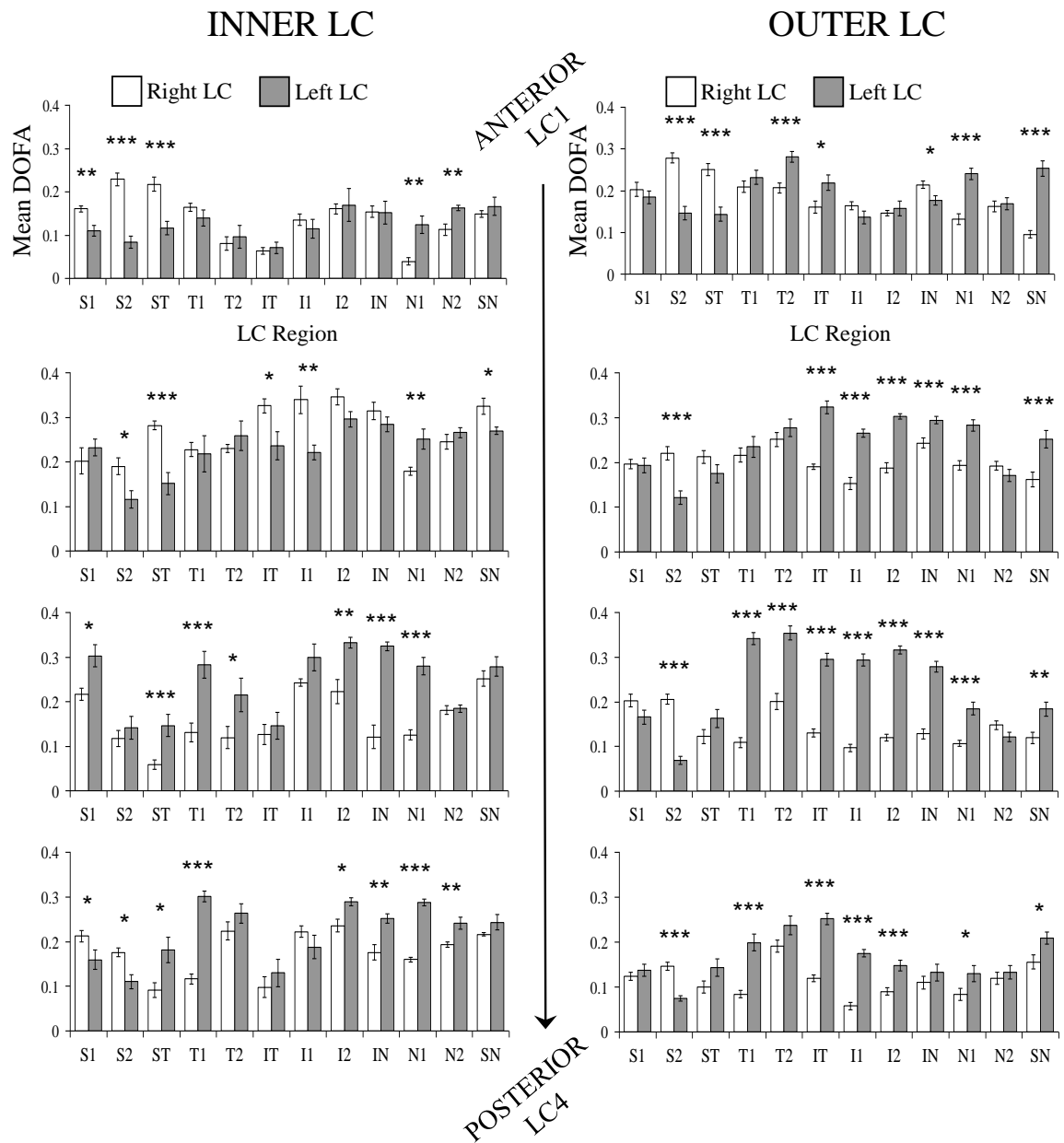
Figure 4.10. Differences in DOFA (mean +/- standard error) between right and left ONHs from the same donor in the inner and outer canal regions of serial transverse LC sections (LC1 to LC4). Significant differences were determined using the independent samples t-test or Mann-Whitney U test (depending on whether the data was normally distributed; *$p<0.05$, **$p<0.005$ and ***$p<0.001$). S = superior, T= temporal, I = inferior, N = nasal

Inter-ocular differences in outer LC DOFA were also apparent in all LC sections ($p<0.05$). The variation between right and left outer LC DOFA was greatest in LC3, in which 9 out of 12 regions showed significant differences (Figure 4.10). Interestingly, unlike the inner LC, inter-ocular variation in DOFA was not identified within the nasal

126

region (N2) and superior region (S1) throughout all LC sections. However, in the temporal (T1 and T2), inferior-temporal (IT), inferior (I2) and nasal (N1) outer LC regions, fibre alignment was greater in the left LC, compared to the right LC in all sections. In addition, the superior (S2) outer region of the right LC showed significantly greater fibre alignment than the left ($p<0.05$).

This data showed that huge variation in DOFA exists throughout the LC within and between different eyes of the same donor. Although it should be noted that DOFA values were relatively low in all LC sections.

4.3.3.2 *Inter-donor Variability in the Human Optic Nerve Head and Surrounding Tissue*

Due to the high intra-donor DOFA variability within the LC and ON canal, DOFA data within the ON canal was pooled per ONH donor section from 3 donors before comparison to the changes in DOFA in the insertion region and peripapillary sclera through the ONH depth (Figure 4.11).

Within the ON canal, the DOFA appeared to increase from prelamina to LC, where it peaked, and then decrease when entering the postlaminar ON in all samples (Figure 4.11A). The insertion region DOFA decreased from the anterior LC to the posterior LC (Figure 4.11B) in two of the elderly ONHs. This trend was subtle in the ONH from the 88 year old donor but more noticeable in the insertion region from the 87 year old donor. The DOFA within the peripapillary sclera also peaked within the region of the LC in all samples and tended to increase from the level of the prelamina to posterior LC, followed by a decrease at the level of the postlaminar ON (Figure 4.11C).
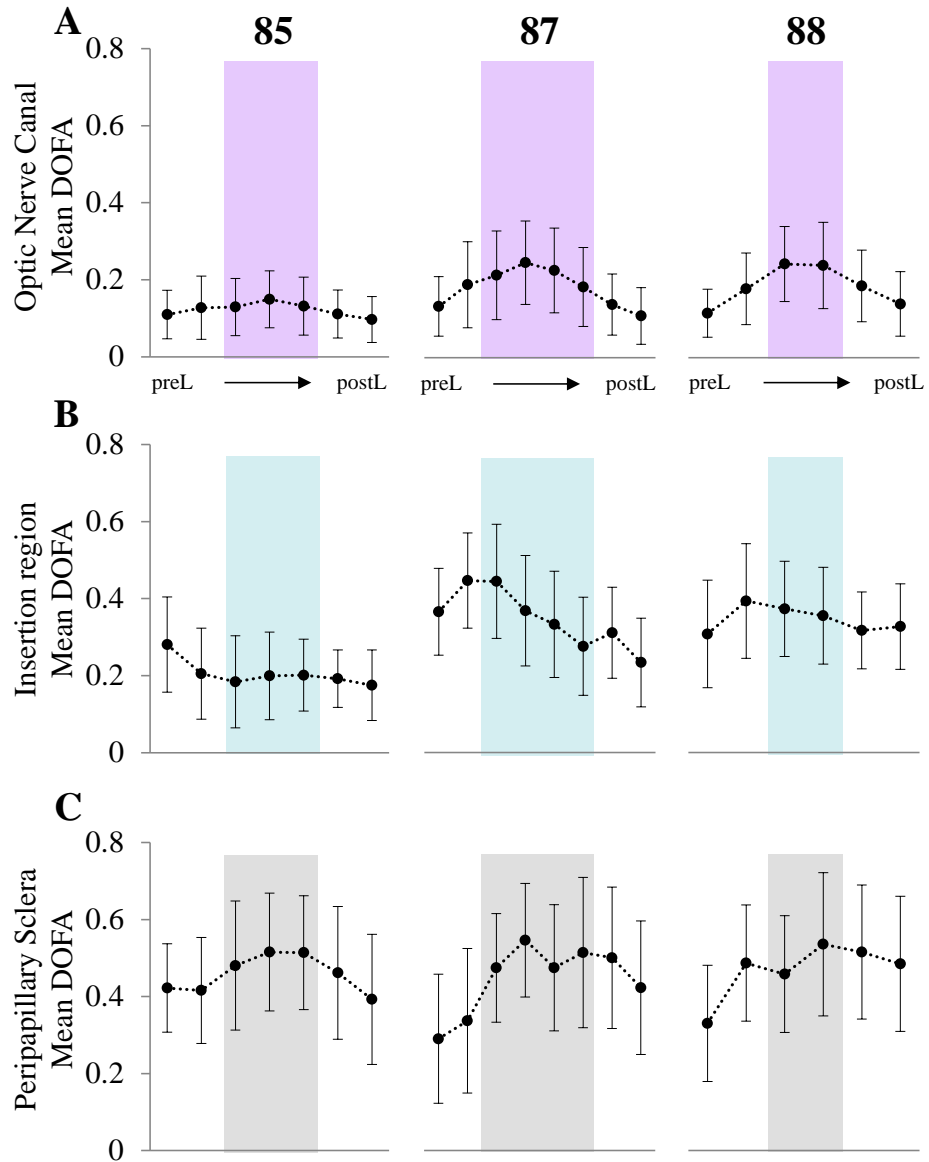
Figure 4.11. DOFA (mean +/- standard deviation) in serial 100μm section, from the level of the prelamina (preL) to postlaminar ON (postL) in the (A) ON canal, (B) insertion region and (C) peripapillary sclera in an 85, 87 and 88 year old ONH. Shaded regions represent sections at the level of the LC.

Note that the peripapillary sclera had higher DOFA values than the insertion regions and LC.

4.3.3.3 Age-related Variability in the Human Optic Nerve Head

Differences in fibre alignment in the ON canal, insertion region and peripapillary sclera between young (n = 3, aged 2, 6 and 21 years old) and elderly (n = 3, aged 85, 87 and 88 years old) donors were determined. DOFA values were pooled from all LC sections. Those sections that included prelamina or postlaminar ON were excluded. For examples of the SALS maps representative of an LC section from each donor ONH see Figure 4.12.
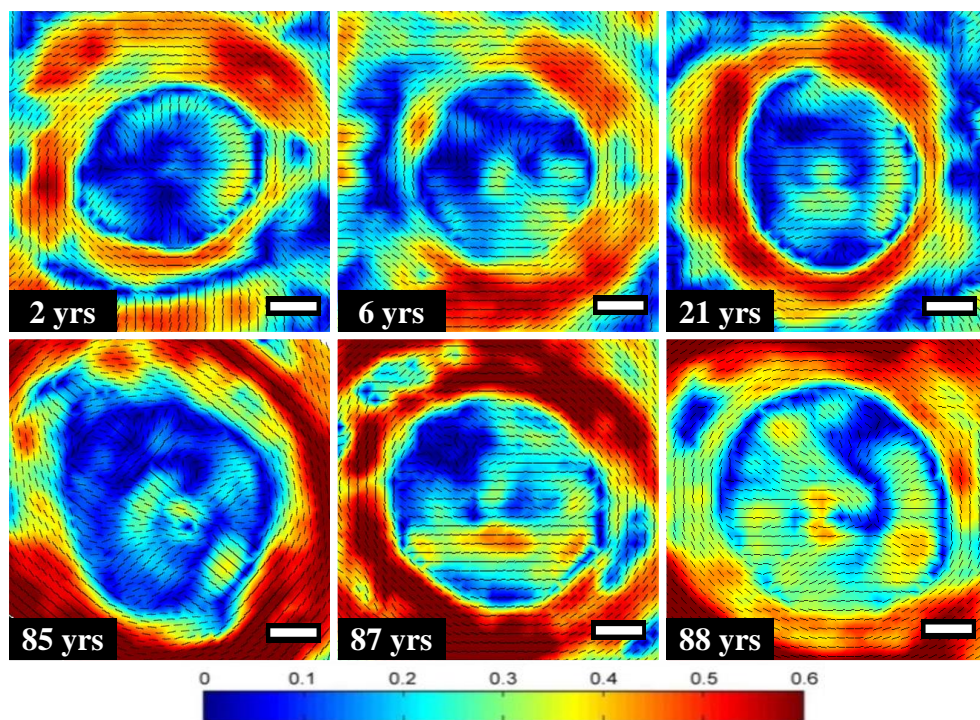
Figure 4.12. SALS fibre maps from representative transverse LC sections from different ages. Colours are indicative of DOFA (blue: low alignment, red: high alignment); black lines at 100μm intervals denote the PFO. Scale bars: 500μm

In all ages the order of DOFA from lowest to highest was LC < insertion region < peripapillary sclera, with significant differences (p<0.0008) occurring between the ONH regions in all samples with the exception of the insertion region and peripapillary sclera of the 6 year old donor ONH (Figure 4.13A). DOFA was significantly greater within the

LCs of the 87 and 88 year old ONHs when compared to the LCs of the young and 85 year old ONHs and significantly greater in the peripapillary sclera in all elderly ONHs when compared to the young ONHs (p<0.0002; Figure 4.13B). Significant differences in insertion region DOFA occurred both within and between the young and elderly age groups (p<0.003; Figure 4.13B).
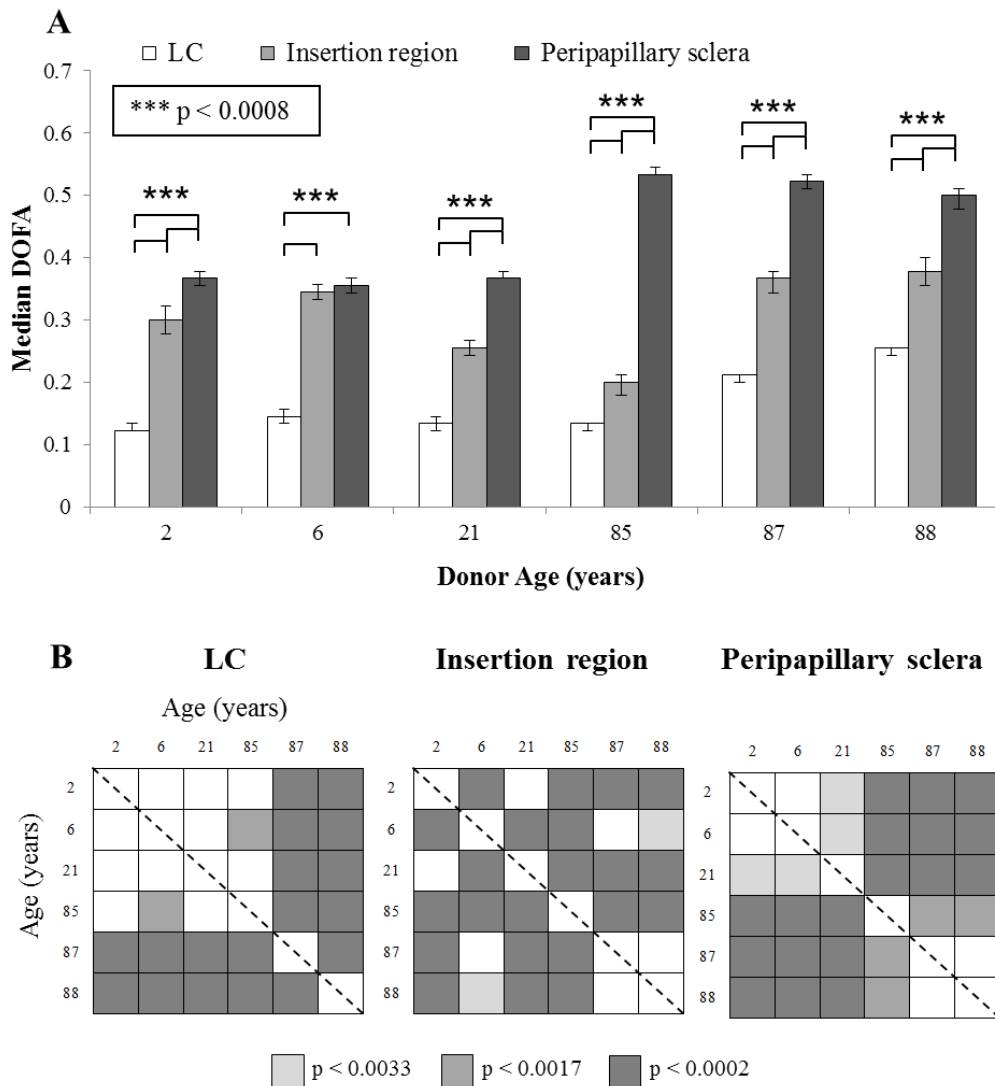
Figure 4.13. Regional differences in DOFA in the LC, insertion region and peripapillary sclera in young and elderly ONHs. (A) DOFA (median +/- 95% confidence intervals) was greatest in the peripapillary sclera followed by insertion region and LC in all samples. (B) The elderly LC (with exception of one sample) and peripapillary sclera DOFAs were significantly greater than the young.. Bonferroni adjusted significant differences were determined using the Mann-Whitney U test (A, ***p<0.0008; B, *p<0.0033, **p<0.0017 and ***p<0.0002)

Figure 4.14 shows examples of SALS fibre maps of longitudinal ONH sections from different aged donors.
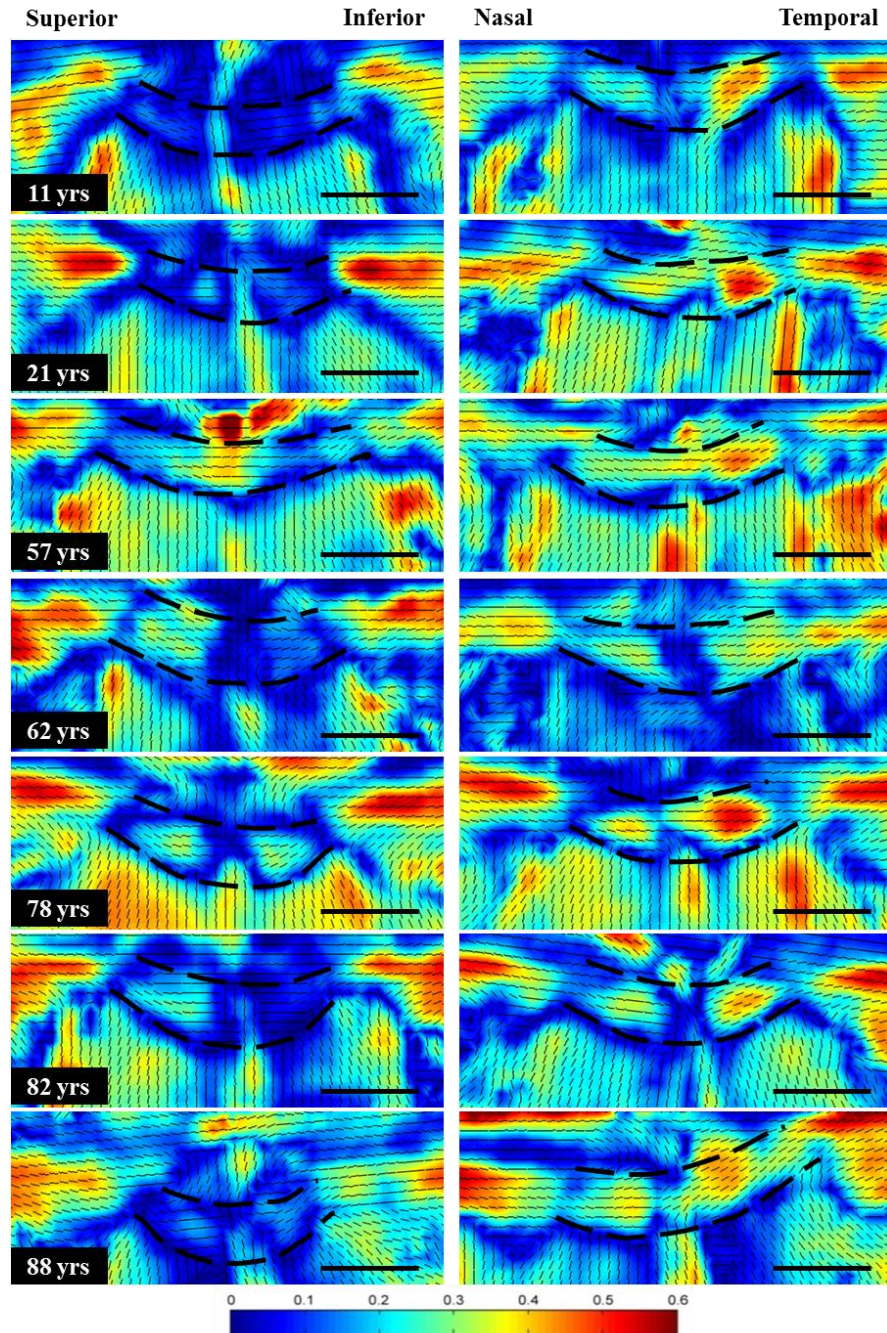
Figure 4.14. SALS fibre maps from longitudinal ONHs sections from different ages. Colours are indicative of DOFA (blue: low alignment, red: high alignment); black lines at 100µm intervals denote the PFO. ONHs were sectioned in superior to inferior (left column) or nasal to temporal (right column) orientations. Note the high alignment in the temporal region in all ages. Dashed lines denote the upper and lower boundaries of the LC. Scale bars: 1000µm

In all ages, a pocket of higher DOFA was localised to the temporal LC cribriform plates (Figure 4.14) which was confirmed when comparing regional LC DOFA values in the different aged donor ONH sections (Figure 4.15A). The order of highest LC DOFA to lowest was temporal > nasal > superior or inferior (Figure 4.15A). Temporal fibre alignment was significantly higher ($p<0.001$) in all samples with exception of the LC from the 82 year old donor.

The superior LC DOFAs in the 11, 21 and 88 year old ONH sections were significantly smaller than the superior LC DOFAs from donors aged between 57 and 82 ($p < 0.01$; Figure 4.15B). Many significant differences were observed between the inferior regions of LCs from donors of all ages ($p < 0.05$). In contrast, few significant differences were observed in the nasal and temporal regions of different aged LCs (Figure 4.15B).
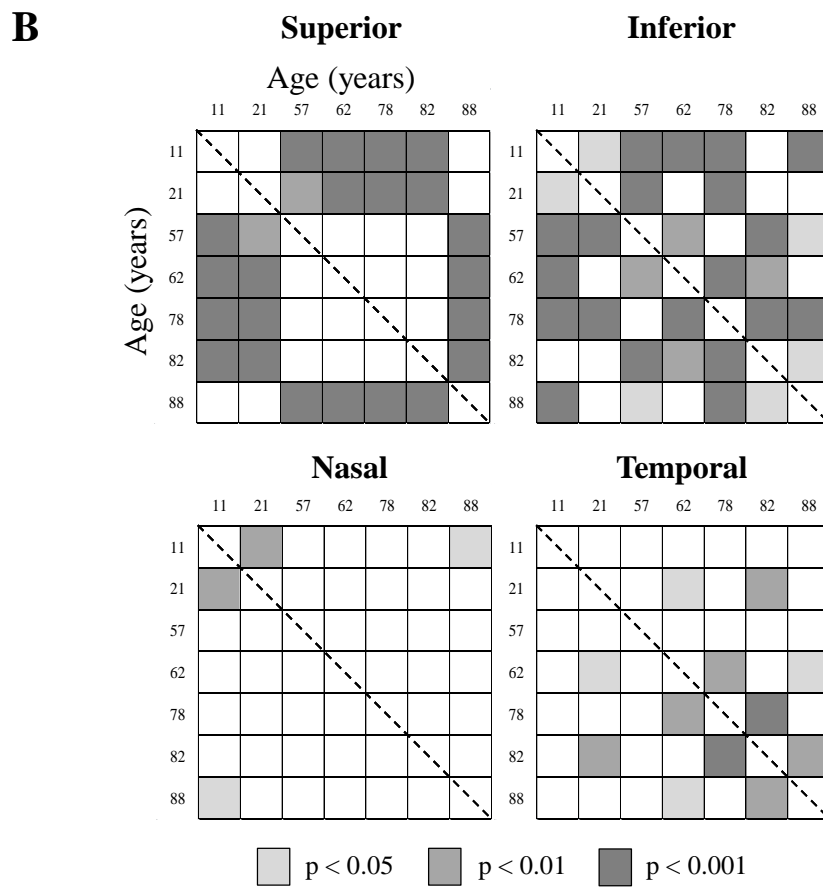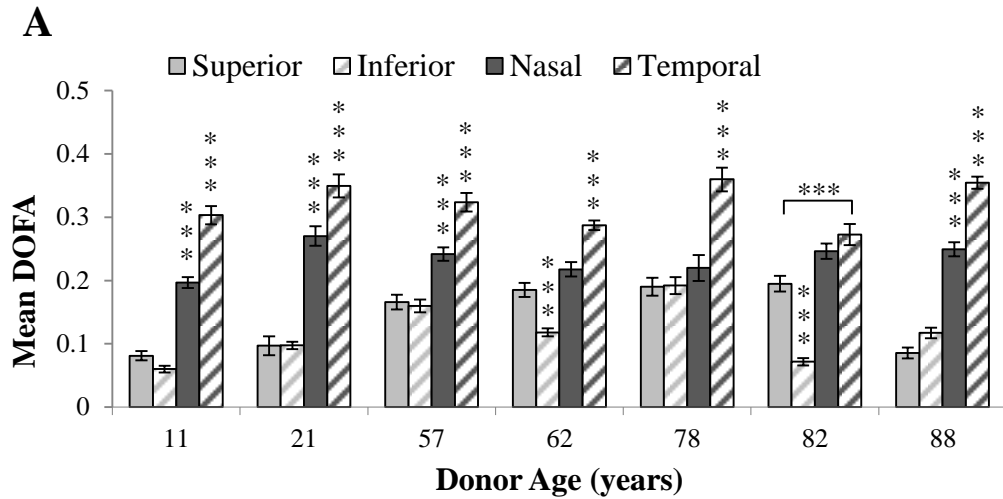
Figure 4.15. Differences in DOFA in the superior, inferior, nasal and temporal LC (A) within (mean DOFA +/- standard error) and (B) between (significant difference charts) ONH sections, cut longitudinal to the ON, from different aged donors. (A) Note that in all ages the temporal LC DOFA was significantly higher than the other LC regions. (B) The superior LC DOFAs in the 11, 21 and 88 year old ONH sections were significantly smaller than the superior LC DOFAs from donors aged between 57 and 82. No age related trends were observed in the other LC regions. Significant differences were determined using ANOVA (***p<0.001).

4.3.4 Quantification of Preferred Fibre Orientation in the Human Lamina Cribrosa

4.3.4.1 Intra-donor Variability in the Human Lamina Cribrosa

A summary of the mean PFOs and angular deviations from LC sections (LC1 to LC4) from the inner and outer LC of a right and left ONH is presented in Figure 4.16. The percentage of vertical (orientations 90º-135° and 225º-270°) and horizontal (orientations 135º-225°) PFOs within the LC sections is plotted in Figure 4.17. In both LCs, the PFOs within both inner and outer nasal and temporal regions were oriented radially towards the centre of the ON canal. In contrast, the outer superior region, closest to the superior-temporal, contained an almost circumferential preferred orientation in each LC section (Figure 4.16). In both eyes the majority of PFOs in the inner and outer LC in all LC sections (LC1 to LC4) indicated that connective tissue fibres were preferentially oriented horizontally (Figure 4.17).
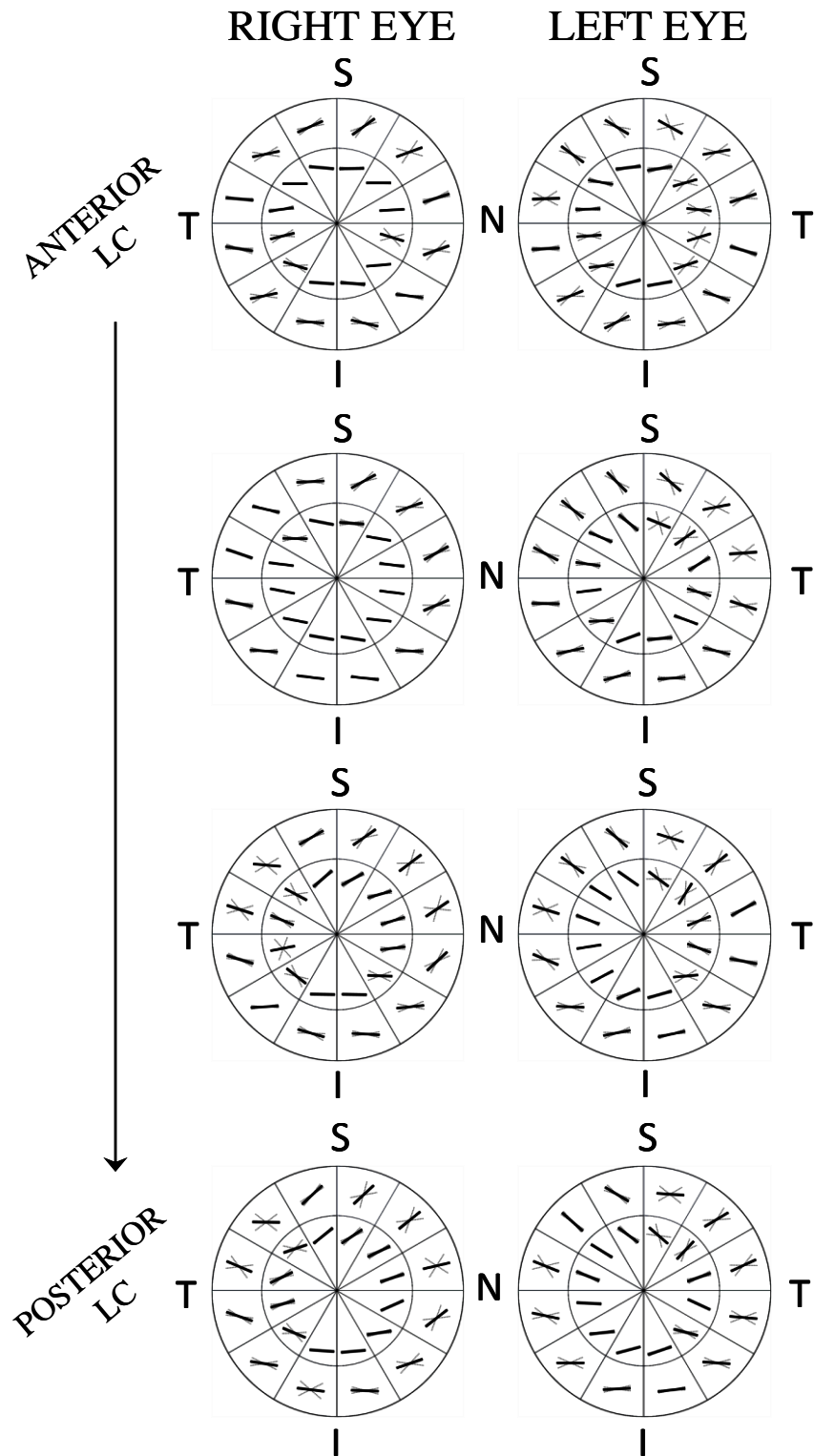
Figure 4.16. Schematic PFO plots of LC sections (LC1 to LC4) in paried right and left ONHs. Mean PFO (thick lines) and angular deviation about the mean (dotted lines) are depicted for 24 regions. S = superior, T= temporal, I = inferior, N = nasal.
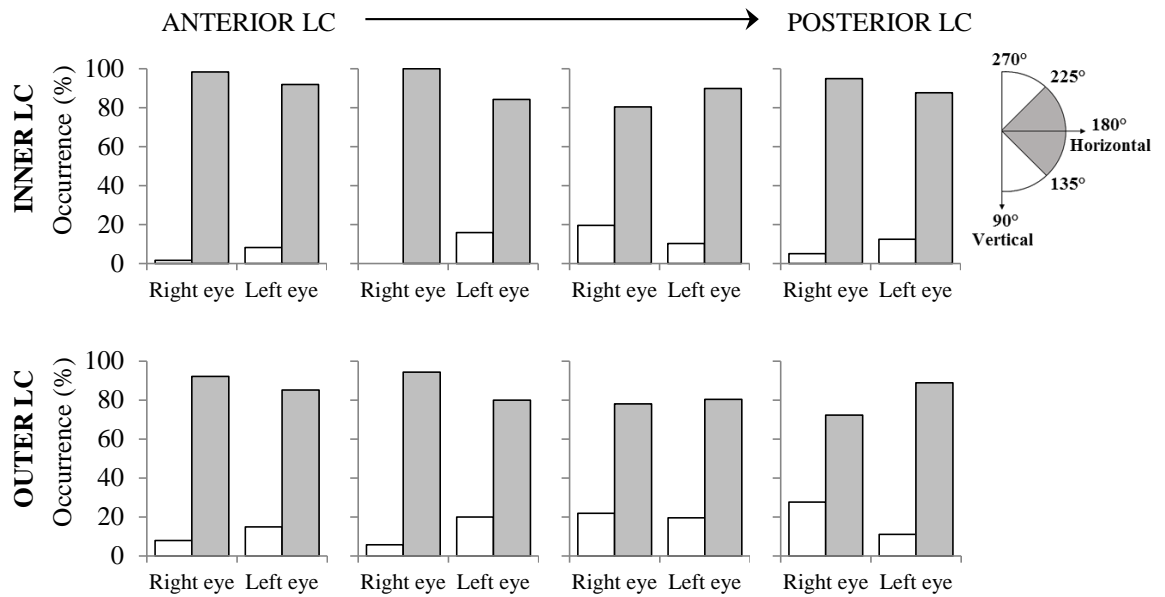
Figure 4.17. Percentage occurrence of vertically (angles 90°-135° and 225°-270°; white bars) and horizontally (angles 135°-225°; grey bars and angle range in coordinate diagram) oriented PFOs in the inner and outer LC in a paired right and left ONHs. In both right and left ONHs the majority of fibre bundles were horizontally inclined from anterior to posterior LC.

4.3.4.2 Age-related Variability in the Human Lamina Cribrosa

The percentage of vertical (orientations 90°-135° and 225°-270°) and horizontal (orientations 135°-225°) oriented PFOs within the LC from a range of donor ages (2 − 88 years old) is plotted in Figure 4.18A. The majority of PFOs in the LC were horizontally oriented in all age groups. The ratio of horizontal to vertical fibres increased from the 2 year old to 87 year old ONH, then decreased in the 88year old ONH (Figure 4.18B).
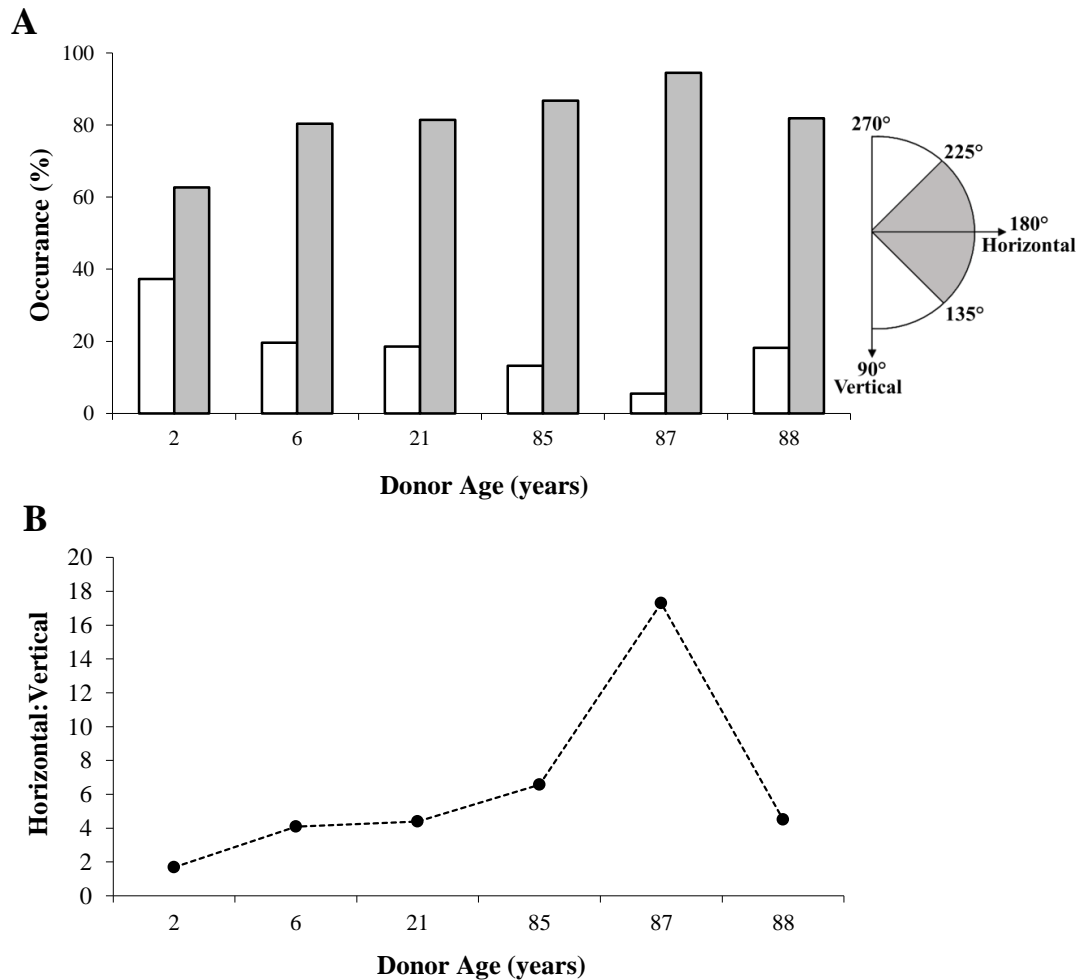
Figure 4.18. Percentage occurrence of vertically (angles 90°-135° and 225°-270°; white bars) and horizontally (angles 135°-225°; grey bars and angle range in coordinate diagram) inclined PFOs from the inner and outer lamina cribrosa (LC; sectioned transverse to the ON) from a range of donor ages (n = 6, 2 – 88 years old). In all LCs the majority of fibre bundles were horizontally inclined.

Regional and age-related variation in mean PFO of LC beams in sections cut longitudinal to the ON was assessed by comparing LC beam orientation as a measure of the absolute difference between LC beam PFO and the anterior LC plane, defined as the plane created between the points of anterior LC insertion (Figure 4.19A). The highest difference, and thus the most posteriorly angled LC beams were observed in the 88 year old inferior LC, closely followed by the inferior LC of the 78 year old donor (Figure 4.19B). No region or age was predominantly more posteriorly angled than the others.
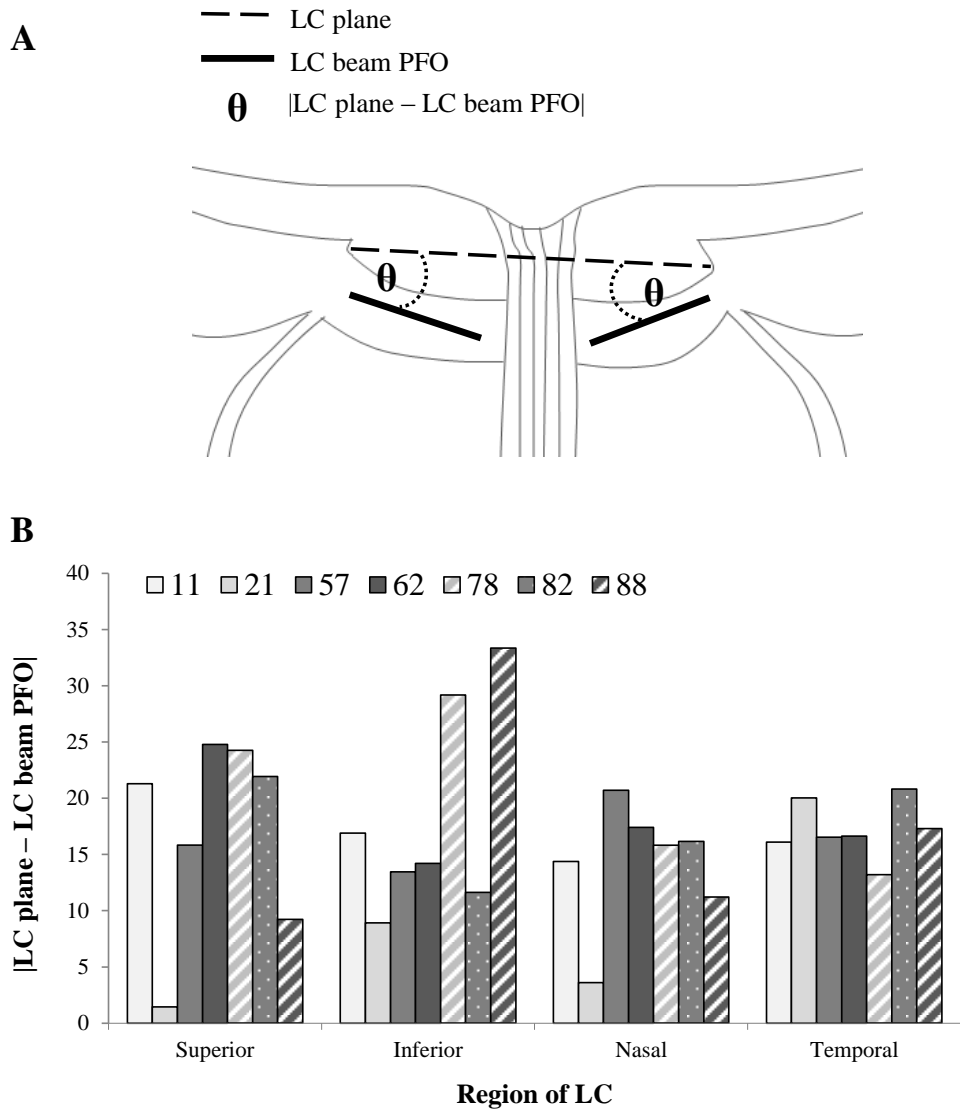
Figure 4.19. Absolute differences (θ in (A)) between LC beam PFO (solid lines in (A)) and LC plane (plane created between the points of anterior LC insertion; dotted line in (A)) in (B) superior, inferior, nasal and temporal regions of LCs from a range of donor ONHs. No region or age showed predominantly larger LC plane to LC PFO differences.

4.4 **Discussion**

One of the major load bearing components of the extracellular matrix of the human ONH is fibrillar collagen. Different fibrillar collagen types (types I, III and V) have been identified in the LC beams, central retinal vessel walls and peripapillary sclera (Hernandez et al., 1986, Rehnberg et al., 1987, Morrison et al., 1989b, Albon et al., 1995). However, even though the distribution of fibrillar collagen has been studied, the orientation of these collagen fibres within the LC has not been quantified in human eyes.

Orientation and alignment of connective tissue fibres depend on the extent and nature of the stresses they experience (Culav et al., 1999). For example, in tendon, the fibre bundles are highly anisotropic enabling them to withstand the longitudinal, transverse and rotational forces during movement (Kannus, 2000). Therefore, the organisation of connective tissue fibres within the ONH will influence how it behaves under stress. Thus, this chapter aimed to quantify the alignment and orientation of fibre bundles throughout the ONH, starting with right and left ONH analysis of the same donor and subsequently in young and elderly ONHs.

Large variation and asymmetry was observed between the LCs of the right and left eye with only a few regions showing consistent similarities in DOFA. However, Jonas et al. (1992) found no significant differences between right and left eyes in ON fibre counts, area or diameter indicating that asymmetry in LC connective tissue fibre organisation may not impact an individual's nerve fibre population.

Interestingly, asymmetry in level of IOP has been shown to occur in healthy and glaucomatous eyes (Realini et al., 2002, Lee et al., 2004, Realini et al., 2004, Sit et al., 2006, Kim et al., 2011) and is associated with ageing (Lee et al., 2004, Kim et al., 2011). The level of asymmetry in IOP has also been shown to be directly related to the likelihood of developing glaucoma (Williams et al., 2013). Further work is required to determine if, like IOP, asymmetry in LC microarchitecture is a function of ageing and if a relationship between IOP asymmetry and age is a risk factor for the predisposition to glaucoma.

In all samples, the highest DOFA occurred in the highly anisotropic peripapillary sclera where fibres aligned circumferentially around the ON canal. This high peripapillary fibre alignment was also inferred from the orientated, collagen-related SAXS reflections 0-500μm from the ON canal border as witnessed in Chapter 3. These findings are consistent with observations from inverse finite element scleral models of the monkey eye (Girard et al., 2009a, Girard et al., 2009b) and studies of donor human eyes (Goldbaum et al., 1989, Morrison et al., 1989b, Pijanka et al., 2012). These circumferential fibres are thought to provide a protective mechanism in limiting IOP-related expansion of the ON canal at the LC and limit in-plane tensile strains (Grytz et al., 2011, Coudrillier et al., 2013). This emphasises the importance of the structure of the peripapillary sclera in response to IOP related stress (Norman et al., 2011).

DOFA within the peripapillary sclera increased with progression from the level of the prelamina to the LC, peaked at the LC level and then decreased at the level of the postlaminar ON. The latter decrease in DOFA may be attributed the emergence of the sub-arachnoidal space of the ON meningeal sheaths. The peak in DOFA at the level of the LC may correspond to the high fibre bundle anisotropy in the mid scleral stroma that

has been reported with WAXS (Pijanka et al., 2012). Collagen fibre bundles within the inner most sclera have previously been described as interwoven and irregular compared to the more regular lamellar bundles in the outer region (Komai and Ushiki, 1991). Though the previous study investigated the equatorial sclera using electron microscopy, a similar scleral structure may be present at the peripapillary region.

Within the ON canal, a low DOFA was observed in the prelamina region. This finding is most probably due to the lack of connective tissue in this region as illustrated previously in Chapter 2. These data highlight the importance of viewing the SALS results in conjunction with an imaging technique that allows for the visualisation of the tissue components and structure.

A decrease in fibre alignment in the ON canal from the LC to postlaminar ON was evident in sections cut transverse and longitudinal to the ON. DOFA decreased at the LC/postlaminar ON boundary as collagen fibre bundles orientated across the canal in the LC became perpendicular ON septa in the postlaminar ON. This region of low alignment may indicate an area of weakness in which transverse axon bundle support is lessened posterior to the more highly aligned LC. However, it is also possible that the aligned, longitudinal connective tissue septae in the postlaminar ON protect ON nerve bundles from forces exerted on the nerve due to eye movements.

SALS analysis of the sections cut longitudinal to the ON revealed the highest fibre alignment within the LC cribriform plates to be in the temporal region of all LCs, with temporal and nasal regions being consistently more aligned than superior and inferior. Temporal and nasal LC regions have been shown to contain higher densities of inter-pore connective tissue than the superior and inferior regions (Quigley and Addicks,

1981, Radius, 1981, Ogden et al., 1988, Jonas et al., 1991) forming a horizontal ridge *in vivo* (Park et al., 2012c). It is believed that the reduced support in the superior and inferior poles predispose the traversing RGC axons to IOP related damage (Quigley and Addicks, 1981, Quigley et al., 1981). In addition to the increased connective tissue density, the higher fibre alignment within the temporal and nasal cribriform plates supports the proposition that these regions offer greater support to RGC axons.

Transverse LC section DOFAs in the young age group (2 to 21 years old) were significantly less than those in the 87 and 88 year old donor eyes, though not different to the 85 year old. It has been proposed that age-related changes in the LC connective tissue, including an increase in non-enzymatic cross linking and total collagen content and alteration in the ratio of collagen types I:III (Albon et al., 1995, Albon et al., 2000a), contributes to reduced mechanical compliance in the elderly LC (Albon et al., 2000b). Therefore, if the elderly LC is stiffer than the young LC, the higher degree of alignment in the 87 and 88 year old eyes may represent an 'unrelaxed' ONH and its state before release of IOP. Therefore, the young LCs may not necessarily be less aligned *in vivo* but have simply relaxed following post-mortem. The same explanation may also apply to the significant differences between young and elderly DOFA in the peripapillary sclera. Akin to the LC, sclera has also been shown to stiffen with age (Friberg and Lace, 1988, Geraghty et al., 2012) which is potentially due to high nonenzymatic cross-link density (Schultz et al., 2008) or retention of proteoglycan complexes (Dunlevy and Rada, 2004). These findings are further supported by the presence of fibrillar collagen crimp in the SHG images from the young ONH (Chapter 2) and may indirectly represent the higher compliance of the young ONH in comparison to the elderly ONH.

142

In all eyes the majority of preferred orientations of the fibre bundles within the LC were horizontally oriented. This infers that most fibre bundles were oriented along the temporal to nasal axis, as confirmed in the summary diagrams of the paired LCs. The orientation of fibres is consistent with the "hourglass" shape of connective tissue in the LC previously described (Quigley and Addicks, 1981, Radius, 1981, Jonas et al., 1991).

Within the SALS fibre maps, the fibre bundles appeared to be radially orientated around the periphery of the LC which is consistent with 3D microarchitecture analysis of the monkey ONH (Roberts et al., 2009) and predictive ONH computational remodelling (Grytz et al., 2011). A radial connective tissue fibre orientation is believed to provide transverse reinforcement to the LC (Grytz et al., 2011) while a preferred horizontal fibre orientation may help withstand a high mechanical stress, which has been predicted to be highest in the temporal region of monkey eyes (Downs et al., 2009, Roberts et al., 2010b).

The tilt angle of the LC cribriform plates was not affected by age or LC region. A higher difference between LC cribriform plate preferred orientation and plane of LC insertion, may indirectly infer a more backward displaced LC. Furthermore, tilt angle of the LC could be used to reflect optic disc cupping which has been shown to increase with age (Garway-Heath et al., 1997). However, the findings presented here indicate that age may not be associated with LC displacement, although a larger sample size and analysis though the LC depth is needed to validate this finding.

A limitation of this study is that DOFA and PFO were measured from unpressurised eyes as the corneas were removed before fixation, although it can be argued that current results may represent base-line ONH architecture. Future work should include pressure

elevation apparatus, like those previously used (Albon et al., 2000b, Coudrillier et al., 2012, Lari et al., 2012), and fixed tissue at a range of pressures to map changes in the degree of alignment and preferred orientation of fibre bundles under different levels of pressure.

4.5 **Conclusion**

In conclusion, SALS is an effective tool for the quantification of fibre alignment and orientation throughout the ONH and surrounding tissues. The degree of alignment of fibre bundles peaked inside the LC when compared to the prelamina and postlaminar ON regions and tended to increase in the peripapillary sclera from prelamina to LC. The LC cribriform plates were more aligned in the nasal and temporal regions when compared to the inferior and superior. Degree of alignment showed an age-related increase in the peripapillary sclera, and to some extent in the LC, implying that the aged sclera and LC are stiffer than the young. In all LCs, the majority of fibre bundles were preferentially horizontal in orientation along the nasal to temporal axis. Together with the degree of alignment data, this is likely to influence how the LC deforms under increased IOP.

Chapter 5 - Connective Tissue Content and Fibre Orientation and Alignment in the Glaucomatous Human Optic Nerve Head

5.1 Introduction

LC deformation, thickening and an increase in connective tissue volume have been indicated in the early stages of glaucoma in an experimental ocular-hypertension monkey model (Yang et al., 2007, Roberts et al., 2009, Yang et al., 2011a). Advanced glaucomatous changes in the human LC include compression and backward displacement of the LC cribriform plates together with posterior LC rotation (Quigley et al., 1981, Quigley et al., 1983) and LC thinning (Jonas et al., 2003, Inoue et al., 2009, Ren et al., 2009, Park et al., 2012a). The peripapillary sclera has also been shown to change in glaucoma and has been reported to thin in an ocular-hypertension monkey model (Downs et al., 2001) but become thicker in post mortem human glaucomatous samples (Coudrillier et al., 2012). Architectural alterations in the glaucomatous ONH are thought to be due to pressure induced tissue deformations and/or remodelling (Hernandez, 2000, Morgan, 2000, Burgoyne et al., 2005, Downs et al., 2011) by activated astrocytes and LC cells (Hernandez, 2000, Morgan, 2000, Burgoyne et al., 2005, Downs et al., 2011).

The inter-individual and age-related variation within the ONH connective tissue fibre bundle alignment and orientation has been previously described in Chapter 4. This chapter aims to use SALS to investigate these architectural parameters in the glaucomatous ONH since they will influence how the ONH responds to IOP.

145

OBJECTIVES

- To quantify the degree of fibre alignment (DOFA) and preferred fibre orientation (PFO) in the glaucomatous ONH

- To determine differences in fibre alignment and orientation between glaucomatous and age-matched control ONHs

5.2 Materials and Methods

5.2.1 Sample Preparation

Eyes from donors diagnosed with POAG (n = 3 eyes total, G1-G3, donor ages ranging 73 to 87 years) were received from the Mayo Clinic, Rochester, Minnesota, USA (see Table 2) and age-matched control eyes (n = 3 eyes total, C1-C3, with no known ocular pathology, aged 88, 87 and 85 years, respectively) were received from Bristol Eye Bank, Bristol, UK. All eyes were fixed in 4% PFA within 48 hours of enucleation.

Donor	Age (years)	Sex	Mean deviation (dB)	Cup/Disc ratio	Year of enucleation	Glaucoma severity
G1 R	86	M	-1.54 in 2002	Unknown	2008	Mild
G2 L	73	M	Unknown	Unknown	2010	Unknown – diagnosed in 2007
G3 L	87	F	-12.81 in 2008	0.9	2009	Advanced

Table 2. Demographics of glaucoma donor eyes. R = right eye, L = left eye

Eyes were prepared and sectioned as stated in section 2.2.1. Eyes were orientated, washed and 100μm thick serial sections, from prelamina to postlaminar ON, were cut from each dissected ONH. Sections were mounted in 1:1 PBS:glycerol then frozen at -80ºC until subjected to SHG imaging and SALS.

5.2.2 Nonlinear Microscopy Techniques: Second Harmonic Generation and Two Photon Excited Fluorescence

ONH sections were subjected to nonlinear optical microscopy TPEF and SHG imaging as previously described (2.2.2.1). Following excitation at 800nm, 3D epi-fluorescent TPEF and forward scattered SHG ONH datasets (256x256x1 pixel) were collected and converted into maximum intensity projections using ImageJ image analysis software.

5.2.3 Small Angle Light Scattering

Small angle light scattering (SALS) images were acquired and processed as described in section 4.2.3. Three serial sections containing the LC from each donor eye were analysed for differences in DOFA and PFO in 12 radial regions of interest within the LC, insertion region and peripapillary sclera, defined using maximum intensity projection SHG images of each section as previously described (4.2.2).

5.2.4 Statistical Analysis

Statistical comparisons of DOFAs between glaucoma and control LCs and at different LC depths were analysed using SPSS version PASW 18 (SPSS Inc., USA). Normality of data was determined using the Shapiro-Wilk test with a significance level of 0.05. DOFAs were compared between the 12 radial regions of each glaucomatous and control

LC, at each of the 3 LC levels, using the independent samples t-test or Mann-Whitney U test.

Since pooled DOFA values from the 3 ONH sections at the level of the LC were not normally distributed, Kruskal-Wallis tests were used to determine if there were any significant differences in the DOFA in the LC, insertion region and peripapillary sclera between glaucoma and age-matched controls. Where appropriate, multiple Mann-Whitney U tests were used with a Bonferroni corrected significance level ($p<0.017$) that accounted for type I errors, to identify where the differences fell. These data are presented as bar charts with 95% confidence intervals of the median error bars (calculated using the Ratio Statistics option in PASW) depicting the precision of each measurement.

To compare PFOs in 12 LC regions of the glaucoma and control ONHs, the appropriate circular statistical tests (Batschelet, 1981) were calculated using Oriana statistical software (Kovach Computing Services, UK). Before comparison, right eye LC regions and PFO angles were mirrored allowing for direct comparisons to left eye PFO angles. All PFO data sets were shown to have a significant directional preference at $p<0.05$ using Rayleigh's Uniformity test (the null hypothesis for the Rayleigh's test is that the fibres were distributed in a uniform manner). However as the majority of PFO data sets did not confer to a von Mises distribution (as determined using Watson's U^2 one-sample test, $p<0.05$), the Watson-Williams F-test could not be used to directly compare the mean PFOs of each LC region. Therefore, the non-parametric Mardia-Watson-Wheeler test was used to determine significant differences between the glaucomatous and control PFO distributions in each LC region using a significance level of 0.05.

5.3 **Results**

5.3.1 **Comparisons of Lamina Cribrosa Connective Tissue Distribution in Glaucomatous and Age-matched Control Donors**

Nonlinear microscopy images of three LC sections from three glaucomatous ONHs (G1-G3) and an age-matched control (C2) are shown in Figure 5.1. The first LC section of C2 contained a region of minimal connective tissue content in the superior LC region which may represent cup within the LC. The glaucomatous LCs also contained regions of minimal connective tissue content, though these regions were larger than in C2 (Figure 5.1) and may indicate greater LC deformation or connective tissue damage.

The first section of the mild glaucomatous (G1) LC contained large areas devoid of connective tissue beams in the superior and inferior-temporal regions while the first section of the unknown glaucomatous (G2) LC contained a large area of limited connective tissue content in the superior-temporal region (Figure 5.1).

The first section of the advanced glaucomatous (G3) LC was also devoid of connective tissue beams in the superior-temporal region and the inferior LC region contained minimal connective tissue content in all LC sections (Figure 5.1).
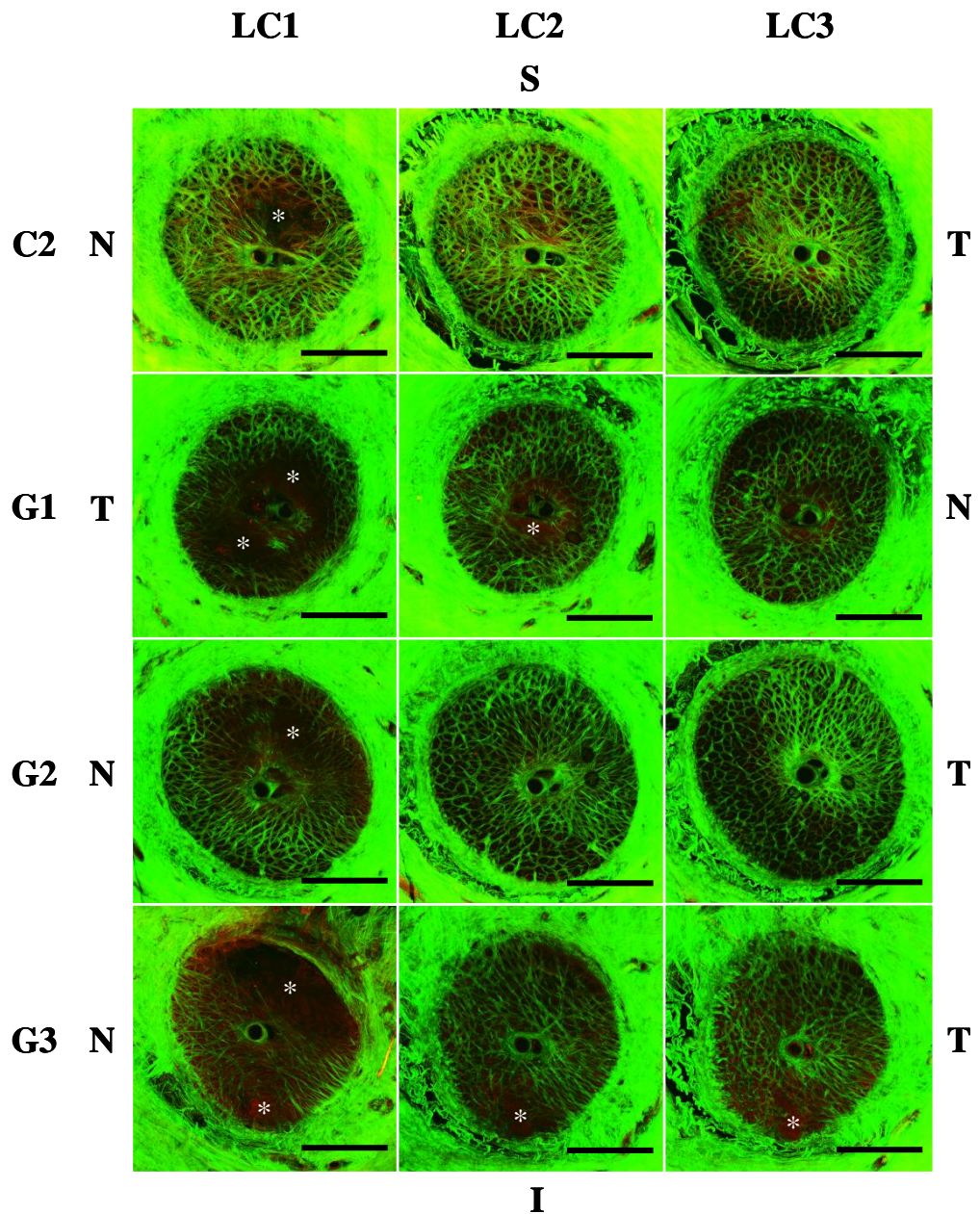
Figure 5.1. Maximum intensity projections of 3D tiled images of the glaucomatous human LC depicting nonlinear signals (SHG = green, TPEF = red) from 3 LC sections (LC1-LC3) of 3 glaucomatous (G1-G3) and 1 age-matched control (C2) donor ONHs. Regions of minimal connective tissue, which may be attributed to LC cupping, are highlighted with an asterisk. The glaucomatous LCs contained larger regions of minimal connective tissue content than the control. S = superior, T = temporal, I = inferior, N = nasal. Scale bars: 1000μm

5.3.2 Comparisons of Degree of Fibre Alignment between Glaucomatous and Age-matched Control Donor Optic Nerve Head Regions at the level of the Lamina Cribrosa

High variation in DOFA occurred within the glaucomatous and age-matched control LCs (Figure 5.2). Pockets of higher DOFA were found in the inferior-temporal LC quadrant within the majority of LC sections which appeared to be more aligned in the glaucomatous sections (Figure 5.2).

In all donors (G1-G3 and C1-C3) the highest DOFA was found in the peripapillary sclera > insertion region > LC (Figure 5.3). Inter-sample variability was higher between the control samples than between the glaucoma donor samples.

G1 LC DOFA was significantly lower than 2 control samples (C1 and C2), but not significantly different from the third control sample (C3) (Figure 5.3A). Fibre bundles were significantly more aligned in G2 and G3 LCs than C1 and C3, but had significantly lower alignment than those of C2.

Within the insertion region, glaucoma samples G1 and G2 demonstrated a significantly higher DOFA than the controls, with exception of C2 which was not significantly different from G2. G3 insertion region was significantly more aligned than C1 and C3 but significantly less aligned then C2 (Figure 5.3A).
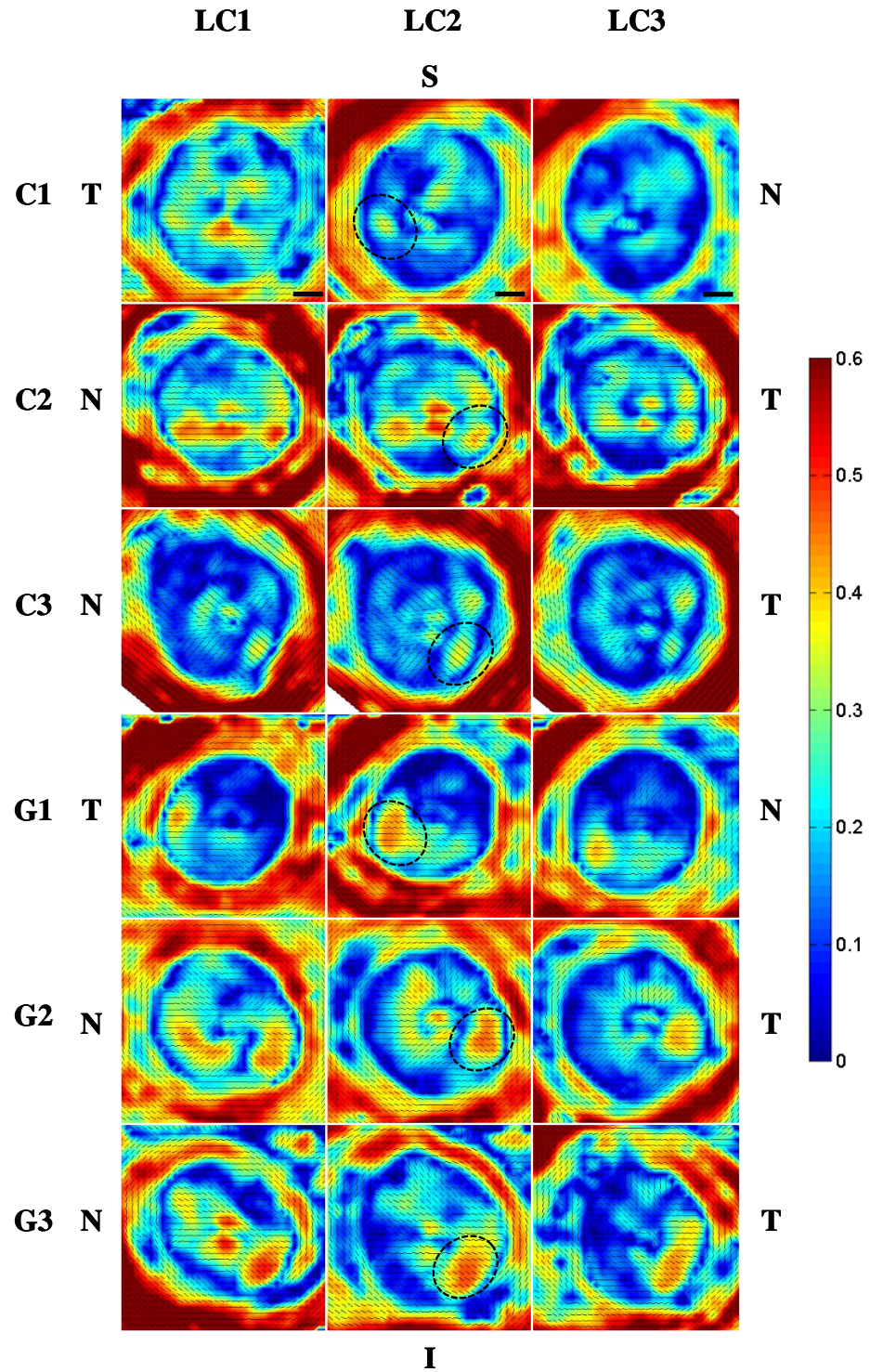
Figure 5.2. SALS fibre maps of glaucomatous and control LC sections. SALS DOFA (blue: low alignment – red: high alignment) and PFO (small black lines) fibre maps from 3 LC sections (LC1-LC3) of 3 glaucomatous (G1-G3) and 3 age-matched control donor ONHs (C1-C3). Note the region of high fibre alignment in the inferior-temporal quadrant in the majority of sections (examples from each donor are circled) which appear higher in the glaucomatous sections. S = superior, T= temporal, I = inferior, N = nasal. Scale bars: 500μm.

The peripapillary sclera of all glaucoma samples were significantly less aligned than the peripapillary sclera of C2 and C3. However, when compared to C1 DOFA, peripapillary sclera was significantly more aligned in G1, less aligned in G3 and not significantly different in G2 (Figure 5.3A).
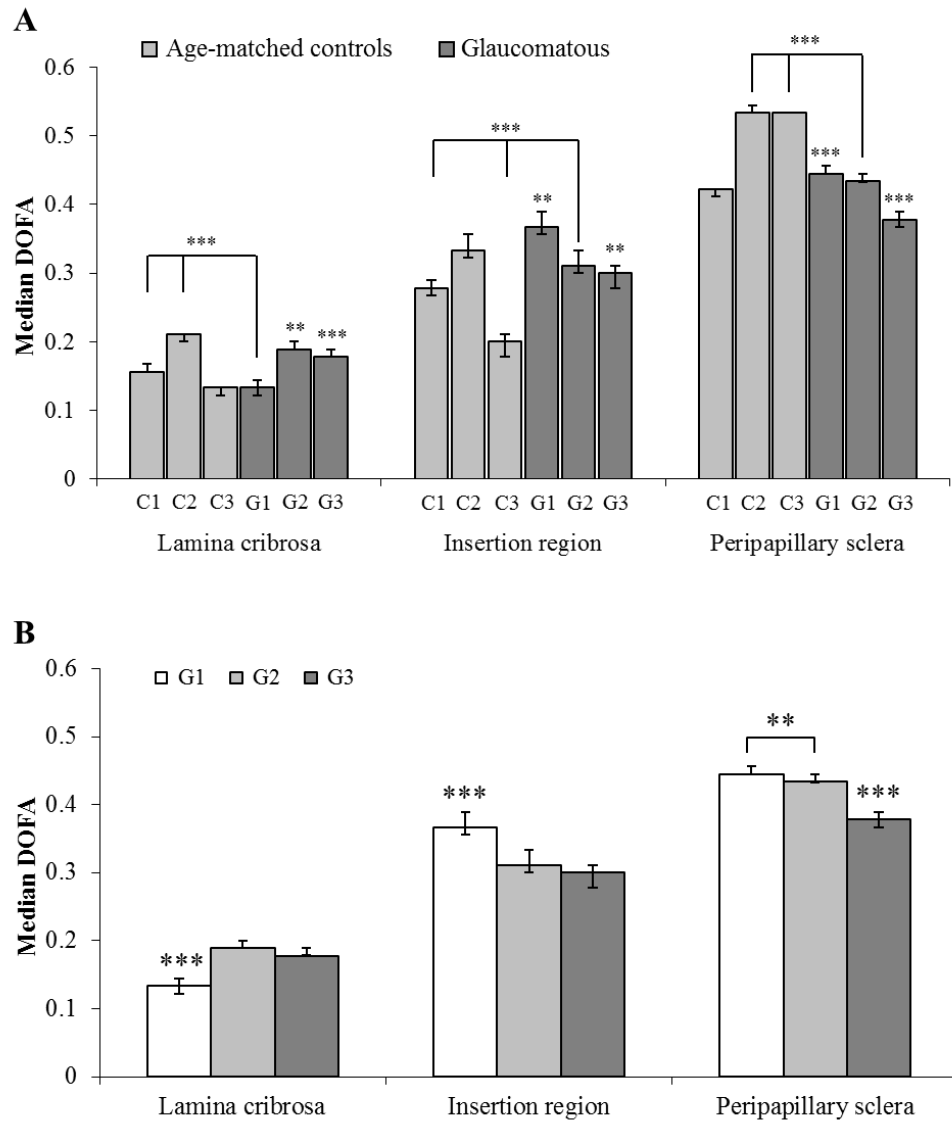
Figure 5.3. Comparisons of glaucoma and age-matched control DOFA. Median DOFAs (+/- 95% confidence intervals) were compared from the LC, insertion region and peripapillary sclera of (A) glaucomatous (G1-G3, dark grey) and age-matched controls (C1-C3, light grey) and (B) between glaucomatous donors. Significant differences were determined using the Mann-Whitney U test ((A), **p<0.01, ***<0.001; (B), Bonferroni adjusted, *p<0.0033, ***p<0.0003).

When comparing DOFA amongst the glaucoma samples, the mild glaucomatous sample (G1) had significantly lower LC DOFA but higher insertion region DOFA than the unknown (G2) and advanced (G3) glaucomatous samples (Figure 5.3B). Peripapillary sclera DOFA was significantly highest in G1 > G2 > G3.

5.3.3 Comparisons of Degree of Fibre Alignment between Glaucomatous and Age-matched Control Donor Lamina Cribrosa Regions

Significant differences between the glaucomatous and control sections DOFAs were observed in the majority of LC regions (Figure 5.4).

There were few similarities in the pattern of glaucoma and control regional differences between the glaucomatous samples (Figure 5.4). Interestingly, the regions within the inferior-temporal glaucoma LC demonstrated significantly higher DOFA than the equivalent region in controls throughout the LC depth in the majority of G1 and G2 sections (Figure 5.4A,B) and in all G3 sections (Figure 5.4C).
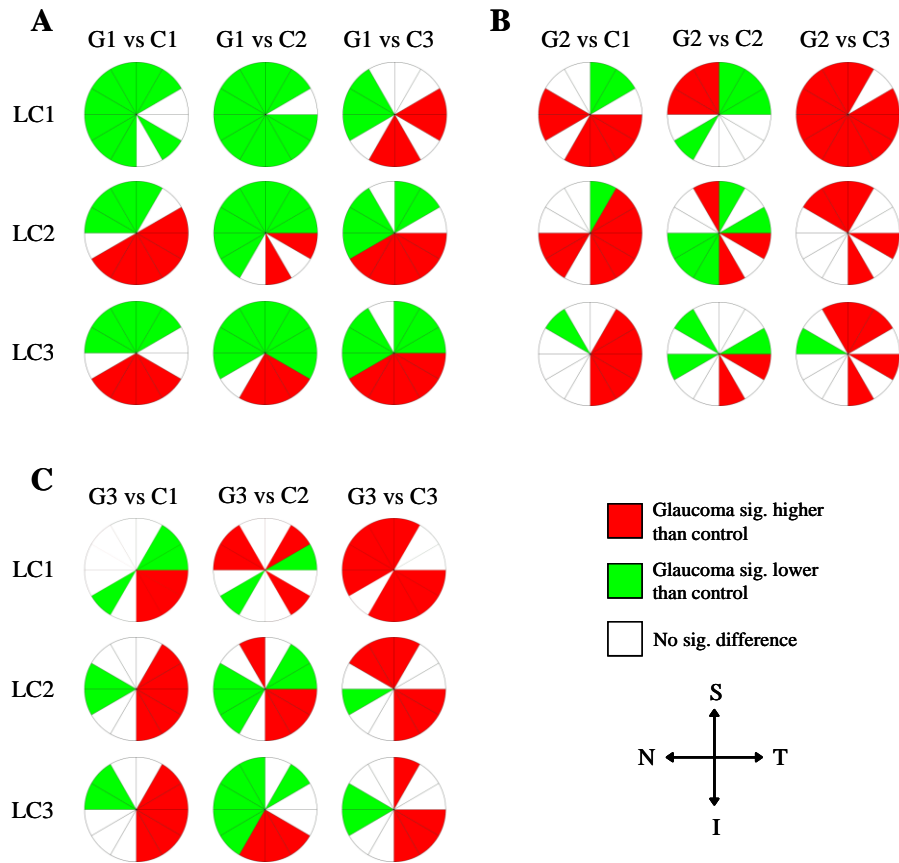
Figure 5.4. Differences in DOFA in the glaucomatous (G1 (A), G2 (B) and G3 (C)) and control LC (determined using the independent sample t test or Mann-Whitney U test; $p<0.05$). Red: glaucoma DOFA > control DOFA. Green: glaucoma DOFA < control DOFA. S = superior, T= temporal, I = inferior, N = nasal.

5.3.4 Comparisons of Preferred Fibre Orientation in Glaucoma and Age-matched Control Lamina Cribrosa

Significant differences were observed between the PFO distributions of the glaucomatous and control samples in the majority of LC regions throughout the LC depth (Figure 5.5).
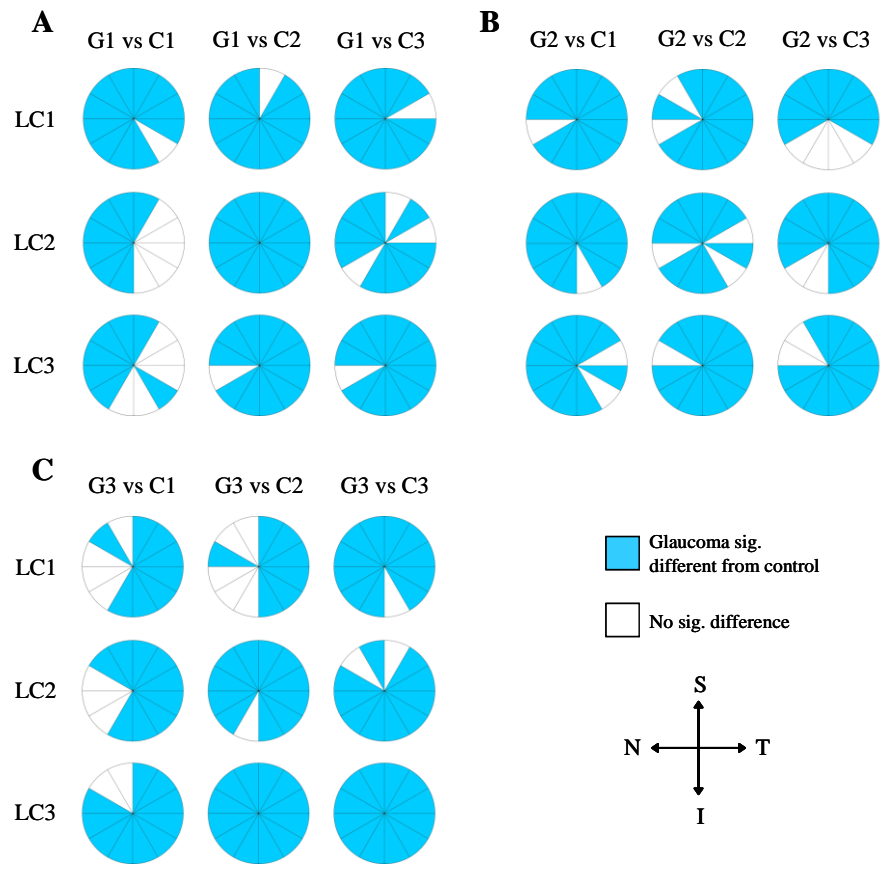
Figure 5.5. Differences in PFO distribution in the glaucomatous (G1 (A), G2 (B) and G3 (C)) and control LC (determined using the Mardia-Watson-Wheeler test; p<0.05). Blue: Glaucoma significantly different from control. S = superior, T= temporal, I = inferior, N = nasal.

Significant differences in PFO distributions were also identified between control sections (0).

In all LC sections there were a larger number of horizontal PFOs compared to vertical PFOs (Figure 5.6A). G3 contained a higher ratio of horizontal to vertical PFOs > G2 > G1 (Figure 5.6B). The glaucoma horizontal to vertical PFO ratios were similar to C1 and C2 but substantially lower than C2.
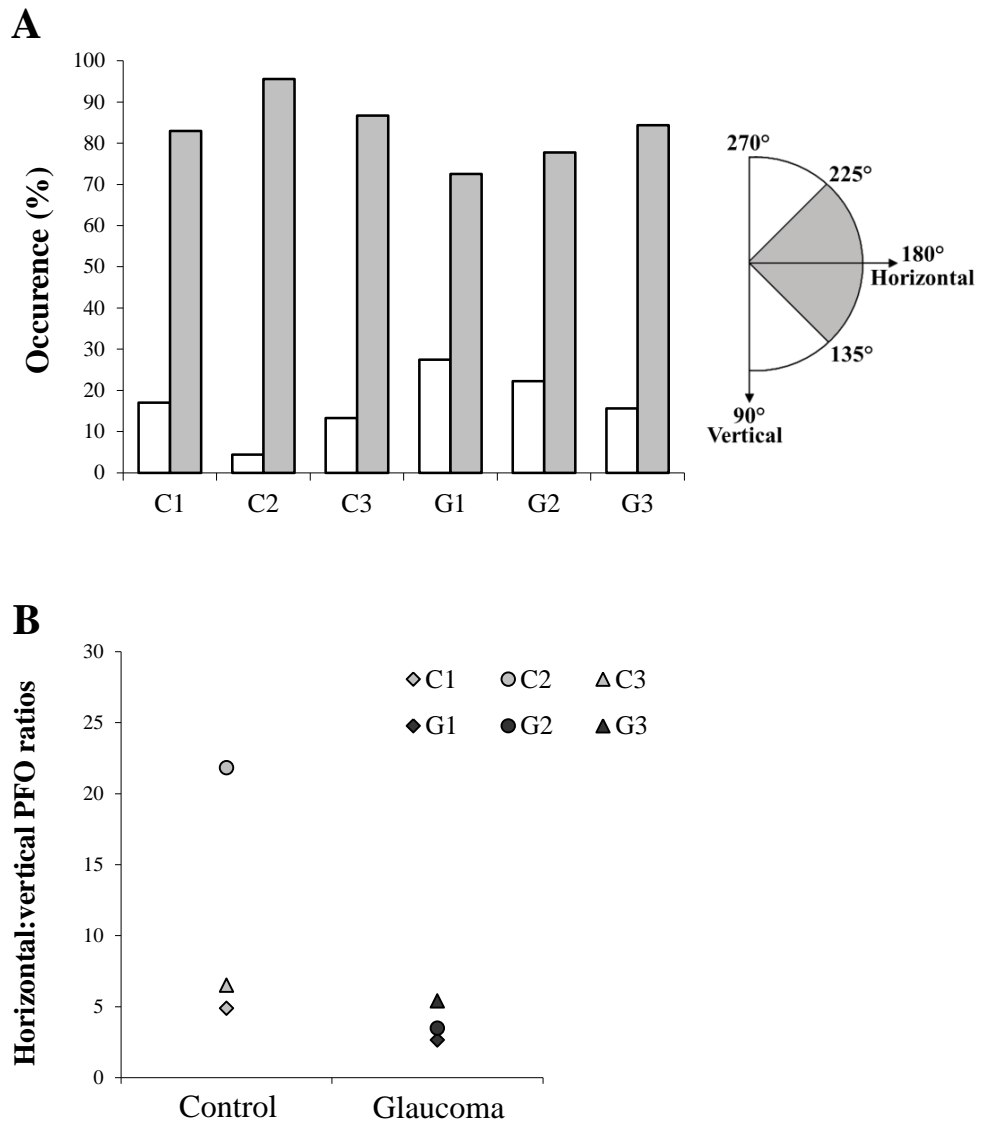
Figure 5.6. (A) Percentage occurrence and (B) ratio of horizontally (angles 135°-225°; grey bars) and vertically (angles 90°-135° and 225°-270°; white bars) orientated PFOs in transverse sections through the LC of control (C1-C3) and glaucoma (G1-G3) ONHs. In all LCs the majority of fibre bundles were horizontally inclined.

5.4 Discussion

The glaucomatous remodelling of the LC (Quigley et al., 1981, Quigley et al., 1983, Yang et al., 2007, Roberts et al., 2009, Yang et al., 2011a), a consequence of axonal loss and IOP elevation, is believed to contribute to the pathogenesis of glaucoma (Burgoyne et al., 2005, Downs et al., 2011). The aim of the current study was to determine if

glaucomatous ONH changes include an alteration in connective tissue fibre bundle degree of anisotropy and orientation.

Significant differences in DOFA occurred in the majority of glaucoma LC sections compared to control. However, due to the physiological inter-control variation, the directions of the differences were not consistent. The mild glaucomatous LC was significantly less aligned than the advanced glaucomatous LC. This increase in anisotropy in the advanced glaucomatous LC may be a direct result of IOP increase, such that alignment resists deformation, or perhaps a downstream LC remodelling effect caused by synthesis of new and possibly abnormal connective tissue components (Hernandez et al., 1994a, Hernandez et al., 1994b) due to altered gene expression in and activation of LC cellular components (Hernandez, 2000, Hernandez et al., 2000, Agapova et al., 2003, Kirwan et al., 2005, Johnson et al., 2007, Ebneter et al., 2010). The increased anisotropy may be a consequence of, or even contribute to the increased stiffening of the LC connective tissue which has been observed with progression of glaucomatous damage (Zeimer and Ogura, 1989).

A pocket of higher DOFA, observed in the inferior-temporal LC quadrant in the majority of samples, was significantly more aligned in glaucomatous LCs. The inferior-temporal LC has previously been shown to contain the most glaucomatous focal defects (Kiumehr et al., 2012) and is the most common site of optic disc haemorrhages in glaucoma (Siegner and Netland, 1996). Glaucomatous neuroretinal rim loss has also been shown to be more pronounced at the inferior-temporal disc margin (Caprioli and Sears, 1986, Jonas et al., 1993, Garway-Heath and Hitchings, 1998). Further investigation is needed to determine whether the increase in inferior-temporal anisotropy in the glaucomatous LC is the cause or result of glaucomatous damage. This

158

area of high alignment may provide effective axonal support during normal physiological conditions, but may become structurally detrimental during or following elevated IOP. Glaucomatous changes in connective tissue composition, distribution and compliance (Tengroth and Ammitzbøll, 1984, Zeimer and Ogura, 1989, Hernandez et al., 1990, Morrison et al., 1990, Quigley et al., 1991a, Quigley et al., 1991b, Fukuchi et al., 1992, Hernandez, 1992, Fukuchi et al., 1994, Pena et al., 1998) may also exacerbate structural failure within this region with disease progression.

Roberts et al. (2009) found that predominant LC beam orientation was not significantly affected in ocular-hypertensive monkey eyes. Using circular statistics, significant differences in PFO distribution were found between the majority of glaucomatous and age-matched control LC regions in the current study but these differences extended beyond the effect of disease and were most probably due to inter-donor variation and sensitivity of the tests used. The ratio of horizontal to vertical orientated fibre bundles was less variable and slightly lower in diseased LCs implying an increase in number of vertically orientated fibre bundles in glaucoma. However an increased sample number is needed to confirm these findings.

The anatomy of the sclera has been shown to play a significant role in the eyes response to IOP (Norman et al., 2011, Coudrillier et al., 2013) with possible glaucomatous changes in scleral thickness (Downs et al., 2001, Coudrillier et al., 2012) and material properties (Girard et al., 2011b) . The current study found that differences between glaucomatous and control peripapillary scleral DOFA did not exceed inter-control variation. This finding was analogous to the LC DOFA results. However, a slight trend of lower peripapillary scleral DOFA in the glaucomatous samples than control samples was observed. With regards to disease stage, the advanced glaucomatous peripapillary

sclera was significantly less aligned than the mild glaucomatous peripapillary sclera. Pijanka et al. (2012) found a reduced fibre anisotropy in glaucoma compared to non-glaucoma in the superior-temporal and inferior-nasal peripapillary sclera and postulated that the differences may either be a response to glaucoma or possibly associated with glaucoma predisposition. The decrease in anisotropy in the advanced glaucomatous peripapillary sclera and insertion region, as witnessed here, may be a late stage example of tissue remodelling or a compensatory mechanism as a result of changes in connective tissue composition(Quigley et al., 1991b, Downs et al., 2005, Girard et al., 2011b, Yang et al., 2011b). Further analysis and an increase in sample size are needed to confirm regional changes in DOFA and PFO in the glaucomatous sclera.

5.5 Conclusion

The inferior-temporal LC quadrant showed a significantly higher fibre bundle alignment in the glaucomatous tissue when compared to control which may account for the LC defects reported in this area. The advanced glaucomatous sample contained significantly more aligned connective tissue fibres in the LC and less aligned insertion region and peripapillary sclera than the mild glaucomatous sample. This implies that the ONH fibre architecture continues to change during glaucoma progression. Further investigations with a larger sample number are needed to fully understand glaucomatous remodelling or possible ONH geometries related to glaucoma susceptibility.

Chapter 6 - X-ray Microtomography: Future Potential in 3D Optic Nerve Head Imaging

6.1 Introduction

Although sectioning of biological tissues is essential for some staining protocols and imaging techniques, the use of histological sections for structural 2D measurements is subject to inaccuracies caused by an oblique sectioning angle or section deformation. The methodology used in chapter 2 highlighted the advantages of 3D analysis of the ONH but relied on highly complex, time consuming computational processes to reconstruct the non-linear microscopy datasets of ONH histological sections. Therefore, the potential of X-ray microtomography (XMT) was assessed in the current chapter as an additional 3D imaging tool.

XMT is a miniaturised version of X-ray computed axial tomography (CAT) scanning which, unlike CAT scanning, can resolve structures at a micrometre level by increasing X-ray dosage and exposure (Davis and Wong, 1996). XMT was first described by Elliott and Dover (1982) and was used to quantify X-ray linear attenuation coefficients (LAC) in small, biological, hard tissue. Since the first generation systems XMT has moved away from accurate quantification of LAC and is now primarily used for imaging and structural quantification of small specimens (Davis et al., 2010).

OBJECTIVES

- To create a 3D dataset of the connective tissue structure of the human optic nerve head using X-ray microtomogaphy

- To identify and segment structures within the 3D optic nerve head to assess regional variation within the lamina cribrosa

6.2 **Materials and Methods**

6.2.1 **Tissue Preparation**

A single eye, from a 90 year old male donor, fixed in 4% PFA and was orientated as previously described in section 2.2.1. The ONH surrounded by a block of sclera was dissected. The ONH tissue block was immersed in 30% ethanol (Sigma-Aldrich, UK) (volume/volume with distilled water) for 2 hours, 50% ethanol for 2 hours and 70% ethanol for 2 hours. After dehydration the tissue block was immersed in 2% phosphotungstic acid (PTA, Sigma-Aldrich, UK; weight/volume in distilled water) in 70% ethanol for 4 days. PTA binds various proteins and connective tissue (Hayat, 1970) and has been previously shown to provide good contrast when using XMT to image soft tissues (Metscher, 2009). The tissue block was then washed in 70% ethanol for 1 hour and placed in a trimmed, polypropylene pipette tip which was filled with 100% ethanol and sealed with epoxy putty (Wickes, UK) (Figure 6.1).
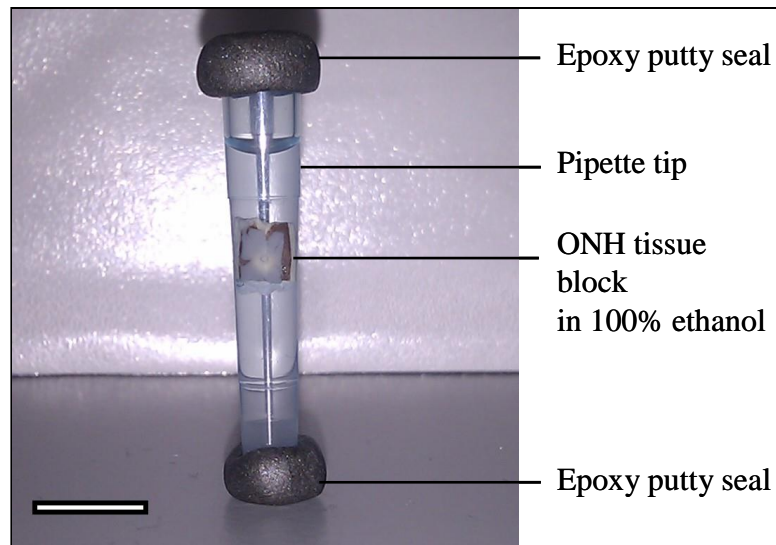
Figure 6.1. Dissected ONH, from a 90 year old donor, in 100% ethanol in a sealed sample holder prepared for XMT imaging. Scale bar = 10mm

6.2.2 X-ray Microtomography

XMT was carried out by Dr. Graham Davis and Dr. David Mills at the Institute of Dentistry, Queen Mary University, London. The XMT apparatus used in this current study was the MuCAT 2 scanner, described previously by Davis and Elliott (1997) and Davis et al. (2010), which has been previously used to image hard tissues such as teeth (Wong et al., 2006) and bone (Potter et al., 2006). The X-ray source used was an X-TEK HMX system (X-TEK Systems Ltd, UK) operating at 90kV and 200μA. The sample was mounted onto a kinematic stage and data were collected using a time-delay integration CCD camera which eliminated ring artefacts by averaging the characteristics of all of the detector elements in each projection (Davis and Elliott, 1997). Over a period of 4h and 44min, 601 projections (330 by 484 pixels) of the ONH were acquired. The data were reconstructed using an in-house, cone-beam back-projection algorithm to form a grey-scaled 3D dataset with dimensions of $4.95 \times 4.95 \times 7.26 \text{ mm}^3$ (Figure 6.2).
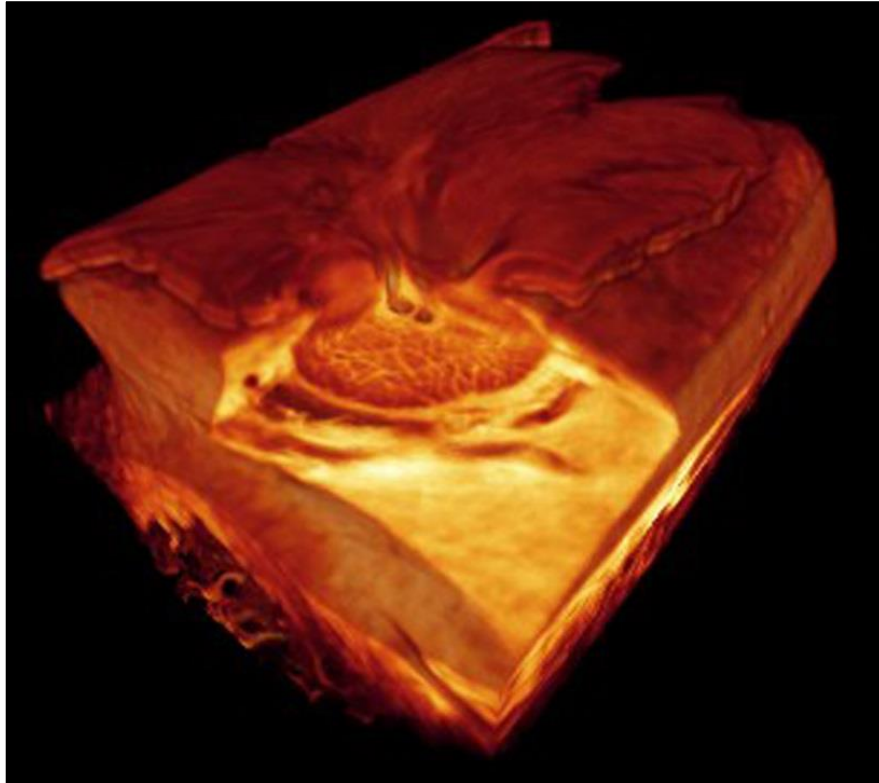
Figure 6.2. Volume rendered XMT ONH dataset. A corner cut in the volume rendered ONH shows the position of the LC within the ON canal.

6.2.3   Analysis of Lamina Cribrosa Structural Parameters

6.2.3.1   Lamina Cribrosa Segmentation

Visualisation, 3D rendering and segmentation of the XMT ONH dataset were carried out in Amira® software (version 5.4.1, Visualization Sciences Group, Germany). The area of the canal that encompassed the LC (i.e. LC volume) and the connective tissue of the LC were manually segmented in each image slice using the brush tool in the Amira® segmentation editor (Figure 6.3A,B). The segmented areas of interest were saved as 8-bit binary image stacks. The LC connective tissue image stack was then inverted in order to identify the LC pores (Figure 6.3C). The central retinal vessels were included in the total LC volume and excluded from the LC connective tissue and pore segmented datasets.

164
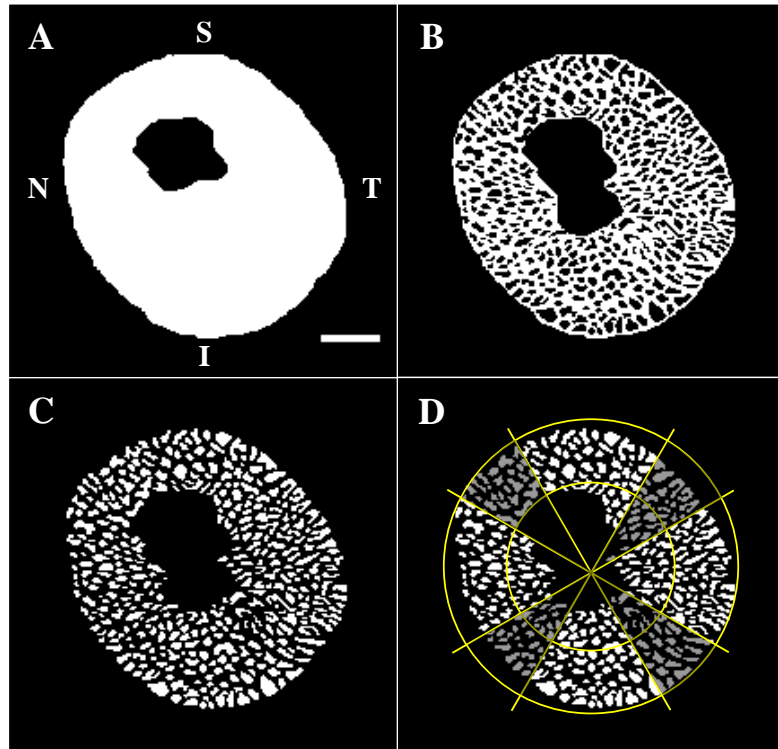
Figure 6.3. Segmented (transverse) binary images of a single slice through the XMT ONH dataset. (A) The ON canal at the LC, (B) connective tissue of the LC beams and (C) LC pores in a single slice of the XMT ONH dataset. (A) A small LC cup is indicated as a black hole and (B-D) the additional central exclusion hole denotes the position of the central retinal vessels. (D) The ON canal was split into inner and outer LC and superior, temporal, inferior and nasal polar quadrants for regional analysis. S = superior, T = temporal, I = inferior, N = nasal. Scale bar: 500μm

6.2.3.2   *Lamina Cribrosa Surface Reconstruction*

Anterior and posterior surfaces of the LC volume were constructed using the landmark tool and PointWrap module in Amira[®]. Using the binary segmented LC volume, multiple landmarks were placed along the anterior and posterior LC surfaces at 12º intervals around the centre of the ON canal. The anterior and posterior LC surface landmarks were then reconstructed into two surfaces using the PointWrap module, allowing for the analysis of the anterior and posterior LC surface area, before being combined to form a continuous surface that enclosed the LC volume (Figure 6.4).
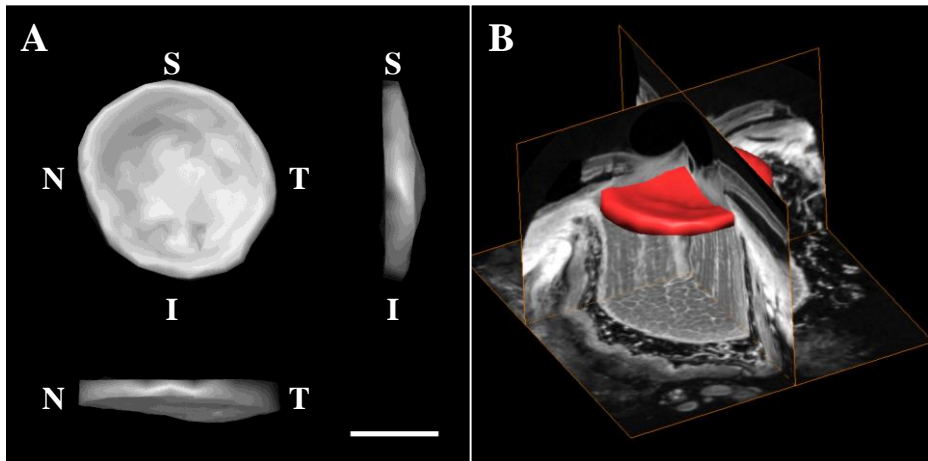
Figure 6.4. Segmented LC volume. (A) LC volume viewed in XY, YZ and XZ orientations. (B) Position of the LC volume in the XMT ONH dataset. S = superior, T = temporal, I = inferior, N = nasal. Scale bar: 1mm

6.2.3.3 *Analysis of Lamina Cribrosa Thickness*

The dataset scale (1 pixel = $15\mu m^2$) was entered into Amira® and the software's 2D ruler was used to measure regional LC thickness at the superior, temporal, inferior and nasal poles in three sequential longitudinal image slices containing the central retinal vessels (Figure 6.5).
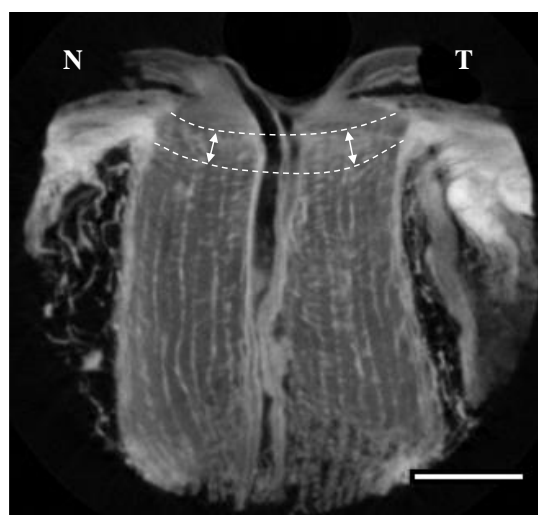
Figure 6.5. LC 2D thickness measurements in XMT ONH image slices. Regional LC thicknesses (arrows) were measured from the anterior to posterior LC boundaries (dotted lines) N = nasal, T = temporal. Scale bar: 1000µm

A 3D LC thickness map was generated from the LC volume enclosed between the combined anterior and posterior surfaces using the Amira® SurfaceThickness module. This function computed the perpendicular distances between opposite surface faces and was used to visualise regional LC thickness.

Anterior and posterior LC surface areas and LC volume was also calculated using the Amira® MaterialStatistics module.

6.2.3.4 Lamina Cribrosa Connective Tissue and Pore Parameters

Connective tissue content and pore parameters were quantified from their representative segmented binary image stacks using the Analyse Particles function in ImageJ (version 1.45s (http://rsb.info.nih.gov/ij)). Connective tissue content, calculated as a percentage of total area, was determined for each transverse image slice enabling the determination of connective tissue content as a function of LC depth, whilst accounting for the bowed nature of the LC. Average pore area and the number of pores (i.e. pore counts) per LC slice were also quantified as a function of LC depth.

To compare regional variation in LC connective tissue content and pore parameters, the ON canal was split into inner and outer regions and also superior, temporal, inferior and nasal quadrants (see Figure 6.3D). The canal was first split into 12 radial sectors; the 2 most polar sectors were then combined to form 4 regional quadrants. To ensure no data overlap between the 4 quadrants, data in sectors between the quadrants were excluded from the analysis. Partial pores that fell on the borders of the inner, outer and regional LC regions were also excluded from the analysis.

6.3 Results

The PTA contrast agent effectively differentiated the ONH connective tissue from the neuronal tissue and blood vessels (Figure 6.6), enabling the distinction between the prelamina (Figure 6.6B), LC (Figure 6.6C) and postlaminar ON (Figure 6.6D).
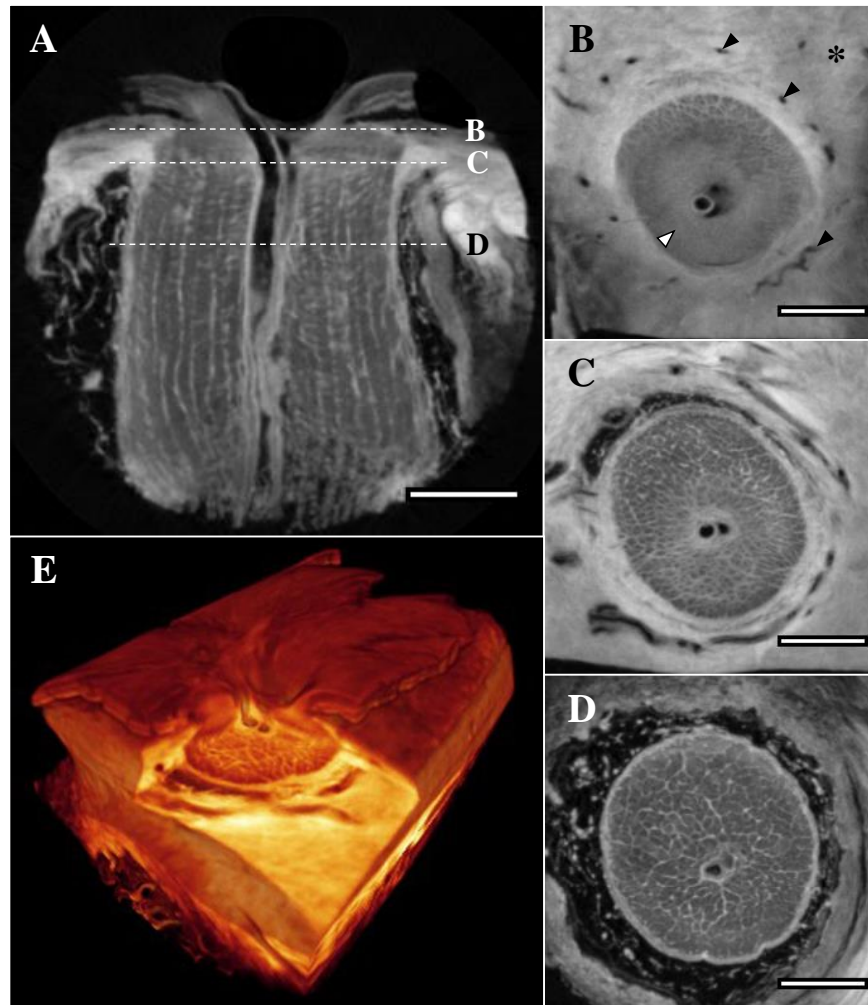
Figure 6.6. XMT of the prelamina, LC and postlaminar ON. (A-D) 2D XMT image slices and (E) volume rendered 3D reconstruction of an ONH tissue block from a 90 year old donor. The PTA contrast agent effectively differentiated the connective tissue (high intensity signal within the sclera (*) and LC beams) from the neuronal tissue (medium intensity signal within the prelamina neural canal (white arrow heads), LC pores and ON bundles) and blood vessels (very low intensities, black arrow heads). Transverse image slices through the (B) prelamina, (C) LC and (D) postlaminar ON: position of image slice is represented as dotted lines in (A) a longitudinal ONH view. (E) A corner cut in the volume rendered ONH shows the position of the LC within the ON canal. Scale bars: 1000μm

6.3.1 Thickness, Surface Area and Volume of the Lamina Cribrosa

The 2D mean regional LC thickness, as determined from 2D measurements of ONH image slices was 280.82µm (±31.37). This was comparable to the mean LC thickness calculated from the 3D segmented LC volume: 279.35µm (±89.82).

The temporal LC region appeared thickest (306.14µm (±34.54)), followed by the nasal (266.13µm (±10.14)), inferior (255.16µm (±13.65)) and superior (239.92µm (±17.90)) regions (Figure 6.7A) in the 2D image slices.
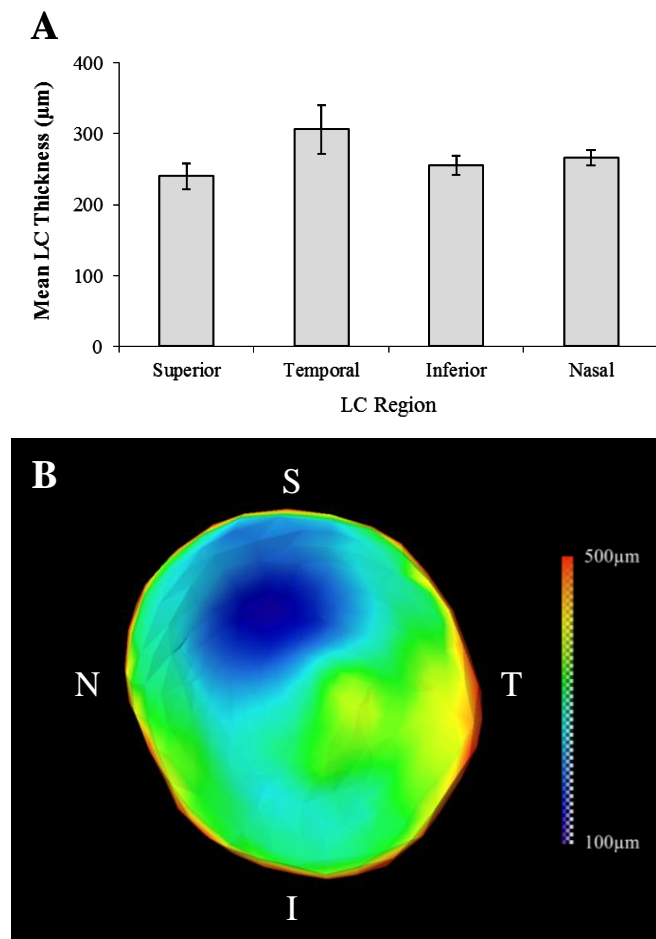
Figure 6.7. Regional LC thickness as measured from (A) 2D image slices and (B) represented in a 3D thickness map. Note that in both plots the thinnest LC region is the superior quadrant and the thickest LC region is the temporal quadrant. Error bars represent 1 standard deviation of three 2D thickness measurements per LC region. S = superior, T = temporal, I = inferior, N = nasal

Regional variation was also apparent in the segmented LC volume and is demonstrated in the resultant LC thickness map (Figure 6.7B). The LC appeared to be thinnest within a small pocket of the superior region, thicker in the temporal region and thickest at the periphery of the ON canal (Figure 6.7B).

The anterior LC surface area was calculated as $3.99mm^2$, 1.22% smaller than the posterior LC surface area of $4.05mm^2$. The total LC volume was $1.06mm^3$.

6.3.2 Connective Tissue Content within the Lamina Cribrosa

Connective tissue content, calculated as a percentage of LC volume containing connective tissue, was 68.80%. LC connective tissue content was slightly higher in the inner LC (70.71%) than in the outer LC (67.37%). Connective tissue content as a function of LC depth did not appear to alter (Figure 6.8A), although an apparent trend towards an increase in connective tissue content was identified in the outer LC (Figure 6.8B).

Regional LC connective tissue content showed little variation and was greatest in the temporal quadrant (71.54%), followed by nasal (70.84%) > superior (69.16%) > inferior (67.52%) quadrants (Figure 6.8D).
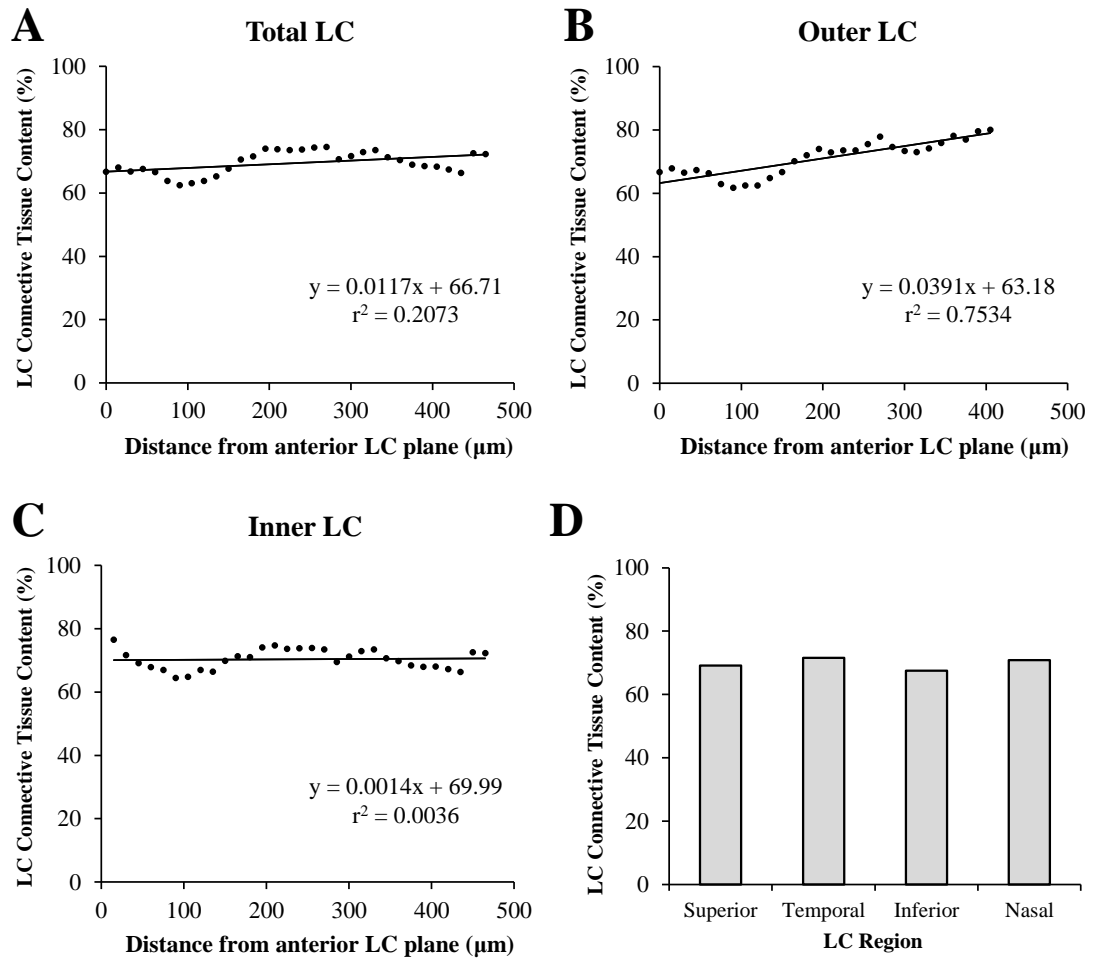
Figure 6.8. Connective tissue content from the anterior to posterior LC (A) the LC, (B) outer LC and (C) inner LC and (D) within the 4 LC regions. Connective tissue content did not vary as a function of LC depth, however a potential trend was observed in the (B) outer LC. (D) Connective tissue content was greatest in the temporal LC region. Lines show linear best fit.

6.3.3 Average Pore Area within the Lamina Cribrosa

Average pore area appeared to decrease from anterior to posterior LC up to 250μm and thereafter remained constant (Figure 6.9A). A similar trend was found in the outer LC region (Figure 6.9B). However, in the inner LC average LC pore area appeared to be relatively consistent through the LC depth with a slight decrease in the mid LC (Figure 6.9C).
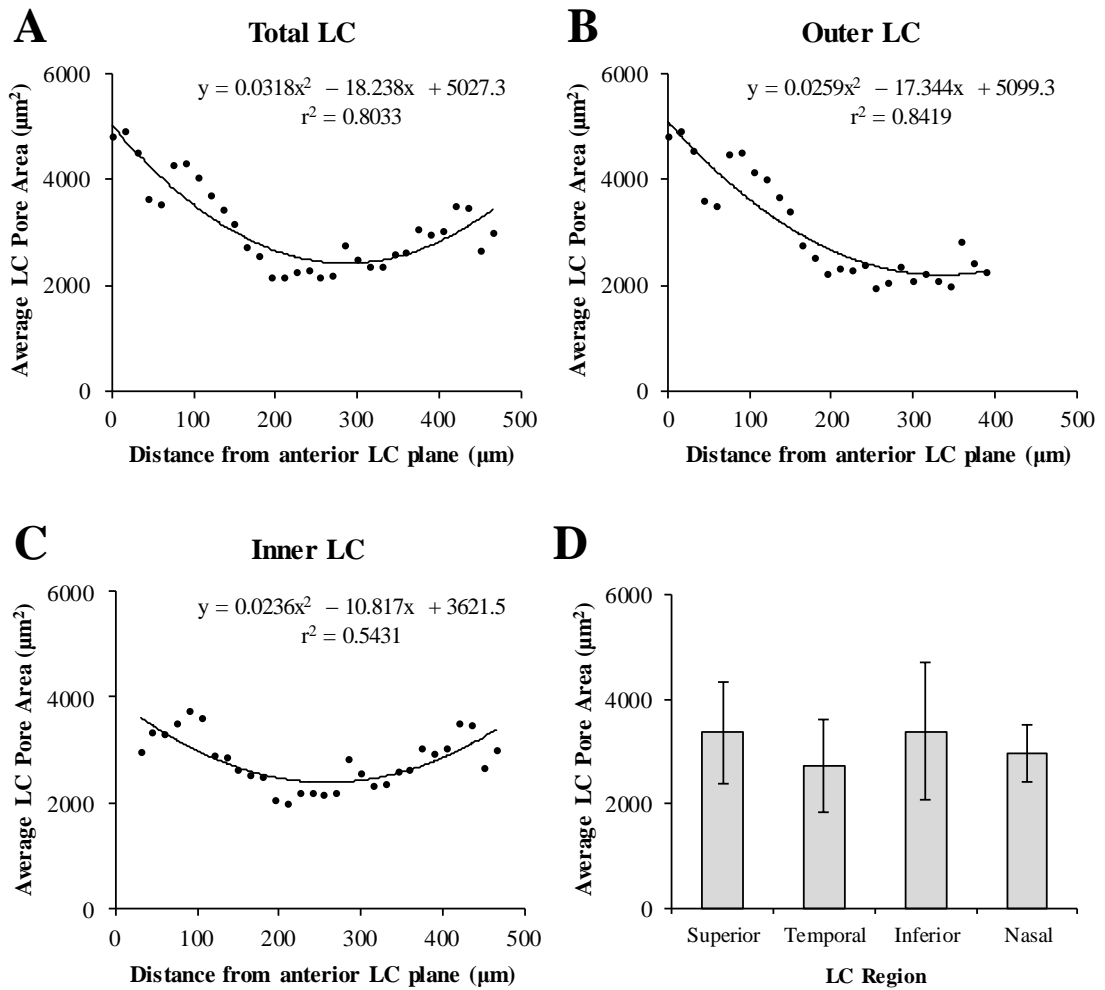
Figure 6.9. Average pore area from the anterior LC plane in (A) the whole LC, (B) outer LC and (C) inner LC and (D) within the 4 LC regions. A decrease in average pore area was more pronounced in the outer LC than inner LC and average pore area was greatest in the inferior LC region. Lines of best fit are fitted second order polynomials. Error bars in (D) represent 1 standard deviation of regional average pore area.

The average pore area was larger in the outer LC (3053.81μm (±1004.50)) than in the inner LC (2781.2μm (±499.92). Regionally, LC pore area was in the order of highest in the inferior quadrant > superior > nasal > temporal (Figure 6.9D).

6.3.4 Pore Counts within the Lamina Cribrosa

Pore counts, as a measure of the number of pores per unit area, increased from anterior to mid LC depth, before decreasing towards the posterior LC (Figure 6.10A). Similar

trends in pore counts were apparent in the outer (Figure 6.10B) and inner (Figure 6.10C) LC.
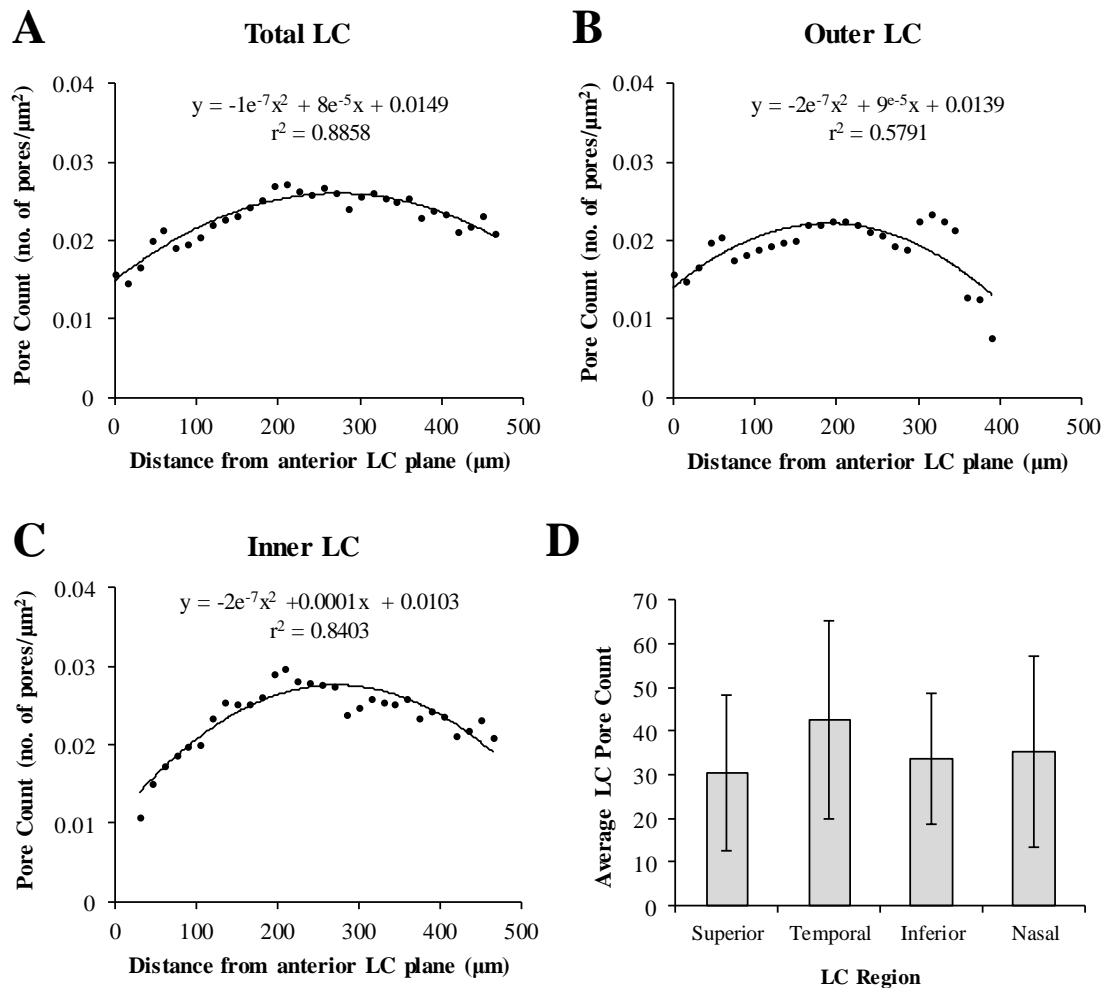
Figure 6.10. The ratio of LC Pore counts to LC area from the anterior LC plane in (A) the whole LC, (B) outer LC and (C) inner LC and (D) average LC pore count in the 4 LC regions. The LC pore counts per LC area increased until the mid LC depth, and then decreased towards the posterior LC. Lines of best fit are fitted second order polynomials. Error bars in (D) represent 1 standard deviation of regional average pore count.

The average pore counts were comparable between the outer LC and inner LC and were 114.78(±87.60) and 115.83(±50.99), respectfully. Average regional LC pore count was highest in the temporal quadrant > nasal > inferior > superior (Figure 6.10D), which was inverse to the average regional LC pore area results.

6.4 **Discussion**

Assessment of the LC connective tissue and pore distribution has been the focus of a large body of research (Quigley and Addicks, 1981, Radius and Gonzales, 1981, Hernandez et al., 1987, Ogden et al., 1988, Morrison et al., 1989b, Jonas et al., 1991, Birch et al., 1997, Brown et al., 2007, Roberts et al., 2009, Winkler et al., 2010). Advances in ONH reconstruction (Birch et al., 1997, Burgoyne et al., 2004, Brown et al., 2007, Winkler et al., 2010) and *in vivo* ONH imaging (Srinivasan et al., 2008, Inoue et al., 2009, Lee et al., 2010, Park et al., 2012b) have allowed accurate quantification of ONH 3D structural parameters to be achieved.

In the current chapter, XMT was used to visualise and quantify the LC connective tissue and pore distribution regionally and through the LC depth without the need of histological sectioning. However, it is important to note that the technique did not provide the specificity or resolution that is associated with non-linear microscopy so should be treated as an adjunct and not a replacement 3D imaging technique if connective tissue fibres are required to be analysed in detail.

LC thickness and surface area results were comparable to those previously published (Jonas et al., 1991, Jonas et al., 2003, Jonas and Holbach, 2005, Kotecha et al., 2006, Ren et al., 2009, Winkler et al., 2010) though possible shrinkage of the tissue due to the dehydration steps during tissue processing may have caused the results presented here to be underestimated (Bacallao et al., 2006). A linear shrinkage factor, as used by Jonas et al. (1991), could be used in the future to correct for tissue shrinkage.

In the past, the thickness of the LC has predominantly been measured in 2D histological sections and confined to central versus peripheral ON canal regions (Jonas and Holbach,

2005, Kotecha et al., 2006, Ren et al., 2009), with the exception of Yang et al. (2007) who, akin to the current study, used landmarks to generate sclera and LC thickness maps of the monkey ONH. Measurements from histological sections without 3D reconstruction may be imprecise due to tissue folding or oblique sectioning angle. Therefore, the thickness calculated from the 3D human LC, as performed in the current study, may be a better representation of the structure *in vivo*.

In this study, it was found that the thinnest part of the LC was a pocket within the superior region and the temporal and peripheral LC contained the thickest parts. The majority of the translaminar pressure gradient has been shown to fall within the region of the LC (Morgan et al., 1995), and it is thought that a thinner LC increases the pressure gradient (Morgan et al., 2008). Therefore, alterations in the translaminar pressure gradient caused by elevation in IOP may be more pronounced in thinner LC regions, such as the superior region in the sample investigated in the current study. Such a finding has implications in regional glaucomatous axonal damage due to pathophysiological events that may include alterations in RGC axon transport and neurofilament properties (Minckler et al., 1977, Quigley et al., 2000, Balaratnasingam et al., 2007) and change in retinal venous pressure (Morgan et al., 1997).

The finding of a higher connective tissue content and pore count, but lower average pore area within the inner LC and the temporal and nasal LC when compared to the outer LC and superior and inferior LC, respectively, concurs with previous qualitative and quantitative findings in the human (Quigley and Addicks, 1981, Radius, 1981, Ogden et al., 1988, Jonas et al., 1991, Brown et al., 2007) and monkey (Roberts et al., 2009) ONH. It has been suggested that LC regions containing higher connective tissue content are better at resisting pressure related distortion (Albon et al., 1995, Winkler et

al., 2010). Therefore the lower connective tissue content in the peripheral LC, and superior and inferior LC may account for the distortion of peripheral pores (Brown et al. 2007), excavation of the anterior LC surface (Quigley et al., 1981, Quigley et al., 1983) and the subsequent pattern of visual field loss in glaucoma.

Ogden et al. (1988) found that LC pores at the level of the sclera were smaller than LC pores from the choroidal level. Our findings are consistent with this as a decrease in pore area and increase in pore number as a function of LC depth was highlighted within the anterior LC. The decrease in pore size towards the posterior LC and increase in connective tissue content in the outer LC may have implications in the axonal blockage that has been observed at the posterior LC in monkey eyes with increased IOP (Minckler et al., 1978) and axonal degeneration at the posterior LC in glaucomatous human eyes (Vrabec, 1976).

6.5 Conclusion

The results presented within this chapter reveal the potential of XMT in imaging, without the need of histological sectioning, the ONH in 3D. Contrasting the tissue with PTA enabled effective differentiation between the connective tissue and neural tissue within the ONH. Quantification of the segmented ONH dataset highlighted the regional variation in LC thickness, connective tissue content, pore area and count, all factors that are likely to have implications in a person's susceptibility to glaucomatous optic neuropathy. Future developments will include XMT imaging at a higher resolution, improving the contrasting protocol so to eliminate the tissue dehydration step, perhaps by experimenting with different contrasting agents that will highlight different ONH components other than connective tissue.

Chapter 7 - General Discussion
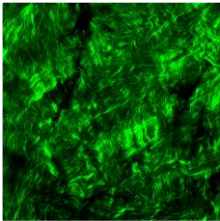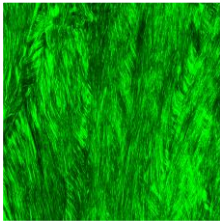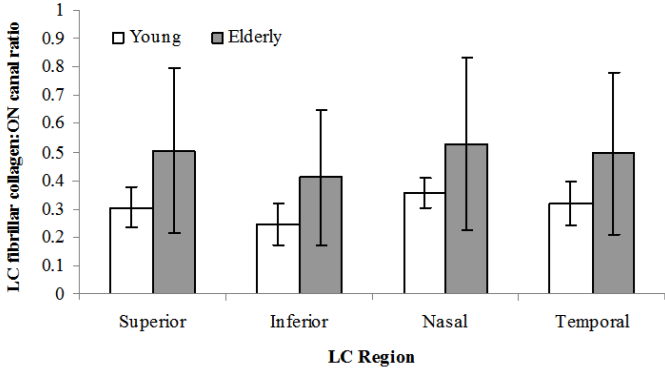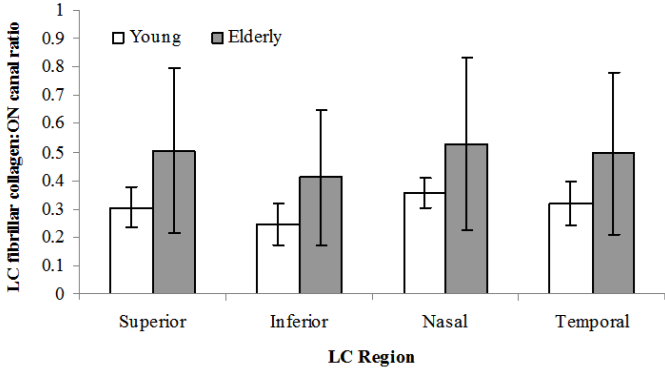
Glaucoma is predicted to afflict 79.6 million people by the year 2020 (Quigley and Broman, 2006) with the average cost of treatment during the lifetime of a single sufferer being £3001 in the UK (Rahman et al., 2013). Treatment of glaucoma currently focuses on delaying vision loss by lowering IOP (Heijl et al., 2002). Treatment steps for POAG include the use of topical medications, laser trabeculoplasty and incisional surgery (Heijl and Traverso, 2008).
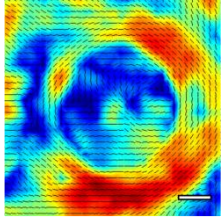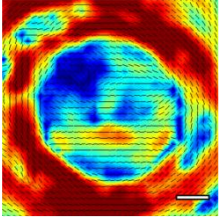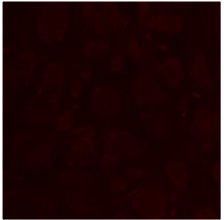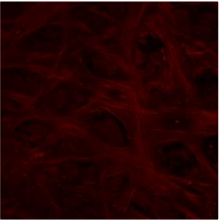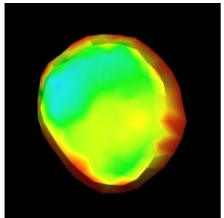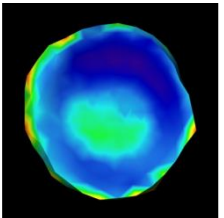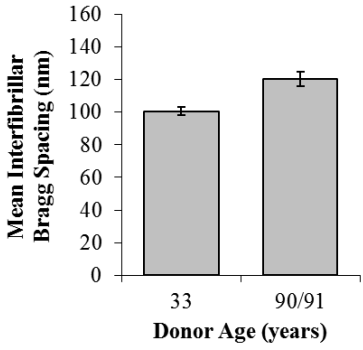
Potential treatment methodologies, independent of IOP reduction, relating to neuroprotection and regeneration of RGCs have been discussed (Baltmr et al., 2010, Wilson and Di Polo, 2012). However, retinal protection and axonal regeneration must take into account the complex mechanical and metabolic environment surrounding the RGC axons within the ONH, as they may be considered most vulnerable as they deviate, unmyelinated, through the LC (Morgan et al., 1998).

However, it appears that the ONH is designed for its purpose. The peripapillary sclera contained the highest degree of connective tissue alignment with connective tissue fibres aligned circumferentially around the ON canal. This well organised connective tissue distribution is thought to provide a protective mechanism in limiting IOP-related expansion of the ON canal and limit in-plane tensile strains (Girard et al., 2009a, Girard et al., 2009b, Grytz et al., 2011, Coudrillier et al., 2013). The relatively low aligned connective tissue meshwork within the LC, as viewed *en face*, and the radially orientated beams around the LC periphery may provide transverse reinforcement (Grytz et al., 2011) to an area which is considered a weak spot in the otherwise continuous

corneo-scleral shell (Downs et al., 2011). Interestingly, areas of highly aligned connective tissue fibres within the LC, such as those witnessed in the inferior-temporal LC quadrant, may predispose the ONH to glaucomatous focal defects (Kiumehr et al., 2012) and optic disc haemorrhages (Siegner and Netland, 1996) likely due to a decrease in regional LC structural compliance.

It is evident from the findings of this thesis that there are a number of differences between the young and elderly ONH connective tissue microarchitecture. The differences primarily relate to the presence of elastic fibres and fibrillar collagen content, alignment and spacing as summarised in Table 3.

	Young ONH	Elderly ONH	Potential Influence
SHG signal	Presence of fibrillar collagen crimp	No observable fibrillar collagen crimp	Increase in stiffness and decrease in compliance in the elderly ONH
3D reconstruction of SHG datasets	Lower relative fibrillar collagen content	Higher relative fibrillar collagen content	

SALS	Lower fibre alignment 	Higher fibre alignment 	Increase in stiffness and decrease in compliance in the elderly ONH
TPEF	No observable TPEF-related elastic fibres in the LC 	Presence of TPEF-related elastic fibres in the LC 	Elderly increase in TPEF-related elastic fibre cross-linking
3D reconstruction of SHG datasets	Thicker LC (as measured in 3D datasets) 	Thinner LC (as measured in 3D datasets) 	Increase in elderly translaminar pressure gradient
SAXS	Lower collagen interfibrillar Bragg spacing in peripapillary sclera 	Higher collagen interfibrillar Bragg spacing in peripapillary sclera	Increase in elderly fibre bundle size
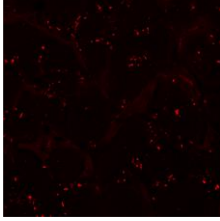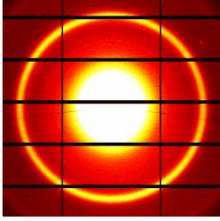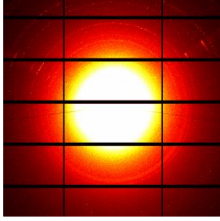
TPEF	No observable TPEF-related lipofuscin	Presence of TPEF-related lipofuscin	Indication of axonal degradation in elderly
SAXS	Presence of strong myelin diffraction patterns	Myelin diffraction patterns weak or absent	

Table 3. Summary of findings relating to age-related changes in the ONH.

Collagen and elastin have a slow tissue turnover rate and are therefore susceptible to alterations during the ageing process (Bailey, 2001). The slow tissue turnover rate suggests that collagen and elastin may accumulate within the LC throughout life.

Total collagen present in the LC, as a percentage of dry tissue weight, has been shown to increase from 20% in the young LC to about 50% in the elderly LC (Albon et al., 1995). Furthermore, collagen types I, III, IV (Hernandez et al., 1989, Hernandez and Neufeld, 1989, Morrison et al., 1989a) and VIII (Tamura et al., 1991) immunoreactivity have all been shown to increase with age.

The current study provides further evidence that fibrillar collagen increases within the LC during ageing. Within the elderly ONH, SHG-related fibrillar collagen appeared denser and was more aligned than in the young ONH. The elderly ONHs also contained a higher relative fibrillar collagen content than the young, however this did not reach

statistical significance. Another interesting observation in the current study was the crimped conformation of fibrillar collagen in the young ONH tissue which was absent in the elderly tissue. Within the elderly ONH, fibrillar collagen appeared straight within the peripapillary sclera and LC beams.

Elastin content within the LC also increases as a function of age. It has been shown to increase from 7% of dry tissue weight in the 0-9 year old LCs to 28% in the 80-89 year old LCs (Albon et al., 2000a). Hernandez (1992) revealed that newborn LCs contained aggregates of elastin associated microfibrils while adult eyes contained long, distinct elastin related elastic fibres which ran longitudinally through the LC cribriform plates. Elastic fibre thickness was also found to increase with adult age (Hernandez, 1992).

Within the current study, TPEF-related elastic fibres were also present as long, distinct fibres within the elderly LC but were absent in the young. However, although the elderly ONH has been shown to contain an increase in elastic fibres, with no evidence of degradation (Hernandez, 1992), it has also been shown to become stiffer with age (Albon et al., 2000b).

One ageing process that affects the mechanical properties of collagen and elastin is non-enzymatic glycation cross-linking (Bailey, 2001). Glycation of collagen in the lens capsule has been shown to increase the rigidity of the tissue (Bailey et al., 1993). Glycation also affects the compliance of elastin and causes it to become stiffer (Winlove et al., 1996). Within the LC, advanced glycation end products have been shown to increase with age (Albon et al., 1995) and glaucoma (Tezel et al., 2007) and may be implicated in the observed stiffening of the ONH (Zeimer and Ogura, 1989, Albon et al., 2000b).

Therefore, an increase in glycation, and subsequent stiffening of connective fibres, may contribute to the decreased elasticity of the ONH even in the presence of increased elastin content.

An increase in glycation may also account for the absence of collagen crimp and higher connective tissue fibre alignment in the elderly LC and peripapillary sclera. Throughout this study, the eyes used to characterise the ONH connective tissue organisation and distribution were enucleated post mortem and therefore not under IOP. This means that the ONH connective tissue studied would be in a "relaxed" state. Therefore, it is likely that the increase in cross-linking of the connective tissue fibres with age is responsible for the elderly ONH collagen fibres remaining in their stress induced configuration, i.e. not crimped, straight and highly aligned, even in the absence of IOP.

Inversely, the crimped, relaxed nature of the young ONH fibrillar collagen may contribute to the more compliant young LC (Albon et al., 2000b) and also its ability to show reverse cupping as witnessed in younger eyes (Lee et al., 2012) and childhood glaucoma (Quigley, 1977).

The role of the stiffer elderly ONH in glaucoma susceptibility is unknown. Albon et al. (2000b) postulated that the stiffer, less resilient elderly ONHs may have a lower elastic limit than young ONHs. The elastic limit is the greatest stress that can be applied to a material under which it still deforms elastically, and thus can return to its original conformation. Beyond this point the material may deform plastically resulting in a portion of the deformation becoming permanent. Therefore, under a certain level of stress, the elderly ONH connective tissue may suffer from irreversible deformation. POAG is an age-related disease and under elevated IOP or high diurnal IOP

fluctuations, this permanent deformation of the LC may result. Interestingly, the LC appeared to increase in stiffness abruptly after 40-50 years of age (Albon et al., 2000b), which is the age at which the incidence of POAG increases (Quigley, 1996). Non-compliant deformation of the LC may result in axonal compression, blockage of axonal transport and/or ischaemic effects consequently leading to RGC death.

In addition to an increase in stiffness, accumulation of advanced glycation end products has also been associated with oxidative stress (Kikuchi et al., 2003) and neurotoxicity (Takeuchi et al., 2000). As mentioned earlier, a higher accumulation of advanced glycation end products has been found in the glaucomatous ONH (Tezel et al., 2007) suggesting an accelerated ageing process in glaucoma that may either predispose the eye to, or is a consequence of, the disease.

Another factor that will influence the mechanical response of the ONH tissue is the LC's collagen content. In this study, the elderly ONH had a greater relative fibrillar collagen content but thinner LC thickness than the young. This infers that the connective tissue in the elderly LC is more compacted than in the young LC.

A thinner, more compact LC may have an increased translaminar pressure gradient compared to a thicker LC as the difference between intraocular and intracranial pressure occurs over a shorter distance. The translaminar pressure gradient has been implicated in glaucoma pathogenesis (Morgan et al., 2008) and past studies have found that POAG and normal tension glaucoma sufferers have a higher translaminar pressure difference than control subjects (Berdahl et al., 2008a, Berdahl et al., 2008b). Translaminar pressure difference has also been shown to be positively correlated with the extent of glaucomatous visual field loss (Ren et al., 2010a). A steeper pressure gradient may

cause compression or shearing forces within the LC or directly damage the RGC axons through inhibition of axonal transport (Hahnenberger, 1980). Therefore, together with the stiffer LC, the thinner elderly LC is another potential factor in the increased susceptibility of the elderly eye to glaucomatous damage.

The stiffer and thinner elderly LCs may predispose the eye to axonal damage, however, not all elderly people suffer from glaucoma.

As previously mentioned, although the average elderly LC was thinner, collectively, the LCs obtained from healthy elderly ONHs in the current study contained a higher relative fibrillar collagen content than the young. This is in agreement with previous studies (Hernandez et al., 1986, Hernandez et al., 1989, Morrison et al., 1989a, Albon et al., 1995). Correlation between connective tissue content and strain using finite element models of monkey eyes revealed that LC regions with a higher connective tissue volume fraction show less strain during IOP elevation (Roberts et al., 2010a). Therefore, even though the elderly LC is thinner, it may be less likely to deform under changes in IOP and may even protect axons from an increased translaminar pressure gradient. Glaucoma sufferers may inherently possess an LC with a lower connective tissue content which is at greater risk of deforming under chronic IOP elevation (Roberts et al., 2010a) and, due to age-related connective tissue stiffening, pathophysiological cupping (Burgoyne and Downs, 2008). This theory is supported by regional differences in IOP-related LC deformation likely due the lower connective tissue content in the superior and inferior poles of the LC (Quigley and Addicks, 1981, Quigley et al., 1983) and may explain why the LC appears thinner in human glaucoma (Jonas et al., 2003, Inoue et al., 2009, Ren et al., 2009, Park et al., 2012a).

However, studies have also shown that LC connective tissue volume fraction increases (Roberts et al., 2009) and the LC becomes thicker (Yang et al., 2007, Yang et al., 2011a) in the early stages of an experimental ocular hypertensive monkey model. The increase in connective tissue content may be a due to a connective tissue remodelling response to glaucoma related stress or axon loss (Hernandez, 2000, Morgan, 2000). This is likely to be caused by cellular activation through mechanotransduction (Kirwan et al., 2004, Kirwan et al., 2005) in the ONHs attempt to restore a healthy stress and strain relationship.

Therefore, it is likely that an individual's ONH geometry may influence their susceptibility to glaucoma. One point that was emphasised in the current findings is the high inter-individual variability in ONH microarchitecture. Variability was evident in the thickness and degree of connective tissue fibre alignment in the LCs studied. Furthermore, few similarities in fibre alignment were observed in eyes from the same donor.

The impact that inter-individual variability in geometry and connective tissue material properties have on the biomechanical response of the ONH to changes in IOP have been predicted using a finite element modeling approach (Sigal and Ethier, 2009). The majority of human ONH finite element models have, in the past, treated the LC as a homogenous structure (Sigal et al., 2004, Sigal et al., 2009). However, as highlighted by the 3D structural analysis in the current thesis and by others (Quigley and Addicks, 1981, Radius, 1981, Ogden et al., 1988, Jonas et al., 1991, Oyama et al., 2006), the LC is a complex structure with regional variations in connective tissue orientation, alignment and content.

Therefore, it is integral that the complexity of the connective tissue of the 3D LC, as demonstrated in this thesis, is incorporated into predictive models of the human ONH to fully understand what combination of ONH structural factors predispose the elderly eye to glaucomatous optic neuropathy.

In conclusion, differences in the microarchitecture and nanoarchitecture of the young and elderly ONH exist. They include the presence of elastic fibres, fibrillar collagen content, alignment and spacing and LC thickness. The findings of this thesis will advance our knowledge of the ONH architecture and how it changes as a function of age and glaucoma. This is important since regional and age-related differences in connective tissue content and organisation likely influence the ageing ONH's biomechanics and its response to IOP. The long-term aim of this research is to determine the most influential ONH structural parameters that predispose the eye to glaucomatous optic neuropathy and then investigate these parameters *in vivo* using techniques such as optical coherence tomography.

7.1 **Future Work**

- The primary goal following completion of this PhD is to increase the sample number in all studies. Increasing sample numbers to include ONHs from a range of donor ages and glaucoma severity will enable further investigation into age and disease-related changes in ONH microstructural parameters and will increase statistical confidence.

- The 3D reconstruction method of the SHG ONH datasets should be improved so as to limit the amount of signal attenuation between sections. This will require further

development of image processing and segmentation techniques to enhance the attenuated signal. The same improvements may allow for accurate 3D reconstruction of the TPEF ONH datasets which, together with the SHG, will enable quantification of the relative contributions of collagen and elastin to the LC and regionally.

- 3D reconstruction of the glaucomatous datasets is also needed to compare relative connective tissue content and LC thickness between the glaucomatous ONH and age-matched controls.

- To analyse the biomechanics of the ageing human ONH, development of pressure elevation apparatus for the analysis of levels of stress and strain throughout the LC and adjacent tissues will be performed. The aim is to use the apparatus, in conjunction with optical coherence tomography or nonlinear microscopy (back scattered SHG), to record pressure-induced changes in the ONH dynamically.

- Due to the lack of measurable SAXS reflections in the LC, other analysis techniques will be pursued to fully investigate differences in SAXS scatter in the ONH and surrounding tissue. One potential technique is principal components analysis (PCA) of SAXS scatter intensity across the ONH. PCA is used to reduce the variables within a dataset into a smaller set of principal components (basis functions) that account for the maximum variance within the data. Each data point within the dataset can be represented as a weighting of each principal component. This statistical method has been previously used to analyse SAXS data from parchment (Kennedy et al., 2004) and breast tissue (Round et al., 2005). Preliminary results, carried out by Dr. Kate Patten and Professor Tim Wess,

indicate that PCA has potential in highlighting differences between ONH regions and between young and elderly ONH tissue sections (Figure 7.1). Further work is required to understand what differences in ONH structure these basis functions are indicating.
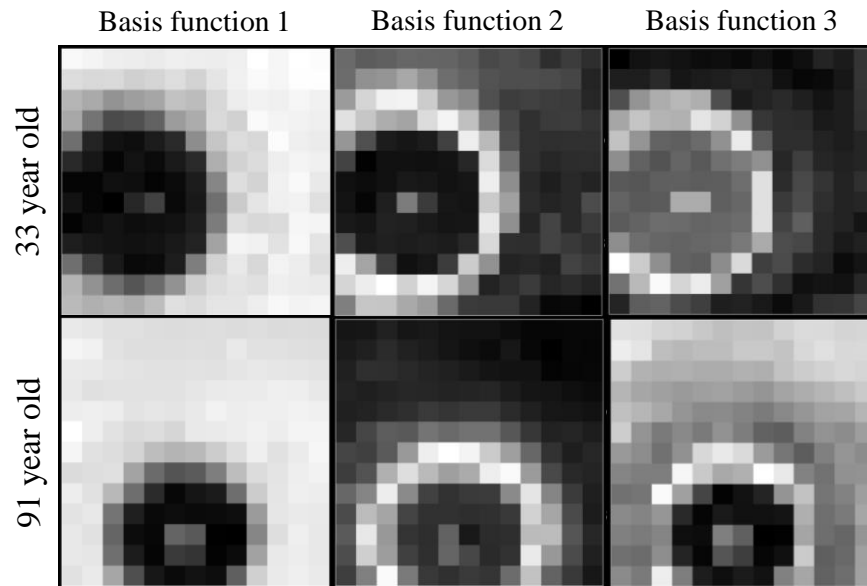
Figure 7.1. Principal components analysis of ONH SAXS datasets. The first basis function emphasises differences between SAXS data in the ON canal and peripapillary sclera while the second depicts the differences between peripapillary sclera within 0-500μm from the ON canal boundary and the sclera beyond 500μm. Interestingly, the third basis function highlights differences between the ON canal and peripapillary sclera between the 33 year old and 91 year old ONH. Grey values depict the weightings of the basis functions at each data point, black = high, white = low.

- This thesis focussed on the microarchitecture of the load-bearing connective tissue of the ONH. To fully understand the ONH structural changes with age and disease, we must also take into account the proteoglycan components of the ONH. Past studies have used cuprolinic blue dye (Sawaguchi et al., 1992, Sawaguchi et al., 1993, Fukuchi et al., 1994) and immunolabelling for chondroitin and dermatan sulphates (Caparas et al., 1991, Morrison et al., 1994) to investigate GAG distribution in the LC. Combining SHG and TPEF imaging and specific

immunolabelling of proteoglycans and their GAG side-chains (Caterson, 2012) will enable the investigation of the relationship between proteoglycans/GAGs and load-bearing connective tissue within the ONH as a function of age and disease. For example, it would be interesting to use these antibodies to investigate the potential formation of the glial scar during connective tissue remodelling in the glaucomatous LC.

- The long term goal of this research is the development of predictive finite element models, similar to the microstructural monkey models developed by Downs et al. (2009), which will be used to determine how changes in the ageing human ONH increase the susceptibility of RGC axons to glaucomatous damage. Connective tissue fibre alignment, orientation and volume fraction from the 3D ONH datasets will also be included in the models to predict stress-strain relationships in the ONH in order to understand those ONHs at risk of developing glaucomatous optic neuropathy.

References

Agapova, O. A., Kaufman, P. L., Lucarelli, M. J., Gabelt, B. T. & Hernandez, M. R. 2003. Differential expression of matrix metalloproteinases in monkey eyes with experimental glaucoma or optic nerve transection. *Brain Research,* 967**,** 132-43.

Albon, J., Karwatowski, W., Avery, N., Easty, D. & Duance, V. 1995. Changes in the collagenous matrix of the aging human lamina cribrosa. *British Journal of Ophthalmology,* 79**,** 368-375.

Albon, J., Karwatowski, W., Easty, D. L., Sims, T. & Duance, V. 2000a. Age related changes in the non-collagenous components of the extracellular matrix of the human lamina cribrosa. *British Journal of Ophthalmology,* 84**,** 311-317.

Albon, J., Purslow, P., Karwatowski, W. & Easty, D. 2000b. Age related compliance of the lamina cribrosa in human eyes. *British Journal of Ophthalmology,* 84**,** 318-323.

Albon, J., Farrant, S., Akhtar, S., Young, R., Boulton, M., Smith, G., Taylor, M., Guggenheim, J. & Morgan, J. 2007. Connective tissue structure of the tree shrew optic nerve and associated ageing changes. *Investigative Ophthalmology & Visual Science,* 48**,** 2134-2144.

Ali, L., Green, E. M., Ellis, R. E., Bradley, D. A., Grossmann, J. G. & Winlove, C. P. 2004. Study of the molecular and supramolecular organisation of elastic tissue by X-ray diffraction. *Radiation Physics and Chemistry,* 71**,** 951–952.

Anderson, D. R. 1969. Ultrastructure of human and monkey lamina cribrosa and optic nerve head. *Archives of Ophthalmology,* 82**,** 800-14.

Anderson, D. R. 1973. Fine structure and function of ocular tissues. The optic nerve. *International Ophthalmology Clinics,* 13**,** 229-42.

Bacallao, R., Sohrab, S. & Phillips, C. 2006. Guiding Principles of Specimen Preservation for Confocal Fluorescence Microscopy. *In:* PAWLEY, J. B. (ed.) *Handbook Of Biological Confocal Microscopy.* Springer US.

Bailey, A. J., Sims, T. J., Avery, N. C. & Miles, C. A. 1993. Chemistry of collagen cross-links: glucose-mediated covalent cross-linking of type-IV collagen in lens capsules. *The Biochemical Journal,* 296 (Pt 2)**,** 489-96.

Bailey, A. J. 2001. Molecular mechanisms of ageing in connective tissue. *Mechanisms of Ageing and Development,* 122**,** 735-755.

Balaratnasingam, C., Morgan, W. H., Bass, L., Matich, G., Cringle, S. J. & Yu, D. Y. 2007. Axonal transport and cytoskeletal changes in the laminar regions after elevated intraocular pressure. *Investigative Ophthalmology & Visual Science,* 48**,** 3632-44.

Baltmr, A., Duggan, J., Nizari, S., Salt, T. E. & Cordeiro, M. F. 2010. Neuroprotection in glaucoma - Is there a future role? *Experimental Eye Research,* 91**,** 554-66.

Batschelet, E. 1981. *Circular Statistics in Biology,* London, England, Academic Press, Inc. (London) Ltd.

Bella, J., Liu, J., Kramer, R., Brodsky, B. & Berman, H. 2006. Conformational effects of Gly-X-Gly interruptions in the collagen triple helix. *Journal of Molecular Biology,* 362**,** 298-311.

Bellezza, A. J., Rintalan, C. J., Thompson, H. W., Downs, J. C., Hart, R. T. & Burgoyne, C. F. 2003. Deformation of the lamina cribrosa and anterior scleral canal wall in early experimental glaucoma. *Investigative Ophthalmology & Visual Science,* 44**,** 623-637.

Berdahl, J. P., Allingham, R. R. & Johnson, D. H. 2008a. Cerebrospinal fluid pressure is decreased in primary open-angle glaucoma. *Ophthalmology,* 115**,** 763-768.

Berdahl, J. P., Fautsch, M. P., Stinnett, S. S. & Allingham, R. R. 2008b. Intracranial pressure in primary open angle glaucoma, normal tension glaucoma, and ocular hypertension: A case-control study. *Investigative Ophthalmology & Visual Science,* 49**,** 5412-5418.

Bettelheim, F. A. & Kumbar, M. 1977. An interpretation of small-angle light-scattering patterns of human cornea. *Investigative Ophthalmology & Visual Science,* 16**,** 233-6.

Bettelheim, F. A. & Magrill, R. 1977. Small-angle light-scattering patterns of corneas of different species. *Investigative Ophthalmology & Visual Science,* 16**,** 236-40.

Bindewald-Wittich, A., Han, M., Schmitz-Valckenberg, S., Snyder, S. R., Giese, G., Bille, J. F. & Holz, F. G. 2006. Two-photon-excited fluorescence imaging of human RPE cells with a femtosecond Ti:Sapphire laser. *Investigative Ophthalmology & Visual Science,* 47**,** 4553-7.

Birch, M., Brotchie, D., Roberts, N. & Grierson, I. 1997. The three-dimensional structure of the connective tissue in the lamina cribrosa of the human optic nerve head. *Ophthalmologica,* 211**,** 183-91.

Bonaldo, P., Russo, V., Bucciotti, F., Doliana, R. & Colombatti, A. 1990. Structural and functional features of the alpha 3 chain indicate a bridging role for chicken collagen VI in connective tissues. *Biochemistry,* 29**,** 1245-54.

Boote, C., Dennis, S., Newton, R. H., Puri, H. & Meek, K. M. 2003. Collagen fibrils appear more closely packed in the prepupillary cornea: optical and biomechanical implications. *Investigative Ophthalmology & Visual Science,* 44**,** 2941-8.

Boulton, M. & Marshall, J. 1985. Repigmentation of human retinal pigment epithelial cells in vitro. *Experimental Eye Research,* 41**,** 209-18.

Brazel, D., Oberbäumer, I., Dieringer, H., Babel, W., Glanville, R. W., Deutzmann, R. & Kühn, K. 1987. Completion of the amino acid sequence of the α1 chain of human basement membrane collagen (type IV) reveals 21 non-triplet interruptions located within the collagenous domain. *European Journal of Biochemistry,* 168**,** 529-536.

Brodsky, B., Eikenberry, E. F. & Cassidy, K. 1980. An unusual collagen periodicity in skin. *Biochimica et Biophysica Acta,* 621**,** 162-6.

Brooks, D., Komaromy, A., Garcia-Fernandez, M., Cutler, T., Samuelson, D. & Kallberg, M. 2000. Immunohistochemistry of the extracellular matrix of the normal equine lamina cribrosa. *Veterinary Ophthalmology,* 3**,** 127-132.

Brown, D., Morishige, N., Neekhra, A., Minckler, D. & Jester, J. 2007. Application of second harmonic imaging microscopy to assess structural changes in optic nerve head structure ex vivo. *Journal of Biomedical Optics,* 12**,** 024029.

Bruce, I., Mckennell, A. & Walker, E. 1991. Blind and partially sighted adults in Britain: the RNIB Survey. 1.

Burgoyne, C., Downs, J. C., Bellezza, A. & Hart, R. 2004. Three-dimensional reconstruction of normal and early glaucoma monkey optic nerve head connective tissues. *Investigative Ophthalmology & Visual Science,* 45**,** 4388-4399.

Burgoyne, C. F., Crawford Downs, J., Bellezza, A. J., Francis Suh, J. K. & Hart, R. T. 2005. The optic nerve head as a biomechanical structure: a new paradigm for understanding the role of IOP-related stress and strain in the pathophysiology of

glaucomatous optic nerve head damage. *Progress in Retinal and Eye Research,* 24**,** 39-73.

Burgoyne, C. F. & Downs, J. C. 2008. Premise and prediction - How optic nerve head biomechanics underlies the susceptibility and clinical behavior of the aged optic nerve head. *Journal of Glaucoma,* 17**,** 318-328.

Campagnola, P. J., Millard, A. C., Terasaki, M., Hoppe, P. E., Malone, C. J. & Mohler, W. A. 2002. Three-dimensional high-resolution second-harmonic generation imaging of endogenous structural proteins in biological tissues. *Biophysical Journal,* 82**,** 493-508.

Caparas, V. L., Cintron, C. & Hernandez-Neufeld, M. R. 1991. Immunohistochemistry of proteoglycans in human lamina cribrosa. *American Journal of Ophthalmology,* 112**,** 489-95.

Caprioli, J. & Sears, M. 1986. Patterns of early visual field loss in open-angle glaucoma. *Transactions of the American Ophthalmological Society,* 84**,** 133-45.

Caterson, B. 2012. Fell-Muir Lecture: Chondroitin sulphate glycosaminoglycans: fun for some and confusion for others. *International Journal of Experimental Pathology,* 93**,** 1-10.

Chandross, R. J., Bear, R. S. & Montgomery, R. L. 1978. An X-ray diffraction comparison of myelins from the human nervous system. *The Journal of Comparative Neurology,* 177**,** 1-9.

Chang, D. K. & Urry, D. W. 1988. Molecular dynamics calculations on relaxed and extended states of the polypentapeptide of elastin. *Chemical Physics Letters,* 147**,** 395-400.

Chen, G., Chen, J., Zhuo, S., Xiong, S., Zeng, H., Jiang, X., Chen, R. & Xie, S. 2009. Nonlinear spectral imaging of human hypertrophic scar based on two-photon excited fluorescence and second-harmonic generation. *British Journal of Dermatology,* 161**,** 48-55.

Chia, L. S., Thompson, J. E. & Moscarello, M. A. 1983. Changes in lipid phase behaviour in human myelin during maturation and aging. Involvement of lipid peroxidation. *FEBS letters,* 157**,** 155-8.

Coleman, A. & Miglior, S. 2008. Risk factors for glaucoma onset and progression. *Survey of Ophthalmology,* 53**,** S3-S10.

Coudrillier, B., Tian, J., Alexander, S., Myers, K. M., Quigley, H. A. & Nguyen, T. D. 2012. Biomechanics of the human posterior sclera: age- and glaucoma-related changes measured using inflation testing. *Investigative Ophthalmology & Visual Science,* 53**,** 1714-1728.

Coudrillier, B., Boote, C., Quigley, H. A. & Nguyen, T. D. 2013. Scleral anisotropy and its effects on the mechanical response of the optic nerve head. *Biomechanics and Modeling in Mechanobiology,* 12**,** 941-963.

Culav, E. M., Clark, C. H. & Merrilees, M. J. 1999. Connective tissues: matrix composition and its relevance to physical therapy. *Physical Therapy,* 79**,** 308-19.

Dai, C., Khaw, P. T., Yin, Z. Q., Li, D., Raisman, G. & Li, Y. 2012. Structural basis of glaucoma: the fortified astrocytes of the optic nerve head are the target of raised intraocular pressure. *Glia,* 60**,** 13-28.

Davis, G. R. & Wong, F. S. 1996. X-ray microtomography of bones and teeth. *Physiological Measurement,* 17**,** 121-46.

Davis, G. R. & Elliott, J. C. 1997. X-ray microtomography scanner using time-delay integration for elimination of ring artefacts in the reconstructed image. *Nuclear Instruments and Methods in Physics Research Section A: Accelerators, Spectrometers, Detectors and Associated Equipment,* 394**,** 157-162.

Davis, G. R., Evershed, A., Elliott, J. & Mills, D. 2010. Quantitative x-ray microtomography with a conventional source. *Proceedings of the SPIE,* 7804**,** 78040I-78040I.

Deyl, Z., Macek, K., Adam, M. & Vancikova, O. 1980. Studies on the chemical nature of elastin fluorescence. *Biochimica et Biophysica Acta,* 625**,** 248-254.

Dolman, C. L., Mccormick, A. Q. & Drance, S. M. 1980. Aging of the optic nerve. *Archives of Ophthalmology,* 98**,** 2053-2058.

Downs, J. C., Ensor, M. E., Bellezza, A. J., Thompson, H. W., Hart, R. T. & Burgoyne, C. F. 2001. Posterior scleral thickness in perfusion-fixed normal and early-glaucoma monkey eyes. *Investigative Ophthalmology & Visual Science,* 42**,** 3202-8.

Downs, J. C., Suh, J. K., Thomas, K. A., Bellezza, A. J., Hart, R. T. & Burgoyne, C. F. 2005. Viscoelastic material properties of the peripapillary sclera in normal and early-glaucoma monkey eyes. *Investigative Ophthalmology & Visual Science,* 46**,** 540-6.

Downs, J. C., Roberts, M. D., Burgoyne, C. F. & Hart, R. T. 2009. Multiscale finite element modeling of the lamina cribrosa microarchitecture in the eye. *Conference Proceedings IEEE Engeering in Medecine and Biology Society,* 2009**,** 4277-80.

Downs, J. C., Roberts, M. D. & Sigal, I. A. 2011. Glaucomatous cupping of the lamina cribrosa: A review of the evidence for active progressive remodeling as a mechanism. *Experimental Eye Research,* 93**,** 133-140.

Dunlevy, J. R. & Rada, J. A. 2004. Interaction of lumican with aggrecan in the aging human sclera. *Investigative Ophthalmology & Visual Science,* 45**,** 3849-56.

Ebneter, A., Casson, R. J., Wood, J. P. & Chidlow, G. 2010. Microglial activation in the visual pathway in experimental glaucoma: spatiotemporal characterization and correlation with axonal injury. *Investigative Ophthalmology & Visual Science,* 51**,** 6448-60.

Eikenberry, E. F., Brodsky, B. & Parry, D. a. D. 1982. Collagen fibril morphology in developing chick metatarsal tendons: 1. X-ray diffraction studies. *International Journal of Biological Macromolecules,* 4**,** 322-328.

Elkington, A. R., Inman, C. B., Steart, P. V. & Weller, R. O. 1990. The structure of the lamina cribrosa of the human eye: an immunocytochemical and electron microscopical study. *Eye,* 4 (Pt 1)**,** 42-57.

Elliott, J. C. & Dover, S. D. 1982. X-ray microtomography. *Journal of Microscopy,* 126**,** 211-213.

Exposito, J. Y., Valcourt, U., Cluzel, C. & Lethias, C. 2010. The fibrillar collagen family. *International Journal of Molecular Sciences,* 11**,** 407-26.

Fernandez De Castro, J. P., Mullins, R. F., Manea, A. M., Hernandez, J., Wallen, T. & Kuehn, M. H. 2013. Lipofuscin in human glaucomatous optic nerves. *Experimental Eye Research,* 111**,** 61-6.

Fontana, L., Bhandari, A., Fitzke, F. & Hitchings, R. 1998. In vivo morphometry of the lamina cribrosa and its relation to visual field loss in glaucoma. *Current Eye Research,* 17**,** 363-369.

Foster, J., Bruenger, E., Gray, W. & Sandberg, L. 1973. Isolation and amino acid sequences of tropoelastin peptides. *Journal of Biological Chemistry,* 248**,** 2876-2879.

Fratzl, P. & Daxer, A. 1993. Structural transformation of collagen fibrils in corneal stroma during drying. An X-ray scattering study. *Biophysical Journal,* 64**,** 1210-4.

Freed, A. D. & Doehring, T. C. 2005. Elastic model for crimped collagen fibrils. *Journal of Biomechanical Engineering,* 127**,** 587-93.

Freund, I. & Deutsch, M. 1986. Second-harmonic microscopy of biological tissue. *Optics Letters,* 11**,** 94-96.

Friberg, T. R. & Lace, J. W. 1988. A comparison of the elastic properties of human choroid and sclera. *Experimental Eye Research,* 47**,** 429-36.

Fukuchi, T., Sawaguchi, S., Hara, H., Shirakashi, M. & Iwata, K. 1992. Extracellular matrix changes of the optic nerve lamina cribrosa in monkey eyes with experimentally chronic glaucoma. *Graefe's Archive for Clinical and Experimental Ophthalmology,* 230**,** 421-427.

Fukuchi, T., Sawaguchi, S., Yue, B., Iwata, K., Hara, H. & Kaiya, T. 1994. Sulfated proteoglycans in the lamina cribrosa of normal monkey eyes and monkey eyes with laser-induced glaucoma. *Experimental Eye Research,* 58**,** 231-244.

Garway-Heath, D., Wollstein, G. & Hitchings, R. 1997. Aging changes of the optic nerve head in relation to open angle glaucoma. *British Journal of Ophthalmology,* 81**,** 840-845.

Garway-Heath, D. F. & Hitchings, R. A. 1998. Quantitative evaluation of the optic nerve head in early glaucoma. *The British Journal of Ophthalmology,* 82**,** 352-61.

Gay, S. & Miller, E. 1978. *Collagen in the physiology and pathology of connective tissue,* New York, Fischer.

Geraghty, B., Jones, S. W., Rama, P., Akhtar, R. & Elsheikh, A. 2012. Age-related variations in the biomechanical properties of human sclera. *Journal of the Mechanical Behavior of Biomedical Materials,* 16**,** 181-91.

Girard, M. J., Downs, J. C., Bottlang, M., Burgoyne, C. F. & Suh, J. K. 2009a. Peripapillary and posterior scleral mechanics, part II: experimental and inverse finite element characterization. *Journal of Biomechanical Engineering,* 131**,** 051012.

Girard, M. J., Suh, J. K., Bottlang, M., Burgoyne, C. F. & Downs, J. C. 2009b. Scleral biomechanics in the aging monkey eye. *Investigative Ophthalmology & Visual Science,* 50**,** 5226-37.

Girard, M. J., Dahlmann-Noor, A., Rayapureddi, S., Bechara, J. A., Bertin, B. M., Jones, H., Albon, J., Khaw, P. T. & Ethier, C. R. 2011a. Quantitative mapping of scleral fiber orientation in normal rat eyes. *Investigative Ophthalmology & Visual Science,* 52**,** 9684-93.

Girard, M. J., Suh, J. K., Bottlang, M., Burgoyne, C. F. & Downs, J. C. 2011b. Biomechanical changes in the sclera of monkey eyes exposed to chronic IOP elevations. *Investigative Ophthalmology & Visual Science,* 52**,** 5656-69.

Goldbaum, M., Jeng, S., Logemann, R. & Weinreb, R. 1989. The extracellular matrix of the human optic nerve. *Archives of Ophthalmology,* 107**,** 1225-1231.

Grant, W. 1955. Facility of flow through the trabecular meshwork. *A.M.A Archives of Ophthalmology,* 54**,** 245-248.

Grant, W. 1958. Further studies on facility of flow through the trabecular meshwork. *A.M.A Archives of Ophthalmology,* 60**,** 523-533.

Greenlee, T., Ross, R. & Hartman, J. 1966. The fine structure of elastic fibers. *The Journal of Cell Biology,* 30**,** 59-71.

Grynpas, M. 1977. Three-dimensional packing of collagen in bone. *Nature,* 265**,** 381-2.

Grytz, R., Meschke, G. & Jonas, J. B. 2011. The collagen fibril architecture in the lamina cribrosa and peripapillary sclera predicted by a computational

remodeling approach. *Biomechanics and Modeling in Mechanobiology,* 10**,** 371-382.

Hahnenberger, R. W. 1980. Inhibition of fast anterograde axoplasmic transport by a pressure barrier. The effect of pressure gradient and maximal pressure. *Acta Physiologica Scandinavica,* 109**,** 117-21.

Hamann, M. C. J., Sacks, M. S. & Malinin, T. I. 1998. Quantification of the collagen fibre architecture of human cranial dura mater. *Journal of Anatomy,* 192**,** 99-106.

Hayat, M. A. 1970. *Principles and Techniques of Electron Microscopy: Biological Applications,* New York, Van Nostrand Reinhold.

Healey, P. R., Mitchell, P., Smith, W. & Wang, J. J. 1997. The influence of age and intraocular pressure on the optic cup in a normal population. *Journal of Glaucoma,* 6**,** 274-8.

Heijl, A., Leske, M. C., Bengtsson, B., Hyman, L. & Hussein, M. 2002. Reduction of intraocular pressure and glaucoma progression: results from the Early Manifest Glaucoma Trial. *Archives of Ophthalmology,* 120**,** 1268-79.

Heijl, A. & Traverso, C. E. 2008. Treatment principles and options. *European Glaucoma Society. Terminology and Guidelines for Glaucoma.* 3rd ed. Savona Italy: Dogma Publications.

Hernandez, M., Igoe, F. & Neufeld, A. 1986. Extracellular matrix of the human optic nerve head. *American Journal of Ophthalmology,* 102**,** 139-148.

Hernandez, M., Luo, X., Igoe, F. & Neufeld, A. 1987. Extracellular matrix of the human lamina cribrosa. *American Journal of Ophthalmology,* 104**,** 567-576.

Hernandez, M., Igoe, F. & Neufeld, A. 1988. Cell culture of the human lamina cribrosa. *Investigative Ophthalmology & Visual Science,* 29**,** 78-89.

Hernandez, M., Luo, X., Andrzejewska, W. & Neufeld, A. 1989. Age-related changes in the extracellular matrix of the human optic nerve head. *American Journal of Ophthalmology,* 107**,** 476-484.

Hernandez, M. & Neufeld, A. 1989. The extracellular matrix of the trabecular meshwork and the optic nerve head. *In:* RITCH, R., SHIELDS, M. B. & KRUPIN, T. (eds.) *The Glaucomas.* Mosby, Inc.

Hernandez, M., Andrzejewska, W. & Neufeld, A. 1990. Changes in the extracellular matrix of the human optic nerve head in primary open-angle glaucoma. *American Journal of Ophthalmology,* 109**,** 180-8.

Hernandez, M., Wang, N., Hanley, N. & Neufeld, A. 1991. Localisation of collagen types I and IV mRNAs in human optic nerve head by in situ hybridisation. *Investigative Ophthalmology & Visual Science,* 32**,** 2169-2177.

Hernandez, M. 1992. Ultrastructural immunocytochemical analysis of elastin in the human lamina cribrosa. Changes in elastic fibers in primary open-angle glaucoma. *Investigative Ophthalmology & Visual Science,* 33**,** 2891-2903.

Hernandez, M., Yang, J. & Ye, H. 1994a. Activation of elastin mRNA expression in human optic nerve heads with primary open-angle glaucoma. *Journal of Glaucoma,* 3**,** 214-225.

Hernandez, M., Ye, H. & Roy, S. 1994b. Collagen type IV gene expression in human optic nerve heads with primary open angle glaucoma. *Experimental Eye Research,* 59**,** 41-52.

Hernandez, M. 2000. The optic nerve head in glaucoma: Role of astrocytes in tissue remodeling. *Progress in Retinal and Eye Research,* 19**,** 297-321.

Hernandez, M., Pena, J., Selvidge, J., Salvador-Silva, M. & Yang, P. 2000. Hydrostatic pressure stimulates synthesis of elastin in cultured optic nerve head astrocytes. *Glia,* 32**,** 122-136.

Hogan, M., Alvarado, J. & Weddell, J. 1971. *Histology of the human eye: an atlas and textbook,* Philadelphia, USA, WB Saunders.

Howell, G., Libby, R., Jakobs, T., Smith, R., Phalan, F., Barter, J., Barbay, J., Marchant, J., Mahesh, N., Porciatti, V., Whitmore, A., Masland, R. H. & John, S. 2007. Axons of retinal ganglion cells are insulted in the optic nerve early in DBA/2J glaucoma. *The Journal of Cell Biology,* 179**,** 1523-1537.

Huang, Y. & Meek, K. M. 1999. Swelling studies on the cornea and sclera: the effects of pH and ionic strength. *Biophysical Journal,* 77**,** 1655-65.

Hukins, D. W. L. & Aspden, R. M. 1985. Composition and properties of connective tissues. *Trends in Biochemical Sciences,* 10**,** 260-264.

Hulmes, D. J. S., Jesior, J. C., Miller, A., Berthetcolominas, C. & Wolff, C. 1981. Electron microscopy shows periodic structure in collagen fibril cross-sections. *Proceedings of the National Academy of Sciences of the United States of America,* 78**,** 3567-3571.

Inoue, R., Hangai, M., Kotera, Y., Nakanishi, H., Mori, S., Morishita, S. & Yoshimura, N. 2009. Three-dimensional high-speed optical coherence tomography imaging of lamina cribrosa in glaucoma. *Ophthalmology,* 116**,** 214-222.

Johnson, E. C., Jia, L., Cepurna, W. O., Doser, T. A. & Morrison, J. C. 2007. Global changes in optic nerve head gene expression after exposure to elevated intraocular pressure in a rat glaucoma model. *Investigative Ophthalmology & Visual Science,* 48**,** 3161-77.

Jonas, J., Muller-Bergh, J., Schlotzer-Schrehardt, U. & Naumann, G. 1990. Histomorphometry of the human optic nerve. *Investigative Ophthalmology & Visual Science,* 31**,** 736-744.

Jonas, J., Mardin, C., Schlötzer-Schrehardt, U. & Naumann, G. 1991. Morphometry of the human lamina cribrosa surface. *Investigative Ophthalmology & Visual Science,* 32**,** 401-405.

Jonas, J., Schmidt, A., Müller-Bergh, J., Schlötzer-Schrehardt, U. & Naumann, G. 1992. Human optic nerve fiber count and optic disc size. *Investigative Ophthalmology & Visual Science,* 33**,** 2012-8.

Jonas, J. B., Gusek, G. C., Guggenmoos-Holzmann, I. & Naumann, G. O. 1988. Variability of the real dimensions of normal human optic discs. *Graefe's Archive for Clinical and Experimental Ophthalmology,* 226**,** 332-6.

Jonas, J. B., Fernandez, M. C. & Sturmer, J. 1993. Pattern of glaucomatous neuroretinal rim loss. *Ophthalmology,* 100**,** 63-8.

Jonas, J. B., Berenshtein, E. & Holbach, L. 2003. Anatomic relationship between lamina cribrosa, intraocular space, and cerebrospinal fluid space. *Investigative Ophthalmology & Visual Science,* 44**,** 5189-5195.

Jonas, J. B. & Holbach, L. 2005. Central corneal thickness and thickness of the lamina cribrosa in human eyes. *Investigative Ophthalmology & Visual Science,* 46**,** 1275-1279.

Joyce, E. M., Liao, J., Schoen, F. J., Mayer, J. E., Jr. & Sacks, M. S. 2009. Functional collagen fiber architecture of the pulmonary heart valve cusp. *The Annals of Thoracic Surgery,* 87**,** 1240-1249.

Kannus, P. 2000. Structure of the tendon connective tissue. *Scandinavian Journal of Medicine & Science in Sports,* 10**,** 312-20.

Karthigasan, J. & Kirschner, D. A. 1988. Membrane interactions are altered in myelin isolated from central and peripheral nervous system tissues. *Journal of Neurochemistry,* 51**,** 228-36.

Keene, D. R., Engvall, E. & Glanville, R. W. 1988. Ultrastructure of type-VI collagen in human-skin and cartilage suggests an anchoring function for this filamentous network. *Journal of Cell Biology,* 107**,** 1995-2006.

Kennedy, C. J., Hiller, J. C., Lammie, D., Drakopoulos, M., Vest, M., Cooper, M., Adderley, W. P. & Wess, T. J. 2004. Microfocus X-ray diffraction of historical parchment reveals variations in structural features through parchment cross sections. *Nano Letters,* 4**,** 1373-1380.

Kikuchi, S., Shinpo, K., Takeuchi, M., Yamagishi, S., Makita, Z., Sasaki, N. & Tashiro, K. 2003. Glycation - a sweet tempter for neuronal death. *Brain Research. Brain Research Reviews,* 41**,** 306-23.

Kim, M. S., Kim, J. M., Park, K. H. & Choi, C. Y. 2011. Asymmetry of diurnal intraocular pressure fluctuation between right and left eyes. *Acta Ophthalmologica,* 89**,** 352-357.

Kirwan, R. P., Crean, J. K., Fenerty, C. H., Clark, A. F. & O'brien, C. J. 2004. Effect of cyclical mechanical stretch and exogenous transforming growth factor-beta1 on matrix metalloproteinase-2 activity in lamina cribrosa cells from the human optic nerve head. *Journal of Glaucoma,* 13**,** 327-34.

Kirwan, R. P., Fenerty, C. H., Crean, J., Wordinger, R. J., Clark, A. F. & O'brien, C. J. 2005. Influence of cyclical mechanical strain on extracellular matrix gene expression in human lamina cribrosa cells in vitro. *Molecular Vision,* 11**,** 798-810.

Kiumehr, S., Park, S. C., Syril, D., Teng, C. C., Tello, C., Liebmann, J. M. & Ritch, R. 2012. In vivo evaluation of focal lamina cribrosa defects in glaucoma. *Archives of Ophthalmology,* 130**,** 552-9.

Klein, B., Klein, R., Lee, K. & Hoyer, C. 2006. Does the intraocular pressure effect on optic disc cupping differ by age? *Transactions of the American Ophthalmological Society,* 104**,** 143-8.

Komai, Y. & Ushiki, T. 1991. The three-dimensional organization of collagen fibrils in the human cornea and sclera. *Investigative Ophthalmology & Visual Science,* 32**,** 2244-58.

Kotecha, A., Izadi, S. & Jeffery, G. 2006. Age-related changes in the thickness of the human lamina cribrosa. *British Journal of Ophthalmology,* 90**,** 1531-1534.

Krag, S. & Andreassen, T. T. 2003. Mechanical properties of the human lens capsule. *Progress in Retinal and Eye Research,* 22**,** 749-67.

Kucharz, E. 1992. *The collagens: biochemistry and pathophysiology,* Berlin, Springer-Verlag.

Kuo, H. J., Maslen, C. L., Keene, D. R. & Glanville, R. W. 1997. Type VI collagen anchors endothelial basement membranes by interacting with type IV collagen. *The Journal of Biological Chemistry,* 272**,** 26522-9.

Lari, D. R., Schultz, D. S., Wang, A. S., Lee, O. T. & Stewart, J. M. 2012. Scleral mechanics: comparing whole globe inflation and uniaxial testing. *Experimental Eye Research,* 94**,** 128-35.

Lee, A. J., Rochtchina, E. & Mitchell, P. 2004. Intraocular pressure asymmetry and undiagnosed open-angle glaucoma in an older population. *American Journal of Ophthalmology,* 137**,** 380-382.

Lee, E. J., Kim, T. W. & Weinreb, R. N. 2012. Reversal of lamina cribrosa displacement and thickness after trabeculectomy in glaucoma. *Ophthalmology,* 119**,** 1359-66.

Lee, K., Niemeijer, M., Garvin, M. K., Kwon, Y. H., Sonka, M. & Abramoff, M. D. 2010. Segmentation of the optic disc in 3-D OCT scans of the optic nerve head. *IEEE Transactions on Medical Imaging,* 29**,** 159-68.

Mcgee, S. H. & Mccullough, R. L. 1984. Characterization of fiber orientation in short-fiber composites. *Journal of Applied Physics,* 55**,** 1394-1403.

Meek, K. M., Elliott, G. F. & Nave, C. 1986. A synchrotron X-ray diffraction study of bovine cornea stained with cupromeronic blue. *Collagen and Related Research,* 6**,** 203-18.

Meek, K. M., Blamires, T., Elliott, G. F., Gyi, T. J. & Nave, C. 1987. The organisation of collagen fibrils in the human corneal stroma: a synchrotron X-ray diffraction study. *Current Eye Research,* 6**,** 841-6.

Meek, K. M., Quantock, A. J., Boote, C., Liu, C. Y. & Kao, W. W. 2003. An X-ray scattering investigation of corneal structure in keratocan-deficient mice. *Matrix Biology: Journal of the International Society for Matrix Biology,* 22**,** 467-75.

Metscher, B. D. 2009. MicroCT for developmental biology: a versatile tool for high-contrast 3D imaging at histological resolutions. *Developmental Dynamics,* 238**,** 632-640.

Minckler, D., Bunt, A. & Johanson, G. 1977. Orthograde and retrograde axoplasmic transport during acute ocular hypertension in the monkey. *Investigative Ophthalmology & Visual Science,* 16**,** 426-441.

Minckler, D. S., Bunt, A. H. & Klock, I. B. 1978. Radioautographic and cytochemical ultrastructural studies of axoplasmic transport in the monkey optic nerve head. *Investigative Ophthalmology & Visual Science,* 17**,** 33-50.

Mohler, W., Millard, A. & Campagnola, P. 2003. Second harmonic generation imaging of endogenous structural proteins. *Methods,* 29**,** 97-109.

Morgan, J., Jeffery, G. & Foss, A. 1998. Axon deviation in the human lamina cribrosa. *British Journal of Opthalmology,* 82**,** 680-683.

Morgan, J. E. 2000. Optic nerve head structure in glaucoma: astrocytes as mediators of axonal damage. *Eye,* 14**,** 437-444.

Morgan, W. H., Yu, D. Y., Cooper, R. L., Alder, V. A., Cringle, S. J. & Constable, I. J. 1995. The influence of cerebrospinal fluid pressure on the lamina cribrosa tissue pressure gradient. *Investigative Ophthalmology & Visual Science,* 36**,** 1163-1172.

Morgan, W. H., Yu, D. Y., Cooper, R. L., Alder, V. A., Cringle, S. J. & Constable, I. J. 1997. Retinal artery and vein pressures in the dog and their relationship to aortic, intraocular, and cerebrospinal fluid pressures. *Microvascular Research,* 53**,** 211-221.

Morgan, W. H., Yu, D. Y. & Balaratnasingam, C. 2008. The role of cerebrospinal fluid pressure in glaucoma pathophysiology: the dark side of the optic disc. *Journal of Glaucoma,* 17**,** 408-13.

Morrison, J., Jerdan, J., L'hernault, N. & Quigley, H. 1988. The extracellular matrix composition of the monkey optic nerve head. *Investigative Ophthalmology & Visual Science,* 29**,** 1141-50.

Morrison, J., Jerdan, J., Dorman, M. & Quigley, H. 1989a. Structural proteins of the neonatal and adult lamina cribrosa. *Archives of Ophthalmology,* 107**,** 1220-1224.

Morrison, J., L'hernault, N., Jerdan, J. & Quigley, H. 1989b. Ultrastructural location of extracellular matrix components in the optic nerve head. *Archives of Ophthalmology,* 107**,** 123-129.

Morrison, J., Dorman-Pease, M., Dunkelberger, G. & Quigley, H. 1990. Optic nerve head extracellular matrix in primary optic atrophy and experimental glaucoma. *Archives of Ophthalmology,* 108**,** 1020-4.

Morrison, J., Rask, P., Johnson, E. & Deppmeier, L. 1994. Chondroitin sulfate proteoglycan distribution in the primate optic nerve head. *Investigative Ophthalmology & Visual Science,* 35**,** 838-845.

Morrison, J., Farrell, S., Johnson, E., Deppmeier, L., Moore, C. & Grossmann, E. 1995. Structure and composition of the rodent lamina cribrosa. *Experimental Eye Research,* 60**,** 127-135.

Nice 2009. Glaucoma: diagnosis and management of chronic open angle glaucoma and ocular hypertension [Online]. Available at: nice.org.uk/nicemedia/pdf/CG85NICEGuideline.pdf [Accessed: 4th July 2010].

Norman, R. E., Flanagan, J. G., Sigal, I. A., Rausch, S. M., Tertinegg, I. & Ethier, C. R. 2011. Finite element modeling of the human sclera: influence on optic nerve head biomechanics and connections with glaucoma. *Experimental Eye Research,* 93**,** 4-12.

Ogden, T., Duggan, J., Danley, K., Wilcox, M. & Minckler, D. 1988. Morphometry of nerve-fibre bundle pores in the optic-nerve head of the human. *Experimental Eye Research,* 46**,** 559-568.

Oliveira, R. G., Schneck, E., Funari, S. S., Tanaka, M. & Maggio, B. 2010. Equivalent aqueous phase modulation of domain segregation in myelin monolayers and bilayer vesicles. *Biophysical Journal,* 99**,** 1500-9.

Orgel, J. P., Miller, A., Irving, T. C., Fischetti, R. F., Hammersley, A. P. & Wess, T. J. 2001. The in situ supermolecular structure of type I collagen. *Structure,* 9**,** 1061-9.

Oster, G. & Riley, D. P. 1952. Scattering from cylindrically symmetric systems. *Acta Crystallographica,* 5**,** 272-276.

Oyama, T., Abe, H. & Ushiki, T. 2006. The connective tissue and glial framework in the optic nerve head of the normal human eye: light and scanning electron microscopic studies. *Archives of Histology and Cytology,* 69**,** 341-356.

Park, H. Y., Jeon, S. H. & Park, C. K. 2012a. Enhanced depth imaging detects lamina cribrosa thickness differences in normal tension glaucoma and primary open-angle glaucoma. *Ophthalmology,* 119**,** 10-20.

Park, S. C., De Moraes, C. G., Teng, C. C., Tello, C., Liebmann, J. M. & Ritch, R. 2012b. Enhanced depth imaging optical coherence tomography of deep optic nerve complex structures in glaucoma. *Ophthalmology,* 119**,** 3-9.

Park, S. C., Kiumehr, S., Teng, C. C., Tello, C., Liebmann, J. M. & Ritch, R. 2012c. Horizontal central ridge of the lamina cribrosa and regional differences in laminar insertion in healthy subjects. *Investigative Ophthalmology & Visual Science,* 53**,** 1610-1616.

Parry, D. A. 1988. The molecular and fibrillar structure of collagen and its relationship to the mechanical properties of connective tissue. *Biophysical Chemistry,* 29**,** 195-209.

Pena, J. D., Netland, P. A., Vidal, I., Dorr, D. A., Rasky, A. & Hernandez, M. R. 1998. Elastosis of the lamina cribrosa in glaucomatous optic neuropathy. *Experimental Eye Research,* 67**,** 517-24.

Pijanka, J. K., Coudrillier, B., Ziegler, K., Sorensen, T., Meek, K. M., Nguyen, T. D., Quigley, H. A. & Boote, C. 2012. Quantitative mapping of collagen fiber orientation in non-glaucoma and glaucoma posterior human sclerae. *Investigative Ophthalmology & Visual Science,* 53**,** 5258-70.

Porta, E. A. 2002. Pigments in aging: an overview. *Annals of the New York Academy of Sciences,* 959**,** 57-65.

Potter, K., Sweet, D. E., Anderson, P., Davis, G. R., Isogai, N., Asamura, S., Kusuhara, H. & Landis, W. J. 2006. Non-destructive studies of tissue-engineered phalanges by magnetic resonance microscopy and x-ray microtomography. *Bone,* 38**,** 350-8.

Preibisch, S., Saalfeld, S. & Tomancak, P. 2009. Globally optimal stitching of tiled 3D microscopic image acquisitions. *Bioinformatics,* 25**,** 1463-5.

Quantock, A. J. & Meek, K. M. 1988. Axial electron density of human scleral collagen. Location of proteoglycans by X-ray diffraction. *Biophysical Journal,* 54**,** 159-64.

Quantock, A. J., Meek, K. M. & Chakravarti, S. 2001. An X-ray diffraction investigation of corneal structure in lumican-deficient mice. *Investigative Ophthalmology & Visual Science,* 42**,** 1750-6.

Quigley, H., Brown, A. & Dorman-Pease, M. 1991a. Alterations in elastin of the optic nerve head in human and experimental glaucoma. *British Journal of Ophthalmology,* 75**,** 552-7.

Quigley, H., Dorman-Pease, M. & Brown, A. 1991b. Quantitative study of collagen and elastin of the optic nerve head and sclera in human and experimental monkey glaucoma. *Current Eye Research,* 10**,** 877-888.

Quigley, H., Pease, M. E. & Thibault, D. 1994. Change in the appearance of elastin in the lamina cribrosa of glaucomatous optic nerve heads. *Graefe's Archive for Clinical and Experimental Ophthalmology,* 232**,** 257-261.

Quigley, H. 1996. Number of people with glaucoma worldwide. *British Journal of Ophthalmology,* 80**,** 389-393.

Quigley, H., Mckinnon, S., Zack, D., Pease, M., Kerrigan-Baumrind, L., Kerrigan, D. & Mitchell, R. 2000. Retrograde axonal transport of BDNF in retinal ganglion cells is blocked by acute IOP elevation in rats. *Investigative Ophthalmology & Visual Science,* 41**,** 3460-6.

Quigley, H. & Broman, A. 2006. The number of people with glaucoma worldwide in 2010 and 2020. *British Journal of Ophthalmology,* 90**,** 262-267.

Quigley, H. A. 1977. The pathogenesis of reversible cupping in congenital glaucoma. *American Journal of Ophthalmology,* 84**,** 358-70.

Quigley, H. A. & Addicks, E. M. 1981. Regional differences in the structure of the lamina cribrosa and their relation to glaucomatous optic nerve damage. *Archives of Ophthalmology,* 99**,** 137-143.

Quigley, H. A., Addicks, E. M., Green, W. R. & Maumenee, A. E. 1981. Optic nerve damage in human glaucoma. II. The site of injury and susceptibility to damage. *Archives of Ophthalmology,* 99**,** 635-49.

Quigley, H. A., Hohman, R. M., Addicks, E. M., Massof, R. W. & Green, W. R. 1983. Morphologic changes in the lamina cribrosa correlated with neural loss in open-angle glaucoma. *American Journal of Ophthalmology,* 95**,** 673-691.

Quigley, H. A. 2011. Glaucoma. *Lancet,* 377**,** 1367-77.

Rada, J. A., Achen, V. R., Penugonda, S., Schmidt, R. W. & Mount, B. A. 2000. Proteoglycan composition in the human sclera during growth and aging. *Investigative Ophthalmology & Visual Science,* 41**,** 1639-48.

Rada, J. A., Shelton, S. & Norton, T. T. 2006. The sclera and myopia. *Experimental Eye Research,* 82**,** 185-200.

Radius, R. 1981. Regional specificity in anatomy at the lamina cribrosa. *Archives of Ophthalmology,* 99**,** 478-480.

Radius, R. & Gonzales, M. 1981. Anatomy of the lamina cribrosa in human eyes. *Archives of Ophthalmology,* 99**,** 2159-2162.

Rahman, M. Q., Beard, S. M., Discombe, R., Sharma, R. & Montgomery, D. M. 2013. Direct healthcare costs of glaucoma treatment. *The British Journal of Ophthalmology,* 97**,** 720-4.

Realini, T., Barber, L. & Burton, D. 2002. Frequency of asymmetric intraocular pressure fluctuations among patients with and without glaucoma. *Ophthalmology,* 109**,** 1367-1371.

Realini, T., Fechtner, R. D., Atreides, S.-P. & Gollance, S. 2004. The uniocular drug trial and second-eye response to glaucoma medications. *Ophthalmology,* 111**,** 421-426.

Regini, J. W., Grossmann, J. G., Burgio, M. R., Malik, N. S., Koretz, J. F., Hodson, S. A. & Elliott, G. F. 2004. Structural changes in alpha-crystallin and whole eye lens during heating, observed by low-angle X-ray diffraction. *Journal of Molecular Biology,* 336**,** 1185-94.

Rehnberg, M., Ammitzböll, T. & Tengroth, B. 1987. Collagen distribution in the lamina cribrosa and the trabecular meshwork of the human eye. *British Journal of Opthalmology,* 71**,** 886-892.

Ren, R., Jonas, J. B., Tian, G., Zhen, Y., Ma, K., Li, S., Wang, H., Li, B., Zhang, X. & Wang, N. 2010a. Cerebrospinal fluid pressure in glaucoma: a prospective study. *Ophthalmology,* 117**,** 259-66.

Ren, R., Li, B., Gao, F., Li, L., Xu, X., Wang, N. & Jonas, J. B. 2010b. Central corneal thickness, lamina cribrosa and peripapillary scleral histomorphometry in non-glaucomatous Chinese eyes. *Graefe's Archive for Clinical and Experimental Ophthalmology,* 248**,** 1579-85.

Ren, R. J., Wang, N. L., Li, B., Li, L. Q., Gao, F., Xu, X. L. & Jonas, J. B. 2009. Lamina cribrosa and peripapillary sclera histomorphometry in normal and advanced glaucomatous chinese eyes with various axial length. *Investigative Ophthalmology & Visual Science,* 50**,** 2175-2184.

Roberts, M. D., Grau, V., Grimm, J., Reynaud, J., Bellezza, A. J., Burgoyne, C. F. & Downs, J. C. 2009. Remodeling of the connective tissue microarchitecture of the lamina cribrosa in early experimental glaucoma. *Investigative Ophthalmology & Visual Science,* 50**,** 681-690.

Roberts, M. D., Liang, Y., Sigal, I. A., Grimm, J., Reynaud, J., Bellezza, A., Burgoyne, C. F. & Downs, J. C. 2010a. Correlation between local stress and strain and lamina cribrosa connective tissue volume fraction in normal monkey eyes. *Investigative Ophthalmology & Visual Science,* 51**,** 295-307.

Roberts, M. D., Sigal, I. A., Liang, Y., Burgoyne, C. F. & Downs, J. C. 2010b. Changes in the biomechanical response of the optic nerve head in early experimental glaucoma. *Investigative Ophthalmology & Visual Science,* 51**,** 5675-84.

Rosenbloom, J., Abrams, W. & Mecham, R. 1993. Extracellular matrix 4: the elastic fiber. *Journal of the Federation of American Societies for Experimental Biology,* 7**,** 1208-1218.

Ross, R. & Bornstein, P. 1969. The elastic fiber: I. the separation and partial characterization of its macromolecular components. *The Journal of Cell Biology,* 40**,** 366-381.

Round, A. R., Wilkinson, S. J., Hall, C. J., Rogers, K. D., Glatter, O., Wess, T. & Ellis, I. O. 2005. A preliminary study of breast cancer diagnosis using laboratory based small angle X-ray scattering. *Physics in Medicine and Biology,* 50**,** 4159-4168.

Sacks, M. S., Smith, D. B. & Hiester, E. D. 1997. A small angle light scattering device for planar connective tissue microstructural analysis. *Annals of Biomedical Engineering,* 25**,** 678-689.

Sacks, M. S., Smith, D. B. & Hiester, E. D. 1998. The aortic valve microstructure: effects of transvalvular pressure. *Journal of Biomedical Materials Research,* 41**,** 131-41.

Sandell, J. H. & Peters, A. 2001. Effects of age on nerve fibers in the rhesus monkey optic nerve. *The Journal of Comparative Neurology,* 429**,** 541-53.

Sawaguchi, S., Yue, B., Fukuchi, T., Iwata, K. & Kaiya, T. 1992. Sulfated proteoglycans in the human lamina cribrosa. *Investigative Ophthalmology & Visual Science,* 33**,** 2388-2398.

Sawaguchi, S., Yue, B., Fukuchi, T., Iwata, K. & Kaiya, T. 1993. Age-related changes of sulfated proteoglycans in the human lamina cribrosa. *Current Eye Research,* 12**,** 685-692.

Sayers, Z., Koch, M. H., Whitburn, S. B., Meek, K. M., Elliott, G. F. & Harmsen, A. 1982. Synchrotron X-ray diffraction study of corneal stroma. *Journal of Molecular Biology,* 160**,** 593-607.

Schindelin, J., Arganda-Carreras, I., Frise, E., Kaynig, V., Longair, M., Pietzsch, T., Preibisch, S., Rueden, C., Saalfeld, S., Schmid, B., Tinevez, J. Y., White, D. J., Hartenstein, V., Eliceiri, K., Tomancak, P. & Cardona, A. 2012. Fiji: an open-source platform for biological-image analysis. *Nature Methods,* 9**,** 676-682.

Schultz, D. S., Lotz, J. C., Lee, S. M., Trinidad, M. L. & Stewart, J. M. 2008. Structural factors that mediate scleral stiffness. *Investigative Ophthalmology & Visual Science,* 49**,** 4232-4236.

Serafini-Fracassini, A., Field, J. M. & Delf, B. 1977. X-Ray Analysis of Enzymically Purified Elastin from Bovine Ligamentum Nuchae. *In:* SANDBERG, L., GRAY, W. & FRANZBLAU, C. (eds.) *Elastin and Elastic Tissue.* Springer US.

Shoulders, M. D. & Raines, R. T. 2009. Collagen structure and stability. *Annual Review of Biochemistry,* 78**,** 929-58.

Siegner, S. W. & Netland, P. A. 1996. Optic disc hemorrhages and progression of glaucoma. *Ophthalmology,* 103**,** 1014-24.

Sigal, I. A., Flanagan, J. G., Tertinegg, I. & Ethier, C. R. 2004. Finite element modeling of optic nerve head biomechanics. *Investigative Ophthalmology & Visual Science,* 45**,** 4378-87.

Sigal, I. A., Flanagan, J. G. & Ethier, C. R. 2005. Factors influencing optic nerve head biomechanics. *Investigative Ophthalmology & Visual Science,* 46**,** 4189-99.

Sigal, I. A. & Ethier, C. R. 2009. Biomechanics of the optic nerve head. *Experimental Eye Research,* 88**,** 799-807.

Sigal, I. A., Flanagan, J. G., Tertinegg, I. & Ethier, C. R. 2009. Modeling individual-specific human optic nerve head biomechanics. Part I: IOP-induced deformations and influence of geometry. *Biomechanics and Modeling in Mechanobiology,* 8**,** 85-98.

Silver, F. H., Horvath, I. & Foran, D. J. 2002. Mechanical implications of the domain structure of fiber-forming collagens: comparison of the molecular and fibrillar flexibilities of the [alpha]1-chains found in types I-III collagen. *Journal of Theoretical Biology,* 216**,** 243-254.

Sit, A. J., Liu, J. H. K. & Weinreb, R. N. 2006. Asymmetry of right versus left intraocular pressures over 24 hours in glaucoma patients. *Ophthalmology,* 113**,** 425-430.

Srinivasan, V. J., Adler, D. C., Chen, Y., Gorczynska, I., Huber, R., Duker, J. S., Schuman, J. S. & Fujimoto, J. G. 2008. Ultrahigh-speed optical coherence tomography for three-dimensional and en face imaging of the retina and optic nerve head. *Investigative Ophthalmology & Visual Science,* 49**,** 5103-10.

Sulzer, D., Mosharov, E., Talloczy, Z., Zucca, F. A., Simon, J. D. & Zecca, L. 2008. Neuronal pigmented autophagic vacuoles: lipofuscin, neuromelanin, and ceroid as macroautophagic responses during aging and disease. *Journal of Neurochemistry,* 106**,** 24-36.

Sung, K. R., Wollstein, G., Bilonick, R. A., Townsend, K. A., Ishikawa, H., Kagemann, L., Noecker, R. J., Fujimoto, J. G. & Schuman, J. S. 2009. Effects of age on optical coherence tomography measurements of healthy retinal nerve fiber layer, macula, and optic nerve head. *Ophthalmology,* 116**,** 1119-24.

Takeuchi, M., Bucala, R., Suzuki, T., Ohkubo, T., Yamazaki, M., Koike, T., Kameda, Y. & Makita, Z. 2000. Neurotoxicity of advanced glycation end-products for cultured cortical neurons. *Journal of Neuropathology and Experimental Neurology,* 59**,** 1094-105.

Tamura, Y., Konomi, H., Sawada, H., Takashima, S. & Nakajima, A. 1991. Tissue distribution of type VIII collagen in human adult and fetal eyes. *Investigative Ophthalmology & Visual Science,* 32**,** 2636-2644.

Tarakanova, A. & Buehler, M. J. 2013. Molecular modeling of protein materials: case study of elastin. *Modelling and Simulation in Materials Science and Engineering,* 21**,** 063001.

Tengroth, B. & Ammitzbøll, T. 1984. Changes in the content and composition of collagen in the glaucomatous eye - basis for a new hypothesis for the genesis of chronic open angle glaucoma - a preliminary report. *Acta Ophthalmologica,* 62**,** 999-1008.

Tezel, G., Trinkaus, K. & Wax, M. 2004. Alterations in the morphology of lamina cribrosa pores in glaucomatous eyes. *British Journal of Ophthalmology,* 88**,** 251-256.

Tezel, G., Luo, C. & Yang, X. 2007. Accelerated aging in glaucoma: immunohistochemical assessment of advanced glycation end products in the human retina and optic nerve head. *Investigative Ophthalmology & Visual Science,* 48**,** 1201-11.

Theodossiou, T. A., Thrasivoulou, C., Ekwobi, C. & Becker, D. L. 2006. Second harmonic generation confocal microscopy of collagen type I from rat tendon cryosections. *Biophysical Journal,* 91**,** 4665-4677.

Tielsch, J. M., Sommer, A., Katz, J., Royall, R. M., Quigley, H. A. & Javitt, J. 1991. Racial variations in the prevalence of primary open-angle glaucoma: The Baltimore eye survey. *The Journal of the American Medical Association,* 266**,** 369-374.

Timpl, R., Wiedemann, H., Van Delden, V., Furthmayr, H. & Kuhn, K. 1981. A network model for the organization of type IV collagen molecules in basement membranes. *European Journal of Biochemistry / FEBS,* 120**,** 203-11.

Tomlin, S. G. & Worthington, C. R. 1956. Low-angle X-ray diffraction patterns of collagen. *Proceedings of the Royal Society of London Series A, Mathematical and Physical Sciences,* 235**,** 189-&.

Varma, R. & Spaeth, G. 1992. *The Optic Nerve in Glaucoma,* Philadelphia, JB Lippincott Co.

Veit, G., Kobbe, B., Keene, D., Paulsson, M., Koch, M. & Wagener, R. 2006. Collagen XXVIII, a novel von willebrand factor A domain-containing protein with many imperfections in the collagenous domain. *Journal of Biological Chemistry,* 281, 3494-3504.

Vogel, H. G. 1974. Correlation between tensile-strength and collagen content in rat skin - effect of age and cortisol treatment. *Connective Tissue Research,* 2, 177-182.

Vrabec, F. 1976. Glaucomatous cupping of the human optic disk: a neuro-histologic study. *Graefe's Archive for Clinical and Experimental Ophthalmology,* 198, 223-34.

Wasserman, Z. R. & Salemme, F. R. 1990. A molecular dynamics investigation of the elastomeric restoring force in elastin. *Biopolymers,* 29, 1613-31.

Weinreb, R. & Khaw, P. 2004. Primary open-angle glaucoma. *The Lancet,* 363, 1711-1720.

Weiss, J. A. & Gardiner, J. C. 2001. Computational modeling of ligament mechanics. *Critical Reviews in Biomedical Engineering,* 29, 303-71.

Wess, T. J. & Orgel, J. P. 2000. Changes in collagen structure: drying, dehydrothermal treatment and relation to long term deterioration. *Thermochimica Acta,* 365, 119-128.

Williams, A. L., Gatla, S., Leiby, B. E., Fahmy, I., Biswas, A., De Barros, D. M., Ramakrishnan, R., Bhardwaj, S., Wright, C., Dubey, S., Lynch, J. F., Bayer, A., Khandelwal, R., Ichhpujani, P., Gheith, M., Siam, G., Feldman, R. M., Henderer, J. D. & Spaeth, G. L. 2013. The value of intraocular pressure asymmetry in diagnosing glaucoma. *Journal of Glaucoma,* 22, 215-8.

Williams, R. M., Zipfel, W. R. & Webb, W. W. 2005. Interpreting second-harmonic generation images of collagen I fibrils. *Biophysical Journal,* 88, 1377-1386.

Wilson, A. M. & Di Polo, A. 2012. Gene therapy for retinal ganglion cell neuroprotection in glaucoma. *Gene Therapy,* 19, 127-36.

Winkler, M., Jester, B., Nien-Shy, C., Massei, S., Minckler, D. S., Jester, J. V. & Brown, D. J. 2010. High resolution three-dimensional reconstruction of the collagenous matrix of the human optic nerve head. *Brain Research Bulletin,* 81, 339-48.

Winlove, C. P., Parker, K. H., Avery, N. C. & Bailey, A. J. 1996. Interactions of elastin and aorta with sugars in vitro and their effects on biochemical and physical properties. *Diabetologia,* 39, 1131-1139.

Wise, S. G. & Weiss, A. S. 2009. Tropoelastin. *The International Journal of Biochemistry & Cell Biology,* 41, 494-7.

Wong, F. S. L., Willmott, N. S. & Davis, G. R. 2006. Dentinal carious lesion in three dimensions. *International Journal of Paediatric Dentistry,* 16, 419-423.

Xu, C., Zipfel, W., Shear, J. B., Williams, R. M. & Webb, W. W. 1996. Multiphoton fluorescence excitation: new spectral windows for biological nonlinear microscopy. *Proceedings of the National Academy of Sciences of the United States of America,* 93, 10763-10768.

Yan, D., Mcpheeters, S., Johnson, G., Utzinger, U. & Vande Geest, J. P. 2011. Microstructural differences in the human posterior sclera as a function of age and race. *Investigative Ophthalmology & Visual Science,* 52, 821-829.

Yang, H., Downs, J. C., Girkin, C., Sakata, L., Bellezza, A., Thompson, H. & Burgoyne, C. F. 2007. 3-D histomorphometry of the normal and early glaucomatous monkey optic nerve head: lamina cribrosa and peripapillary

scleral position and thickness. *Investigative Ophthalmology & Visual Science,* 48**,** 4597-607.

Yang, H., Thompson, H., Roberts, M. D., Sigal, I. A., Downs, J. C. & Burgoyne, C. F. 2011a. Deformation of the early glaucomatous monkey optic nerve head connective tissue after acute IOP elevation in 3-D histomorphometric reconstructions. *Investigative Ophthalmology & Visual Science,* 52**,** 345-63.

Yang, H., Williams, G., Downs, J. C., Sigal, I. A., Roberts, M. D., Thompson, H. & Burgoyne, C. F. 2011b. Posterior (outward) migration of the lamina cribrosa and early cupping in monkey experimental glaucoma. *Investigative Ophthalmology & Visual Science,* 52**,** 7109-21.

Ye, H. & Hernandez, M. 1995. Heterogeneity of astrocytes in human optic nerve head. *The Journal of Comparative Neurology,* 362**,** 441-52.

Zeimer, R. C. & Ogura, Y. 1989. The relation between glaucomatous damage and optic-nerve head mechanical compliance. *Archives of Ophthalmology,* 107**,** 1232-1234.

Zipfel, W., Williams, R. & Webb, W. 2003a. Nonlinear magic: multiphoton microscopy in the biosciences. *Nature Biotechnology,* 21**,** 1369-1377.

Zipfel, W. R., Williams, R. M., Christie, R., Nikitin, A. Y., Hyman, B. T. & Webb, W. W. 2003b. Live tissue intrinsic emission microscopy using multiphoton-excited native fluorescence and second harmonic generation. *Proceedings of the National Academy of Sciences of the United States of America,* 100**,** 7075-7080.

Zoumi, A., Lu, X. A., Kassab, G. S. & Tromberg, B. J. 2004. Imaging coronary artery microstructure using second-harmonic and two-photon fluorescence microscopy. *Biophysical Journal,* 87**,** 2778-2786.

Appendices

Appendix 1   - Copyright Licence Agreement Figure 1.1

AMERICAN MEDICAL ASSOCIATION LICENSE
TERMS AND CONDITIONS

Sep 20, 2013

This is a License Agreement between Hannah Jones ("You") and American Medical Association ("American Medical Association") provided by Copyright Clearance Center ("CCC"). The license consists of your order details, the terms and conditions provided by American Medical Association, and the payment terms and conditions.

License Number	3233071152890
License date	Sep 20, 2013
Licensed content publisher	American Medical Association
Licensed content publication	Archives of Ophthalmology
Licensed content title	Ultrastructure of Human and Monkey Lamina Cribrosa and Optic Nerve Head
Licensed content author	Anderson, Douglas R.
Licensed content date	Dec 1, 1969
Volume number	82
Issue number	6
Type of Use	Dissertation/Thesis
Requestor type	student
Format	print and electronic
Portion	figures/tables/images
Number of figures/tables/images	1
List of figures/tables/images	Schematic diagram of the optic nerve head
Will you be translating?	no
Circulation/distribution	3
Distributing to	Worldwide
Order reference number	None
Title of your thesis / dissertation	Ageing of the Human Optic Nerve Head
Expected completion date	Sep 2013
Billing Type	Credit Card
Credit card info	Visa ending in 3785
Credit card expiration	02/2015
Total	**24.93 GBP**
Terms and Conditions	

American Medical Association's Terms and Conditions

1. The publisher for the copyrighted material you seek permission to license ("Licensed Material") is the American Medical Association ("Publisher"). By clicking "accept" in connection with completing this licensing transaction, you agree that the following terms and conditions apply to this transaction (along with the Billing and Payment terms and conditions established by Copyright Clearance Center, Inc. ["CCC"] at the time that you opened your Rightslink account and that are available at any time at http://myaccount.copyright.com).

2. Publisher hereby grants to you a non-exclusive license to use the Licensed Material subject to the limitations set forth herein. Licenses are for one-time use only and are limited to the use identified in your request with a

206

Appendix 2   - Copyright Licence Agreement Figure 1.2 and 1.7

ELSEVIER LICENSE
TERMS AND CONDITIONS

Aug 16, 2013

This is a License Agreement between Hannah Jones ("You") and Elsevier ("Elsevier") provided by Copyright Clearance Center ("CCC"). The license consists of your order details, the terms and conditions provided by Elsevier, and the payment terms and conditions.

All payments must be made in full to CCC. For payment instructions, please see information listed at the bottom of this form.

Supplier	Elsevier Limited The Boulevard,Langford Lane Kidlington,Oxford,OX5 1GB,UK
Registered Company Number	1982084
Customer name	Hannah Jones
Customer address	School of Optometry and Vision Science Cardiff, CF244LU
License number	3210820366101
License date	Aug 16, 2013
Licensed content publisher	Elsevier
Licensed content publication	The Lancet
Licensed content title	Glaucoma
Licensed content author	Harry A Quigley
Licensed content date	16–22 April 2011
Licensed content volume number	377
Licensed content issue number	9774
Number of pages	11
Start Page	1367
End Page	1377
Type of Use	reuse in a thesis/dissertation
Intended publisher of new work	other
Portion	figures/tables/illustrations
Number of figures/tables/illustrations	2
Format	both print and electronic
Are you the author of this Elsevier article?	No
Will you be translating?	No
Order reference number	

Title of your thesis/dissertation	Ageing of the Human Optic Nerve Head
Expected completion date	Sep 2013
Estimated size (number of pages)	250
Elsevier VAT number	GB 494 6272 12
Permissions price	0.00 GBP
VAT/Local Sales Tax	0.0 USD / 0.0 GBP
Total	0.00 GBP
Terms and Conditions	

INTRODUCTION

1. The publisher for this copyrighted material is Elsevier. By clicking "accept" in connection with completing this licensing transaction, you agree that the following terms and conditions apply to this transaction (along with the Billing and Payment terms and conditions established by Copyright Clearance Center, Inc. ("CCC"), at the time that you opened your Rightslink account and that are available at any time at http://myaccount.copyright.com).

GENERAL TERMS

2. Elsevier hereby grants you permission to reproduce the aforementioned material subject to the terms and conditions indicated.

3. Acknowledgement: If any part of the material to be used (for example, figures) has appeared in our publication with credit or acknowledgement to another source, permission must also be sought from that source. If such permission is not obtained then that material may not be included in your publication/copies. Suitable acknowledgement to the source must be made, either as a footnote or in a reference list at the end of your publication, as follows:

"Reprinted from Publication title, Vol /edition number, Author(s), Title of article / title of chapter, Pages No., Copyright (Year), with permission from Elsevier [OR APPLICABLE SOCIETY COPYRIGHT OWNER]." Also Lancet special credit - "Reprinted from The Lancet, Vol. number, Author (s), Title of article, Pages No., Copyright (Year), with permission from Elsevier."

4. Reproduction of this material is confined to the purpose and/or media for which permission is hereby given.

5. Altering/Modifying Material: Not Permitted. However figures and illustrations may be altered/adapted minimally to serve your work. Any other abbreviations, additions, deletions and/or any other alterations shall be made only with prior written authorization of Elsevier Ltd. (Please contact Elsevier at permissions@elsevier.com)

Appendix 3   - Copyright Licence Agreement Figure 1.4

**ELSEVIER LICENSE
TERMS AND CONDITIONS**

Aug 16, 2013

This is a License Agreement between Hannah Jones ("You") and Elsevier ("Elsevier") provided by Copyright Clearance Center ("CCC"). The license consists of your order details, the terms and conditions provided by Elsevier, and the payment terms and conditions.

All payments must be made in full to CCC. For payment instructions, please see information listed at the bottom of this form.

Supplier	Elsevier Limited The Boulevard,Langford Lane Kidlington,Oxford,OX5 1GB,UK
Registered Company Number	1982084
Customer name	Hannah Jones
Customer address	School of Optometry and Vision Science
	Cardiff, CF244LU
License number	3210270253001
License date	Aug 15, 2013
Licensed content publisher	Elsevier
Licensed content publication	Structure
Licensed content title	The In Situ Supermolecular Structure of Type I Collagen
Licensed content author	Joseph P.R.O Orgel,Andrew Miller,Thomas C Irving,Robert F Fischetti,Andrew P Hammersley,Tim J Wess
Licensed content date	November 2001
Licensed content volume number	9
Licensed content issue number	11
Number of pages	9
Start Page	1061
End Page	1069
Type of Use	reuse in a thesis/dissertation
Portion	figures/tables/illustrations
Number of figures/tables/illustrations	1
Format	both print and electronic
Are you the author of this Elsevier article?	No
Will you be translating?	No
Order reference number	
Title of your thesis/dissertation	Ageing of the Human Optic Nerve Head

Expected completion date	Sep 2013
Estimated size (number of pages)	250
Elsevier VAT number	GB 494 6272 12
Permissions price	0.00 GBP
VAT/Local Sales Tax	0.0 USD / 0.0 GBP
Total	0.00 GBP

Terms and Conditions

INTRODUCTION

1. The publisher for this copyrighted material is Elsevier. By clicking "accept" in connection with completing this licensing transaction, you agree that the following terms and conditions apply to this transaction (along with the Billing and Payment terms and conditions established by Copyright Clearance Center, Inc. ("CCC"), at the time that you opened your Rightslink account and that are available at any time at http://myaccount.copyright.com).

GENERAL TERMS

2. Elsevier hereby grants you permission to reproduce the aforementioned material subject to the terms and conditions indicated.

3. Acknowledgement: If any part of the material to be used (for example, figures) has appeared in our publication with credit or acknowledgement to another source, permission must also be sought from that source. If such permission is not obtained then that material may not be included in your publication/copies. Suitable acknowledgement to the source must be made, either as a footnote or in a reference list at the end of your publication, as follows:

"Reprinted from Publication title, Vol /edition number, Author(s), Title of article / title of chapter, Pages No., Copyright (Year), with permission from Elsevier [OR APPLICABLE SOCIETY COPYRIGHT OWNER]." Also Lancet special credit - "Reprinted from The Lancet, Vol. number, Author (s), Title of article, Pages No., Copyright (Year), with permission from Elsevier."

4. Reproduction of this material is confined to the purpose and/or media for which permission is hereby given.

5. Altering/Modifying Material: Not Permitted. However figures and illustrations may be altered/adapted minimally to serve your work. Any other abbreviations, additions, deletions and/or any other alterations shall be made only with prior written authorization of Elsevier Ltd. (Please contact Elsevier at permissions@elsevier.com)

6. If the permission fee for the requested use of our material is waived in

https://s100.copyright.com//CustomerAdmin/PLF.jsp?ref=e41b8... 16/08/2013

210

Appendix 4 - Copyright Licence Agreement Figure 1.5

This is a License Agreement between Hannah Jones ("You") and Elsevier ("Elsevier") provided by Copyright Clearance Center ("CCC"). The license consists of your order details, the terms and conditions provided by Elsevier, and the payment terms and conditions.

All payments must be made in full to CCC. For payment instructions, please see information listed at the bottom of this form.

Supplier	Elsevier Limited The Boulevard,Langford Lane Kidlington,Oxford,OX5 1GB,UK
Registered Company Number	1982084
Customer name	Hannah Jones
Customer address	School of Optometry and Vision Science
	Cardiff, CF244LU
License number	3210281506282
License date	Aug 15, 2013
Licensed content publisher	Elsevier
Licensed content publication	Progress in Retinal and Eye Research
Licensed content title	Mechanical properties of the human lens capsule
Licensed content author	Susanne Krag,Troels T Andreassen
Licensed content date	November 2003
Licensed content volume number	22
Licensed content issue number	6
Number of pages	19
Start Page	749
End Page	767
Type of Use	reuse in a thesis/dissertation
Portion	figures/tables/illustrations
Number of figures/tables/illustrations	1
Format	both print and electronic
Are you the author of this Elsevier article?	No
Will you be translating?	No
Order reference number	
Title of your thesis/dissertation	Ageing of the Human Optic Nerve Head

Expected completion date	Sep 2013
Estimated size (number of pages)	250
Elsevier VAT number	GB 494 6272 12
Permissions price	0.00 GBP
VAT/Local Sales Tax	0.0 USD / 0.0 GBP
Total	0.00 GBP

Terms and Conditions

INTRODUCTION

1. The publisher for this copyrighted material is Elsevier. By clicking "accept" in connection with completing this licensing transaction, you agree that the following terms and conditions apply to this transaction (along with the Billing and Payment terms and conditions established by Copyright Clearance Center, Inc. ("CCC"), at the time that you opened your Rightslink account and that are available at any time at http://myaccount.copyright.com).

GENERAL TERMS

2. Elsevier hereby grants you permission to reproduce the aforementioned material subject to the terms and conditions indicated.

3. Acknowledgement: If any part of the material to be used (for example, figures) has appeared in our publication with credit or acknowledgement to another source, permission must also be sought from that source. If such permission is not obtained then that material may not be included in your publication/copies. Suitable acknowledgement to the source must be made, either as a footnote or in a reference list at the end of your publication, as follows:

"Reprinted from Publication title, Vol /edition number, Author(s), Title of article / title of chapter, Pages No., Copyright (Year), with permission from Elsevier [OR APPLICABLE SOCIETY COPYRIGHT OWNER]." Also Lancet special credit - "Reprinted from The Lancet, Vol. number, Author (s), Title of article, Pages No., Copyright (Year), with permission from Elsevier."

4. Reproduction of this material is confined to the purpose and/or media for which permission is hereby given.

5. Altering/Modifying Material: Not Permitted. However figures and illustrations may be altered/adapted minimally to serve your work. Any other abbreviations, additions, deletions and/or any other alterations shall be made only with prior written authorization of Elsevier Ltd. (Please contact Elsevier at permissions@elsevier.com)

6. If the permission fee for the requested use of our material is waived in

https://s100.copyright.com//CustomerAdmin/PLF.jsp?ref=d780c...   16/08/2013

212

Appendix 5   - Copyright Licence Agreement Figure 1.6

**ELSEVIER LICENSE
TERMS AND CONDITIONS**

Sep 29, 2013

This is a License Agreement between Hannah Jones ("You") and Elsevier ("Elsevier") provided by Copyright Clearance Center ("CCC"). The license consists of your order details, the terms and conditions provided by Elsevier, and the payment terms and conditions.

All payments must be made in full to CCC. For payment instructions, please see information listed at the bottom of this form.

Supplier	Elsevier Limited
	The Boulevard,Langford Lane
	Kidlington,Oxford,OX5 1GB,UK
Registered Company Number	1982084
Customer name	Hannah Jones
Customer address	School of Optometry and Vision Science
	Cardiff, CF244LU
License number	3211960649470
License date	Aug 18, 2013
Licensed content publisher	Elsevier
Licensed content publication	The International Journal of Biochemistry & Cell Biology
Licensed content title	Tropoelastin
Licensed content author	Steven G. Wise,Anthony S. Weiss
Licensed content date	March 2009
Licensed content volume number	41
Licensed content issue number	3
Number of pages	4
Start Page	494
End Page	497
Type of Use	reuse in a thesis/dissertation
Intended publisher of new work	other
Portion	figures/tables/illustrations
Number of figures/tables/illustrations	1
Format	both print and electronic
Are you the author of this Elsevier article?	No
Will you be translating?	No
Order reference number	

213

Title of your thesis/dissertation	Ageing of the Human Optic Nerve Head
Expected completion date	Sep 2013
Estimated size (number of pages)	250
Elsevier VAT number	GB 494 6272 12
Permissions price	0.00 GBP
VAT/Local Sales Tax	0.0 USD / 0.0 GBP
Total	0.00 GBP
Terms and Conditions	

INTRODUCTION

1. The publisher for this copyrighted material is Elsevier. By clicking "accept" in connection with completing this licensing transaction, you agree that the following terms and conditions apply to this transaction (along with the Billing and Payment terms and conditions established by Copyright Clearance Center, Inc. ("CCC"), at the time that you opened your Rightslink account and that are available at any time at http://myaccount.copyright.com).

GENERAL TERMS

2. Elsevier hereby grants you permission to reproduce the aforementioned material subject to the terms and conditions indicated.

3. Acknowledgement: If any part of the material to be used (for example, figures) has appeared in our publication with credit or acknowledgement to another source, permission must also be sought from that source. If such permission is not obtained then that material may not be included in your publication/copies. Suitable acknowledgement to the source must be made, either as a footnote or in a reference list at the end of your publication, as follows:

"Reprinted from Publication title, Vol /edition number, Author(s), Title of article / title of chapter, Pages No., Copyright (Year), with permission from Elsevier [OR APPLICABLE SOCIETY COPYRIGHT OWNER]." Also Lancet special credit - "Reprinted from The Lancet, Vol. number, Author(s), Title of article, Pages No., Copyright (Year), with permission from Elsevier."

4. Reproduction of this material is confined to the purpose and/or media for which permission is hereby given.

5. Altering/Modifying Material: Not Permitted. However figures and illustrations may be altered/adapted minimally to serve your work. Any other abbreviations, additions, deletions and/or any other alterations shall be made only with prior written authorization of Elsevier Ltd. (Please contact Elsevier at permissions@elsevier.com)

6. If the permission fee for the requested use of our material is waived in this instance, please be advised that your future requests for Elsevier materials may attract a fee.

7. Reservation of Rights: Publisher reserves all rights not specifically granted in the combination of (i) the license details provided by you and accepted in the course of this licensing transaction, (ii) these terms and conditions and (iii) CCC's Billing and Payment terms and conditions.

214

Appendix 6 - Copyright Licence Agreement Figure 1.8

**WOLTERS KLUWER HEALTH LICENSE
TERMS AND CONDITIONS**

Sep 20, 2013

This is a License Agreement between Hannah Jones ("You") and Wolters Kluwer Health ("Wolters Kluwer Health") provided by Copyright Clearance Center ("CCC"). The license consists of your order details, the terms and conditions provided by Wolters Kluwer Health, and the payment terms and conditions.

All payments must be made in full to CCC. For payment instructions, please see information listed at the bottom of this form.

License Number	3233021229243
License date	Sep 20, 2013
Licensed content publisher	Wolters Kluwer Health
Licensed content publication	Journal of Glaucoma
Licensed content title	Premise and Prediction—How Optic Nerve Head Biomechanics Underlies the Susceptibility and Clinical Behavior of the Aged Optic Nerve Head
Licensed content author	Claude Burgoyne and J. Downs
Licensed content date	Jan 1, 2008
Volume Number	17
Issue Number	4
Type of Use	Dissertation/Thesis
Requestor type	Individual
Author of this Wolters Kluwer article	No
Title of your thesis / dissertation	Ageing of the Human Optic Nerve Head
Expected completion date	Sep 2013
Estimated size(pages)	250
Billing Type	Invoice
Billing address	School of Optometry and Vision Science
	Maindy Road
	Cardiff, CF244LU
	United Kingdom
Total	0.00 GBP
Terms and Conditions	

Terms and Conditions

1. A credit line will be prominently placed and include: for books - the author(s), title of book, editor, copyright holder, year of publication; For journals - the author(s), title of article, title of journal, volume number, issue number and inclusive pages.

Appendix 7 - Laboratory Stock Solutions

Preparing Phosphate Buffered Saline (PBS)

10X PBS stock:

To make 1000 ml of 10X stock solution:

1) To 800 ml double distilled water, add:

    i. 80 g sodium chloride (NaCl; Sigma, UK)

    ii. 2 g potassium chloride (KCl; Sigma, UK)

    iii. 14.4 g sodium phosphate dibasic (Na_2HPO_4; Sigma, UK)

    iv. 2.5 g potassium phosphate (KH_2PO_4; Sigma, UK)

2) pH solution to 7.4, and top up to 1000 ml with double distilled water

1X PBS solution:

Dilute 10X stock solution by a dilution factor of 10

Preparing 4% Paraformaldehyde (PFA)

4% Paraformaldehyde:

To make 100ml of 8% stock solution:

1) In the fume cupboard, dissolve 8g of paraformaldehyde (Fisher Scientific, UK) into 50ml double distilled water, warming initially to approximately 60ºC whilst stirring on a magnetic hot plate stirrer (e.g. Thermolyne Nuova, Thermo Scientific, UK)

2) When paraformaldehyde has dissolved, add NaOH (Fisher, UK) dropwise until solution clears.

3) Add 50 mls double distilled water, allow to cool and store stock solution in aliquots in the freezer.

To make 4% solution:

1) Warm up 8% stock solution at room temperature until it is clear.

2) Add an equal amount of 2X phosphate buffered saline (PBS) to make a 4% solution. pH solution to approximately pH 7.4

Appendix 8   - Copyright Licence Agreement Figure 4.1

Copyright Clearance Center

RightsLink®

| Account Info | Help |

Title:	Investigative ophthalmology	Logged in as: Hannah Jones
Publication:	Publication1	Account #: 3000686116
Publisher:	CCC Republication	
Date:	Jan 1, 1977	LOGOUT
	Copyright © 1977, CCC Republication	

Order Completed

Thank you very much for your order.

This is a License Agreement between Hannah Jones ("You") and Investigative Ophthalmology and Visual Science/ARVO ("Investigative Ophthalmology and Visual Science/ARVO") The license consists of your order details, the terms and conditions provided by Investigative Ophthalmology and Visual Science/ARVO, and the payment terms and conditions.

License number	Reference confirmation email for license number
License date	Sep 20, 2013
Licensed content publisher	Investigative Ophthalmology and Visual Science/ARVO
Licensed content title	Investigative ophthalmology
Licensed content date	Jan 1, 1977
Type of use	Thesis/Dissertation
Requestor type	
Format	Print, Electronic
Portion	chart/graph/table/figure
Number of charts/graphs/tables/figures	1
Title or numeric reference of the portion(s)	Figure 2. The SALS apparatus
Title of the article or chapter the portion is from	Quantitative Mapping of Scleral Fiber Orientation in Normal Rat Eyes
Editor of portion(s)	N/A
Author of portion(s)	Michael J A Girard
Volume of serial or monograph	N/A
Page range of portion	9685
Publication date of portion	2011
Rights for	Main product
Duration of use	Life of current edition
Creation of copies for the disabled	no
With minor editing privileges	yes
For distribution to	Worldwide
In the following language(s)	Original language of publication
With incidental promotional use	no
Lifetime unit quantity of new product	0 to 499
Made available in the following markets	Worldwide
The requesting person/organization	Hannah Jones, Cardiff University
Order reference number	
Author/Editor	Miss Hannah Jones
The standard identifier	H Jones Thesis 2013

Title	Connective tissue changes in the ageing optic nerve head
Publisher	Cardiff University
Expected publication date	Jan 2014
Estimated size (pages)	200
Billing Type	Invoice
Billing address	School of Optometry and Vision Science
	Maindy Road
	Cardiff, CF244LU
	United Kingdom
Total (may include CCC user fee)	0.00 USD

CLOSE WINDOW

218

Appendix 9 - Significant Differences between Control (C1-C3) Preferred Fibre Orientations (PFO) within 3 LC Sections